Author:
Gaxiola Peralta, Agustin De Jesus

Title:
An experimental-modelling pitch link formulation for an induced ice damaged blade and its usage in vibration-based rotorcraft-blade health monitoring

Author:
Gaxiola Peralta, Agustin De Jesus

Title:
An experimental-modelling pitch link formulation for an induced ice damaged blade and its usage in vibration-based rotorcraft-blade health monitoring

Author's declaration

I declare that the work in this dissertation was carried out in accordance with the requirements of the University's **Regulations and Code of Practice for Research Degree Programmes** and that it has not been submitted for any other academic award. Except where indicated by specific reference in the text, the work is the candidate's own work. Work done in collaboration with, or with the assistance of, others, is indicated as such. Any views expressed in the dissertation are those of the author.

SIGNED: DATE:

An experimental-modelling pitch link formulation for an induced ice damaged blade and its usage in vibration-based rotorcraft-blade health monitoring

By

AGUSTIN DE JESUS GAXIOLA PERALTA

Department of Engineering

UNIVERSITY OF BRISTOL

A dissertation submitted to the University of Bristol in accordance with the requirements of the MASTER OF RESEARCH in the Faculty of Engineering.

September 2018

Word Count: 37103

Initial proposed title and abstract topic

"Vibration-based health monitoring in active helicopter rotors".

Future rotating-wing aircraft rotors will have stiff composite blades equipped with some form of Individual Blade Control (IBC). Examples of these methods include active Pitch Links and lag dampers, distributed or discrete inertial absorbers, actively controlled surfaces or all-blade shape morphing. These technologies will be complemented by a range of motion or deformation sensors. A combination of actuator and sensor technologies will impart identity to individual rotating blades. This project will look at the health-monitoring potential of a selected subset of these IBC technologies. The existing actuator-sensor network will be used for damage detection in parallel with the primary objectives behind the IBC deployment (vibration and load management, performance etc.). A combined analytical-experimental approach to the problem of detecting changes in rotating blades based on identified dynamics will be adopted. Multi-body dynamics methods and first principle-based component models will be at the centre of analytical efforts and further work will involve tests and identification studies in the scaled rotating blade models.

"Thesis" keywords:

- *Helicopter structural dynamics.*
- *Experimental dynamic testing.*
- *Structural damage detection.*
- *Sensitivity/Vibration analysis on rotors.*
- *Pitch-link/Lead-lag damper approaches.*

Acknowledgements

To God for always being around and guiding me in this beautiful journey.

To my whole Family, my mother, my father, my sister, my brother, my sister in law and my nieces. My unconditional love for every moment and advise.

To my supervisor Dr. Branislav Titurus, thanks for every fantastic moment I have experienced with. Thanks for the amount of lessons and knowledge he have transferred me. I will always be grateful in life, for trust in me since the day one and accepting me to be an overseas postgraduate student at the University of Bristol. This experience will provide a brighter future ahead for us.

Thank you very much to all the staff and students in this University. Thankful with Dr. Jonathan Cooper, Dr. Dario Di Maio, Dr. Djamel Rezgui, Dr. Simon Neild, Dr. Anton Shterenlikht, Dr. Alexander Velichko, Dra. Tatiana Fry, Dra. Natalya Gogolitsyna. Thanks to Sarah, Emma, Irina, Reza, Irene, Nandor, Julian, Vijaya, Andrea, Eduardo, Luana, Tom, David, Ashley, Elpida, Ryamir, Xiaofu, Chris[2], Daniel, Teresa, Abdel, Robert, Samson, Elham, Jie, Salman, Alessandro, Ricardo, Giampaolo, Olivia, Robbie, Dario, Oliver, Tania, Victoria, Lena, Elena, Simon, Alia, Andrew, Kaitlyn, Clive, Mictroy, Adrian, Lisa, Denis, and family Allt.

Very special Thank you to the family Linares Dawson.

Always In my Memory: Anna Aleksandrovna Melnik.

Special mention to Mexican sponsor CONACyT for making this academic growth possible, lots of working hours were dedicated on the whole process.

Last but not least, Thanks to United Kingdom for friendly warm hospitality.

Abstract and Title of Thesis

"An experimental- modelling pitch link formulation for an induced ice damaged blade and its usage in the vibration-based rotorcraft-blade health monitoring"

Rotorcraft blades and harmonically controlled mechanisms as Pitch Links, are integrated in main rotor, these substructures are highly important because they directly influence helicopter control, performance and stability. As these rotor blade system begin to accumulate damage, structural dynamics of main rotor hub and its substructures progressively changes. In this thesis, an MBB Bo-105's rotorcraft blade model configuration was excited harmonically to obtain frequency response functions for non-rotating and rotating frames of references, different Pitch Link damages and also a few parametric uncertainties thought out blade were adopted. In parallel, an experimental case study was explored on 2 Aluminium beams, deepening experimental-modelling comparisons were carried out in only 1 beam since both are quite similar. Four models are used to perform harmonic forced vibration analysis which features coupling on both flapping-torsional deflections. This thesis covers and shows computational insights, ways how solver works, its functionality and how the model frameworks can be exploited on aero elastic rotating blades exposed to Aerodynamic and Vacuum effects. The aim behind this research is to apply sequential damages on the Pitch Link model configuration and modify the Pitch Link's properties while rotor experiences systematically changes. Monitoring results indicates that damage identifications are plausible done by using different exploration routes and suggest that by controlling Pitch Link properties, one can fully govern blade's dynamics. It was found that increasing damages in Pitch Link arm and adding Ice on the blade's tip promotes substantial changes on both first fundamental bending and torsional resonant frequencies, these were found to be highly sensitive to rotorcraft blade configurations.

Content

6.- APPLICATION: HELICOPTER DAMAGED BLADE DETECTION

7.- CONCLUSIONS AND OUTLOOK

8.- APPENDICES

CHAPTER 1 INTRODUCTION

1.1.- Helicopter world overview

Recently, the aerospace engineering industry are demanding integrity and the increase of reliability and performance in very critical rotorcraft components during flight missions and multiple actions during the travel. Normally these complex machines receive all the attention in the following aspects:

- Enhance crew efficiency and hence whole safety.
- Increase reliability of mechanical equipments.
- Monitoring fatigue lives of structural components.

From above reasons, the active helicopter vibration reduction methods have been executed potentially to attenuate and reduce vibrations. For such objectives and strategies for reducing vibration includes:

- *Higher Harmonic Control (HHC)* - By generating forces with higher harmonic loads at rotor hub, to mitigate and cancel original loads that cause vibration.
- *Individual Blade Control (IBC)* - Independent pitched blade and/or active flaps for vibration reduction and constantly looking the health monitoring.
- *Active Control of Structural Response (ACSR)* - Cockpit seats monitoring that sends signal to actuators at airframe to decrease vibration magnitude.
- *Rotor Track and Balance (RTB)* -Monitoring per cycle of rotation vertical location of each blade tip and control of mass balance distribution per blade.

In this research, the approach used is a intermix between IBC and RTB.

1.2.- Description and hypothesis of the problem under study

The rotational and centrifugal effects that occurs on the helicopter rotor blades must be operate under an acceptable threshold of displacement and/or deformation amplitudes. This ideal scenario must be perpetual and constant per revolution. However, on real performances this expected behaviours fluctuates progressively depending on the location and the extent of damages on the blade. Main hypothesis is that by monitoring the damaged vibrational response in specific locations must provide the amount of desirable data to detect and diagnose what to apply in terms of operational configuration of rotorcraft and/or apply rapidly a developing preventive and corrective maintenance. From the previous discussion, a few questions arises which implies and suggest possible routes to tackle the problems described on the hypothesis, as it follows:

- What are the best and appropriate methods used to smooth helicopter vibrations induced from the main and tail rotors?
- Which methods are the most efficient?
- What are the biggest areas of improvement that can be made in today's popular techniques for smoothing helicopter vibrations?
- Vibration problems due to defects in as-cast fabrication materials or due to improper installation of the helicopter components?
- Rotor head/blades might be affected when subjected to different weather (ice, moisture, dust, sand, etc.) cyclic changes during flight?

1.3.- Research motivations and objectives

The main research motivations in this thesis, are to perform more complex experimental and modelling methodologies that contributes scientific routes to detect and diagnose extent of damage location in the rotorcraft damaged blade. These procedures should provide data in order to prevent and mitigate failures of any kind of nature during stationary or flight condition. The mechanical vibrations behave in quite difficult forms to track down, so worldwide engineering departments have to establish efforts to control vibrations and with these actions prolonging the lifetime of the aircraft and most important the safety of all passengers on board.

Main objectives

1. Obtaining modelling platforms capable to compute the healthy and damaged resonant frequencies and normalized mode shapes.

2. Being able to introduce the descriptive equations of motions for the formulation of a Pitch Link actuator and the Ice Accretion cases.

3. Provide structural health monitoring methods base in vibrational data capable to detect and induce damages.

These objectives are chosen due to the current demand of diagnose and predict potential damages cases, therefore the combination of the three of them are needed to reach the desire state.

CHAPTER 2 LITERATURE REVIEW

2.1.- Review of Structural Health and Monitoring (SHM)

The typical SHM system's general task is to provide in return specific data that indicates the presence of damages in the best possible way. Ideally, rotational configuration and structural components are time varying domains with a potential measurement process capable to be performed for different working routines is highly desire for better performances. Deepening on HUMS aspects, Hezaham Azzam **[1]**, sums research that have been targeted at identifying strategies for the next generation of HUMS that might generate diagnostics on rotational faults and be further used in condition-based maintenance. All the efforts included the Aerodynamic models, FEM models, and a vast library of damage simulations. These were coupled with the in-service flight or the operational data to generate relationships between diagnostic, vibrations, loads and damages.

The research community by studying previews topics can be used to establish requirements for an advanced HUMS; it was concluded that transmission and rotor track and balance diagnostics could be integrated with advanced rotor diagnostics and the usages of models. HUMS was conceived, early 1980s due to the involvement of the UK Royal's Navy in vibration monitoring. Normally, the flight data and information of the existing HUMS has the following aspects: drive-train diagnostics, the rotor track and balance, exceedance monitoring, engine power assurance, monitoring usage. An important part when designing on-line SHM for rotating structures is the identification element and being able to remove the noise and isolate only vibration data from the existing damage on the evaluated system.

Over this work influence of delamination on composite disk rotors is evaluated, to identify qualitative link when changing thickness “delamination” on specific locations and study post changes of modal parameters. As the interest on SHM methods increase due the pursuit of preserving rotation systems under healthy state and good performance, the early detection of rotor blade damages is highly desired, as these elastic blades accumulates damage these can turn in to a catastrophic event.

Operational Modal Analysis (OMA) method was introduced to understand the modal parameters to detect and localize damages. As many know that damage obviously changes resonant frequencies, although in order that those changes could be observable normally a significant grow in damage must be present. The OMA work explored is better redefined and explored on **[2],** where it is also known as output only modal analysis data, which identifies modal parameters when using operation measurements in situ such as accelerations of specific sections on the blade. The OMA reasoning is that the behaviours of systems is too different when was tested structures on the laboratory, such as non-linearity, external influences, real and different conditions. On the vibration based SHM field exists four different stages to explore such as detection, localization, estimation and the predictions. In other hand, Friswell, Titurus *et. al.* **[3-5],** uses an inverse method in the damage detection and location, by using measured vibration data. For these purposes, it is suggested the use of a sensitivity-based method to identify physical parameters using a subset selection for error localization. With the additional difficulties of presence of modelling errors between model, structure and environmental factors.

Other works **[6, 7],** have used a successive parameter subset selection and multiple modal response residuals for damage detection. It was explored novel approach on this method **[6]** which is characterized by the successive application of the homogeneous modal response residuals. On research **[7],** a novel damage detection was proposed, followed by three main stages: At the first stage, the natural frequency residuals were used to indicate damage location. The second stage used local sensitivity matrix analyses which provides the understanding of the system parameter effect symmetries. The third stage propose damage detection based purely on the measured normal mode shape residuals.

2.2.- Review of damaged wind turbine rotor blades

Genariwala *et al.* **[8],** worked on the approach of detecting cracks by using modal analysis. Their principles were to detect changes in modal parameters in order to indicate physical damage. Comparing changes between operating and baseline modal parameters with certain warning levels will provide the capability to show and indicate when blades of a wind turbine have suffered physical damage. Conclusion of the tests showed that by monitoring changes in modal frequency of the first seven modes may be enough to declare and diagnostic failures on wind turbine blades. Where an independent monitoring system must be carried out by examining each blade. Modal analysis in complex structures such as CX-100 wind turbine **[9]** was obtained to validate numerical model along dynamic experimental characterization, these validation processes are quite usual exercises on the field, in order to understand the effects of structural damage responses.

Damage detection **[9]** wasn't fully approached due the lack and need of additional studies on blade, although 8 Macro-Fiber Composite (MFC) actuators were fixed on blade's centerline to evaluate effective frequency ranges, resulting that last locations towards the tip decrease response, which indicated that those locations are not effective for SHM studies. In other interesting research on SHM methods, was based as a statistical pattern recognition methodology **[10],** where the modelling components were used to study operational response for HAWT's wind turbine under three damages. Wind turbine's resonant frequencies were reduced 4% by a given 25% reduction in the root's stiffness parameter in one blade. MAC was introduced by showing modal contributions per each resonant mode, this was applied to be compared with modes that were more sensible to change in natural frequencies. The modal analysis in situ can be considered highly valuable source of structural dynamics understanding, where a SHM research of different delamination effects **[11]** was calibrated and modelled using experimental data. An important part when designing on-line SHM for rotating structures is the identification element and being able to remove the noise and isolate only vibration data from the existing damage on the evaluated system. Nevertheless, strange research tasks and detection are utilized when structures are not under operation excitations, the acoustic emission research line and their sensors are widely used for cracks, delamination, deformation on blades **[12],** PZT actuators for high frequency ranges of elastic waves on rotor blades **[13],** and the damage detection efforts in Shear Web Disbonds (SWD) in HAWTs **[14]** in order to lowering and optimized to the minimum operation and maintenance costs. During the SWD cases the reduction in torsional stiffness on the model causes noticeable effects which indicates the locations of damages. In other more precise details, by

checking percentage on flap-wise, edge-wise, axial and torsional stiffness. Since interest in SHM methods increase, the pursuit of preserving rotation systems under healthy state and good performance and the early detection of rotor blade damages is highly desired. As these elastic blades accumulates damage these can turn in to a catastrophic event. For this purpose, experimental data from the vibration analysis was obtained from a 9-meter CX-100 blade along with implementation of the machine learning **[15]** approaches for the SHM. Using high frequency response functions can permit to have a significant connection with the blade parameters such as mass or stiffness on a blade element, also wavelength of mode is a bit smaller, therefore, more sensitive to small type of damages. The main disadvantages that were found on this work was the need of 7000 Hz and lot of fatigue load cycles till reaching visible crack for a serious amount of days for a test history compilation, even though this research is for wind turbine blades this could be very negative for an on-line SHM helicopter, especially if pilot need quick directions for maintenance. SHM work on wind turbine was carried out **[16],** where a sixth DOF model was used to model a rotating rotor and also the supporting tower structure. Each blade arm was integrated with two segments connected by a torsion spring with a certain value of stiffness, in that sort of way damage was introduced by decreasing stiffness introducing a blade anisotropy into the wind turbine model. Wind turbine flap wise mode shapes can be used to detect failures, although not that easily to accomplish when is under operation **[16].** The rotation from 7200 seconds were processed which correspond to 1152 revolutions that was sampled at 50 Hz. The Floquet analysis transforms the time-periodic system of the sixth DOF wind turbine into a time invariant one, although during this transformation both periodic mode shapes and the blade coordinates are

expanded into Fourier series. The wind turbine analysis was done in non-rotating conditions, when using OMA contrary from **[16],** Floquet analysis was changed by the Multi-Blade Coordinate (MBC) transformation. The applications of OMA under operational reference was studied for a wind turbine when using an Aeroelastic mode, according to the result OMA can be applied in a straightforward way for non-rotating cases and when you are rotating few further steps are necessary in order to apply OMA. This method could help to the wind turbine society to apply post-analysis methods for the damage detection. McGugan et al. **[17],** design a method for wind turbine by applying a condition monitoring approach along a damage tolerance index that relates amount of damage for the specific material in a structure, for the only purpose of controlling the damage propagation. Main attraction of using SHM is to be able to predict in advance presence in the most accurate way, its precise position on a structure, depending the material how quick the damages “cracks” will evolve thought-out, types of defects would depend on the turbine blade design and its severity combined together will influence their remaining system operation life **[17].** Damage detection method used on **[18]** is fully based on the unsupervised anomaly technique. This is solely applied on modelling data for a healthy state, firstly is based on the training ‘learning’ stage, where it was declared the healthy state data, secondly the detection stage on which a new data is being put into comparison between healthy data. Where final detection steps on this SHM system, is based on the evaluation of which elements in the covariance matrix are the most critical affected. The recent and advanced methods of OMA have shown the steps to detect directly from modal parameters from rotating blades, which proves its applicability for the identification of damages. Most of results are good to be applied in rotors of wind turbine. Novel damage

detection on the SHM **[19],** for a wind turbine are integrated by modal-based recognition patterns by using mode shape asymmetry caused by a blade damage. Similar as **[16],** simple sixth DOF for a rotating Aeroelastic model and using Floquet Analysis for iso/anisotropy rotor blades. This method can be used on experimental and Aeroelastic modelling data. All these damage cases explored on this work can be obtained using OMA. The output from a survey has displayed that the wind turbine rotor blade itself causes more damages and problems than the gearbox and generator components. Trustworthy rotor blade SHM method has not been fully accomplish currently **[20].** So far, it looks very promising usage of strain gauges, which are popular in the laboratory of wind turbine to detect and locate damage that occurs closer to blade surfaces. However, strangely are unable to detect damages that are away from any blade surface (joint/dampers failures), which makes sensible the detection on this research.

2.3.- Review of damaged helicopter rotor blades

The rotorcraft is a multi-purposes piece of equipments “machine”, which utilizes highly flexible rotating blades to provide the action of lift, propulsion and controlling all the interactive forces. The effects of these flexible blades, its rotation and asymmetric loading conditions when is experiencing the forward flight leads to a several vibration loads. Moreover, systems are highly sensitive to progressive damage accumulation on the rotor mechanisms or in localized damages on blades named as the composite matrix cracking, delamination, fibre rupture and so many others. To overcome these hurdles and problems in real industrial machinery **[21]**, the development of Health and Usage Monitoring Systems (HUMS) has been on the spotlight for many helicopter communities on past and recent years.

A factual report shows that there were 25 reportable UK offshore helicopter accidents from 1992 to 2013. Having an overall rate of over 1 per year, which is 1.35 accidents per 100,000 flight hours. Only 7 represents technical causes, and 85% of those cases were related to rotor and transmission failures, with evidence of a tendency towards faults caused by deficiencies in designs and/or certifications in aircraft **[22]**. Furthermore, Hezaham Azzam **[23],** shows the models of rotor blade with the Aerodynamic failures that were simple and basic by promoting deviations in Aerodynamic coefficients of damages using individual blade concept where Aerodynamics, geometrical and structural properties were possible to have variations across blade, and additional input of individual blades to occasioned vibration can be further evaluated.

The first works were done by Hezaham Azzam *et al.* **[23]**, where detects crack location and size can be done by monitoring blade's natural frequency perturbations using a damage failure cases on a five bladed articulated rotor. These failures are adopted in a mathematical model where damages in the chordwise mass imbalance and the mechanical damages such faulty lag damper. This research concludes that a maximum modification or change in modal frequency happens when the failure is caused at location where input of mode to the bending moment is at its maximum. Ranjan Ganguli *et al.* **[24,25]**, use a rotor blade model and damage cases. According with the model, it was able to be modelling dissimilar or different type of blades and the damage was considered within only 1 blade, as shown in Fig. 1 **a)**.

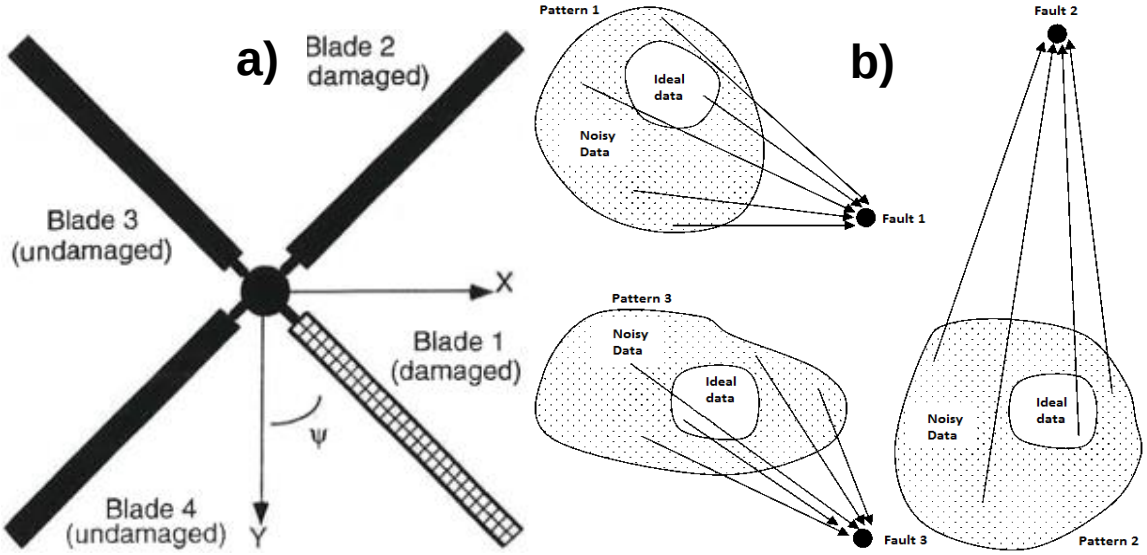

Figure 1. Blade: a) Damage blade, b) How to recognize the pattern of problem.

Ranjan Ganguli *et al.* applied finite element model to simulate damages in hovering and forward flight in an articulated four-bladed rotor. The failure cases were moisture absorption, loss of trim mass, damage in the pitch control, lag damper, structural damage, and the Pitch Link. The best part of Ganguli research was to show a range of rotor system damages estimate that can be done based on all measurements. After model development of the damaged system, they create an algorithm capable to detect damage from realistic data. Since data was noisy, there is a higher need to develop algorithms to recognize damage from noisy measurement. Model-based methods for damage detection in rotor blade are developed by solving an inverse problem using pattern recognition methods. System responses were shown as *N*-dimensional vector of real numbers, which shows a single point in an *N*-dimensional space just like in Fig. 1 **b)**. Which it simulates responses for many isolated failures into different sectors and can be related with few patterns. All 'ideal' data symbolize model predictions without noise. The method in this system worked by learning patterns for particular failures.

For instance, patterns were supposed to be detectable in different spatial regions. Sometimes it is hard to detect failures from the data with too much noise. This neural network approach is a pattern-recognition way to detect damages from the noisy data. Ranjan Ganguli *et al.* **[26, 27]**, created and used a neural network based on damage detection using simulations of a noisy rotor system. 2 neural networks were used, first to detect types of damages and second to quantify the size of it. Results shows that can detect and quantify blade damage from the noisy data. Ranjan Ganguli **[28]**, create a ground-based health monitoring system for a rotor blade by implementing a Fuzzy Logic System (FLS). It was able to work accurately at 100% of noise levels below 15% when using non-rotating frequencies and capable to decide the “undamaged’ condition up to noise levels of 30%. He created an FLS **[29]**, with failure isolation accompanied of aeroelastic analysis and using damages based on previous **[26,27].** The outcomes show that FLS isolates damages with an accuracy of 90-100%. The Stevens work **[30]** uses damages from Ranjan Ganguli *et al.* **[26]** along with the extensions of a more real crack models compatible when using model updating methods. Stevens **[30]** create an active interrogation concept for rotor failures by using trailing edge flap actuation. On this work, the rotor was modelled by using FEM with flap and torsional degrees of freedom. Many reviews point out that frequency response function (FRF) based structural damage detection techniques have been exhibited to have several advantages over modal based method “damage detection methods have a bigger tendency of work better with higher frequencies”. However, blades present several unique challenges such as centrifugal stiffening and coupling between mass and stiffness due rotation, high Aerodynamic damping.

A vibration-based model update approach derived by Yap and Zimmerman **[31]** was implemented by using a frequency domain adaptation of the asymmetric minimum rank perturbation theory. Cattarius and Inman **[32]** presented one method that was based by using time-domain and utilizes response signals only applied to a clamped section of a helicopter rotor blade. The modal methods works well with frequencies, mode shapes and the frequency response functions are also used for structural damage detection. Most of the damage detection methods can be arranged according with different dynamic characteristics and/or techniques to manage the identification of damage directly from measured data. Normally the mentioned dynamic characteristics are natural frequencies, mode shapes **[33],** mode shape curvatures **[34],** and frequency response functions **[35].** As it is known a helicopter rotor blade is no more than a long with flexible characteristics, some of the techniques that has been created for the structural damage detection in beams can be used for the diagnostics in rotor blades, more specifically when this structure is in a ground-based setting. Moreover, Kiddy and Pines **[36]** studied the applications of eigenstructure assignment methods to rotor blades. They did both analytical and two experimental works to the rotor blade for mass and stiffness damage detection. On the first experimental work, a long slender Aluminium blade was tested while rotating inside of a Vacuum chamber and actioned with a pair of piezoceramic wafers and obtaining transfer function measurements by strain gauge. The second experimental work was applied under a non-rotating condition by using an anticipated damaged TH-55A rotor blade. From the tests, it was found that stiffness changes can be properly tackled and detected by this eigenstructure method, however the mass changes were a bit difficult to detect.

This research work was extended in order to consider the rotational effects **[37].** The work was attempting to consider the mass damage which has a subsequent effect in both system's mass and stiffness matrices, related to centrifugal forces. Contrary approach **[36]**, where did not have any consideration on the effect of mass damage on the stiffness of the structure. Broadly speaking, it was possible to show the damage detection only if the damage occurred closer to a high modal energy region. Nevertheless, the damage in regions of lower modal energy were not easy to be detected with a modal-based approach. Hwang and Kim **[38],** created an approach to locate and measure the severity the damage in structures using the frequency response functions data. Purekar and Pines **[39]** simulate delamination damage ply removal of composite by using Dereverberated Transfer Function (DTF) response on helicopter flex beams. Where the structure is damage between 2 sensors, DTF response should give in return a corresponding phase change which is proportional to material degradation as waves pass through that region. Lakshmanan and Pines **[40]** utilize a wave mechanics focusing for detection of cracks in a composite beam**.** This approach, is related on local constant description of structural dynamics, uses predicted scattering patterns in order to detect/locate damages. Juan Pablo Piatti **[41]** focus his research on Euler-Bernoulli beam models, in which flaws are proved under different regions of its length. His objective was to compare the results obtained by damage indicators, and then asses its safeness throughout the length of the beam. For these purposes, it is suggested the use of a sensitivity-based method to identify physical parameters using a subset selection for error localization. With the additional difficulties of presence of modelling errors between model and structure and environmental factors. But, only one research team has specifically looked at

applying structural damage detection techniques to complex helicopter rotor system **[42].** These researchers showed some success in applying modal based technique to helicopter blade damage; however, it is difficult to measure mode shapes in flight. Over past 20 years, it has been done a significant development on experimental modal analysis techniques to get accurate measurements of modal parameter for different structures. Messina **[43]** worked on a correlation coefficient named the Multiple Damage Location Assurance Criterion (MDLAC) by introducing two methods to estimate size of damage on a structure (Locating damages at a single and multiple sites). In order to do so it is necessary ten modes and a modest number of FRF measurements are required. Furthermore, Banerjee **[44]** obtains expressions for the dynamic stiffness matrix for coupled bending-torsional vibration of a uniform beam element by using the governing differential equation of motions. However, this was done to obtain coupled natural frequencies and mode shapes with a notable amount of coupling between bending and torsional motion. An independent monitoring system must be carried out by examining each blade. One of the main trends is that at higher frequency modes the indicators are strong to localized blade cracks. A numerical aeroelastic framework and full-scale wind tunnel test was used **[45],** to explore potential of an Individual Blade Control (IBC) system to mitigate noise and vibration and improving performance of a UH-60. The acquired wind tunnel data set includes measurements of rotor performance, steady and dynamic hub forces and moments, rotor loads, control system loads, and Blade Vortex Interaction (BVI) noise. IBC motions were produced by hydraulic actuators that replaced normally rigid Pitch Links of helicopter control system. First investigations started with called Higher Harmonic Control (HHC) which has been currently replaced by the Individual Blade Control (IBC). Researches **[46],** have

been discussed the challenges of helicopter deficiencies such as noise, vibrations, etc. Regarding solving previous cases a way out was the use of active rotor control. Which can be implemented as HHC or IBC. IBC can be done by different types of concepts like multi-swashplate, smart actuators for active twist and fixed frame. Benefits of HHC and IBC have been proven many times. IBC turned out to be better than HHC due to fewer constraints. IBC can mitigate lots of typical helicopter problems, which could be considered as good news. And the bad is that for 58 years of research and development on HHC and IBC have passed by, no helicopters are equipped with those systems. A lot of research works has been done for decades on structural health monitoring using a large number of different techniques based on ultrasound, genetic algorithms, and vibration methods **[47]**, Salawu approach is channelized with the fact that natural frequencies are sensitive indicators of structural integrity and also these can be used to provide an inexpensive structural assessment. Q. Lu *et al.* **[48]** was seeking efficient methods for multiple damage locations in a beam structure where studied two different methods based in FEM. Firstly a reinforced concrete beam to compute changes in flexibility and flexibility curvature to study damage patterns. Secondly, a good correlation between relative frequency changes and analytical frequency changes were confirmed with FEM. The MDLAC is based on frequency changes and completely assumes that one frequency change pattern matches with one damage pattern. Changes in flexibility seems quite sensitive to local damages and damage successfully detected. Ranjan Ganguli **[49],** found that for a fixed-fixed beam condition, on spatial domain using the Fourier coefficients vary with the damage location and size.

Later M. Chandrashekhar and R. Ganguli **[50],** worked on a Fuzzy Logic System (FLS) with new fault isolation known as “Sliding window”, this was proposed for structural damage detection using the modal curvatures method. Damage detection in commercial and military helicopters has been studied for many authors in the past 50 years **[1].** Notwithstanding damage detection is often used for several types of structures. Literature report shows research for beam-like structure [**28**, **33**-**34**, **38**-**41**, **44, 48-55**], a metal spar [**32**], a blade [**24**, **29**, **36**-**37**, **8**], some Aluminium frames [**6**-**7**, **43**] and a full-scale rotor blade [**45**-**46**]. A 3D FEM model has been used in [**49**] to obtain mode shapes of cracked beam damage, but only to compare the results from a 1D Timoshenko beam FEM [**51**].

One pioneer work on Timoshenko beam models was evaluated [**52**], which the detection of crack location method was based on the frequency measurements. Having into account all effects of shear deformation and rotational inertia through the Timoshenko beam theory and modelling crack as a rotational spring. On research **[51,53]** assumes a Timoshenko beam model with crack, which was modelled as a sharp-edge variations of beam cross section. More recently Sergey Shevtsov *et al.* **[54],** worked in crack dentification with Timoshenko beam model. On this work it was assumed the uncertainty of monitored vibration data about the natural mode shapes and their curvatures, that caused by inaccuracy of measuring the vibrations amplitudes and surfaces strains by the set of distributed sensors. Another approaches has been the use of parameter identification of linear contact interfaces was considered by Hassan Jalali **[55],** such as joint or the boundary conditions. The model decomposes the stiffness matrix on the contact interface providing information about the parameters in that modelling region. A challenging and systematic discussions on damage prognosis **[56],** was done providing

overviews of how the solutions of problems must be addressed, a flowchart is presented where the main input elements are physics/data based. SHM method starts with testing, analyzing, maintenance period, this information is used to create the combination of sensing hardware, data interrogation and models that are intended to identify and display the system-level integrity. The dual physic-data based correlations creates a multidisciplinary method for detection, the use of an electromechanically piezo-ceramic actuator (PZT) patch is explored in **[57],** this approach is done by adding a PZT to a structure, some self-sensing actuator, by applying voltage a displacement is created in the structure and same happens when the structure is displaced a voltage is created in PZT. Authors concluded a disappointing lack of success, claiming that impedance method was unsuccessful in detecting the damages, however an increase of excitation voltage may augment sensitivity of method. Also, the understanding damage detection source **[58]** of structural dynamics it is highly important. In other interesting topics the SHM research for different delamination effects **[59]** was then calibrated and modelled using the experimental data. For this purpose, experimental data from the vibration analysis was obtained from a 9-meter CX-100 blade along with the implementation of machine learning **[60]** approaches for SHM. Using high frequency response functions can permit to have a significant connection with the blade parameters such as mass or stiffness on a blade element, also wavelength of the mode is a bit smaller, therefore, more sensitive to small damages. This type of transformation could be possible considered for a rotorcraft model, if is introduced a twelve DOF system with three segments per each blade for a four blade MBB Bo-105 rotorcraft configuration, where four root torsional spring can be considered as the Pitch Link effects on the blade dynamics.

Also, the consideration on changing the coordinates must be considered, for these purposes the BVP4c solver should be able to provide similar solving properties such as ode45. No damage extent is being explored on this work and modal contributions per modes could be desirables. The state of the art on damage sensing is wide and extent, many elements are involved at the same time, composites elements, different purposes of sensors, hardware control and cables to integrate the global network equipment within the rotor blades responses itself. Different methodologies and ideas has been under the table of discussion, some magnetic inserts in the blade's cross sections, that way a crack to be detected when the magnetic particles are suddenly exposed on blade surfaces, permitting that those magnetic particles being identifying by external sensors. Monitoring techniques and approaches are based in the damage material tolerances and structural designs, which are combines along with sensors within the rotorcraft blade structure to evaluate the healthy and damage transitions and its subsequent evolutions.

The damage detection method used on **[61]** is fully based on the unsupervised anomaly technique. This is solely applied on modelling data for a healthy state, firstly is based on the training 'learning' stage, where it was declared the healthy state data, secondly the detection stage on which a new data is being put into comparison between healthy data. Where final detection steps on this SHM system, is based on the evaluation of which elements in the covariance matrix are the most critical affected. The research outputs on **[62]** shows the application of OMA method for monitoring rotating blades in-flight missions.

2.4.- Review of literature on blade models with Ice accretion

All the modelling efforts have been undertaken and followed in order to reproduce real scenarios for rotor Ice accretion to investigate causes and their effects. Therefore, for a specific structure requires different perspectives, approaches and more specific to involve the physics environments which describes a particular action. The Ice rotor performances are being reported to produce a substantial torque **[63]** when an accumulative ice is formed away axis of rotation, vibration augments along with distortion of the air flow field around leading edge, as the results that the glaze horns becomes even more pronounced. Moreover, the aircraft parameters are then altered due changes in the body-physics, the 3D shape of the accreting body will tend to be more sensitive especially for the slender blades **[64],** performance degradation occurs when known “lobster tail” appears which is a common typical shape of the ice body similar like the curvature of a horn. Temperature ranges from -2^oC to -10^oC plays a significant role since in the period the ice starts to form and most of the cases Ice accretion shape is not that sharpie, the most similar the shape of ice is with respect to aero foil length the less sensible drag coefficient C_D will be. Later the numerical analysis on LEWICE code **[65]** was used to model ice accumulation normal to the surface “ice growth rate”, which is defined by freezing fraction and redefined to obtain ice thickness. This iced reference is then calculated in order to be re-updated for new airfoil surface, similar approach is considered on this study. A 2D blade airfoil profile **[66]** was subjected to pressure distribution analysis as this was calculated around a pre-selected ice profile. Few angles of attack and Mach numbers were explored to calculate surface pressures. This approach could play an interesting role while this is applied to ice profile within the domains of Pitch Link like structure. Calculated shear forces could

be used potentially to describe responses of the PL arm when ice around. The proper use of the known Aerodynamics coefficients like C_l, C_d, and C_m. Named as lift, the drag and the Aerodynamic moment coefficients respectively **[67].** These coefficients were analyzed vs. variation of angles of attack on clean and iced airfoil profiles. A set of remarkable differences are reported between the lift vs. drag coefficients, more specifically for the changes in the shapes of the artificial ice, for more complex sharp-edged plates such as horns, more drag will provide with less lift coefficient. This type of shape might provide a reduction on the system's damped torsional frequencies. In other interesting aspects on blade performance is the effects of ice on the operation conditions **[67,68],** the resultant lift force creates shear forces and bending moments related with blade/ice adhesion, which eventually will turn in breaking off the formed ice, this resultant lift force previously mentioned must and could be modelled and include into the Aerodynamic loads in ODE's from the BVP4c formulation. In the wind turbine industry and manufacturers, rather than inspecting and detecting Ice accretion, they are just monitoring the power outputs **[69]** coming from nacelle anemometer.

A power reduction of around 25% is reported to be main causes of the presence of ice on the blades. Some other measures the sky temperature and compare it with air temperature around the wind turbine towers **[70]** while inspecting power curves, endless application on blade heaters are been under study although they don't have the power enough to de-icing in rightly way. Global mass of the ice should be used as an axial force **[71],** which must be taken into account, therefore an additional centrifugal force should be introduced into BVP4c, in the following form, $F_I = m_{ice} r\Omega^2$. If there are more than 1 blocks of ice, therefore additional forces should be introduced as well, in contrary than a longitudinal and

homogenous block of ice is formed, only 1 centrifugal force should be applied. A vertical lift research center of excellence in Pennsylvania, implement an Adverse Rotor Test Stand (AERTS), which eventually was evolving into AERTS Rotor Icing Shedding & Performance Model (ARISP) **[72].** ARISP code differs with the fact that the condition changes as the time passes, the sectional angles of attack might be changing due to ice, when time passes ice profiles requires to be constantly updated. Also, a model analysis should contain a series of elements/calculations per each considered ice bodies attached, some calculation on adhesion and cohesion forces coming from ice blade are adopted.

Most of the studies related to wind turbine towers and Ice accretion on blades, provide general output indicators that concludes and confirmed changes that were observed in the responses of the flap (bending) measurement **[73].** Although winter normally brings with it, with favorable and nice wind conditions. As ice is accumulated under operation, both centrifugal and shear forces act on both ice/blade surfaces of contact, when these components are closer to rotational speeds of zero or near, the centrifugal forces and Aerodynamic moments tends to be smaller, also it permits to accumulate even more ice on the blade airfoil. When blade rotational speed increases bending moment and shear forces creates the break of the ice, the magnitude of this actions are being reported to pose a risk to civil structures and life. On **[74],** ice is attempted it to be simulated by increasing the blade mass density in close order of $1/20^{th}$ of the nominal value on the applicable blade elements, also the coefficient of lift C_l was reduced $1/10^{th}$. Modelling criteria has many issues involve **[75]** in their processes: The thickness of the sections of study, both blade radius and chord altered in the mass distribution, changes in the Aerodynamic load due ice, some possible blade iced,

some others not, imbalances on the rotor, etc. Later stages a 2D Ice accretion TURBICE model platform **[76]** was explored with a different set parameter from our approach, which investigates the changes on the lift coefficient C_l on time domain and analyses the stall. Even though, they explore opposite things to BVP4c, main finding contribution is than Lift coefficient C_l decrease while Drag coefficient C_d increase when ice augments, this can be set as input parameter in Aerodynamic loading on the BVP4c field equations along with air density of cold winter region plus adding a punctual mass of total Ice accretion body acting as gravity force.

Among the existing wind turbine ice detection, power curve is reported to be an effective blade-based method **[77],** as performs only when the rotor is under operation. Ice Meister 9732 was designed for aircraft and suitable for wing/blade tips, capable to assess the ice formation by using Bluetooth wireless data transfer. For modelling purposes, a specific geometry for Ice accretion body is reported to be applied for experimental purposes **[78],** since normally tips have higher angular velocities and reaches higher elevations ice usually forms around tip with more presence and less toward the blade root, resulting as a triangular-like load on the tip. This principle was already assumed on the model of this research. For some researches while running Ice accretion experiments **[79],** its comes handy and useful usage of environmental temperatures in rotational chamber, proper and good regulations on the injections of micro-size water droplets in order to get the Liquid Water Content (LWC) at the desired levels, all parameters compared under time domain should influence directly growth rate on injected regions, experimental morphologies of ice must be implemented for modelling purposes, which shows higher density of ice on tip and some radial iced lines as a result of the airflow.

Towards modelling accurately, Aerodynamic loads and Ice accretion distribution is hard to estimate which would be the ice differences from different blade sections**,** therefore the estimation of blade tip Aerodynamic properties are very important as they influence the blade responses. The resultant lift force should alter the torsional frequencies, as a result of more torque present compared with a healthy condition torque. These changes affects the helicopter power outputs, especially when the system requires to perform smoothly and safe a specific mission under ice environments.

2.5.- Review of literature on Pitch Link (PL) models

In this research work, a novelty approach for Pitch Link boundary conditions are derived using its physics (Its geometrical characteristics and the L-shape arm interconnected with the swashplate, therefore the bending displacements, angle due bending and torsional deformations were adopted) and adding intersegmental discretization to introduce the Pitch link loads which induces changes on the rotor blade motions and therefore subsequent damages cases are adopted, which makes this research highly attractive. The most contrasting elements to consider are the usage of operational modal data as the main motivation for the damage detection investigation, since it is the closest possible scenario of the real rotorcraft behaviours. In this thesis, the Pitch Link force **[80]** was adopted by assuming the forces generated by the actuator, therefore the governing equation of motion was derived by using 2 pressurized chambers that are related with the flow rates generated through the chamber orifices.

An active (hydraulically controlled using time-domain while system rotates) Pitch Link **[81]** was used with 2 springs that allows only the horizontal displacement to control the in-plane deformations. Researchers represent a 15-DOF nonlinear beam elements **[82],** where the components are connected by the hinge joints to introduce a Pitch Link, flapping hinge, and lag dampers. These previous elements were treated as linear spring-damper force elements. The summation of the forces between both the helicopter blade and the Pitch Link **[83,84]**, results from many geometrical characteristics of the components and assuming the properties of the elastomer bearing such as the Pitch Link stiffness and damping. The spring's mass is connected with the swashplate, where the deformations of this spring causes displacements and accelerations in response to the applied Pitch Link force that depends completely of the torsional deformations and the geometrical dimensions of the L-shape arm. These previous references were used in this thesis, since it was considered to be the best suitable features to be modelled. When analyzing these Pitch Link loads **[85,86],** some researchers take into account the 3 Pitch Link controls and also 2 rotor angles were adopted to solve the equilibrium equations. The fluidlastic isolator is described by a tuning mass which is constantly controlled to absorb the kinetic energies that are produced, and therefore changes in the natural frequency "NF", the NF is proportional to the Pitch Link stiffness, the tuning mass, and the ratio between the distances of the tuning mass and the Pitch Link device. This tuning frequency is presented by using the desired frequency of the harmonic load to be isolated, a Tuned Vibration Absorber (TVA) type of approach.

CHAPTER 3

MODELLING METHODOLOGY

3.1.- Rotorcraft blade problem definition and the spatial axis system

In this research, four different cantilever beam models were developed, and directly implemented for simulation on a non-rotating helicopter pitched blade-like experimental rig, and model 4 was selected to be representing the MBB Bo-105 helicopter blade structural dynamics. Each model would be introduced and further explained in the next sections, where main justification of using 4 models is related with comparative framework analysis between them. From spatial point of view and fully based from real rotor blades as shown in Fig. 2, helicopter models have a composite cross section blade with asymmetry mass and elastic axis that plays a significant role. The rotorcraft blades experiences constant rotation speed about its main hub, where system is cyclically controlled by the Pitch Link coupled and interconnected with swashplate, which is a rotating component that governs the angular deformation per each blade. The rotor blade itself can be treated as a single element body, where the dynamics of the system can be altered when exposed under different Pitch Link L-shape arm critical damages, the external Aerodynamic effects and progressive Ice accretion conditions.

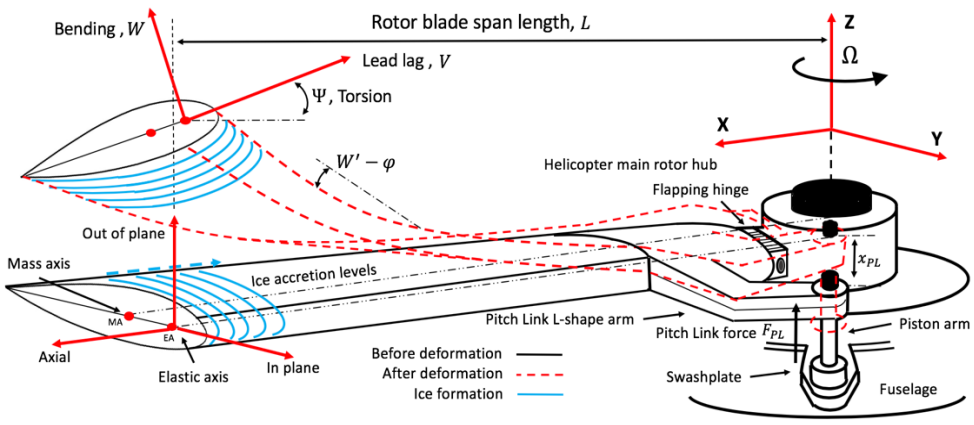

Figure 2. Rotorcraft pitched blade spatial axis system.

The four model formulations for experimental non-rotating Advanced beams assumes that both mass axis and elastic axis are coincident about a chord axis. To obtain the equations of motions of the models the Hamilton's principle was then applied for deformable bodies and their variations in elastodynamics elements in the 4 models as in the equations (1):

$$d\int_{t_1}^{t_2}(U - Á - W)dt = 0 \qquad \textbf{(1)}$$

Where:
δ = Variational operator,
t_1 = Initial interval from dynamic deflection,
t_2 = Final interval from dynamic deflection,
U = Kinetic energy,
$\Im$ = Potential energy,
W = Damping energy,

All models can be derived by obtaining both kinetic and potential energies equations for the systems. Models are linear and is assumed that performs a free vibration without the damping forces involved, therefore the terms δW would be considered equal to zero. The definition of the nature of damping effect is to remove the energy from a system under vibration, understanding this concept can describe a blade under rotation like a simple element connected at the rotor hub which only depends purely from its mass and stiffness, therefore the energy lost due to the damping is not considered to being transmitted away from the system using any mechanism capable to dissipate energy within the system. Another reason of removing the damping forces is that magnitude of the damping forces is considered to be small compared with the elastic and inertia forces. Force vibration can be assumed that occurs when modelling the effects of the forces coming from the Pitch Link and swashplate system, as this applied force is altered by modifying Pitch Link Stiffness, this would be further explained in detail in the chapter 3.5.

Four beam models were implemented to calculate structural dynamics of an experimental non-rotating blade-like rig. Main justification and reason of using four models is to apply same parametrical cases of studies from the experiments, subsequently the results were compared, benchmarked and validated the physical responses as is expected to behave similar since the applied physics onto the modelled blade are meant to involved similar physical boundary conditions. These four models discussed in chapter 3.2 were introduced to analyze the performance of the rotational blade and centrifugal effects on both Vacuum and Aerodynamic environment. For this purpose, parameters based in German MBB Bo-105 **[87,88]** helicopter were adopted to model the cases of study explored in the experimental beam. It is highly desirable outlining each modelling system in an independent way as they contain their unique nomenclature and assumptions. Model 1-2 are without rotations and model 3-4 are develop in rotations. In contrast with Houbolt-Brooks model derivations, where assumes coupling about inertia and centrifugal force and does not consider deformation due shear, although considers pre-twisted angle on blade. In this research pre-twisted angle in the blade was not considered.

3.2.- Mathematical models and derivation of the equations of motions

3.2.1.- Model 1: Coupled bending-torsional “Euler Bernoulli”

The first model is related to a static beam approach using Euler-Bernoulli equation for a free vibration case, equations are referred and shown in Fig. 3, **[89].** The system describes the relationship between beam’s deflection and the coupling torsional effects resulting from the application of a distributed load at any location away from the “neutral” elastic axis. Where comprehends of two coupled bending and torsional descriptive sets of differential equation of motions that are given in the equations (2) and (3) respectively.

From these, the bending moments will be coupled, and its deflections would depend with the amount of torsional angular deformation, this torque effect will be greater if this occurs with greater distances away from the neutral axis, Ref **[89]:**

$$\frac{\partial^2}{\partial y^2}\left(EI\frac{\partial^2 h}{\partial y^2}\right)+m\frac{\partial^2 h}{\partial t^2}-mx_a\frac{\partial^2 y}{\partial t^2}=0 \quad \textbf{(2)}$$

$$\frac{\partial}{\partial y}\left(GJ\frac{\partial y}{\partial y}\right)+mx_a\frac{\partial^2 h}{\partial t^2}-I_a\frac{\partial^2 y}{\partial y^2}=0 \quad \textbf{(3)}$$

Where:

EI = Bending rigidity, [Nm^2].
GJ = Torsional rigidity, [Nm^2].
m = Mass per unit length, [Kg/m].
I_α = Polar mass moment of inertia per unit length about Y-axis, [Kgm].
x_α = Distance between centroid (Gs) to shear centre (Es) axis, [m].
H = Bending vertical displacement,
Ψ = Torsional angular deformation,

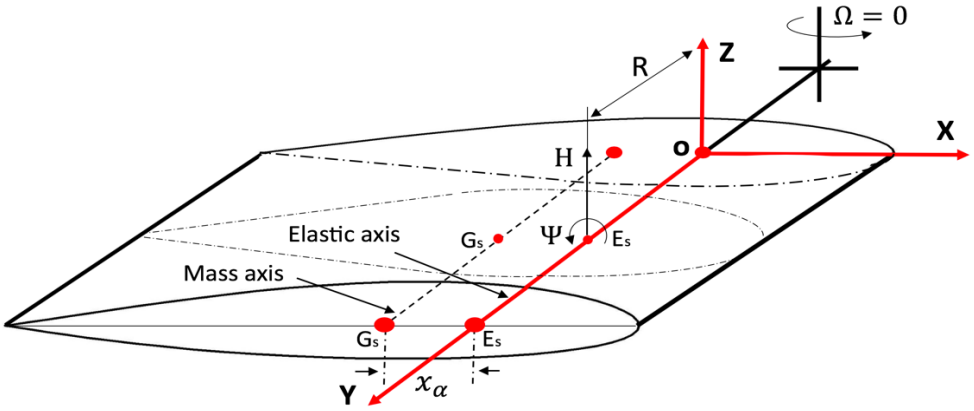

Figure 3. Coupled bending-torsional beam vibration coordinate system.

It was assumed a sinusoidal variation for *h* and ψ with respect to the circular frequency ω, then responses result as follows:

$$h(y,t)=\mathrm{H}(y)\cos wt \quad \textbf{a)} \qquad y=\mathrm{Y}(y)\sin wt \quad \textbf{b)} \quad \textbf{(4)}$$

Where $\mathrm{H}(y)$ and $\Psi(y)$ describes the amplitude of the sinusoidally variations in vertical displacement and torsional rotation. Substituting equations 4 **a)** and 4 **b)** into (2) and (3) is obtained coupled bending-torsional Equation of Motions (EoM's):

$$EI\frac{d^4\mathrm{H}}{dy^4}-mw^2\mathrm{H}+mx_a w^2\mathrm{Y}=0 \quad \textbf{(5)}$$

$$GJ\frac{d^2\mathrm{Y}}{dy^2}+I_a w^2\mathrm{Y}-w^2 mx_a\mathrm{H}=0 \quad \textbf{(6)}$$

The number of BC's of this model are six, four for bending deflection and two for torsional deformation. From the previous EoM's, the transverse "Flapping" vibration will always be coupled with torsion; Therefore, these coupled motions will be an interaction between bending deflections and torsional angular deformations. Where the larger the separations of those axis the more coupled and stronger would be the torsional vibration.

3.2.2.- Model 2: Transverse-lateral vibration with torsional coupling "Euler Bernoulli"

Second model studies an ideal helicopter blade along 2 axes of deflections. It contains a non-coincident mass and elastic axis with respect to in plane and out of plane airfoil cross section, as shown in the Fig. 4 **[90].**

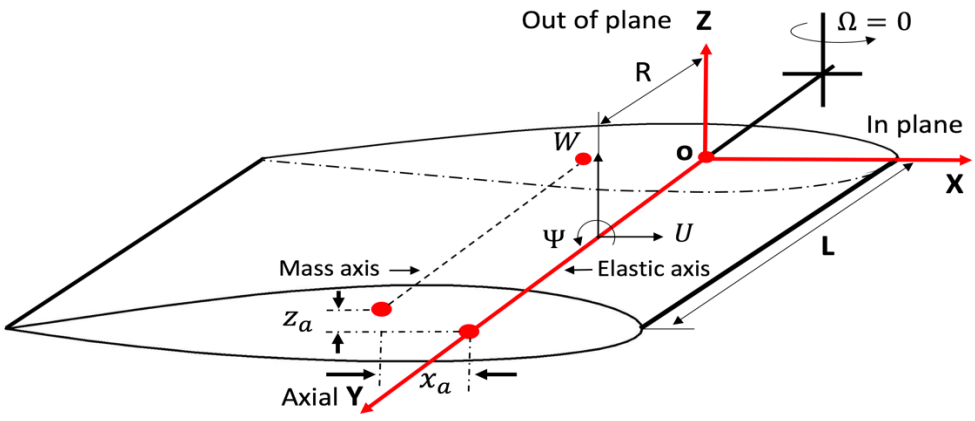

Figure 4. Beam view of bending-torsional coupled beam.

The system allows to deflect on out of plane $w(y,t)$ and permits to rotates about "o" by $\Psi(y,t)$. The mass moment of inertia per unit length about mass axis is shown in (7). The governing differential equations results from the kinetic energy and potential energy of a bending-torsional coupled beam as equations (8) and (9).

$$I_G = I_a - m\left(x_a^2 + z_a^2\right) \tag{7}$$

$$U = \frac{1}{2}\int_0^L \left[m\left(\dot{u} + \dot{w} + 2\dot{u}z_a\dot{\psi} - 2\dot{w}x_a\dot{\psi}\right) + I_\alpha\dot{\psi}^2 \right] dy \tag{8}$$

$$\Im = \frac{1}{2}\int_0^L \left[EI_1\left(w''\right)^2 + EI_2\left(u''\right)^2 + GJ\left(y'\right)^2 \right] dy \tag{9}$$

Substituting both kinetic and potential energies into the Hamilton's equation (1) and integrating all terms by parts, the resulting and collected terms are obtained as the following governing differential equations, Ref **[90]:**

$$EI_2 u'''' + m\ddot{u} + mz_a\ddot{\psi} = 0 \quad \textbf{(10)}$$

$$EI_1 w'''' + m\ddot{w} - mx_a\ddot{\psi} = 0 \quad \textbf{(11)}$$

$$GJ\psi'' - mz_a\ddot{u} + mx_a\ddot{w} - I_\alpha\ddot{\psi} = 0 \quad \textbf{(12)}$$

Free Euler Bernoulli beam undamped $(W = 0)$ vibration and its oscillations also were assumed to be harmonic in this system, then:

$$u(y,t) = U(y)e^{i\omega t} \quad \textbf{a)} \qquad w(y,t) = W(y)e^{i\omega t} \quad \textbf{b)} \qquad y(y,t) = \Upsilon(y)e^{i\omega t} \quad \textbf{c)} \quad \textbf{(13)}$$

Therefore, the assumption solutions from 13 a), 13 b), and 13 c) were then introduced into the equations (10), (11), and (12) to become the final set of Ordinary Differential Equations (ODE's) as in (14), (15), and (16). The number BC's in this model are 10, 4 for bending, 4 for lead-lag and 2 tor torsion:

$$U'''' - \frac{m\omega^2}{EI_2}U - \frac{m\omega^2}{EI_2}z_a\Upsilon = 0 \quad \textbf{(14)}$$

$$W'''' - \frac{m\omega^2}{EI_1}W + \frac{m\omega^2}{EI_1}x_a\Upsilon = 0 \quad \textbf{(15)}$$

$$\Upsilon'' + \frac{m\omega^2}{GJ}z_aU - \frac{m\omega^2}{GJ}x_aW - \frac{I_a\omega^2}{GJ}\Upsilon = 0 \quad \textbf{(16)}$$

Where:

EI_1 = Bending rigidity about in plane axis (lead-lag), [Nm^2].
EI_2 = Bending rigidity about out of plane (flapping), [Nm^2].
GJ = Torsional rigidity, [Nm^2].
m = Mass per unit length, [Kg/m].
I_α = Polar mass moment of inertia per unit length about Y-axis, [Kgm].
x_a = Distance between elastic axis to mass axis, [m].
z_a = Distance between in-plane axis to mass axis, [m].
ω = Frequency of oscillation, [rad/s].
U = Lead-lag amplitudes of u,
W = Bending amplitudes of w,
Ψ = Torsional amplitudes of ψ,

3.2.3.- Model 3: Rotating flap, lead-lag, with torsional coupling "Timoshenko"

Rotating Timoshenko beam theory was studied for free undamped vibration analysis by obtaining EoM's for both flap-wise and chord-wise bending-torsional based as shown in the Fig. 5, **[91].** Main contrast and comparison between Euler Bernoulli theory are that Timoshenko theory considers the shear deformation coupled with rotational inertia "bending" effects. In other words, during testing the beam's cross section become curved, this contribution comes from the shear deformation which will provide accuracy in total deformation. This approach is desirable to interpret behaviours of thick beams or composite beams "rotor blades". Broadly speaking, Timoshenko predicts more accurate due to the 6 fundamental kinematic variables as shown in (17), compared with 4 fundamental kinematic variables on Euler Bernoulli, being "z" flapping axis, and "y" lead-lag axis. Note that on this model the next 3 notations $[xx,hh,xh]$ are related to the coordinates $[Z,Y,ZY]$.

$$\left[w_z, w_y, j_z, j_y, y_z, y_y\right] \tag{17}$$

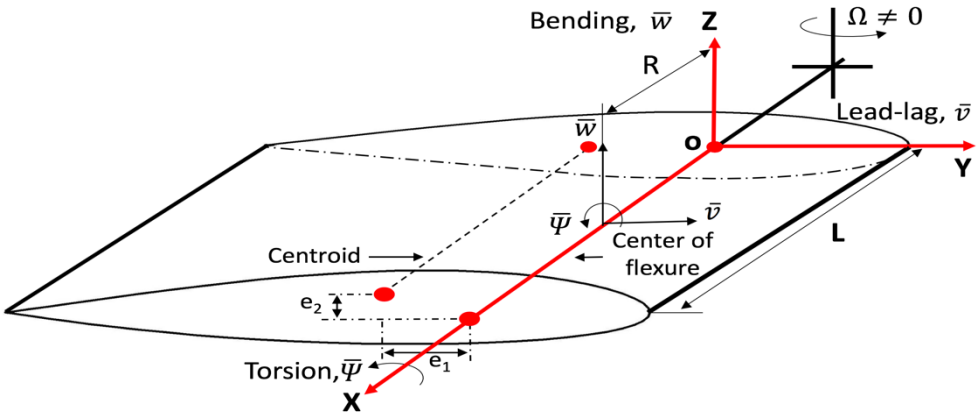

Figure 5. Rotating Timoshenko beam with asymmetric airfoil cross section.

The resulting final EoM's of model 3, was derived from the combination of the total "potential" strain energy expression, as equation (18) and the total "kinetic" energy expressions, are shown in the equation (19):

$$U = \frac{1}{2}\int_0^L \left[T(x)\left[(v')^2 + (w')^2 + \frac{I_a}{rA}(y')^2 - 2e_1 j_y - 2e_2 j_z \right] + EI_{xx}(j_y')^2 + EI_{hh}(j_z')^2 + kAG(w' - j_z)^2 + kAG(v' - j_y)^2 + GJ(y')^2 \right] dx \quad \textbf{(18)}$$

$$\Im = \frac{1}{2}\int_0^L \Big\{ 2\rho A e_1 \left[\Omega^2 v + \dot{w}\dot{\psi} - \Omega^2 (R+x)(\psi\varphi_z + \varphi_y) \right] - 2\rho A e_2 \left[\Omega^2 v\psi + \dot{v}\dot{\psi} + \Omega^2 (R+x)(\psi\varphi_y + \varphi_z) \right] + \rho I_{\xi\xi}(\dot{\varphi}_y^2 + \Omega^2\varphi_y^2) + \rho I_{\eta\eta}(\Omega^2\psi + \Omega^2\varphi_z^2 + \dot{\varphi}_z^2) + 2\rho I_{\xi\eta}(\dot{\varphi}_z\dot{\varphi}_y + \Omega^2\varphi_z\varphi_y - \Omega^2\psi) + \rho A(\dot{v}^2 + \dot{w}^2 - \Omega^2 v^2) + I_\alpha\dot{\psi}^2 \Big\} \quad \textbf{(19)}$$

Global associated EoM's were obtained by applying Hamilton's equation (1). The resulting final ODE's are shown in (20), (21), (22), (23), and (24), Ref **[86].** Number BC's in this model are 10, 2 for bending, lead-lag and torsion plus 2 for rotational angles about chord and flapwise directions.

$$(T\bar{v}')' + kAG(\bar{v}' - \bar{j}_y)' - rAW^2(e_2\bar{y} - \bar{v}) + rAw^2(\bar{v} - e_2\bar{y}) = 0 \quad \textbf{(20)}$$

$$(T\bar{w}')' + kAG(\bar{w}' - \bar{j}_z)' + rAw^2(\bar{w} - e_1\bar{y}) = 0 \quad \textbf{(21)}$$

$$\frac{I_a}{rA}(T\bar{y}')' + GJ\bar{y}'' - rAW^2\left[(R+x)(e_1\bar{j}_z - e_2\bar{j}_y) + e_2\bar{v} \right] + rW^2 I_{hh}\bar{y} + rAw^2(e_1\bar{w} - e_2\bar{v}) + I_a w^2\bar{y} = 0 \quad \textbf{(22)}$$

$$EI_{xx}\bar{j}_y'' + kAG(\bar{v}' - \bar{j}_y) + rAW^2(R+x)e_2\bar{y} + rW^2(I_{xx}\bar{j}_y + I_{xh}\bar{j}_z) + rw^2(I_{xx}\bar{j}_y + I_{xh}\bar{j}_z) = 0 \quad \textbf{(23)}$$

$$EI_{hh}\bar{j}_z'' + kAG(\bar{w}' - \bar{j}_z) - rAW^2(R+x)e_1\bar{y} + rW^2(I_{hh}\bar{j}_z + I_{xh}\bar{j}_y) + rw^2(I_{hh}\bar{j}_z + I_{xh}\bar{j}_y) = 0 \quad \textbf{(24)}$$

Where:

T = Centrifugal force, [N].
kAG = Shear rigidity, [N].
ρA = Mass distribution, [Kg/m].
Ω = Constant rotational speed, [rad/s].
ω = Circular natural frequency of oscillation, [rad/s].
I_α = Mass moment of inertia about elastic axis, [m].
GJ = Torsional rigidity, [Nm^2].
e_1, e_2 = Distance from center of flexure to centroid about Y and Z-axis, [m]
$I_{\eta\eta}$, $I_{\xi\xi}$ = Second moment of inertia about Y-axis and Z-axis, [m^4].
$I_{\xi\eta}$ = Polar moment of inertia about X-axis, [m^4].
$EI_{\xi\xi}$ = Bending rigidity about flap-wise deformations, [Nm^2].
$EI_{\eta\eta}$ = Bending rigidity about chord-wise deformations, [Nm^2].
$\bar{v}$ = Lead-lag bending displacement,
$\bar{w}$ = Flapping bending displacement,
$\bar{\Psi}$ = Torsional angle of deformation,
$\bar{\varphi}_y$ = Rotation angle due chord-wise bending,
$\bar{\varphi}_z$ = Rotation angle due flap-wise bending,

3.2.4.- Model 4: Rotating bending-torsional coupling “Timoshenko”

The final fourth model is related to the rotating Timoshenko beam theory applied to free undamped vibration analysis for system shown in the Fig. 6, **[92].** Model features coupling between both flap-wise bending and torsional vibration, the expressions for Bending-Torsional kinetic energy are shown as in (25):

$$U = \frac{1}{2}\int_0^L \left\{ EI_y\left(j'\right)^2 + \mathrm{T}\left[\left(w'\right)^2 + \frac{I_a}{rA}\left(y'\right)^2\right] + kAG\left(w' - j\right)^2 + GJ\left(y'\right)^2 \right\} dx \qquad \textbf{(25)}$$

The potential energy expression is given by equation (26), as a result of the global combination of velocities components from three coordinates:

$$\Im = \frac{1}{2}\int_0^L \left\{ \rho A\dot{w}^2 + \rho I_y\left[\Omega^2\varphi^2 + \dot{\varphi}^2 + 2\Omega\left(\dot{\psi}\varphi - \dot{\varphi}\psi\right)\right] + I_\alpha\dot{\psi}^2 + \rho\left(I_y - I_z\right)\Omega^2\psi^2 + 2\rho I_z\Omega\left(\dot{\psi}\varphi + \dot{\varphi}\psi\right) + 2\rho Ae\left[\dot{w}\dot{\psi} - \left(R + x\right)\Omega^2\right]\psi\varphi \right\} dx \qquad \textbf{(26)}$$

The equations (25) and (26) were substitute into the Hamilton’s equation (1). In this research, these final equations are evaluated for 2 cases as shown in the (27), (28), (29) for non-rotating, and (30), (31), (32) for rotating system, Ref **[92]**:

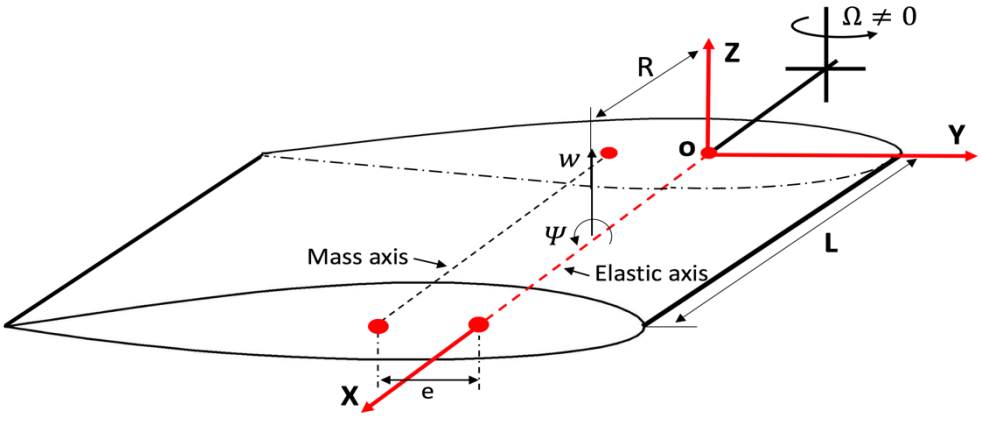

Figure 6. Rotating cantilever Timoshenko beam model.

Case 1: When $\Omega = 0$ (Non-rotating blade), to model modal testing of beams.

$$\omega^2 \rho A\bar{w} + \omega^2 \rho Ae\bar{\gamma} + kAG\left(\bar{w}'' - \bar{\varphi}'\right) = 0 \quad \textbf{(27)}$$

$$\rho I_y \omega^2 \bar{\varphi} + EI_y \bar{\varphi}'' + kAG\left(\bar{w}' - \bar{\varphi}\right) = 0 \quad \textbf{(28)}$$

$$\omega^2 I_\alpha \bar{\gamma} + \omega^2 \rho Ae\bar{w} + GJ\bar{\gamma}'' = 0 \quad \textbf{(29)}$$

Case 2: When $\Omega \neq 0$ (Rotating frame of reference), to model aeroelastic cases.

$$\omega^2 \rho Aw + \omega^2 \rho Ae\gamma + \left(Tw'\right)' + \left[kAG\left(w' - \varphi\right)'\right]' = 0 \quad \textbf{(30)}$$

$$\rho I_y \omega^2 \varphi + \rho I_y \Omega^2 \varphi + \left(EI_y \varphi'\right)' + kAG\left(w' - \varphi\right) - \rho Ae\Omega^2 \left(R + x\right)\gamma + 2\rho I_y \Omega\dot{\gamma} = 0 \quad \textbf{(31)}$$

$$\omega^2 I_\alpha \gamma + \omega^2 \rho Ae w + \rho\left(I_y - I_z\right)\Omega^2 \gamma + \left(GJ\gamma'\right)' + \left(T\frac{I_\alpha}{\rho A}\gamma'\right)' - \rho Ae\Omega^2 \left(R + x\right)\varphi - 2\rho I_y \Omega\dot{\varphi} = 0 \quad \textbf{(32)}$$

Where:

T = Centrifugal force, [N].
kAG = Shear rigidity, [N].
ρ = Material density, [Kg/m^3].
ρA = Mass distribution, [Kg/m].
Ω = Constant rotational speed, [rad/s].
ω = Circular natural frequency of oscillation, [rad/s].
I_α = Mass moment of inertia about elastic axis, [Kgm].
GJ = Torsional rigidity, [Nm^2].
e = Distance between centroid of cross section and elastic axis, [m].
I_y = Second moment of inertia about Y-axis (in plane), [m^4].
I_z = Second moment of inertia about Z-axis (out of plane), [m^4].
E = Young's modulus, [N/m^2].
w = Flapping bending displacement,
Ψ = Torsional angle of deformation,
φ = Rotation angle due to bending,

3.3.- Solving the Ordinary Differential Equations (ODE's) in Matlab

A numerical-mathematical computational package known as BVP4c **[A]** was then adopted, which is a Boundary Value Problem (BVP) solver from Matlab, that attempts to encounter many solutions for given descriptive Collocation Method. More specifically, the models aims to execute several calculations on two following directions: Firstly, analytically undamped free coupled bending-torsional vibrations in helicopter blade models (for different cases of study). Secondly, experimental modal analysis on complex and advanced Aluminium pitched blade-like structures, for helicopter blade structural health monitoring studies for damage detection applications. A representation of the pitched blade-like system is shown in Fig. 7.

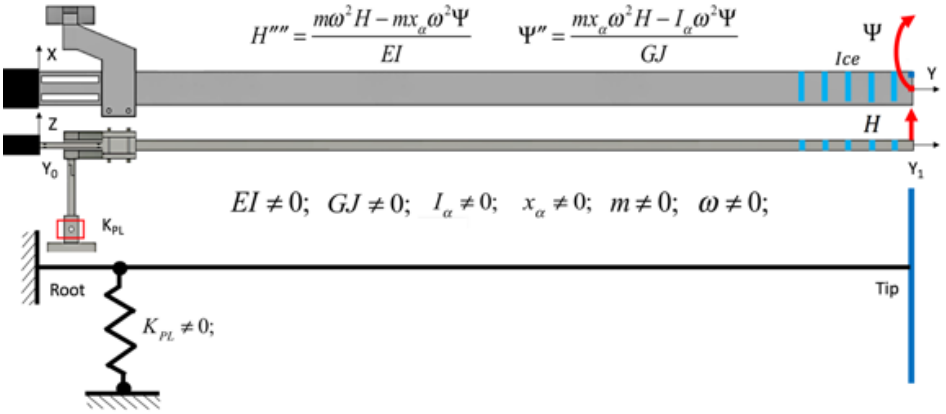

Figure 7. Aerial and side view of the coupled cantiever beam under analysis.

Based in previous beam and the Model 1 as practical reference of example. Proceeds now to describe how it runs BVP4c solver as shown in Fig. 8. Firstly, introducing physical beam parameters to define "control parameters". The usage of ODEs in BVP4c solver can provide solutions to a descriptive phenomenon which change continuously as you modify all variables involved. Notwithstanding, in the practice, it can only satisfy for only two conditions (e.g. considering function named H'''', and the beam's geometrical mesh of $[y0\ \text{"root"}\ ,\ y1\ \text{"}tip\text{"}]$,) shown in Fig. 7.

[A] https://www.mathworks.com/help/matlab/ref/bvp4c.html

BVP method would be described in equation $H''''(y) = \frac{m\omega^2 H(y) - mx_\alpha \omega^2 \Psi(y)}{EI}$ (where y stands for axial location, plus the H and Ψ for bending and torsional deflection solutions) after many calculations provides only 1 solution in the problem. The first boundary condition (BC) says that all solutions will always start to develop from initial point $y0 = 0$, known as first estimate solution. As the solver iterates from different domain of interest on each location of y ($y0$ stands for root and $y1$ for tip), where will have six deformations $y = [H, H', H'', H''', \Psi, \Psi']$ per each beam station. From the previous example for fourth order and second order ODEs $(4 + 2 = 6)$, the sixth order implies that there will be 6 points of BCs per each beam location. Considering bending deflection function $H(y, S)$ as solution of fourth order is then evaluated starting from root as $H(y0) = A$, throughout beam until it reaches the tip $H(y1) = B$. The solution A stands as deflection in the root (no deflections) and term S will be unknown initial guess estimate that satisfies the problem, considered as continuous function "cubic polynomial" on each subinterval $[y_n, y_{n+1}]$ or allocated position in $[y0, y1]$. Thereby, every calculation on $H(y, S)$ will attempt to get closer to value $H = y1$, the code will search which value for "S" complement $H(y1, S) = B$ Each iteration delivers a match for $H(y, S)$, then BVP can be call satisfactory.

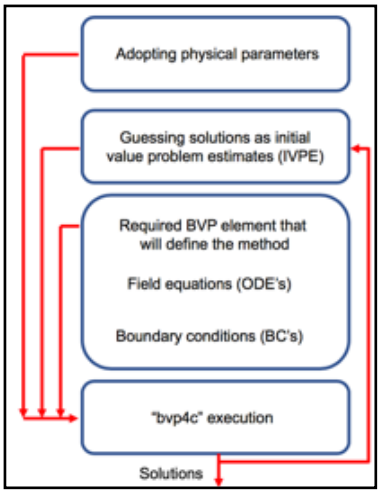

Figure 8. Layout schematic of the BVP4c structure used for calculations.

To obtain BVP4c solution is needed to describe the system shown in Fig. 7. From the Matlab point of view the element "fcn_bc" boundary condition function which computes system in starting from left $y0$ (root) to the right $y1$ (tip) hand side, and according with the sixth order differential equation system, there will be four elements for the bending deflection and two for torsional deformations to complete matrix function as shown in (33):

$$fcn\_bc = \begin{bmatrix} H_0 & H_1 \\ H_0' & H_1' \\ H_0'' & H_1'' \\ H_0''' & H_1''' \\ \mathrm{Y}_0 & \mathrm{Y}_1 \\ \mathrm{Y}_0' & \mathrm{Y}_1' \end{bmatrix} \tag{33}$$

The equation (34), contains the matrix function "fcn_ode", which delivers the arranges of all the ODEs per its deflection and derivatives.

$$fcn\_ode = \frac{d}{dy}\begin{bmatrix} H \\ H' \\ H'' \\ H''' \\ \mathrm{Y} \\ \mathrm{Y}' \end{bmatrix} = \begin{bmatrix} H' \\ H'' \\ H''' \\ \dfrac{mw^2 H - mx_a w^2 \mathrm{Y}}{EI} \\ \mathrm{Y}' \\ \dfrac{mx_a w^2 H - I_a w^2 \mathrm{Y}}{GJ} \end{bmatrix} \tag{34}$$

Last but not least, function named "i_guess" as shown in (35), is considered to apply a pattern for the initial slope estimates of the boundary conditions (e.g. prediction of the maximum tip deflections for bending and torsion are equal to 1).

$$i\_guess = \begin{bmatrix} 1 \\ 0 \\ 0 \\ 0 \\ 1 \\ 0 \end{bmatrix} \tag{35}$$

The selected 3 equations shown in (33), (34), and (35), are used for beam example shown in Fig. 7 and equation (36), where $y0$ is the root of beam and the "$y1$" is the free end of beam, "n" is number of mesh points used between $y0$ to $y1$. Also applies a guessing solution vector "i_guess", solution from equation (35).

$$soli = bvpi\left(\left(y0, y1, n\right), i\_guess\right) \quad \textbf{(36)}$$

$$sol = bvp4c\left(fcn\_ode, fcn\_bc, soli, N\max\right) \quad \textbf{(37)}$$

From equation (37), has a guess structure which resulted from (36) defined by term "$soli$". Following BVP4c example structure shown in Fig. 8, implements all computed outputs or "solutions" are named sol and the term "$Nmax$" is used to calculate a solution accurately in terms of number of grid points and therefore obtain better resolutions to plot the normal mode shapes. Geometry mesh is then determined by calculations and are stored in "sol", which is the BVP4c results. Therefore, all similar solutions to the geometry mesh points are stored in "$sol.y$", in other words, for each mesh-point of discretization of the blade will then store a cell of [1x6 elements] for the bending deflection and the torsional deformations. From these stored results, the mode shapes are then plotted using the extracted information from vector solution conventionally named "$sol.x$". More precisely $sol.x$ will provide locations throughout the blade and $sol.y$ will provide the complete profile of deflection and derivatives for bending-torsion. Reference **[93]** highlights that when is about to provide properly good guesses on the Collocation Method as in (35), this task can turn to be the most difficult part to tackle and solve in all BVP4c structural models. Main outputs from the ODE's in (34) are related to calculations of the coupled bending-torsional natural frequencies and normal mode shapes which will be more explained ahead this document.

3.3.1.- Field equations for Boundary Value Problem (BVP) formulation

Previous discussed models which were subjected and applied as next easy example from Matlab solver point of view, where the model 4 was evaluated in order to display how is integrated the field equations and what are the elementary information needed to incorporate ODE's onto a matrix with the complete set of equations. Where model 4 is calculated using the field equation known as $dydx$, where the 6 terms in rectangle with dashed green lines are the beam's elements. Elements are calculated in $dydx$ as in red rectangle, where rectangles with dashed orange lines are bending, angle due bending, and torsion respectively. The BVP solver calculates the constituent parts $[Root, Tip]$ as a single domain or field, these ODE's are evaluated troughtout all locations x, for all 6 systems deformations on y terms as shown in Fig. 9. The detailed applications of the eigenfrequency and the eigenvalue analysis are discussed in the chapter 3.3.4.

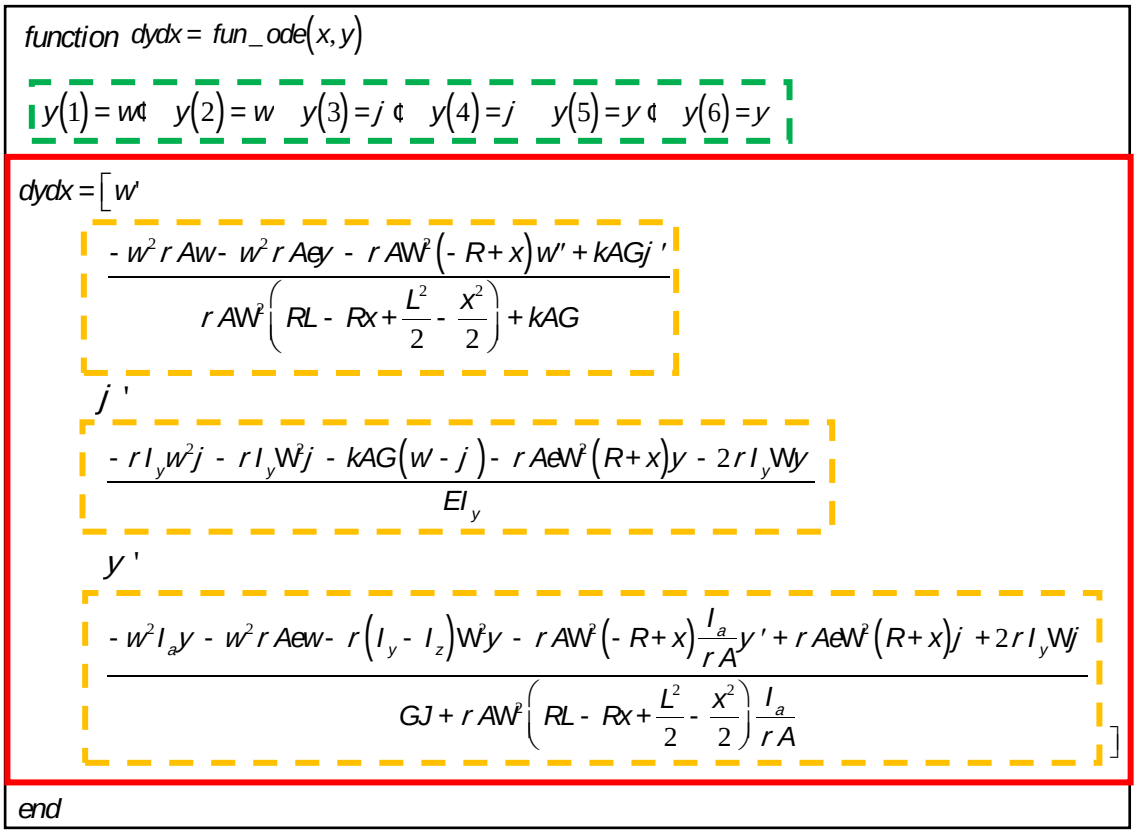

Figure 9. Example of field equation for rotating Bending-Torsional coupling "Timoshenko".

3.3.2.- Classical Boundary Conditions (BC's) for rotor blade models

After applying the Hamilton's principle to obtain final EoM's from chapter 3.2, a subsequent BC's are needed for BVP4c solver. From all models, both geometrical and natural BC's implemented are shown in tables 1-4 **[89,90,91,92].** These BC's were implemented in field equations to perform calculations within Collocation Method for both frequency and eigenvalue analysis. The model 1,4 contains 6 BC's (3 at root + 3 at tip) as maximum order of equations sums 6, and model 2,3 has 10 BC's (5 at root + 5 at tip) as maximum order of equations sums 10. The natural BC's are further explained and used in chapter 3.3.3. and 3.3.5.

Y = 0 "ROOT" (GEOMETRICAL)		Y ≠ (0,L) "SPANWISE" (NATURAL)		Y = L "TIP" (GEOMETRICAL)	
BENDING SHAPE	$H(0,t)=0$	BENDING MOMENT	$EI_y H''=0$	NO DEFORMATION	$H''=0$
BENDING DERIVATIVE	$H'(0,t)=0$	SHEAR FORCE	$TH'-EI_y H'''=0$		$H'''=0$
TORSIONAL DEFORMATION	$\Upsilon(0,t)=0$	TORSIONAL MOMENT	$GJ\Upsilon'=0$		$\Upsilon'=0$

Table 1.- BC's for model 1: coupled bending-torsional "Euler Bernoulli".

LATERAL BENDING SHAPE	$U(0,t)=0$	LATERAL BENDING MOMENT	$EI_2 U''=M_z$	NO DEFORMATION	$U''=0$
LATERAL BENDING DERIVATIVE	$U'(0,t)=0$	TRANSVERSE BENDING MOMENT	$-EI_1 W''=M_x$		$U'''=0$
BENDING SHAPE	$W(0,t)=0$	LATERAL SHEAR FORCE	$EI_2 U'''=S_x$		$W'=0$
BENDING DERIVATIVE	$W'(0,t)=0$	TRANSVERSE SHEAR FORCE	$EI_1 W'''=S_z$		$W'''=0$
TORSIONAL DEFORMATION	$\Upsilon(0,t)=0$	TORSIONAL MOMENT	$-GJ\Upsilon'=T_y$		$\Upsilon'=0$

Table 2.- BC's for model 2: transverse-lateral vibration with torsional coupling "Euler Bernoulli".

CHORDWISE BENDING	$\bar{v}(0,t)=0$	CHORDWISE BENDING MOMENT	$EI_{xx}\bar{f}_y'=0$	NO CENTRIFUGAL FORCE	$\bar{v}'-\bar{f}_y=0$
FLAPWISE BENDING	$\bar{w}(0,t)=0$	FLAPWISE BENDING MOMENT	$EI_{hh}\bar{f}_z'=0$		$\bar{w}'-\bar{f}_z=0$
ANGLE DUE CHORDWISE	$\bar{f}_y(0,t)=0$	CHORDWISE SHEAR FORCE	$T\bar{v}'+kAG(\bar{v}'-\bar{f}_y)=0$		$\bar{f}_y'=0$
ANGLE DUE FLAPWISE	$\bar{f}_z(0,t)=0$	FLAPWISE SHEAR FORCE	$T\bar{w}'+kAG(\bar{w}'-\bar{f}_z)=0$		$\bar{f}_z'=0$
TORSIONAL DEFORMATION	$\bar{y}(0,t)=0$	TORSIONAL MOMENT	$T\frac{I_a}{rA}\bar{y}'=0$		$\bar{y}'=0$

Table 3.- BC's for model 3: rotating flap, lead-lag, with torsional coupling "Timoshenko".

BENDING MOMENT	$w(0,t)=0$	BENDING MOMENT	$EI_y j'=0$	NO CENTRIFUGAL FORCE	$j'=0$
ANGLE DUE BENDING	$j(0,t)=0$	SHEAR FORCE	$Tw'+kAG(w'-j)=0$		$w'-j=0$
TORSIONAL DEFORMATION	$y(0,t)=0$	TORSIONAL MOMENT	$GJy'=0$		$y'=0$

Table 4.- BC's for model 4: rotating Bending-Torsional coupling "Timoshenko".

3.3.3.- Collocation Method formulations

Numerical approach implies a function based on ODE's is studied into two-points BC's, this is then evaluated in interval of a mesh $[Root, Tip]$. The main and final step is to collocate at both ends of differential equations and also in mid-points of each subdomains (see analysis in Multi-Point BVP in chapter 3.3.5). A general flowchart for Collocation Method is shown in Fig. 10 for model 4, using table 4 BC's. This schematic is shown in details in the Fig. 11. Initially is considered control parameters that defines sectional properties of beam, the set values are the purple dashed line box. To calculate normal mode shapes an estimates or descriptive mode equations for bending, angle due bending and torsion are applied onto BVP4c. Field equations with ODE's are orange dashed line box. The Collocation Methodology for beam is the black dashed line box, therefore 3 geometrical BC's are root and 3 geometrical BC's for tip; Note that BC's contains a "-1" to applied an excitaion force (1 Newton) at the tip as a normalization condition.

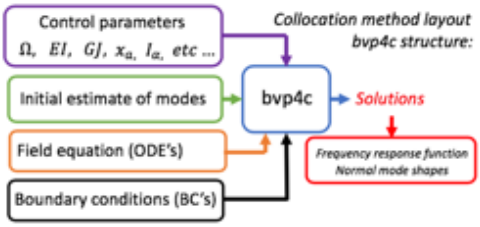

Figure 10. Collocation Method flowchart.

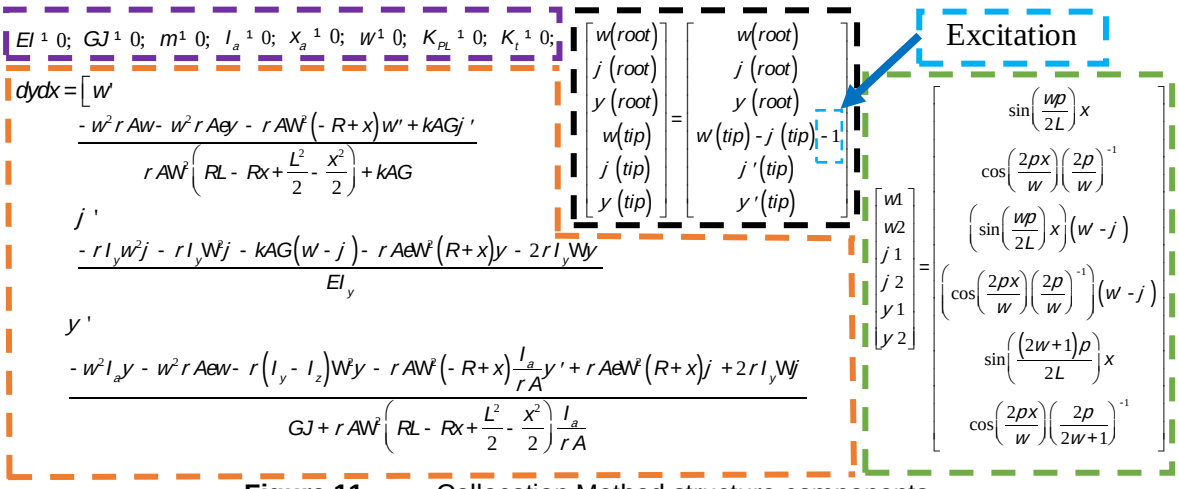

Figure 11. Collocation Method structure components.

3.3.4.- Methodology for frequency and eigenvalue analysis

The analytical approaches were performed in 2 research lines, as example the Model 4 will be used: Firstly, frequency analysis (get natural frequencies by harmonic oscillations), and Secondly, the eigenvalue analysis (get eigenvectors by mode shape functions). First approach can be successfully completed by applying the Collocation Method as shown in Fig. 10. Where the field equation shown in the Fig. 12, is the used to apply the harmonic analysis assumptions, therefore the beam vibrates forced under excitations at the beam's tip in a selected range of vibrational frequencies (ω) showed in red color inside the blue dashed line boxes in Fig. 12. During process it collects and stored the frequency response functions data and also the harmonical normal modes. The approach used in the eigenvalue analysis is generated by exciting the system with a selected and known frequency value of excitation, similar how modal testing occurs by exciting the experimental rig cyclically with electromagnetic shaker using a desired frequency value.

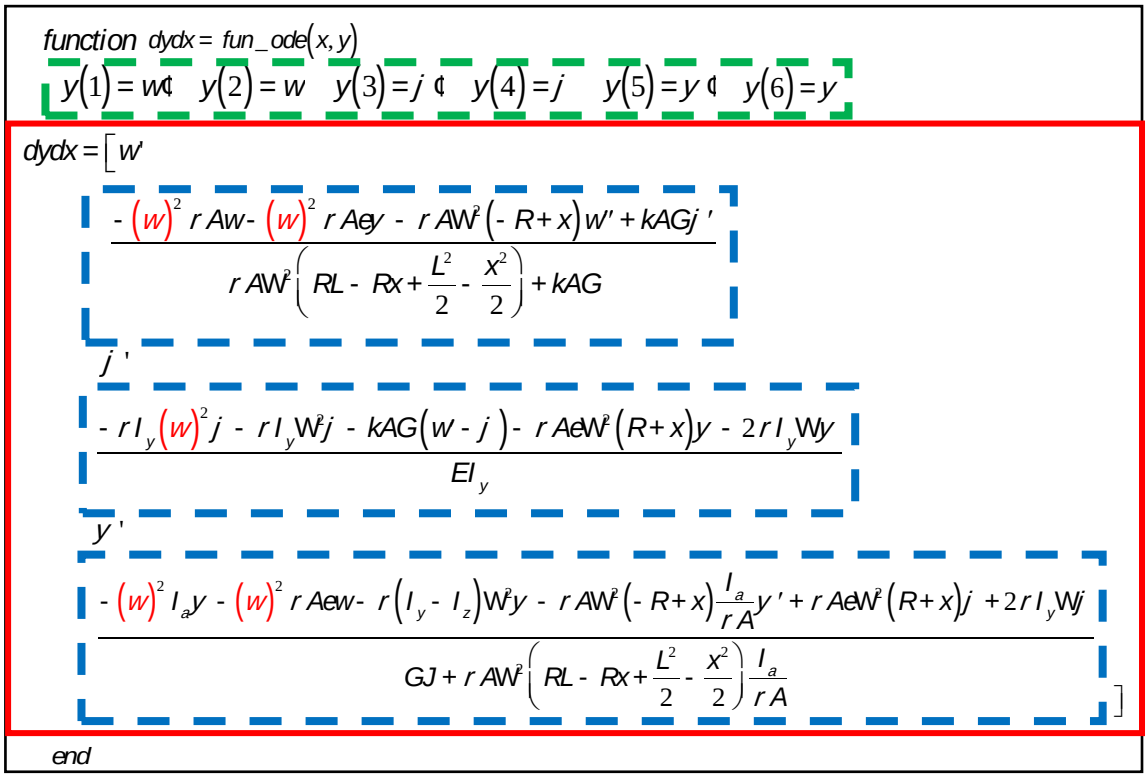

Figure 12. Example of frequency and eigenvalue analysis for the Collocation Method.

3.3.5.- Multi-Point Boundary Value Problem (MPBVP) formulation

The implementation of several multi-elements or subdomains into beam's system is highly desirable when solving certain problem solutions under specific locations to incorporate the produced loads that occurs when modelling Pitch Links and Ice accretion effects. Main modelling novel features and upgrades included in this thesis was to incorporate the Multi-Point Boundary Value Problem (MPBVP). This was implemented using BVP4c solver on Matlab **[B],** as shown in Fig. 12, this method is capable to iterate and calculate across a defined interval [UR, UT]. In other words, these sets of Multi-Points will be assigned from UR to UT into virtual space of beam, where the beam locations UR= $U_0 < U_1 < \ldots < U_n$ = UT are then discretized. Where the last points UR_1, UR_2, …, UR_{n-1} represents the physical interfaces from those sub-domains. These specific Collocation Methods allows to assign positions by enumerating those regions from the left side to the right side, a more practical perspective for these types of features are shown in the example introduced in the following system case. In this Thesis, the rotorcraft blade models were segmented into 6 Multi-Points throughout the span wise. As example case, it can be named blade's positions, "UR" as Root location, "UT" as Tip location, and "PL" as Pitch Link location, as shown in the Fig. 13. Where vertical red line is assigned as PL boundary condition location, and further implementations are then explained from Matlab solver point of view. The Multi-Points boundary conditions were applied as observed in Fig. 14, where the experimental rotorcraft blade, is then discretized into two zones or segments where there are 12 elements between each zone (red box) that describes the continuity of the system of bending moment, shear forces and torsion moment, and also their first derivatives too.

[B] https://www.mathworks.com/help/matlab/ref/bvp4c.html#bt5uooc-23

Notice green box terms are considered the root's boundary conditions and the red box is the inter segmental phase under study.

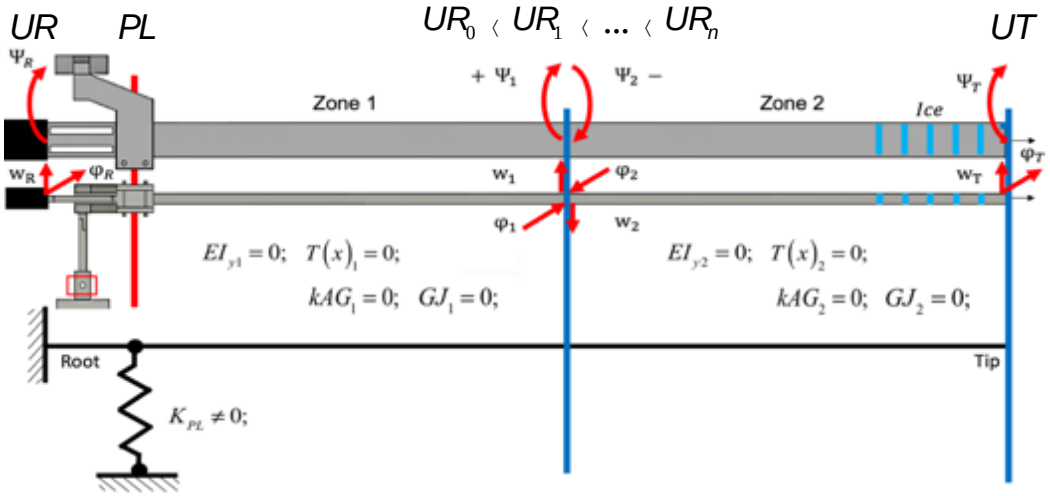

Figure 13. Experimental helicopter blade's Multi-Point example for 2 subdomains.

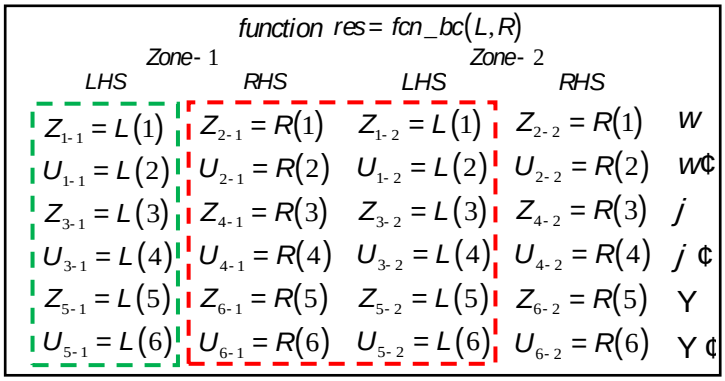

Figure 14. Collocation structures are placed in order and accordingly its position on the blade longitudinal axis.

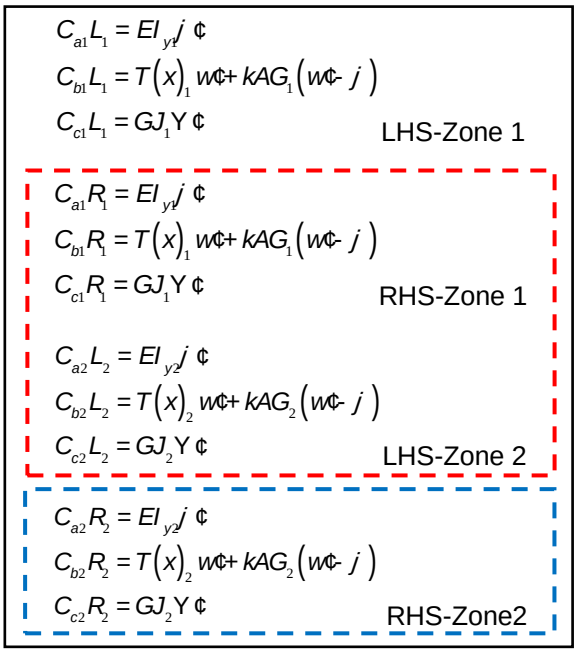

Figure 15. Internal bending, shear forces and torsional moments.

From the Fig. 16, the blue box represent the Tip's boundary conditions and the red box is the physical interphase described by its bending moments, shear forces and torsional moments. In order to introduce the complete function for the boundary condition shown in Fig. 15, the Matlab solver use the matrix "res", which is constitue by various boundary condition terms such as the root (green box) to the tip (blue box) of the experimental helicopter blade from Fig. 13, additionally is then created a middle interphase section (red box) that represents the boundaries that are interpreted as the internal moments between the sections (also known as the kinematic type conditions) where the right segment conditions is then cancel out (momentum conservation) with the elements from the left segment conditions. As was explained previously, all the models explored in this thesis along with the MBB Bo-105 helicopter blade sectional parameters in chapter 6 and both advanced aluminum beam sectional properties were then used to build a segmental MBB Bo-105 blade with 6 Multi-Points and advanced aluminum beam with 16 Multi-Points respectively. These four models under the Multi-Point boundary conditions approach were then evaluated under specific eigenfrequency and eigenvalue analysis cases in non-rotating sstructures and further rotating aeroelastic blade applications explored in this thesis.

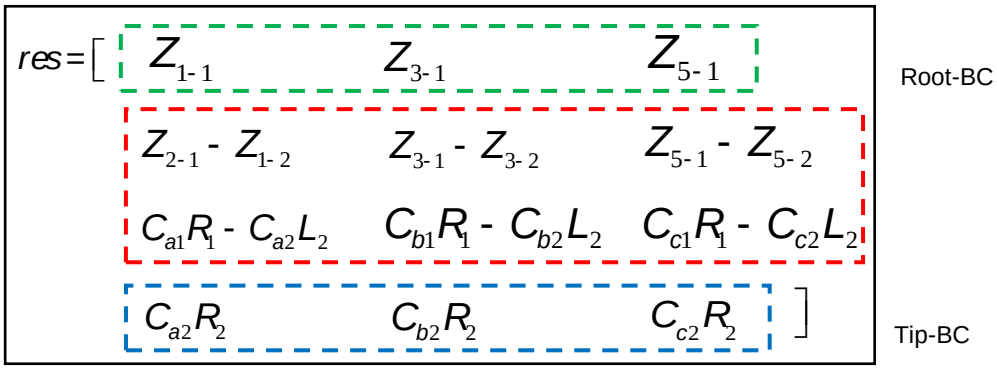

Figure 16. Internal moments on middle sections are being cancel out by establishing an interphase equilibrium momentum.

3.4.- Helicopter blade model incorporation of Pitch Link arm jointed at rotor hub swashplate

Concept of stiffness is directly related to body resistant due deformations. This can be idealized when applying loads and evaluate how much strain occurs, therefore stiffer a system is the less deformation will occur. When a structural element preserve its factory “healthy” parameters, this will mean unchanged stiffness, in other words under certain loadings in the structural mechanisms no deformations will be produced since the stiffness will be constant (undamaged). Inspired from stiffness concept, any machinery with multi elements (such as joints, arms, bolts, frames, etc.) will play a significant role and its undamaged state would be responsible from good performance. The undeformed spring element shown in Fig. 17 **a)**, is a proper element that will represent a helicopter Pitch Link arm due to its ability of deformation on a single axis or coordinate. Necessary and allowed spring deformation x_{spring} for a needed force F_{spring} as in Fig. 17 **b)**, is proportional to the stiffness value K_{spring} is shown in equation (38). This simple spring case was implemented to model the Pitch Link configuration of experimental testing.

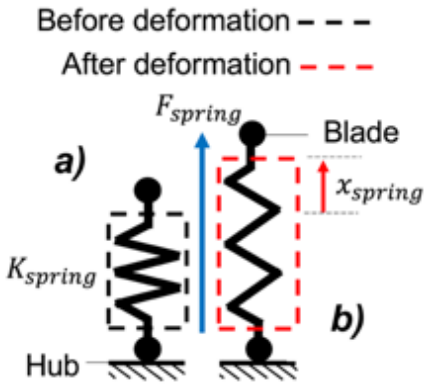

Figure 17. Simple spring case: **a)** Before Deformation (BD), **b)** After Deformation (AD).

$$F_{spring} = K_{spring} x_{spring} \quad \textbf{(38)}$$

Where:
F_{spring} = Restoring force, [N]
K_{spring} = Spring stiffness, [N/m]
x_{spring} = Spring deformation, [m]

From the previous concept of a simple spring deformation, the incorporation of the Pitch Link model in this thesis was refined into a more complete and robust detailed form. Therefore, configuration of the Pitch Link model was inspired by the configuration of the helicopter main rotor hub from Fig. 18 **[C],** which its blades in rotation are cyclically controlled via the applied swashplate angular deformation that couples flapping and torsional deflection at the L-shaped arm attached blade.

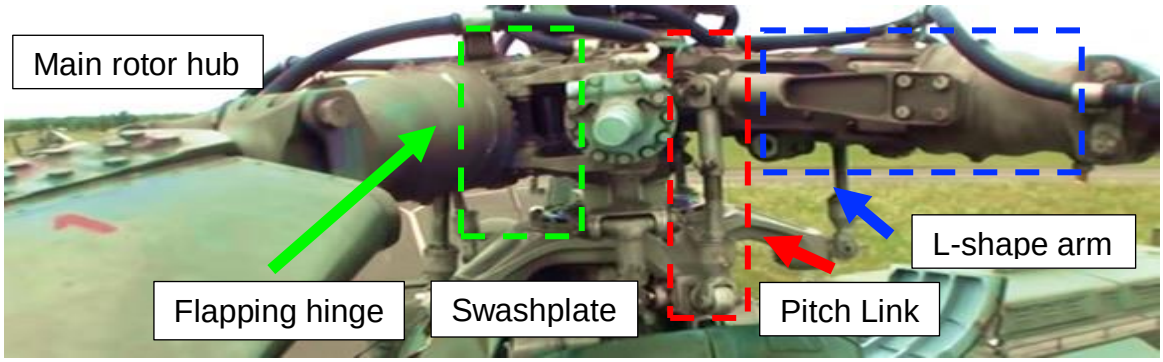

Figure 18. Helicopter blade and its Pitch Link configuration.

The visualization of deformations and/or deflections that a Pitch Link device applies on rotor blades are the steady state as in Fig. 19 **b)** and after deformations in Fig. 19 **a)** and **c)**. Which are crucially reflected by the capablility of changes on the blade's angle of attack while the rotating four bladed system is constantly sppining at a specific rotating frame of reference. The theory and assumptions of PL model in this thesis are focused in applying approximately similar principles and dynamics, therefore the boundary conditions and descriptive equations of motions of this device are discussed in detail in next page.

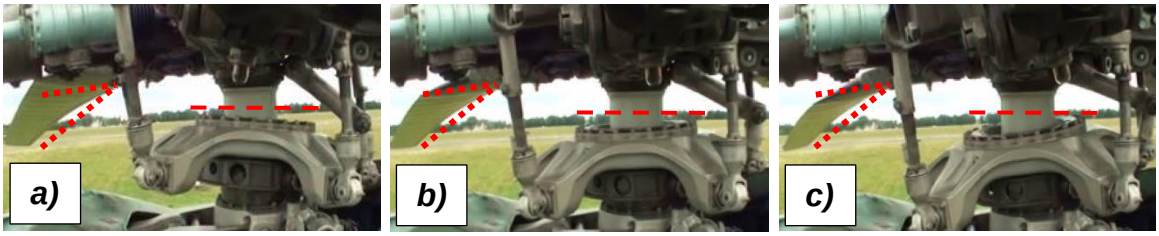

Figure 19. Sequential Swashplate-Pitch Link deformations.

C https://www.youtube.com/watch?v=LFN3O4E_umU

A detailed schematic diagram that correspond internal Pitch Link device is shown in Fig. 20 **a) [83,84].** Component in Fig. 20 **a)** has a piston ram of area A on the inside and a piston's mass m_P, which is integrated/sealed with elastomer composite material of damping C_D and a Pitch Link Stiffness K_{PL}. The piston element contains a main chamber with hydraulic oil capacitance C_P and pressure P, which is generated by piston motion. This action subsequently forces all volumetric fluid V into fluid track slot, in order to push away the piston ram. The discussed characteristics of PL device are incorporated also assuming that internal fluid acts with a constant pressure or locked mode, (e.g. no cross flow occurs).

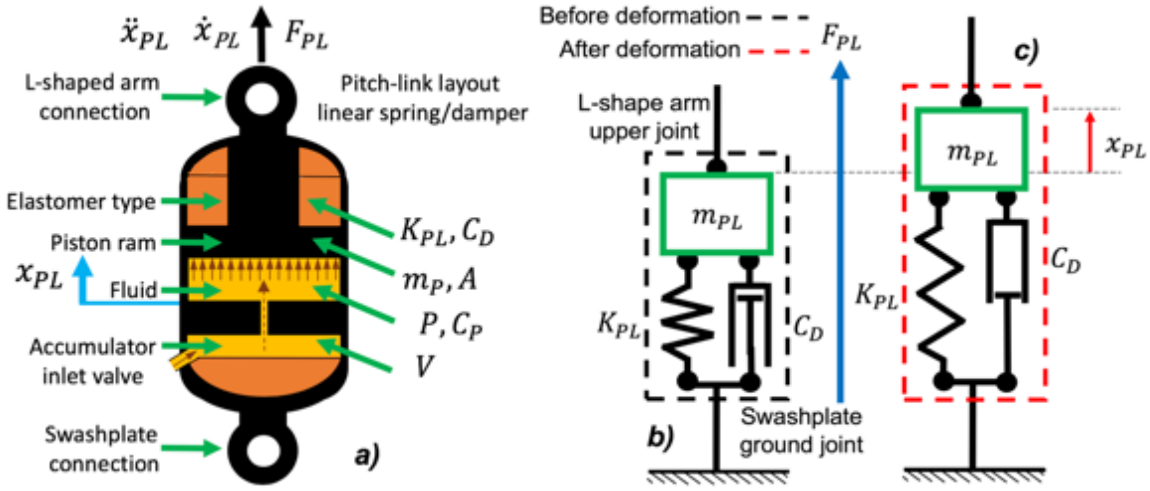

Figure 20. Pitch Link schematic: **a)** Abstract view, **b)** Steady state, and **c)** After deformation.

In this thesis, total force of piston F_{PL} in Fig. 20 **a)** and **b)**, and also the Pitch Link arm deformation x_{PL} shown in the Fig. 20 **a)** and **c)** are responsible in inducing the blade's dynamical moment. The total deformation is related with the coupling effects between the bending deflections "w", the rotating angle due bending "φ", and the torsional angular deformations "Ψ" that occurs within blade and Pitch Link L-shaped arm system. The calculated total Pitch Link force, the assumptions related with geometrical characteristics of the device and the equations were derived using the references of the Fig. 21,22, and 23, ahead this section.

The Pitch Link boundary conditions from all models aims to obtain the coupled interaction on the in-plane and out of-plane deformation that were derived by considering the angle of rotation due bending φ, the characteristic angle of the Timoshenko beam model in Fig. 21 **b)**, the small angle was incorporated into model even though the bending rotations might be small. Deformations are evaluated from initial and final coordinates of references $[P_0, P]$, also the maximum coupling distance for the Pitch Link torque moment e_P was integrated.

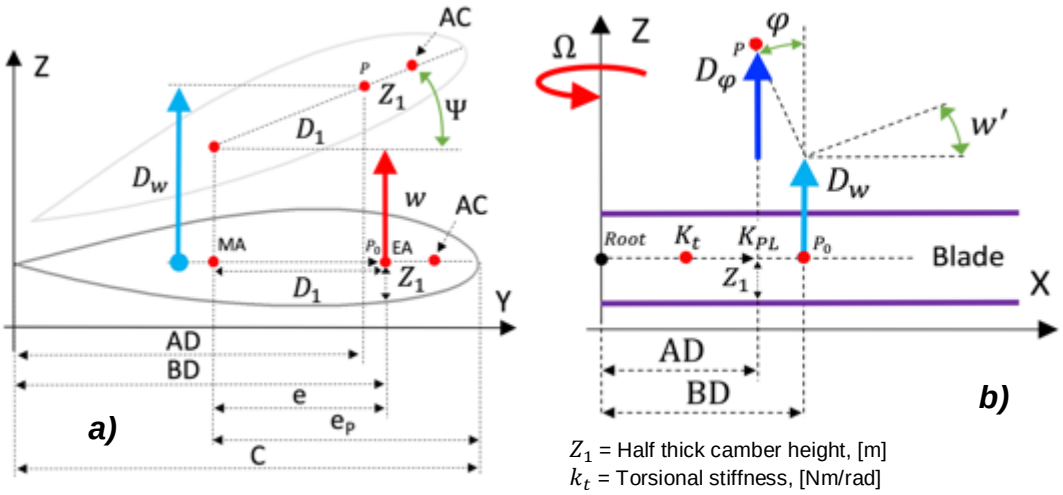

Figure 21. Rotor blade deformations from: **a)** Cross sectional, and **b)** Lateral view.

However, this was used to obtain an additional coupled vertical deformation that will depend on the amount of rotation angle due bending $(w' - \varphi)$, referred as the vertical dark blue arrow D_φ. All models assumes the blade coordinates and deformations, which are related derivations of the internal vertical deformation D_w, represented with the vertical light blue arrow pointing upwards. The last but not least additional deformation describes the torsional angular deformation that occurs between the pitched blade system shown in the Fig. 21 **a)**, referred as the vertical light green arrow pointing upwards D_Ψ. A more complete and detailed description from these coupled deformations are displayed in the rotor blade Pitch Link system shown in Fig. 22.

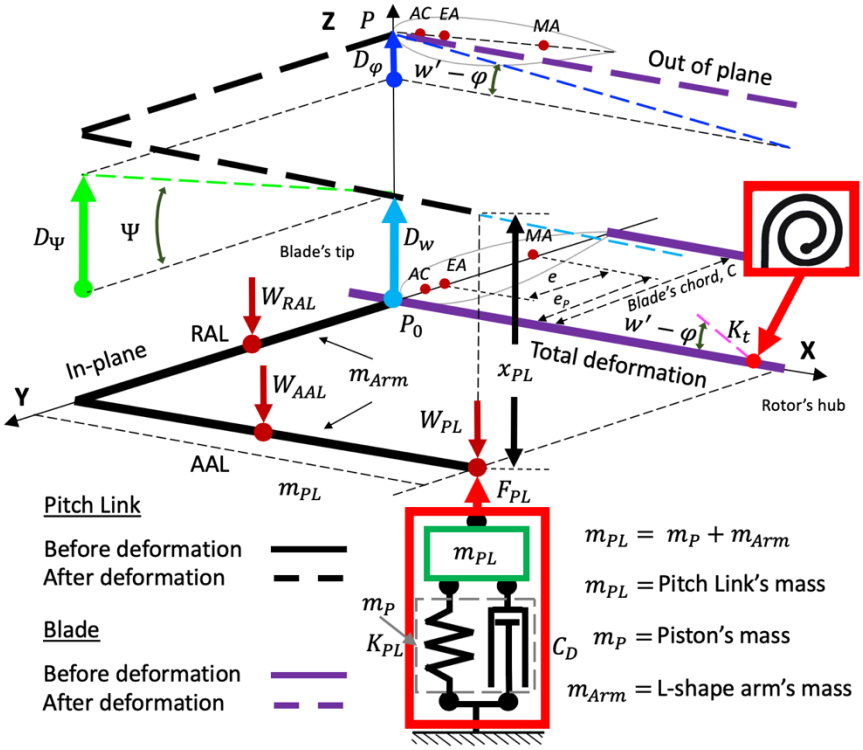

Figure 22. Rotor blade Pitch Link articulation system in before and after deformation.

Where:

RAL, AAL = Radial and Axial arm length, [m]

W_{RAL}, W_{AAL}, W_{PL} = Force acting through centre of gravity of RAL, AAL, and PL, [N]

From Fig. 22, the whole complete interaction is shown as before and after deformation due to the applied upward force F_{PL}, coming from the Pitch Link (PL) marked rectangle element. As it was evaluated in the simple model from Fig. 17, the Pitch Link force will depend on the total deformation x_{PL} of the pitched blade system. From all the models the total deformations were obtained accordingly with their coordinates and nomenclatures and are presented in the Table 5. The total deformations are a summation from both bending, small rotational angles and torsional deflections. More details from Fig. 22 were used in next derivations.

MODEL REF.	*VERTICAL DEFORMATION*	*ANGULAR ROTATION*	*TORSIONAL DEFORMATION*	*TOTAL DEFORMATION*
1- [84]	$D_{H1} = H + Z_1(Y) + D_1(Y)$	$D_{a1} = AAL(H\text{¢})$	$D_{Y1} = (RAL + e_P)Y$	$x_{PL1} = D_{H1} + D_{a1} + D_{Y1}$
2- [85]	$D_{W2} = W + Z_1(Y) + D_1(Y)$	$D_{a2} = AAL(W\text{¢})$	$D_{Y2} = (RAL + e_P)Y$	$x_{PL2} = D_{W2} + D_{a2} + D_{Y2}$
3- [86]	$D_{\bar{w}3} = \bar{w} + Z_1(\bar{y}) + D_1(\bar{y})$	$D_{\bar{j}_3} = AAL(\bar{w}\text{¢} - \bar{j}_z)$	$D_{\bar{y}3} = (RAL + e_P)\bar{y}$	$x_{PL3} = D_{\bar{w}3} + D_{\bar{j}3} + D_{\bar{y}3}$
4- [87]	$D_{w4} = w + Z_1(Y) + D_1(Y)$	$D_{j4} = AAL(w\text{¢} - j)$	$D_{Y4} = (RAL + e_P)Y$	$x_{PL4} = D_{w4} + D_{j4} + D_{Y4}$

Table 5.- Maximum deformations from the Pitch Link arm-blade per each model.

The Fig. 23 display the free body diagram in order to obtain the loads and BC's for the Pitch Link (PL) and Flapping Hinge (FH). The subsequent final BC's are used to calculate total Pitch Link forces, which are later shown in tables 6,7,8,9. All the forces and moments acts at point A and B for PL and FH respectively, these were derived and presented as the following solutions, from equations (39) to (50):

Pitch Link Solutions at location A:

$$\sum Fx = 0 \qquad F_{PL-X} = 0 \qquad \textbf{(39)}$$

$$\sum Fy = 0 \qquad F_{PL-Y} = 0 \qquad \textbf{(40)}$$

$$\sum Fz = 0 \qquad F_{PL-Z} + F_{PL} - W_{AAL} - W_{RAL} - W_{PL} = 0 \quad F_{PL-Z} = -F_{PL} + W_{AAL} + W_{RAL} + W_{PL} \qquad \textbf{(41)}$$

$$\sum Mx = 0 \qquad -M_{PL-X} - F_{PL}\left(RAL + e_P\right) + W_{RAL}\left(\frac{RAL}{2} + e_P\right) + W_{AAL}\left(RAL + e_P\right) + W_{PL}\left(RAL + e_P\right) = 0$$

$$M_{PL-X} = -F_{PL}RAL - F_{PL}e_P + \frac{W_{RAL}RAL}{2} + W_{RAL}e_P + W_{AAL}RAL + W_{AAL}e_P + W_{PL}RAL + W_{PL}e_P \qquad \textbf{(42)}$$

$$\sum My = 0 \qquad M_{PL-Y} + F_{PL}\left(AAL\right) - W_{AAL}\left(\frac{AAL}{2}\right) - W_{PL}\left(AAL\right) = 0 \quad M_{PL-Y} = -F_{PL}AAL + \frac{W_{AAL}AAL}{2} + W_{PL}AAL \qquad \textbf{(43)}$$

$$\sum Mz = 0 \qquad M_{PL-Z} = 0 \qquad \textbf{(44)}$$

Flapping Hinge Solutions at location B:

$$\sum Fx = 0 \qquad F_{FH-X} = 0 \qquad \textbf{(45)}$$

$$\sum Fy = 0 \qquad F_{FH-Y} = 0 \qquad \textbf{(46)}$$

$$\sum Fz = 0 \qquad F_{FH-Z} = 0 \qquad \textbf{(47)}$$

$$\sum Mx = 0 \qquad M_{FH-X} = 0 \qquad \textbf{(48)}$$

$$\sum My = 0 \qquad M_{FH-Y} + K_t\left(w\text{¢} - j\right) = 0 \quad M_{FH-Y} = -K_t\left(w\text{¢} - j\right) \qquad \textbf{(49)}$$

$$\sum Mz = 0 \qquad M_{FH-Z} = 0 \qquad \textbf{(50)}$$

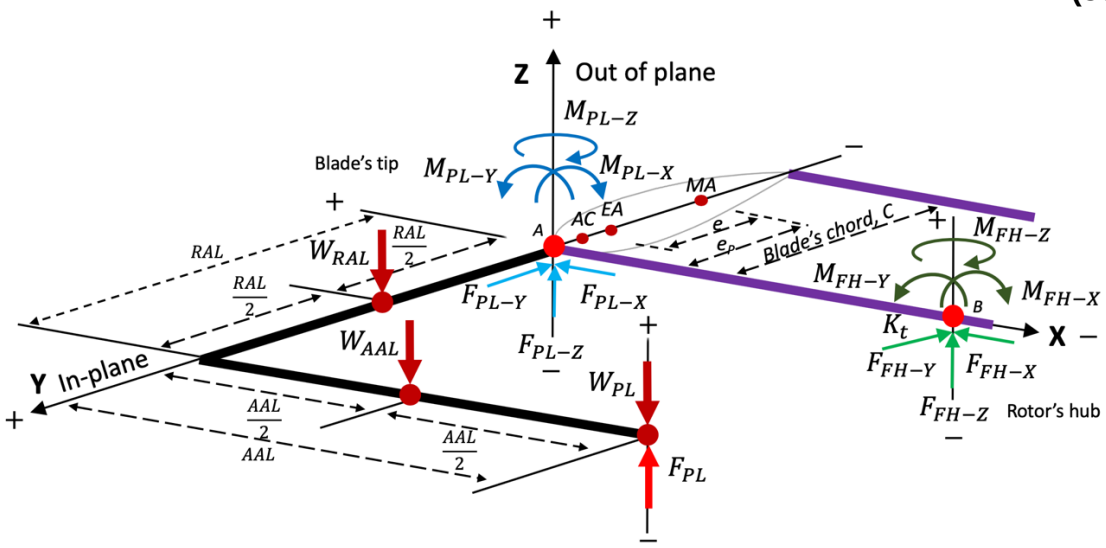

Figure 23. Pitch Link and Flapping Hinge free body diagram.

At this point the total deformations or displacements from the PL L-shape am is shown in the Table 5, which were then derived twice to obtain velocities and accelerations that occur in the L-shape system. The complete derivation of the equations for velocities and accelerations are shown in (51) and (52) respectively.

PL L-shape arm Velocity Solutions:

$$
\begin{aligned}
x_{PL} &= D_W + D_Y + D_j \\
x_{PL} &= \left[w + Z_1 Y + D_1 Y \right] + \left[\left(RAL + e_P \right) Y \right] + \left[AAL\left(w - j \right) \right] \\
x_{PL} &= w + Z_1 Y + D_1 Y + RALY + e_P Y + AALw\text{¢} - AALj \\
\dot{x}_{PL} &= \dot{w} + Z_1 \dot{\Psi} + D_1 \dot{\Psi} + RAL\dot{\Psi} + e_P \dot{\Psi} + AAL\dot{w}' - AAL\dot{\varphi} \\
\dot{x}_{PL} &= \dot{w} e^{i\omega t} + Z_1 \dot{\Psi} e^{i\omega t} + D_1 \dot{\Psi} e^{i\omega t} + RAL\dot{\Psi} e^{i\omega t} + e_P \dot{\Psi} e^{i\omega t} + AAL\dot{w}' e^{i\omega t} - AAL\dot{\varphi} e^{i\omega t} \\
\dot{x}_{PL} &= i\omega \dot{w} e^{i\omega t} + i\omega Z_1 \dot{\Psi} e^{i\omega t} + i\omega D_1 \dot{\Psi} e^{i\omega t} + i\omega RAL\dot{\Psi} e^{i\omega t} + i\omega e_P \dot{\Psi} e^{i\omega t} + i\omega AAL\dot{w}' e^{i\omega t} - i\omega AAL\dot{\varphi} e^{i\omega t} \\
\dot{x}_{PL} &= i\omega w + i\omega Z_1 \Psi + i\omega D_1 \Psi + i\omega RAL\Psi + i\omega e_P \Psi + i\omega AALw' - i\omega AAL\varphi \\
\dot{x}_{PL} &= i\omega \left(w + \left(Z_1 + D_1 + RAL + e_P \right) \Psi + AAL\left(w' - \varphi \right) \right)
\end{aligned}
\qquad \textbf{(51)}
$$

PL L-shape arm Acceleration Solutions:

$$
\begin{aligned}
\dot{x}_{PL} &= i\omega w + i\omega Z_1 \Psi + i\omega D_1 \Psi + i\omega RAL\Psi + i\omega e_P \Psi + i\omega AALw' - i\omega AAL\varphi \\
\ddot{x}_{PL} &= i\omega \dot{w} + i\omega Z_1 \dot{\Psi} + i\omega D_1 \dot{\Psi} + i\omega RAL\dot{\Psi} + i\omega e_P \dot{\Psi} + i\omega AAL\dot{w}' - i\omega AAL\dot{\varphi} \\
\ddot{x}_{PL} &= i\omega w e^{i\omega t} + i\omega Z_1 \Psi e^{i\omega t} + i\omega D_1 \Psi e^{i\omega t} + i\omega RAL\Psi e^{i\omega t} + i\omega e_P \Psi e^{i\omega t} + i\omega AALw' e^{i\omega t} - i\omega AAL\varphi e^{i\omega t} \\
\ddot{x}_{PL} &= i\omega^2 w e^{i\omega t} + i\omega^2 Z_1 \Psi e^{i\omega t} + i\omega^2 D_1 \Psi e^{i\omega t} + i\omega^2 RAL\Psi e^{i\omega t} + i\omega^2 e_P \Psi e^{i\omega t} + i\omega^2 AALw' e^{i\omega t} - i\omega^2 AAL\varphi e^{i\omega t} \\
\ddot{x}_{PL} &= i\omega^2 w + i\omega^2 Z_1 \Psi + i\omega^2 D_1 \Psi + i\omega^2 RAL\Psi + i\omega^2 e_P \Psi + i\omega^2 AALw' - i\omega^2 AAL\varphi \\
\ddot{x}_{PL} &= i\omega^2 \left(w + \left(Z_1 + D_1 + RAL + e_P \right) \Psi + AAL\left(w' - \varphi \right) \right)
\end{aligned}
\qquad \textbf{(52)}
$$

The incorporation of the PL-L-shape arm's total displacement, velocities and accelerations were adopted to obtain the total Pitch Link force. For this purpose, the descriptive equations of motions for this system was approached by assuming that exist a constant pressure acting inside piston's chambers. This constant pressure allows the pressurization of the internal walls inside the chamber.

Since this piston mechanism assumes two degrees of motions (one due to the vertical piston's ram displacement + one due to the fluidic oil motion), therefore the complete piston actions can be observed in the presented free body diagram shown in Fig. 24. Where total Pitch Link force was calculated using all parameters from the Appendix A4 shown in Equations 1.

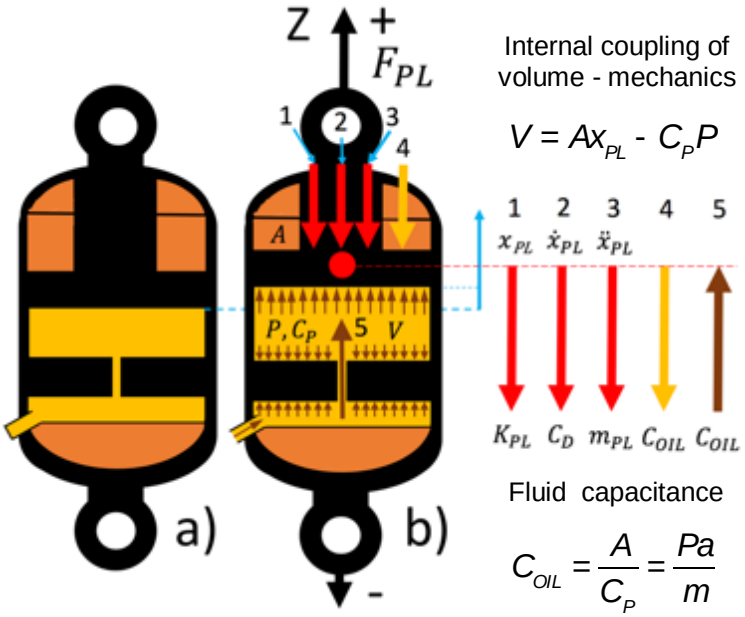

Figure 24. Total piston's force free body diagram: **a)** Steady state, **b)** After piston's motion.

The internal "fluidic" volumetric and mechanical coupling "V" equation is substituted in the final EoM (53), resulting in the total Pitch Link hydraulic force F_{PL}.

Total Pitch Link Force Solutions:

$$\sum Fx = 0 \qquad F_{PL\text{-}X} = 0$$

$$\sum Fy = 0 \qquad F_{PL\text{-}Y} = 0$$

$$\sum Fz = 0 \quad F_{PL} - K_{PL}x_{PL} - C_D\dot{x}_{PL} - m_{PL}\ddot{x}_{PL} - C_{OIL}Ax_{PL} + C_{OIL}V - m_{PL}g_e = 0$$

$$F_{PL} = K_{PL}x_{PL} + C_D\dot{x}_{PL} + m_{PL}\ddot{x}_{PL} + C_{OIL}Ax_{PL} - C_{OIL}V + m_{PL}g_e$$

$$F_{PL} = K_{PL}x_{PL} + C_D\dot{x}_{PL} + m_{PL}\ddot{x}_{PL} + \frac{A^2}{C_P}x_{PL} - \frac{A}{C_P}V + m_{PL}g_e \qquad \textbf{(53)}$$

From the modelling point of view each Pitch Link has a main chamber with a capacitance C_P with constant pressure P and a piston diameter with ram's area A. The term $C_P P$ in volumetric-mechanical equation means a reduction in volume due to the incompressible properties of the oil inside chamber. The transmitted total Pitch Link force results from the two degrees of freedoms (Firstly, the independent motion from piston's ram + Secondly, the constant fluid flow through the fluid track). The hydraulic capacitance C_P, is defined as storage potential energy in chamber and the necessary energy to generate a unit change in piston's head, in other words changes in volumetrically stored liquid m^3 over changes in piston's head m. From equation (53), term $\frac{A}{C_P}$, describes piston capability to change a meter unit per a pressure unit $\frac{Pa}{m}$. Therefore, Total Pitch Link Force (54) results from the substitution of equations (51) and (52) into equation (53), these forces are incorporated with BC's for both PL and FH solutions as shown in Tables 6,7,8,9:

$$\begin{aligned} F_{PL} = m_{PL} i w^2 \left(w + \left(Z_1 + D_1 + RAL + e_P \right) Y + AAL \left(w\text{¢} - j \right) \right) \\ + C_D i w \left(w + \left(Z_1 + D_1 + RAL + e_P \right) Y + AAL \left(w\text{¢} - j \right) \right) \\ + \left(K_{PL} + \frac{A^2}{C_P} \right) \left(w + \left(Z_1 + D_1 + RAL + e_P \right) Y + AAL \left(w' - j \right) \right) \\ - \frac{A}{C_P} A \left(w + \left(Z_1 + D_1 + RAL + e_P \right) Y + AAL \left(w\text{¢} - j \right) \right) - C_P P + m_{PL} g_e \end{aligned} \quad \textbf{(54)}$$

Where:

F_{PL} = Total Pitch Link force, [N]
V = Volume of the hydraulic fluid, [m^3]
A = Area of piston ram, [m^2]
C_P = Capacitance of hydraulic fluid, [m^3/Pa]
P = Pressure of the hydraulic fluid, [MPa]
m_{PL} = Mass of the Pitch Link (Arm + Piston), [Kg]
C_D = Damping constant of the elastomer, [Ns/m]
K_{PL} = Stiffness of the elastomer, [N/m]
x_{PL} = Total Pitch Link arm deformation, [m]
$\dot{x}_{PL}$ = Pitch Link arm velocity, [rad/s]
$\ddot{x}_{PL}$ = Pitch Link arm acceleration, [rad/s^2]
g_e = Earth's gravitational constant, [m/s^2]

Final contribution of BC's is the Flapping Hinge (FH) "k_t", at a closer location from rotor's hub as shown in Fig. 22 and 23. FH's nature consists in allowing out of plane vibration or rotation only at hinge. Where rotation depends proportionally on the amount of slope generated in (w') using the Euler Bernoulli theory, and the slope $(w' - \varphi)$ using the Timoshenko beam theory. The FH BC's results from both moments in equation 55 **a)**, where coupling reaction results between the FH's rotations and natural/internal deflections happens in equation 55 **b)**:

$$EI_y j' = K_t\left(W' - j\right) \quad \textbf{a)} \qquad FH_{(BC)} = j' - \left(\frac{K_t\left(W' - j\right)}{EI_y}\right) \quad \textbf{b)} \qquad \textbf{(55)}$$

TYPE	Y = PITCH LINK LOAD EQUILIBRIUM	Y = FLAPPING HINGE LOAD EQUILIBRIUM
	$[Left] = [Right]$	$[Left] = [Right]$
BENDING MOMENT	$EI_y H'' + M_{PL-Y} = EI_y H''$	$EI_y H'' + K_t H' = EI_y H''$
SHEAR FORCE	$TH' - EI_y H''' + F_{PL-Z} = TH' - EI_y H'''$	$TH' - EI_y H''' = TH' - EI_y H'''$
TORSIONAL MOMENT	$GJY' - M_{PL-X} = GJY'$	$GJY' = GJY'$

Table 6.- Pitch Link and Flapping Hinge BC's for model 1.

LATERAL BENDING MOMENT	$EI_2 U''' = EI_2 U'''$	$EI_2 U'' = EI_2 U''$
TRANSVERSE BENDING MOMENT	$-EI_1 W'' + M_{PL-Y} = -EI_1 W''$	$EI_1 W'' + K_t W' = EI_1 W''$
LATERAL SHEAR FORCE	$EI_2 U''' = EI_2 U'''$	$EI_2 U''' = EI_2 U'''$
TRANSVERSE SHEAR FORCE	$EI_1 W''' + F_{PL-Z} = EI_1 W'''$	$EI_1 W''' = EI_1 W'''$
TORSIONAL MOMENT	$-GJY' - M_{PL-X} = -GJY'$	$-GJY' = -GJY'$

Table 7.- Pitch Link and Flapping Hinge BC's for model 2.

CHORDWISE BENDING MOMENT	$EI_{xx}\bar{j}' = EI_{xx}\bar{j}'$	$EI_{xx}\bar{j}' = EI_{xx}\bar{j}'$
FLAPWISE BENDING MOMENT	$EI_{hh}\bar{j}_z' + M_{PL-Y} = EI_{hh}\bar{j}_z'$	$EI_{hh}\bar{j}_z' + K_t\left(\bar{w}' - \bar{j}_z\right) = EI_{hh}\bar{j}_z'$
CHORDWISE ROTATION	$T\bar{v}' + kAG\left(\bar{v}' - \bar{j}_y\right) = T\bar{v}' + kAG\left(\bar{v}' - \bar{j}_y\right)$	$T\bar{v}' + kAG\left(\bar{v}' - \bar{j}_y\right) = T\bar{v}' + kAG\left(\bar{v}' - \bar{j}_y\right)$
FLAPWISE ROTATION	$T\bar{w}' + kAG\left(\bar{w}' - \bar{j}_z\right) = T\bar{w}' + kAG\left(\bar{w}' - \bar{j}_z\right)$	$T\bar{w}' + kAG\left(\bar{w}' - \bar{j}_z\right) = T\bar{w}' + kAG\left(\bar{w}' - \bar{j}_z\right)$
TORSIONAL MOMENT	$T\frac{I_a}{rA}\bar{y}' - M_{PL-X} = T\frac{I_a}{rA}\bar{y}'$	$T\frac{I_a}{rA}\bar{y}' = T\frac{I_a}{rA}\bar{y}'$

Table 8.- Pitch Link and Flapping Hinge BC's for model 3.

BENDING MOMENT	$EI_y j' + M_{PL-Y} = EI_y j'$	$EI_y j' + K_t\left(w' - j\right) = EI_y j'$
SHEAR FORCE	$Tw' + kAG\left(w' - j\right) + F_{PL-Z} = Tw' + kAG\left(w' - j\right)$	$Tw' + kAG\left(w' - j\right) = Tw' + kAG\left(w' - j\right)$
TORSIONAL MOMENT	$GJy' - M_{PL-X} = GJy'$	$GJy' = GJy'$

Table 9.- Pitch Link and Flapping Hinge BC's for model 4.

3.5.- Rotorcraft blade Ice accretion modelling approach

3.5.1.- Rotating blade modelling approach

The Ice accretion models in this thesis were implemented by using two different approaches. First approach is related with the rotating, centrifugal and Aerodynamic effects incorporated along with the growing and development of ice into the MBB Bo-105 blade's airfoil surfaces. The growing directions assumptions started from the leading edge side of the cross section towards the trailing edge, three segments or regions were taken into account as shown in the Fig. 25 and are further introduced in presented applications shown in chapter 6 later this document. The second approach is related with the simulation of changes into the Advanced beam's mass distribution, it was calculated the experimental non rotating Ice accretion testing explained in the chapter 4.

The Structural Health and Monitoring (SHM) methodologies for Ice accretion problem following the first approach was done by increasing in five progressive levels the ice formed on the helicopter's tip as shown in the Fig. 25. Where each of the cases of ice increases much more the thickness of the layer at the blade's leading edge. In other words, the ice starts developing slightly on top and low airfoil's surfaces towards the direction of elastic axis. It can be noticed that each section as 1, 2, and 3 of the blade's airfoil provides different weights per segments. Where each one of these 3 regions contributes progressive changes in the bending moments, shear forces and torsional moments, since each centroid on these regions have different distances about the elastic axis. The calculated volume of Ice accretion is obtained by using the length of the segment and the surface area, later that volume is converted into equivalent mass using specific density of ice.

When the ice layer increases, the chord's length and height of thick camber augments too, this means that these new values are then re-updated only for that tip section. Similar situation occurs for the sectional mass distribution and sectional moment of inertia about the in-plane axis. From the previous it is implied that for maximum case of Ice accretion there will be more loading causing the increase of the torsional moment, shear forces and bending moments. The critical type of Ice accretion 5 from Fig. 25, could be considered as a very extreme case of study since the body of ice would have a thickness layer of a subjective magnitude. This case recognized as Ice 5 can be comparable as the extreme case where the thickness of ice layer attached on the leading edge is around 1 meters, a case that in reality normally never happens while helicopter is in an operational flight mission, it was explored with the intention to observe the outputs.

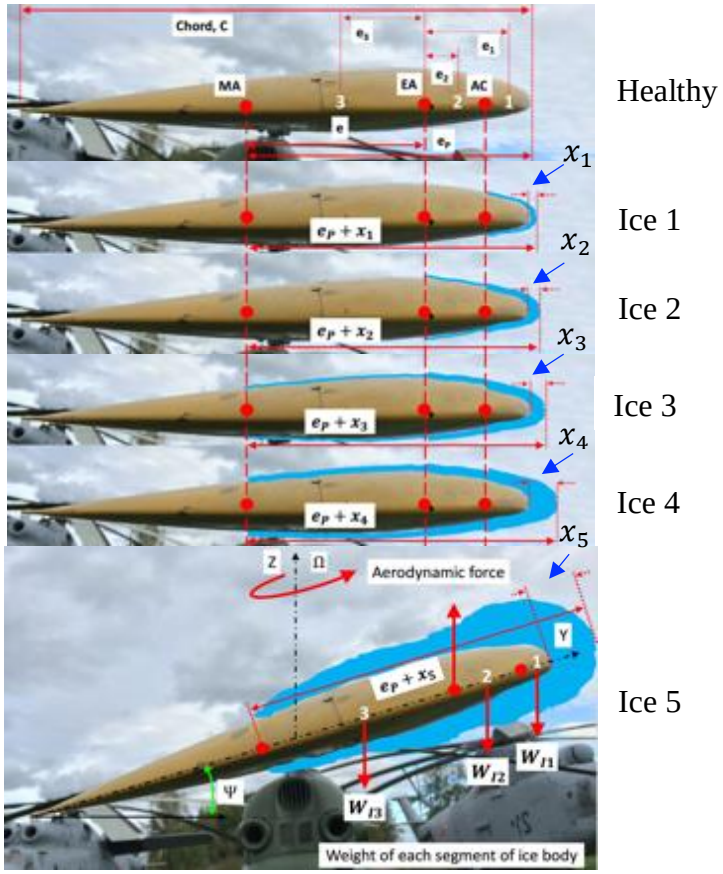

Figure 25. Layout of blade's cross sectional exposure of Ice accretion levels.

The introduction of Ice accretion onto the models is been selected firstly from helicopter blade cross section point of view (assuming geometries from an airfoil), and secondly, experimental cantilever beam perspective (simple mass addition). From rotorcraft point of view, all starts when the Ice increases with incremental $x_{(n)}$ $[m]$ as shown in Fig. 26, where n stands for the number of Ice accretion levels. The physics of Ice accretion model involve the usage of gradient factors as in (56), which implies that when the layer of ice grows 1mm in section 1, the layer's thickness on section 2 and 3 would be 0.4mm and 0.2mm respectively. The blade nominal and ice density are assumed to be 2600 $\frac{Kg}{m^3}$, and 934 $\frac{Kg}{m^3}$. **[D].** When the ice appears the blade's nominal density $\rho_{Ice(n)}$ gets updates and increases using the equivalent area method as in 57 **a)**, and consequently the updated chord $C_{Ice(n)}$ as in 57 **b)** and coupling distance $e_{Ice(n)}$ as in 57 **c)** augments since it considered to be the addition of superficial layer and modifying the area of airfoil. Following the Fig. 25-26, The coupling distances for torques e_P, e_1, e_2, e_3 from centroid of body of ice about the elastic axis as shown in equation (58)

$$\mathrm{D}_{Ice1} = x_{(n)} \quad \textbf{a)} \qquad \mathrm{D}_{Ice2} = \frac{x_{(n)}}{2.5} \quad \textbf{b)} \qquad \mathrm{D}_{Ice3} = \frac{x_{(n)}}{5} \quad \textbf{c)} \qquad \textbf{(56)}$$

$$r_{Ice(n)} = 934\left(1 - \left(\mathrm{D}_{Ice1}e + \mathrm{D}_{Ice2}\frac{C}{4} + \mathrm{D}_{Ice3}\frac{C}{8}\right)\right) + 2600 \quad \textbf{a)} \qquad C_{Ice(n)} = C + x_{(n)} \quad \textbf{b)} \qquad e_{Ice(n)} = 0 + x_{(n)} \quad \textbf{c)} \qquad \textbf{(57)}$$

$$e_P = e + \frac{C_{Ice(n)}}{8} + \frac{C_{Ice(n)}}{4} \quad \textbf{a)} \qquad e_1 = \frac{C_{Ice(n)}}{4} + \frac{C_{Ice(n)}}{16} \quad \textbf{b)} \qquad e_2 = \frac{2C_{Ice(n)}}{8} \quad \textbf{c)} \qquad e_3 = \frac{e_{Ice(n)}}{2} \quad \textbf{d)} \qquad \textbf{(58)}$$

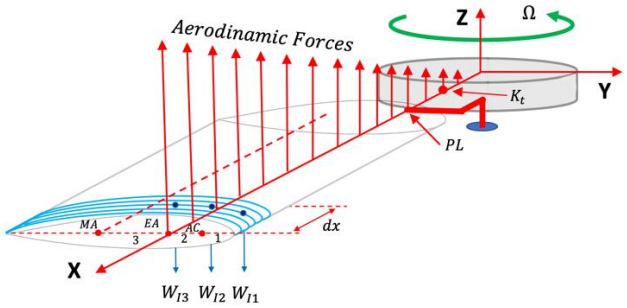

Figure 26. Free body of diagram of the Ice accretion model.

D https://en.wikipedia.org/wiki/Ice

The mass of Ice accretion segment 1,2, and 3 are calculated as in equations (59), respectively. The weights due to ice W_{I1}, W_{I2}, W_{I3} were then converted into gravitational forces. Where these 3 forces shown in the equations (60) acts through the center of gravity of each segment, therefore are used later to incorporate torque moments into blade's tip.

$$m_{I1} = \left[\frac{C_{Ice(n)}}{4}\frac{p}{2}\right] dx \frac{x_{(n)}}{D_{Ice1}} r_{Ice(n)} \quad \textbf{a)} \qquad m_{I2} = \left[\frac{C_{Ice(n)}}{8} dx \frac{x_{(n)}}{D_{Ice2}} r_{Ice_{(n)}}\right] 2 \quad \textbf{b)} \qquad m_{I3} = \left[e_{Ice(n)} dx \frac{x_{(n)}}{D_{Ice3}} r_{Ice(n)}\right] 2 \quad \textbf{c)} \quad \textbf{(59)}$$

$$W_{I1} = \frac{m_{I1}}{dx} g \quad \textbf{a)} \qquad W_{I2} = \frac{m_{I2}}{dx} g \quad \textbf{b)} \qquad W_{I3} = \frac{m_{I3}}{dx} g \quad \textbf{c)} \quad \textbf{(60)}$$

Where:

e_P, e_{I1}, e_{I2}, e_{I3} = Coupling distances for torque per segment due to ice, [m]
Δ_{Ice1}, Δ_{Ice2}, Δ_{Ice3} = Proportional gradient factors related to ice formation, [-]
m_{I1}, m_{I2}, m_{I3} = Mass per segment due to ice, [Kg]
W_{I1}, W_{I2}, W_{I3} = Gravitational weights per segments, [N]
$x_{(n)}$ = Tip's thickness of ice layer, [m]
dx = Axial length of body of ice, [m]

Blade's mass distribution in the model is affected and is shown as healthy reference as in 61 **a)** and contrasted from the Ice accretion as in equation 61 **b)**:

$$r A = \frac{r_{Blade} A_{Airfoil} dx}{dx} \quad \textbf{a)} \qquad r A_{Ice(n)} = \frac{r_{Blade} A_{Airfoil} dx + m_{I1} + m_{I2} + m_{I3}}{dx} \quad \textbf{b)} \quad \textbf{(61)}$$

Where:

ρA = Mass distribution at the blade's tip, [Kg/m]
$\rho A_{Ice(n)}$ = Changes in mass distribution at the blade's tip due to ice, [Kg/m]
$A_{Airfoil}$ = Airfoil cross sectional area, [m^2]

As the Ice accretion starts to adhere onto the system, the blade's properties also are affected. Therefore, the blade's mass moment of inertia I_α is analyzed in the equation 62 **a)** referred as the healthy and the dynamically affected helicopter blade tip due ice as shown in 62 **b)**.

$$I_a = \frac{r A\left(Z_1^2 + C^2\right)}{12} + r Ae^2 \quad \textbf{a)} \qquad I_{a\,Ice(n)} = \frac{r Ae_{Ice(n)}\left(Z_1^2 + C_{Ice(n)}{}^2\right)}{12} + r Ae_{Ice(n)}{}^2 \quad \textbf{b)} \quad \textbf{(62)}$$

Main justification of applying these changes is due to smaller modifications in blade's airfoil cross section at the ice affected segment. Four blade's sectional constants **[E,F]** shown as in (63) are used to calculate healthy flexural and torsional

rigidities are equations 64 **a)** and 65 **a)**, respectively. Subsequently modifications on blade's tip due ice formation are equations 64 **b)** and 65 **b)**. Next additional step of analysis is the incorporation and assumptions that occurs between added layers of ice and blade specially when blade is rotating. Therefore, 3 additional physics were considered: Firstly, the centrifugal forces that appears when blade is moving in circular orientation and these forces are directed away from the rotor's hub as shown in equation 66 **b)** by using the calculated accreted ice mass shown in 66 **a)**. Secondly, the cohesion force that represents the ice strength is given by 66 **c)**, by using cohesion surface area and the cohesive (tensile) ice strength from the reference **[G,H].** Thirdly, the adhesive shear force between ice and blade interface, where this represents the mechanical bonds and internal molecular arrangement on both bodies and is given by equation 66 **d)**.

$$j = 0.036 \quad \textbf{a)} \qquad q = 5.33 \quad \textbf{b)} \qquad k = 3.36 \quad \textbf{c)} \qquad s = 0.33 \quad \textbf{d)} \qquad \textbf{(63)}$$

$$EI_y = \left[jCZ_1\left(Z_1^2 + C^2\right)\right]E \quad \textbf{a)} \qquad EI_{yIce(n)} = \left[jC_{Ice(n)}Z_1\left(Z_1^2 + C_{Ice(n)}{}^2\right)\right]E \quad \textbf{b)} \qquad \textbf{(64)}$$

$$GJ = \frac{E}{2\left(1+s\right)}\left\{\left[q - k\frac{Z_1}{C}\left(1 - \frac{Z_1^4}{12C^4}\right)\right]CZ_1\right\} \quad \textbf{a)} \qquad GJ_{Ice(n)} = \frac{E}{2\left(1+s\right)}\left\{\left[q - k\frac{Z_1}{C_{Ice(n)}}\left(1 - \frac{Z_1^4}{12C_{Ice(n)}{}^4}\right)\right]C_{Ice(n)}Z_1\right\} \quad \textbf{b)} \qquad \textbf{(65)}$$

$$m_{I(n)} = V_{I(n)}r_{Ice} \quad \textbf{a)} \qquad F_{Ce(n)} = m_{I(n)}r_{Element}W^2 \quad \textbf{b)} \qquad F_{Co(n)} = AC_{Ice}s \quad \textbf{c)} \qquad F_{Ad(n)} = t\,S_{Contact}dx \quad \textbf{d)} \qquad \textbf{(66)}$$

Where:

$m_{I(n)}$ = Mass of the body of ice, [Kg]
$V_{I(n)}$ = Volume of the body of ice, [m^3]
ρ_{Ice} = Density of the body of ice, [Kg/m^3]
$F_{Co(n)}$ = Cohesion force, [N]
AC_{Ice} = Cohesion surface or area of contact, [m^2]
σ = Cohesive ice strength, [kPa]
$F_{Ad(n)}$ = Shear adhesion force, [N]
τ = Shear adhesion strength, [kPa]
$S_{contact}dx$ = Volume of the body of ice, [m^3]
$F_{Ce(n)}$ = Centrifugal force, [N]

E https://www.google.co.uk/search?q=torsional+constant+rectangle&source=lnms&tbm=isch&sa=X&ved=0ahUKEwimrvzu0rbdAhVSTBoKHUMuAwQQ_AUICigB&biw=1278&bih=1104#imgrc=-N0j-6pOKlVaPM:

F https://en.wikipedia.org/wiki/Torsion_constant#cite_note-Roark7-5

G https://www.tandfonline.com/doi/abs/10.1080/01694243.2017.1297588?src=recsys&journalCode=tast20&

H https://etd.ohiolink.edu/!etd.send_file?accession=case1283536362&disposition=inline

The previous discussed forces that are generated when the rotor blade is rotating are displayed in the Fig. 27. Additionally, as shown in the Fig. 28, Lift force causes shear force and bending moment between ice and blade, resulting in break off of the ice. However, the total Aerodynamic lift force are dramatically reduced, these reductions are proportional to extent of ice acting on blade's tip. The greater the presence of ice, worst performance will be in the helicopter.

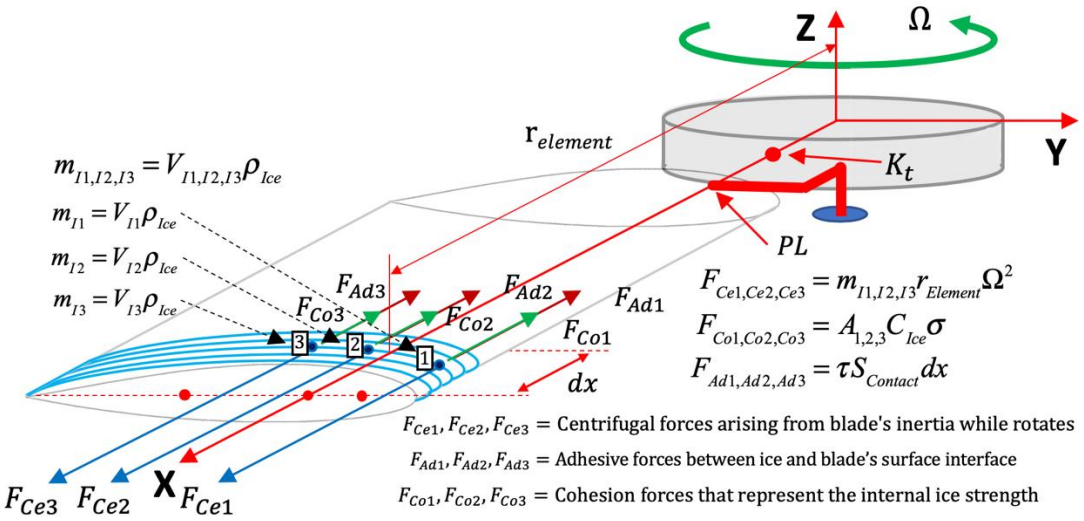

Figure 27. Free body of diagram of forces due blade's rotations.

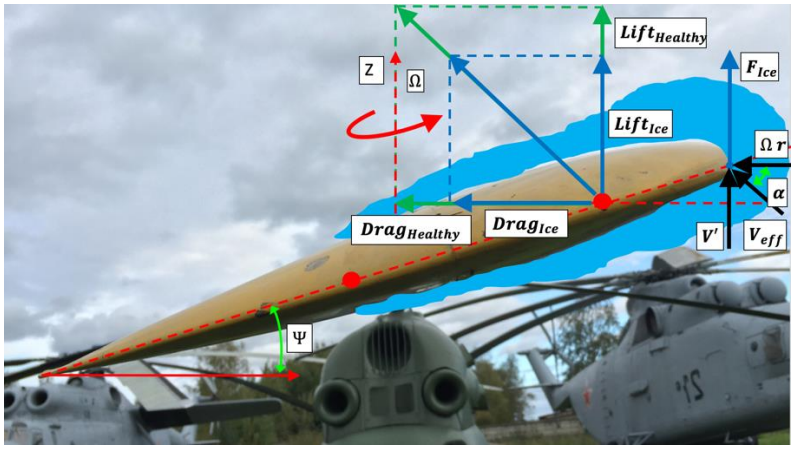

Figure 28. Free body of diagram of the effects of the Ice accretion.

Where:

$Lift_{Healthy}$, $Drag_{Healthy}$ = Lift and drag healthy forces, [N]
$Lift_{Ice}$, $Drag_{Ice}$ = Lift and drag reduced forces due Ice damage, [N]
V_{eff} = Effective velocity of the airfoil, [rad/s]
V' = Reduced wind speed of the rotor, [rad/s]
α = Angle of attack,
Ω = Angular velocity of the rotor, [rad/s]
F_{Ice} = Aerodynamic force acting on the leading edge, [N]

3.5.2.- Non-rotating blade experimental approach

From the experimental model point of view when the formed ice increases with the incremental $x_{(n)}$, shown in the equations (67) (which changes the distance between mass axis to elastic axis). It is assumed that experimental Ice accretion conditions occurs at the lateral face in the beam's tip as shown in the Fig. 29.

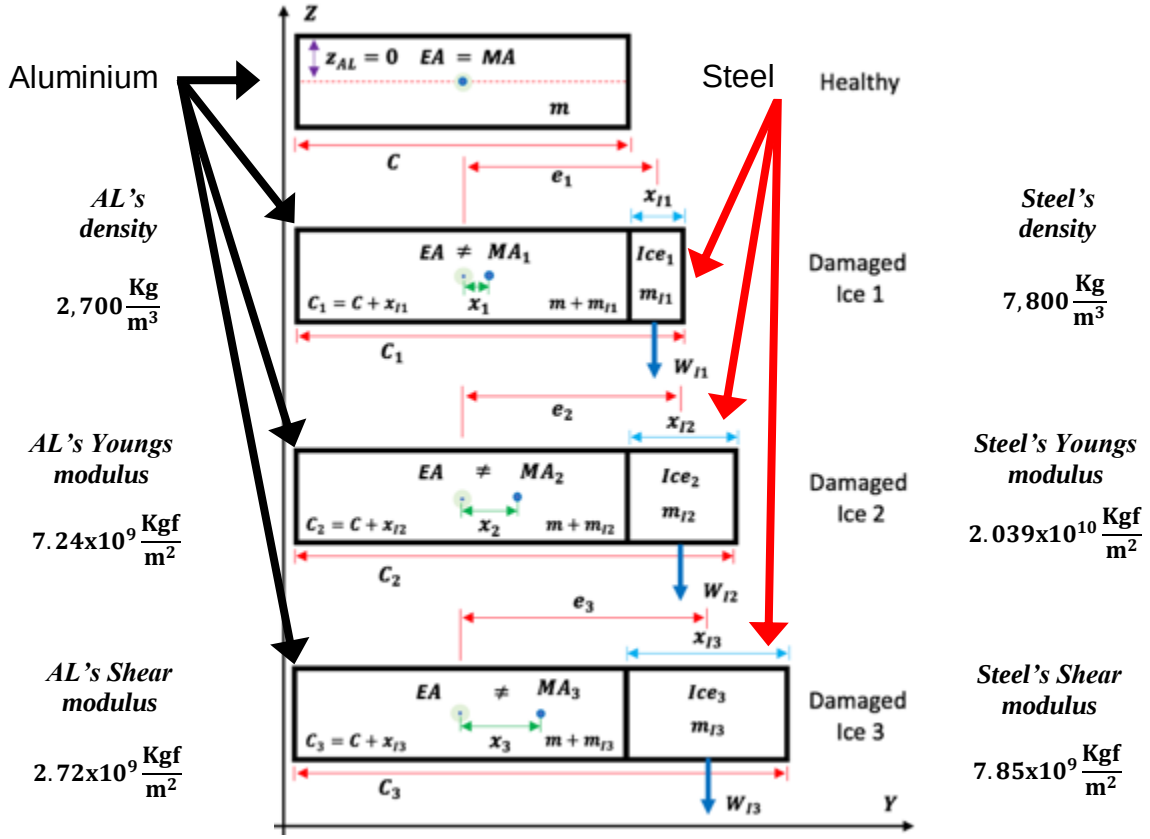

Figure 29. Experimental and modelling features for Ice accretion formulation.

$$e = 0 \rightarrow M_A = E_A \quad \textbf{a)} \qquad C_{(n)} = C + x_{I(n)} \quad \textbf{b)} \qquad x_{(n)} = \frac{x_{I(n)}}{2} \quad \textbf{c)} \quad \textbf{(67)}$$

These mass additions of each Steel blocks introduces coupling distances between the centroid of mass of each Steel's strips about the elastic axis that are shown in the equations (68), which are later used to applied torques.

$$e_1 = \frac{C}{2} + \frac{x_{I(1)}}{2} \quad \textbf{a)} \qquad e_2 = \frac{C}{2} + \frac{x_{I(2)}}{2} \quad \textbf{b)} \qquad e_3 = \frac{C}{2} + \frac{x_{I(3)}}{2} \quad \textbf{c)} \quad \textbf{(68)}$$

These previously added Steel's strips changes the dynamics starting with modifying the chord's or width of the beam, this re-updated chord value changes the cross-section area as shown in (69)

$$\begin{aligned} Area_{AL} &= Height_{AL} C \\ Area_{Ice(n)} &= Height_{Ice(n)} x_{I(n)} \\ Area_{Total(n)} &= Area_{AL} + Area_{Ice(n)} \end{aligned} \quad \textbf{(69)}$$

This new area due to added body introduce more mass altering the mass of each sections as in (70).

$$\begin{aligned} m &= Area_{AL} \text{Length}_{Beam} r_{AL} \\ m_{I(n)} &= Area_{Ice(n)} \text{Length}_{Ice} r_{Steel} \\ m_{Total(n)} &= m + m_{I(n)} \end{aligned} \quad \textbf{(70)}$$

The incorporated masses influence the mass distributions of the Aluminium beam as shown as in the equations (71).

$$\begin{aligned} Ma &= \frac{m}{\text{Length}_{Beam}} \\ Ma_{I(n)} &= \frac{m_{I(n)}}{\text{Length}_{Ice}} \\ Ma_{Total(n)} &= Ma + Ma_{I(n)} \end{aligned} \quad \textbf{(71)}$$

The added Steel's strips introduces gravitational forces due to the block's weight that acts through the centroid of each block as shown in the equations (72), these gravitational forces adds torques from the centroid of mass about the elastic axis as shown in the equations (73). Where these boundary conditions will play a significant role as introduces more torsional moment at the beam's tip model.

$$W_{I1} = Ma_{I1} g_e \left[N \right] \textbf{ a)} \quad W_{I2} = Ma_{I2} g_e \left[N \right] \textbf{ b)} \quad W_{I3} = Ma_{I3} g_e \left[N \right] \textbf{ c)} \quad \textbf{(72)}$$

$$BC_{T1} = W_{I1} e_1 \left[Nm \right] \textbf{ a)} \quad BC_{T2} = W_{I2} e_2 \left[Nm \right] \textbf{ b)} \quad BC_{T3} = W_{I3} e_3 \left[Nm \right] \textbf{ c)} \quad \textbf{(73)}$$

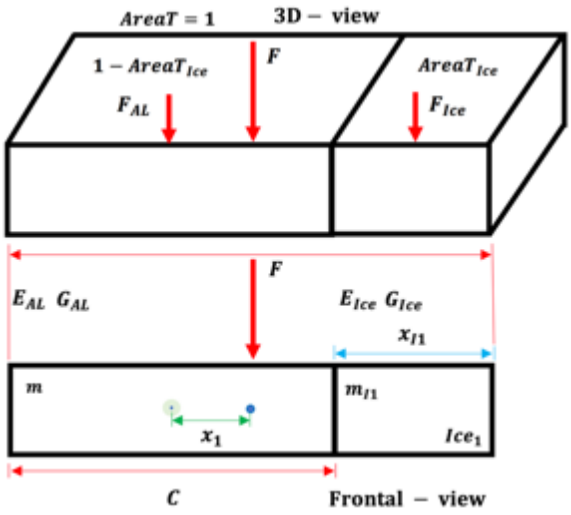

Figure 30. Composite element resulting of a bonding between dissimilar bodies.

To obtain Youngs and Shear modulus it was assumed that the beam region affected with Ice accretion can be treated as a composite as shown in Fig. 30. These elements are considered to be in equilibrium, so the applied forces also are assuming to be equal and balance between both sections (Aluminium and Steel). When force is perpendicular aligned, then the stress is established to be equal to effective Youngs modulus per the strain in material. This was approached using Hooke's Law as shown in (74) which states that the stress (force) that a material experience is proportional to the strain (deflection). For compatibility purposes, strains on both elements are assumed to be the same, therefore effective Young and Shear modulus were calculated as shown in (75) and (76) respectively.

$$F = F_{AL} + F_{Ice} \qquad s = s_{Ice} AreaT_{Ice(n)} + s_{AL}\left(1 - AreaT_{Ice(n)}\right)$$

$$s = eE_{effective} \tag{74}$$

Perpendicular and aligned to composite body as in F_A Solutions:

$$\frac{s}{E_{effective}} = \frac{s_{Ice}}{E_{Ice}} x_{I(n)} + \frac{s_{AL}}{E_{AL}} C \qquad \frac{s}{E_{effective}} = \frac{s}{E_{Ice}} x_{I(n)} + \frac{s}{E_{AL}} C \qquad \frac{1}{E_{effective}} = \frac{1}{E_{Ice}} x_{I(n)} + \frac{1}{E_{AL}} C$$

$$E_{effective} = \frac{E_{AL} E_{Ice}}{C E_{AL} + x_{I(n)} E_{Ice}} \tag{75}$$

$$G_{effective} = \frac{G_{AL} G_{Ice}}{C G_{AL} + x_{I(n)} G_{Ice}} \tag{76}$$

At this stage, the previous calculations will modify beam's mass distributions, mass moment of inertias, second moment of inertias and the torsional constants are then calculated from base Aluminium material and then the re-updated due damaged ice as shown in (77), (78), and (79) respectively:

$$I_{a\,AL} = \frac{Ma\left(Height_{Beam}{}^{2} + C^{2}\right)}{12} + Max_{(n)}{}^{2}$$

$$I_{a\,Ice(n)} = \frac{Ma_{I(n)}\left(Height_{Ice}{}^{2} + x_{I(n)}{}^{2}\right)}{12} + Ma_{I(n)}\left(\frac{C}{2} + \frac{x_{I(n)}}{2}\right)^{2}$$

$$I_{a(n)} = I_{a\,AL} + I_{a\,Ice(n)} \quad \textbf{(77)}$$

$$I_{y\text{-}AL} = \frac{Height_{AL}{}^{3}C}{12} + Area_{Al}z_{AL}{}^{2}$$

$$I_{y\text{-}Ice(n)} = \frac{Height_{Ice(n)}{}^{3}x_{I(n)}}{12} + Area_{Ice(n)}z_{Ice(n)}{}^{2}$$

$$EI_{y} = E_{effective}\left(I_{y\text{-}AL} + I_{y\text{-}Ice(n)}\right) \quad \textbf{(78)}$$

$$J_{AL} = \left[\frac{1}{3} - \left(0.021\frac{Height_{AL}}{C}\right)\left(1 - \frac{Height_{AL}{}^{4}}{12C^{4}}\right)\right]Height_{AL}{}^{3}C$$

$$J_{Ice(n)} = \left[\frac{1}{3} - \left(0.021\frac{Height_{Ice(n)}}{x_{I(n)}}\right)\left(1 - \frac{Height_{Ice(n)}{}^{4}}{12x_{I(n)}{}^{4}}\right)\right]Height_{Ice(n)}{}^{3}x_{I(n)}$$

$$GJ = G_{effective}\left(J_{AL} + J_{Ice(n)}\right) \quad \textbf{(79)}$$

Where:

C, $C_{(n)}$ = Healthy and re-updated chord (width) on the beam section, [m]
e, $x_{(n)}$ = Healthy and re-updated distance due ice (mass to elastic axis), [m]
$Height_{AL}$, $Height_{Ice(n)}$ = Healthy and re-updated height on beam section due ice, [m]
$Length_{beam}$,$Length_{Ice}$ = Healthy and re-updated length on beam section due ice, [m]
$Area_{AL}$, $Area_{Ice(n)}$ = Healthy and re-updated cross-sectional area of airfoil due ice, [m^2]
ρ_{AL}, ρ_{Steel} = Density of Aluminium and Steel, [Kg/m^3]
Ma, $Ma_{I(n)}$ = Healthy and re-updated mass distribution due ice, [Kg/m]
$I_{\alpha AL}$, $I_{\alpha Ice(n)}$ = Healthy and re-updated mass moment of inertia due ice, [Kgm]
E_{AL}, E_{Ice} = Aluminium and Steel's youngs modulus, [Kgf/m^2]
I_{y-AL}, $I_{y-Ice(n)}$ = Healthy and re-updated second moment of inertia due ice, [m^4]
G_{AL}, G_{Ice} = Aluminium and Steel's shear modulus, [Kgf/m^2]
J_{AL}, $J_{Ice(n)}$ = Healthy and re-updated torsional constants due ice, [m^4]
e_1, e_2 , e_3 = Distances of rotation to the force points per Steel's strip, [m]
W_{I1}, W_{I2} , W_{I3} = Gravitational forces of each Steel's strip studied cases, [N]
BC_{T1}, BC_{T2} , BC_{T3} = Boundary conditions for the torsional moments, [Nm]

3.6.- Rotating aero elastic rotorcraft pitched blade model

The rotating aero elastic modelling were approached using three ideal environmental circumstances, these would be explained in following sections.

3.6.1.- Vacuum Chamber (VC) theory assumptions

Taking as a reference the fourth model, which is the rotating Bending-Torsional coupling “Timoshenko”, from the 3 coupled equations of motions below, it can resume that elements on the right-hand side are related to external loading that the system is experiencing during the calculation and parametric evaluations. Those 3 sets of red zeros on the external right-hand side of each equations provide the assumption that rotor blade system is spinning cyclically under influence of close chamber environment, an environment completely adiabatic where nothing from out the closed chamber is interfering on the rotating frame of reference.

Bending moment equation

$$\omega^2 \rho A w + \omega^2 \rho A e \gamma + \left(T w'\right)' + \left[kAG\left(w' - \varphi\right)' \right]' = 0$$

Rotation due to bending equation

$$\rho I_y \omega^2 \varphi + \rho I_y \Omega^2 \varphi + \left(E I_y \varphi'\right)' + kAG\left(w' - \varphi\right) - \rho A e \Omega^2 \left(R + x\right)\gamma + 2\rho I_y \Omega \dot{\gamma} = 0$$

Torsional moment equation

$$\omega^2 I_a \gamma + \omega^2 \rho A e w + \rho \left(I_y - I_z\right)\Omega^2 \gamma + \left(GJ\gamma'\right)' + \left(T \frac{I_a}{\rho A} \gamma' \right)' - \rho A e \Omega^2 \left(R + x\right)\varphi - 2\rho I_y \Omega \dot{\varphi} = 0$$

3.6.2.- Quasi-Steady Aerodynamic (QSA) external loading theory

In this thesis, every BVP4c model that was used to study the structural dynamics is assumed that performs motions under a free tip undamped vibration, this means that there is no external loading acting at any location on the beam span.

From this previous assumption, and from an equation point of view as following the simple equation $y + x = 0$. This equational system suggests a balance between left-hand side "$y + x$" and right-hand side "0". From the element "0", is assumed to represent zero external loading, therefore a proper Aerodynamic loading was explored using two different research lines that will be discussed independently. Firstly, the derivation set of the Quasi-Steady Aerodynamics (QSA) loading theory is discussed. From this theory both resultant elemental lift and drag forces involved are described using strip theory. Since "BVP4c" models are already discretized by several stations or subdomains on helicopter longitudinal blade axis with different blade's cross section per segment. Therefore, the velocities, angles, distances and forces in the system are shown in the Fig. 31. Certain assumptions were made and used in the Aerodynamic formulations. Due the tangential velocity U_T is greater than perpendicular component U_P, ($U_T \gg U_P$) it is assumed that free stream resultant velocity would adopt form as equation (80):

$$U_{¥} = \sqrt{U_P^{\,2} + U_T^{\,2}} \;@U \qquad \textbf{(80)}$$

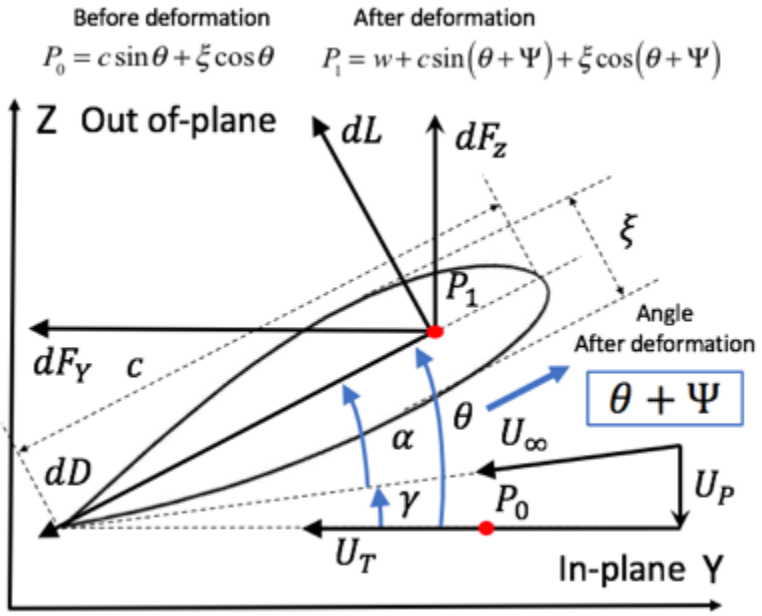

Figure 31. Free body of diagram of the Aerodynamic loadings acting on rotor blade cross section airfoil surfaces for Quasi-Steady Aerodynamics.

This assumption is consistent and valid everywhere except the rotor blade's hub. Also, the induced inflow angle γ involved were assumed to be very small as in (81) **[94,95,96,97,98]**:

$$\sin g @g \quad \textbf{a)} \quad \cos g @1 \quad \textbf{b)} \quad U_P/U_T = \tan g @g \quad \textbf{c)} \qquad \textbf{(81)}$$

Therefore, the effective angle of attack is shown in equation (82):

$$a = q - g @q - U_P/U_T \qquad \textbf{(82)}$$

From the Fig. 31, and considering previous assumptions, the expressions used as sectional lift and the sectional drag forces that acts on the blade element of length dr, are then expressed in next equations (83) and (84) respectively. Also, the Aerodynamic pitching moment is written as in (85):

$$dL = \frac{\rho_\infty ca}{2}\left(-U_T U_P + \frac{c}{a}U_T\dot{\varepsilon} - \frac{c}{4}\dot{U}_P - \left(\frac{c}{4}\right)^2\ddot{\varepsilon}\right)dr \qquad \textbf{(83)}$$

$$dD = \frac{\rho_\infty ca}{2}\left(U_P{}^2 - \frac{c}{2}U_P\dot{\varepsilon} - \frac{C_d}{a}U_T{}^2\right)dr \qquad \textbf{(84)}$$

$$M_\Psi = \frac{\rho_\infty ca}{2}\left(\left(\frac{c}{4}\right)^2\left(U_T\dot{\varepsilon} - \dot{U}_P + \frac{3c}{4}\ddot{\varepsilon}\right)\right)dr \qquad \textbf{(85)}$$

Where:
U_p = Perpendicular velocity component, [rad/s^2]
U_T = Tangential velocity component, [rad/s^2]
θ = Built-in blade pitch angle, [rad]
γ = Pitch angle respect to induced inflow, [rad]
α = Effective angle of attack, [rad]
dL = Lift force, [N]
dD = Drag force, [N]
dr = Blade Element length, [m]
a = Lift curve slope,
c = Chord length, [m]

According to the coordinates shown in the Fig. 31, it can be concluded that the resultant vertical and in-plane forces can be, as equations (86) and (87):

$$dF_Z = dL\cos g - dD\sin g @dL - dDg \qquad \textbf{(86)}$$

$$dF_Y = dL\sin g + dD\cos g @dLg - dD \qquad \textbf{(87)}$$

Equations (83) and (84), are then substituted into equations (86) and (87):

$$dF_Z = \frac{\rho_\infty ca}{2}\left(-U_T U_P + \frac{c}{a}U_T\dot{\varepsilon} - \frac{c}{4}\dot{U}_P - \left(\frac{c}{4}\right)^2 \ddot{\varepsilon} - \left(U_P{}^2 - \frac{c}{2}U_P\dot{\varepsilon} - \frac{C_d}{a}U_T{}^2 \right)\gamma \right) dr \quad \textbf{(88)}$$

$$dF_Y = \frac{\rho_\infty ca}{2}\left(\left(-U_T U_P + \frac{c}{a}U_T\dot{\varepsilon} - \frac{c}{4}\dot{U}_P - \left(\frac{c}{4}\right)^2 \ddot{\varepsilon} \right)\gamma - \left(U_P{}^2 - \frac{c}{2}U_P\dot{\varepsilon} - \frac{C_d}{a}U_T{}^2 \right) \right) dr \quad \textbf{(89)}$$

From here, considering and analyzing the in plane and out of plane axis on blade's airfoil shown in the Fig. 31, where all the relative velocity components are considered in equations (88) and (89). The induced inflow vi shown in 90 **a)**, was considered to be steady and uniform throughout blade, also the blade angle at location 75% of its length is assumed to be equal to the blade collective pitch plus the equilibrium elastic angle, and σ is the blade solidity as shown in 90 **b)**:

$$vi = \operatorname{sgn}\left[\theta + \phi_0(0.75R)\right]\Omega R\frac{\pi\sigma}{8}\left(\sqrt{1 + \frac{12}{\pi\sigma}\left|\theta + \phi_0(0.75R)\right|} - 1\right) \quad \textit{a)} \quad \sigma = \frac{bc}{\pi R} \quad \textit{b)} \quad \textbf{(90)}$$

$$U_T = \Omega x \quad \textit{a)} \quad U_P = vi + \dot{w} - \Omega x\left(\theta + \Psi\right) \quad \textit{b)} \quad \dot{\varepsilon} \cong \dot{\Psi} + \Omega\left(\beta_{PC} + w'\right) \quad \textit{C)} \quad \textbf{(91)}$$

Where:

dF_Z = Vertical force, [N]

dF_Y = In-plane force, [N]

V_i = Induced inflow velocity, [rad/s^2]

V_c = Climbing velocity, [m/s^2]

$\dot{\varepsilon}$ = Pitch angular velocity, [rad/s^2]

B_{PC} = Precone angle, [rad]

Substituting equations (90) into equations 91 **a)** and 91 **b)**, results into final equation form of both perpendicular U_p and tangential U_T velocity components. Additional equation 91 **c)**, contains reference for pitch angular velocity in the blade. Therefore, the equations 91 **a)** and 91 **b)** are substitute into (88) and (89), in order to derivate and obtain the final force expressions shown in (92) and (93). Where the equation (92) was substituted on right-hand side for both ODE's related to bending and angle due bending moments.

For the case of the equation (93), was substituted on ODE's related to torsion moment. As these represents the Aerodynamic torsional moments, resulting the following equations **[94,95,96,97,98]**:

$$F_Z = \frac{\rho_\infty ac}{2}\left\{-\Omega x v i + \Omega^2 x^2\left(\theta + \Psi\right) + \Omega^2 \frac{xc}{2} w' - \Omega x \dot{w} + \frac{3}{4} c\Omega x \dot{\Psi} - \frac{c}{4}\ddot{w}\right.$$
$$\left. + W^2 x\left(\left(c\sin q + x\cos q\right) + \left(w + c\sin\left(q + Y\right) + x\cos\left(q + Y\right)\right)\right)\left(w' - j\right)\right\}$$

$$F_Z = \frac{r_\infty ac}{2}\left\{- W x v i + W^2 x^2\left(q + Y\right) + W^2 \frac{xc}{2} w' - i w W x w + i w \frac{3}{4} c W x Y - i w^2 \frac{c}{4} w\right.$$
$$\left. + W^2 x\left(\left(c\sin q + x\cos q\right) + \left(w + c\sin\left(q + Y\right) + x\cos\left(q + Y\right)\right)\right)\left(w' - j\right)\right\} \quad \textbf{(92)}$$

$$M_\Psi = -\frac{\rho_\infty ca}{2}\left(\frac{c^2}{4}\Omega x \dot{\psi}\right)$$

$$M_Y = - i w \frac{r_\infty ca}{2}\left(\frac{c^2}{4} W x y\right) \quad \textbf{(93)}$$

The complete equations of motions from the model 4 that performs rotation along with the Quasi-Steady Aerodynamic (QSA) terms marked with blue dashed rectangles in the next equations, where the breakdown of these equations are the bending moment, rotating due to bending deflection, and torsional moments as shown in equations (94), (95), and (96) as follows:

$$w^2 r A w + w^2 r A e y + \left(T w'\right)' + \left[kAG\left(w' - j\right)'\right]' = \boxed{F_Z R} \quad \textbf{(94)}$$

$$r I_y w^2 j + r I_y W^2 j + \left(E I_y j'\right)' + kAG\left(w' - j\right) - r A e W^2\left(R + x\right) y + 2 r I_y W y = \boxed{F_Z R} \quad \textbf{(95)}$$

$$w^2 I_a y + w^2 r A e w + r\left(I_y - I_z\right) W^2 y + \left(GJy'\right)' + \left(T\frac{I_a}{rA} y'\right)' - r A e W^2\left(R + x\right) j - 2 r I_y W j =$$
$$\boxed{- i w \frac{r_\infty ca}{2}\left(\frac{c^2}{4} W x y\right)} \quad \textbf{(96)}$$

3.6.3.- Blade Element Method (BEM) external loading theory

Secondly, the Blade Element Method (BEM) theory was applied in a similar way from the QSA theory. The BEM assumes that each one of the blade sections acts as a 2 dimensional airfoil to produce Aerodynamic forces. The blade in this theory is divided into multiple sections and all the calculations using BVP4c produces 2-D Aerodynamics. All the velocities, angles, distances and forces in the system can be observed in Fig. 32. The in-plane, out of plane, and total relative velocities are shown in 97 **a)**, 97 **b)**, and 97 **c)** respectively, **[Equations 1,99]:**

$$U_T = Wx \quad \text{a)} \quad U_P = Vc + vi \quad \text{b)} \quad U_T \gg U_P \rightarrow U_\infty = \sqrt{U_P^{\,2} + U_T^{\,2}} \approx U \quad \text{c)} \qquad \textbf{(97)}$$

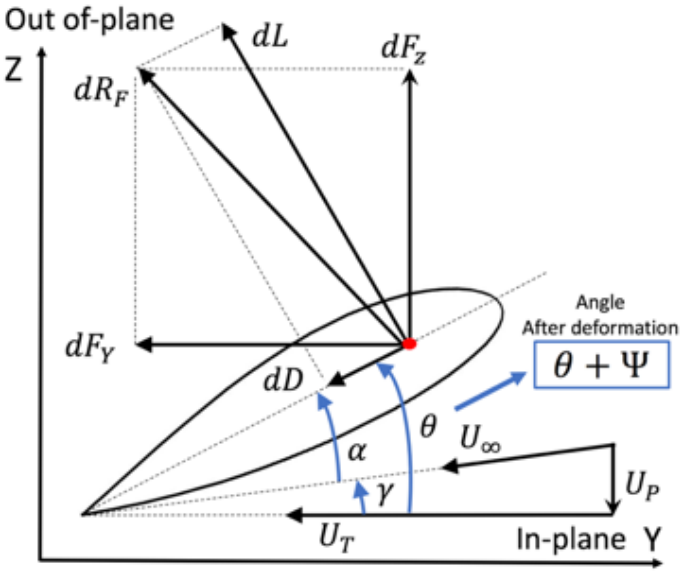

Figure 32. Free body of diagram of the Aerodynamic loadings acting on rotor blade cross section airfoil surfaces for Blade Element Method.

Also, the incremental lift and drag per unit span are shown in the equations (98) and (99) respectively. Other quantities are the parallel and perpendicular forces to the rotor disk plane are shown in equations (100). Substituting equations (98) and (99) into the equations 100 **a)** and 100 **b)**. These final derivations delivers the equations (101) and (102), for perpendicular and parallel forces.

[I] https://fenix.tecnico.ulisboa.pt/downloadFile/282093452028195/7-Blade%20element%20theory.pdf

$$dL = \frac{1}{2} r_{¥} U_{¥}{}^{2} c C_{1} dr \qquad dL = \frac{r_{¥} c C_{1}}{2} \left(U^{2}\right) dr \tag{98}$$

$$dD = \frac{1}{2} r_{¥} U_{¥}{}^{2} c C_{d} dr \qquad dD = \frac{r_{¥} c C_{d}}{2} \left(U^{2}\right) dr \tag{99}$$

$$dF_{Z} = dL \cos\left(q + Y\right) - dD \sin\left(q + Y\right) \quad \textit{a)}$$
$$dF_{Y} = dL \sin\left(q + Y\right) + dD \cos\left(q + Y\right) \quad \textit{b)} \tag{100}$$

$$dF_{Z} = \frac{r_{¥} c C_{1}}{2} \left(U^{2}\right) \cos\left(q + Y\right) dr - \frac{r_{¥} c C_{d}}{2} \left(U^{2}\right) \sin\left(q + Y\right) dr$$

$$dF_{Z} = \frac{r_{\infty} c C_{1}}{2} \left(\sqrt{\left(Vc + vi\right)^{2} + \left(Wx\right)^{2}}\right)^{2} \cos\left(q + Y\right) dr - \frac{r_{\infty} c C_{d}}{2} \left(\sqrt{\left(Vc + vi\right)^{2} + \left(Wx\right)^{2}}\right)^{2} \sin\left(q + Y\right) dr$$

$$F_{Z} = \frac{r_{\infty} c C_{1}}{2} \left(W^{2} x^{2} Y + Vi^{2} Y\right) - \frac{r_{\infty} c C_{d}}{2} \left(W^{2} x^{2} Y + Vi^{2} Y\right) \tag{101}$$

$$dF_{Y} = \frac{r_{¥} c C_{1}}{2} \left(U^{2}\right) \sin\left(q + Y\right) dr + \frac{r_{¥} c C_{d}}{2} \left(U^{2}\right) \cos\left(q + Y\right) dr$$

$$dF_{Y} = \frac{r_{\infty} c C_{1}}{2} \left(\sqrt{\left(Vc + vi\right)^{2} + \left(Wx\right)^{2}}\right)^{2} \sin\left(q + Y\right) dr + \frac{r_{\infty} c C_{d}}{2} \left(\sqrt{\left(Vc + vi\right)^{2} + \left(Wx\right)^{2}}\right)^{2} \cos\left(q + Y\right) dr$$

$$F_{Y} = \frac{r_{\infty} c C_{1}}{2} \left(W^{2} x^{2} Y + Vi^{2} Y\right) + \frac{r_{\infty} c C_{d}}{2} \left(W^{2} x^{2} Y + Vi^{2} Y\right) \tag{102}$$

Where:
dR_F = Resultant force, [N]
dF_Z = Vertical force, [N]
dF_Y = In-plane force, [N]
ρ_∞ = Free stream density, [Kg/m^3]
U_∞ = Free stream velocity, [rad/s^2]
C_1 = Sectional lift coefficient,
C_d = Sectional drag coefficient,
V_i = Induced inflow velocity, [rad/s^2]
V_c = Climbing velocity, [rad/s^2]

The final form of the BEM Aerodynamic forces are shown in the equations (103), (104), (105). Where the equation (103) is the resultant coupled force between the lift and drag components. Equations (104) and (105) represents the resultant Aerodynamic lift and torsional moments respectively, where the resultant lift force is then multiplied by the distance from the leading edge about the mass axis causing torsional moment and the length of the blade to introduce bending moment, which results the following equations, **[Equations 1,99]:**

$$R_F = \sqrt{F_Z^{\,2} + F_Y^{\,2}}$$

$$R_F = \sqrt{\left(\left(\frac{r_\infty cC_1}{2} - \frac{r_\infty cC_d}{2}\right)\left(W^2 x^2 Y + Vi^2 Y\right)\right)^2 + \left(\left(\frac{r_\infty cC_1}{2} + \frac{r_\infty cC_d}{2}\right)\left(W^2 x^2 Y + Vi^2 Y\right)\right)^2} \quad \textbf{(103)}$$

$$M_Z = F_Z R \quad \textbf{(104)}$$

$$M_Y = F_Z\left(e + \frac{c}{8} + \frac{c}{4}\right) \quad \textbf{(105)}$$

The complete equations of motions from the model 4 that performs rotation along with the Blade Element Method (BEM) terms marked with orange dashed rectangles in the next equations, where the breakdown of these equations are the bending moment, rotating due to bending deflection, and torsional moments as shown in equations (106), (107), (108) as follows:

$$w^2 r A w + w^2 r A e y + \left(T w'\right)' + \left[kAG\left(w' - j\right)'\right]' =$$

$$\boxed{M_Z} \quad \textbf{(106)}$$

$$r I_y w^2 j + r I_y W^2 j + \left(E I_y j'\right)' + kAG\left(w' - j\right) - r A e W^2 \left(R + x\right) y + 2 r I_y W y =$$

$$\boxed{M_Z} \quad \textbf{(107)}$$

$$w^2 I_a y + w^2 r A e w + r\left(I_y - I_z\right) W^2 y + \left(GJy'\right)' + \left(T\frac{I_a}{rA} y'\right)' - r A e W^2 \left(R + x\right) j - 2 r I_y W j =$$

$$\boxed{M_Y} \quad \textbf{(108)}$$

CHAPTER 4 EXPERIMENTAL SET UP AND MODAL ANALYSIS

4.1.- Motivations

The efforts that were followed as a part of the experimental motivational work in this thesis are related to two principal factors: Firstly, establishing a test rig with similarities according to helicopter blade's system in steady state, and Secondly, evaluate the sensitivity on the blade's bending-torsional dynamics under different experimental studied cases.

4.2.- Modal Analysis

Most of the practical vibration and noise problems are directly related to the resonance phenomena, where the forces excite one or the many vibration modes. When running a vibration test with any forced or free excitation in any structural configuration can be further reduced in obtaining the modal parameter data set. These modal parameters (modal frequency, modal damping, and mode shape) for specific modes, within the frequency range of interest, and the coupled dynamic description for a set of cantilever Advanced beams were adopted. Modal analysis is a process of determining complete modal parameters, where sufficient data is then used to formulate mathematical dynamic models. In this thesis, the fourth previously discussed mathematical models in chapter 3 are desired and necessary, for these reasons:

- To understand how any structure, behave under dynamic loads.
- To predict/simulate responses to assumed external forces.
- To simulate dynamical changes, due to physical modifications.

Mathematical models are simulations of the structure's dynamic behaviours, constrained by assumptions and its boundary conditions. Where the mathematical models are constructed using measured modal data, therefore the model needs to be simulated based with similar measured conditions. Modal data includes a range of applications such:

- Checking the modal frequencies and improving analytical models.
- Creating qualitative description for the mode shapes.
- Formulation to computer simulation for advanced prototype development.

According to previous bullet points, and for the research work done in this thesis, primarily it needed this:

- Predict response of assumed excitation and evaluate dynamic performance.
- Predict necessary physical modification required to obtain desired dynamic.
- Predict behaviours when two or more structures are coupled together.

The modal analysis carried out is a quasi-static analysis, where a load was applied on specific beam's spanwise locations. The dynamic analysis in this thesis provides a 1-to-1 relationship between an input (force applied) and output (beam's displacement due initial load). All structures contains internal resonant frequency where the structure can naturally vibrate. This test evaluates responses throughout frequency ranges, as range increase towards "resonant frequency", the amplitude of this response therefore goes to infinity. In simpler words, the modal analysis results displays data in 2 [x,y] axis "frequencies and amplitudes" which shows the values of frequencies at which the amplitude increases to infinity.

4.3.- Test rig design

Non-rotating helicopter blade-like experiments were carried out by using two cantilever Advanced beams that have different rectangular cross sections which were obtained by manufacturing bars of forged aluminum. This manufacturing work was performed at the machining centre of the University of Bristol. Both structures are similar except from the root section as shown in Fig. 33. Observing the root details of this design on beam's hinge (rectangular cut-outs and rounded notches will provide softening effects of coupled bending and torsional responses) and its implementations in the modal testing, these two are expected to be part of a comparison analysis framework for the bending-torsional responses. Dimensions for both Advanced beams are presented in Table 10, later this document. From the Fig. 33, notice the thicker section 1 of the left end was used in order to clamp it at the experimental working table using a big vice to constraint the beam at the root.

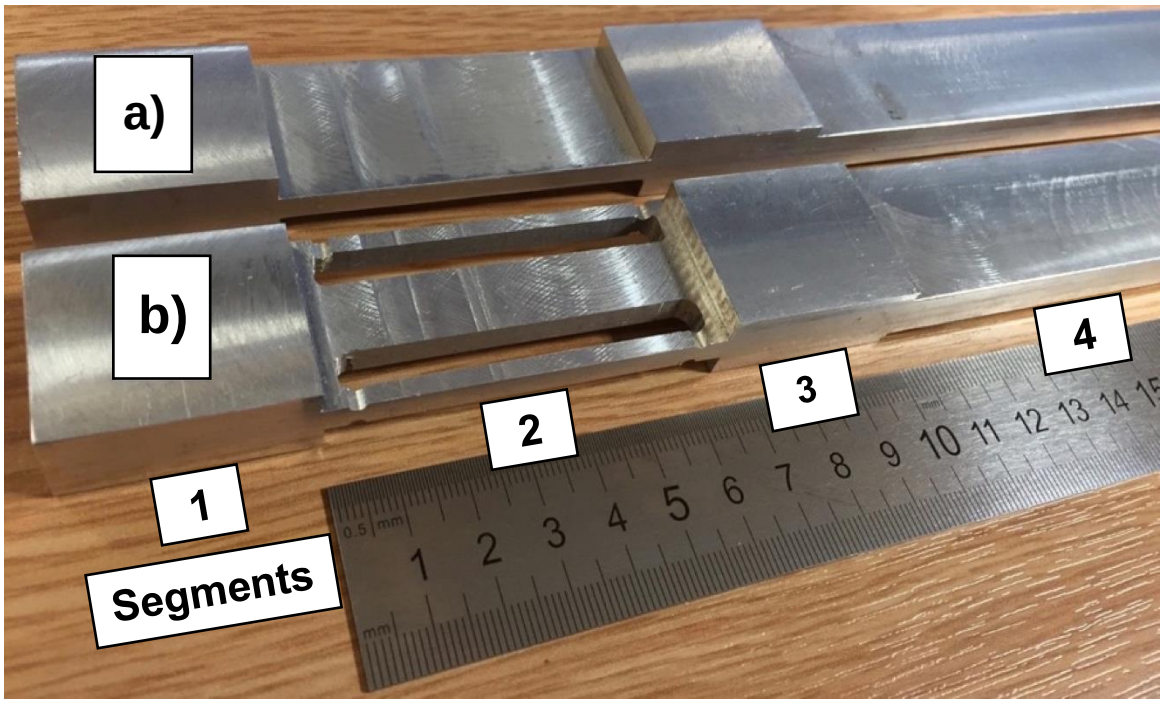

Figure 33. **a)** Normal Advanced beam, and **b)** Flexible Advanced beam which was modified on the root/hinge area for softening the torsional effects.

From the Fig. 34, it can be noticed that the third segment of the Advanced beams (similar clamping root section 1) from left to the right, was designed in order to incorporate onto the blade-like a Pitch Link (PL) L-shaped arm configuration. The proposed configuration and design of this arm is shown in the Fig. 34, where this configuration is capable to be installed in two formats. Firstly, the format of an integral and solid vertical PL arm, and secondly a three segmented bolted solid vertical PL arm. The main purpose behind these two proposed PL L-shaped arms are to explore how much is the percentage change in terms of the resonant natural frequencies values and explored what are the influences of having a 3 segmented bolted arm (this arm would be assumed to be partially damaged and/or altered) and observe its changes in the coupled bending and torsional structural dynamics. The previous was done for both advanced aluminum beams under the influence of the two Pitch Link versions, the compilation of the experimental results proposed in the chapter 4.4 are then presented and discussed in detail over the chapter 5, later in this document.

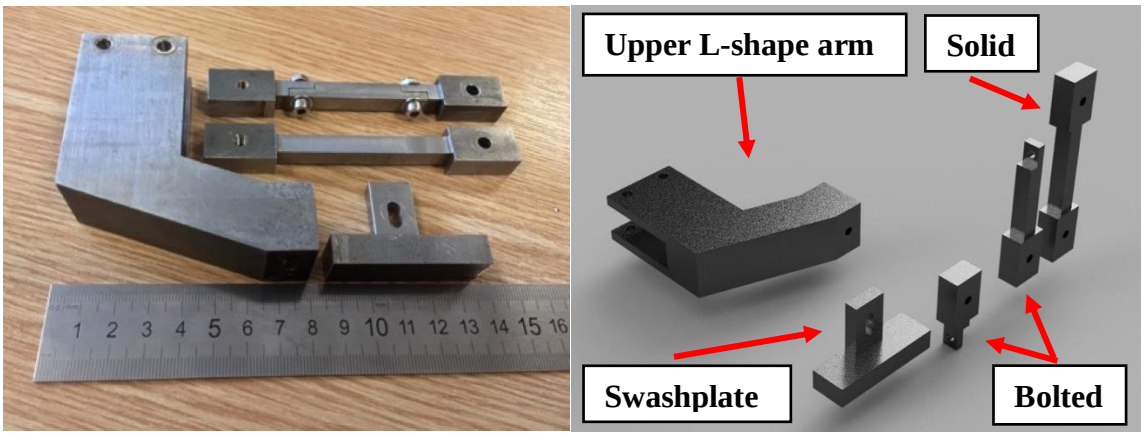

Figure 34. Pitch Link arm design for the experimental modal testing.

In this thesis, the selected devices and materials for this modal testing are shown in the Fig. 35 and Table 10 and are briefly described as it follows:

- ***Data acquisition -*** Matlab with drivers installed for external data acquisition box from National Instruments. The frequency response functions were stored in a frequency range of 0 to 1000 Hz. A sampling of 10 grid point per 1 Hz was adopted in all experimental conditions.
- ***Measurement -*** Two single axis accelerometers were used at the beam's tip and at the Pitch Link L-shape arm, each accelerometer weights 5.8 grs and sensitivity of 1.183 mV(m/s^2). They were mounted using wax method.
- ***Excitation -*** Manual excitation was applied using a modal hammer with a weight of 0.32 Kg and a sensitivity of 1.033 mV/N. The impacts were done using the plastic hard tip, depending in current environmental noises inside the dynamic laboratory the usage of earplugs was adopted.
- ***Other -*** 3 beams (2 advanced and 1 C-channel aluminum beam), Pitch Link assembly parts, Steel strips for Ice accretion simulations. Many sets of bolts and nuts for installation, Allen keys and torque wrench extension adaptors.

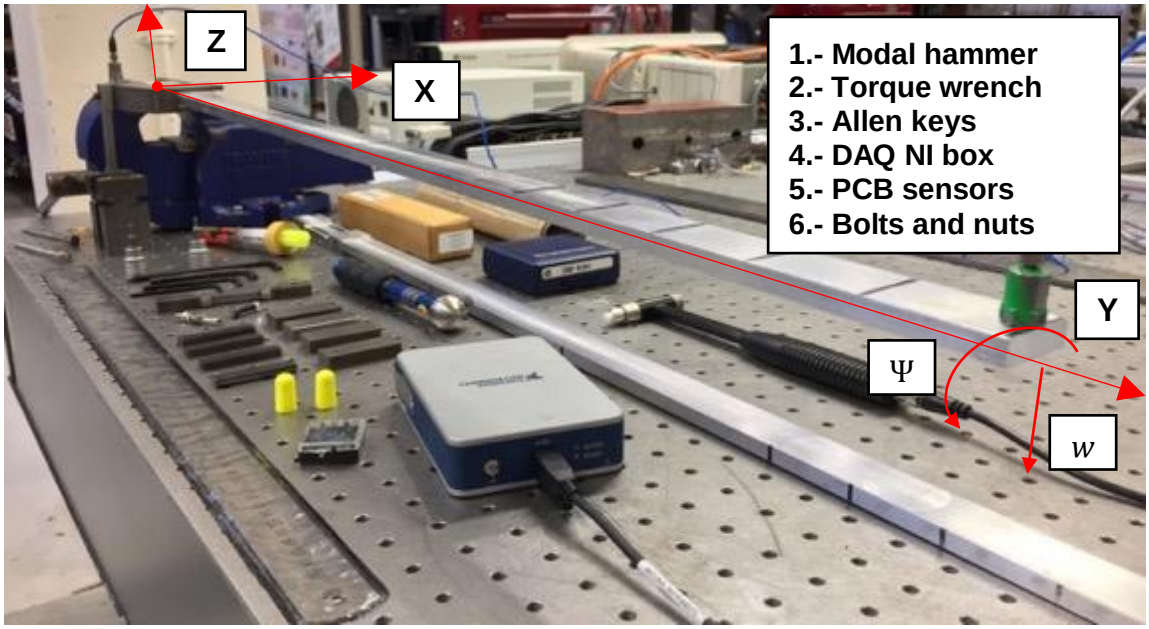

Figure 35. Experimental modal analysis and the used equipment.

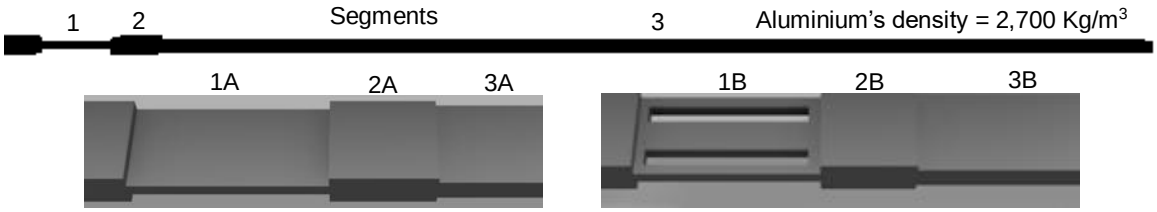

Segment	Height [m]	Width [m]	Length [m]	Volume [m^3]	Mass [Kg]
1A	0.0049 m	0.0301 m	0.0656 m	$9.6753x10^{-6}$ m^3	0.0261 Kg
2A	0.0151 m	0.0301 m	0.034 m	$1.5453x10^{-5}$ m^3	0.0417 Kg
3A	0.0099 m	0.0301 m	0.8025 m	$2.3914x10^{-4}$ m^3	0.6457 Kg
		Total =	0.9021 m	Total =	*0.7135 Kg*
			Mass distribution [Kg/m]		*0.7909* Kg/m
1B	0.0049 m	0.0301 m	0.0656 m	$9.1975x10^{-6}$ m^3	0.0248 Kg
2B	0.0145 m	0.0301 m	0.034 m	$1.4839x10^{-5}$ m^3	0.0401 Kg
3B	0.0099 m	0.0301 m	0.8045 m	$2.3973x10^{-4}$ m^3	0.6473 Kg
		Total =	0.9041 m	Total =	*0.7122 Kg*
			Mass distribution [Kg/m]		*0.7877* Kg/m

Pitch Link arm configuration

Segment	Length [m]	Mass [kg]
RAL	0.064 m	
AAL	0.05 m	
L-shape	0.114 m	0.4679 Kg
Solid		
PL	0.1015 m	0.0852 Kg
PL L-shape	0.2155 m	
	Total =	0.5531 Kg
Bolted		
PL	0.1015 m	0.0876 Kg
PL L-shape	0.2155 m	
	Total =	0.5555 Kg

Ice accretion Steel strips

Segment	Volume [m^3]	Mass [Kg]
Small strips for Tip ice		
Ice 1	$2.94x10^{-6}$ m^3	0.0224 Kg
Ice 2	$2.96x10^{-6}$ m^3	0.0225 Kg
Ice 3	$3x10^{-6}$ m^3	0.0228 Kg
Ice 4	$2.98x10^{-6}$ m^3	0.0227 Kg
Total =	$11.88x10^{-6}$ m^3	0.0904 Kg
Big strips for Longitudinal ice		
Ice 1	$10x10^{-5}$ m^3	0.0774 Kg
Ice 2	$10x10^{-5}$ m^3	0.0774 Kg
Ice 3	$9.97x10^{-5}$ m^3	0.0772 Kg
Ice 4	$9.97x10^{-5}$ m^3	0.0772 Kg
Ice 5	$9.48x10^{-5}$ m^3	0.0733 Kg
Total =	$49.42x10^{-6}$ m^3	0.3825 Kg

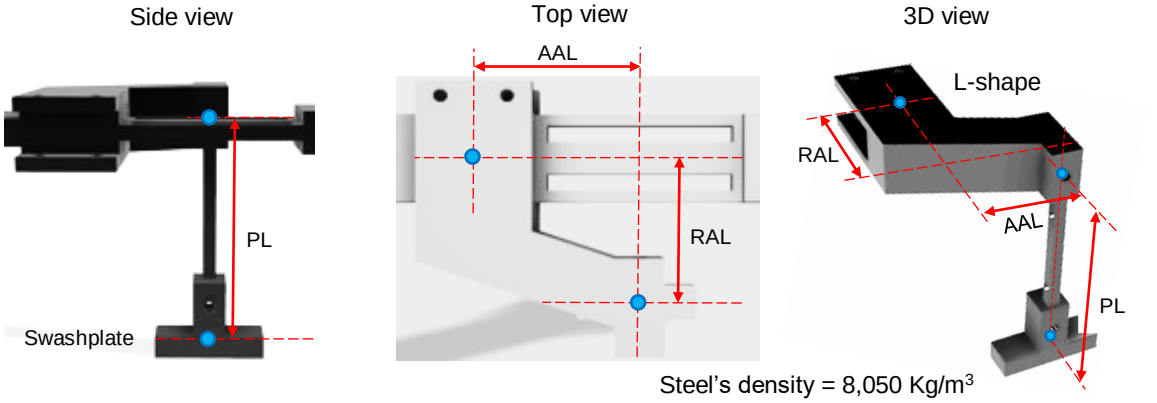

Table 10.- Specification of beams, Pitch Link and materials for modal testing.

4.4.- Test plan design

The complete assembly of Advanced beam with Pitch Link is shown in the Fig. 36. It shows the entire installation of experimental rig from a lateral upper view of the working table station in the dynamics laboratory. Notice two indicated deformation directions "W and Ψ" about axes "Z and Y", respectively. The modal analysis testing was done by impacting the beam using a modal hammer and exciting the beam over the yellow axis shown in Fig. 37, with the maximum offset about the beam's neutral axis ("Centroid" axis). The excitations via modal hammer was applied on 10 spanwise locations ("Green dots") shown in the Fig. 37. For monitoring healthiness on the beam's tip and Pitch Link arm, it was implemented two accelerometers. The first sensor was placed in the tip's edge at the mass axis, and the second sensor was attached on top of the PL L-shape arm.

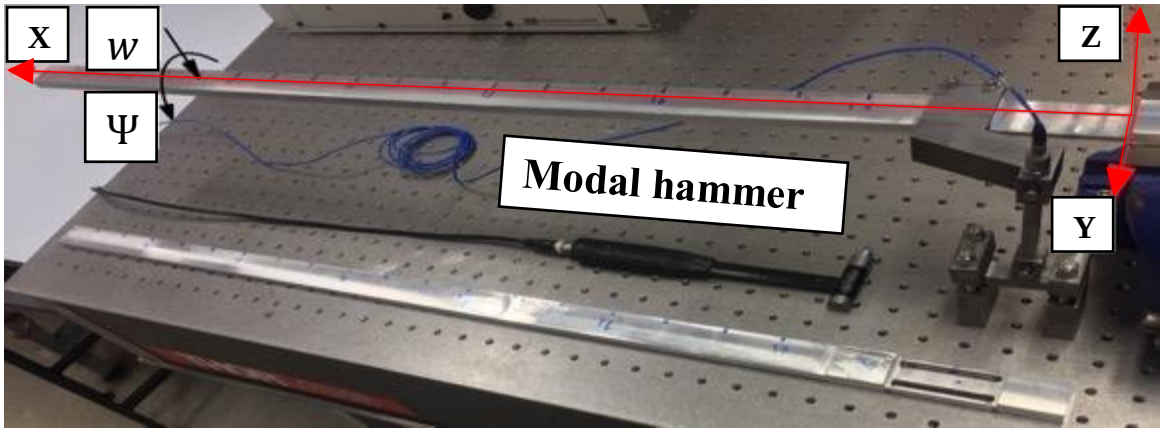

Figure 36. General view of the cantilever Advanced beam with the Pitch Link attached.

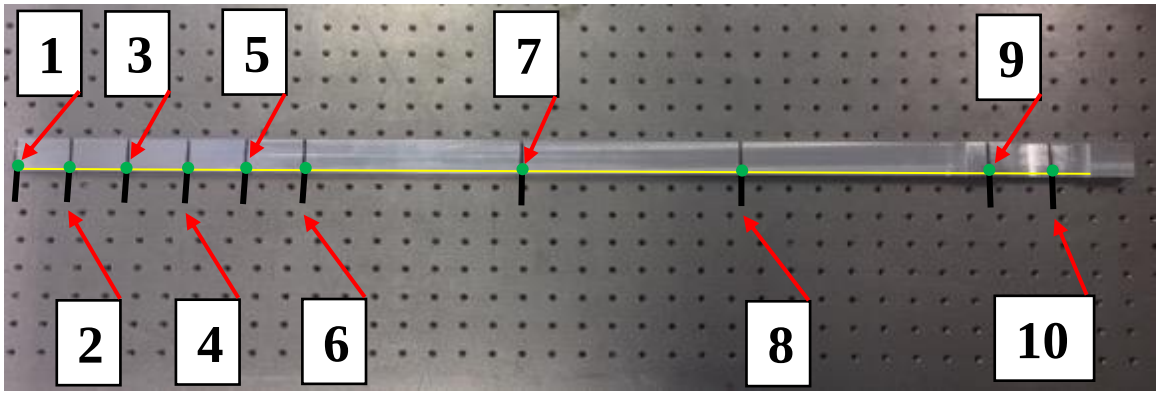

Figure 37. Beam locations for the excitations with the modal hammer.

4.4.1.- Damaged beam due changes in the Pitch Link (PL)

The complete experimental layout in the modal analysis carried out in this thesis were approached in three stages: Firstly, the main core-work is related to evaluate the applied sequential damage on the PL L-shape arm. Secondly, the initial explorations of Ice accretion testing was done by adding progressively four Steel strips on lateral face at the tip. Thirdly, after exploring the maximum case of ice on the tip, it was assumed that Ice accretion starts to propagate towards the beam's root direction in the axial coordinate. All complete parameters and more details for experimental framework are shown in Table 11. For PL's purposes a torque wrench tool was used to apply changes in the tightening torque values in a bolt at a lower joint of the vertical arm with the ground base ("swashplate") indicated by blue arrow in the Fig. 38, three levels of torque were applied and also fully disconnected arm from swashplate condition was approached. Last but not least test was a fully disconnected joint at the PL L-shape arm ("upper arm") indicated by the green arrow in Fig. 38.

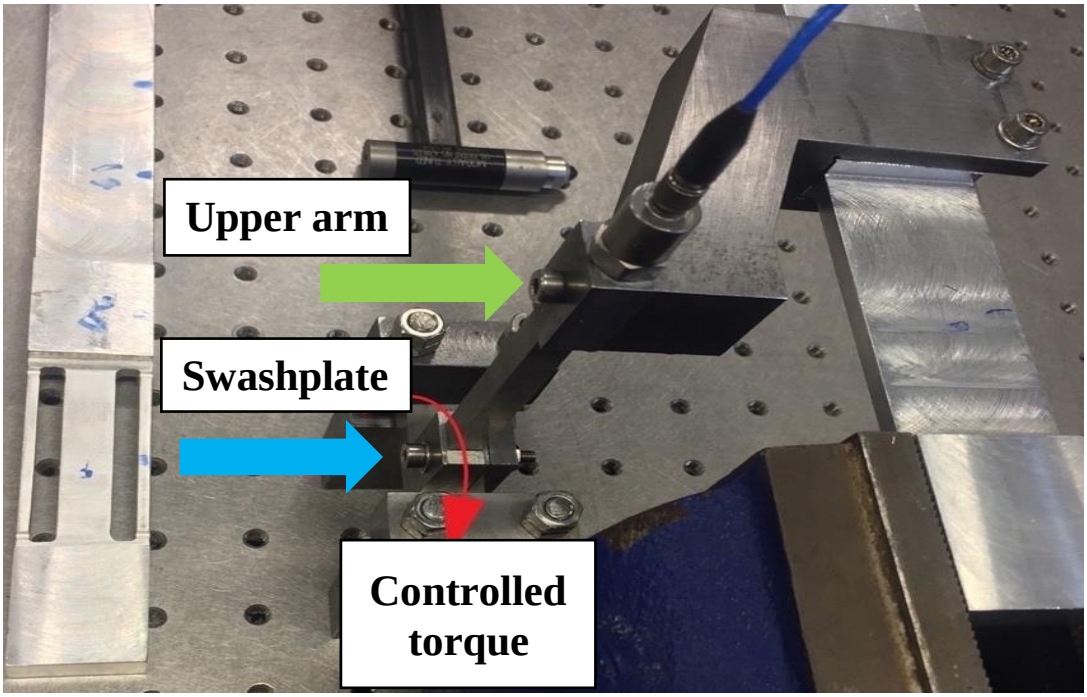

Figure 38. Tightening position to modify clamping torque of Pitch Link (PL) configuration.

4.4.2.- Damaged beam due Ice accretion at the tip

The second experimental stage is related to addition of mass (rectangular Steel strips or blocks) at the lateral face of beam's tip location as in Fig. 39, and therefore changes in mass distribution. This mass distribution is then formulated and modeled as the typical winter blade damaged or flying in dramatically lower temperature environment known as Ice accretion exposure. The main purpose of this test is the observe the small changes happening in the beam's structural dynamics as the low values of mass weight are increasing by small increments. Last test "Ice 4" is assumed to be the initial stage for third experiment due weight.

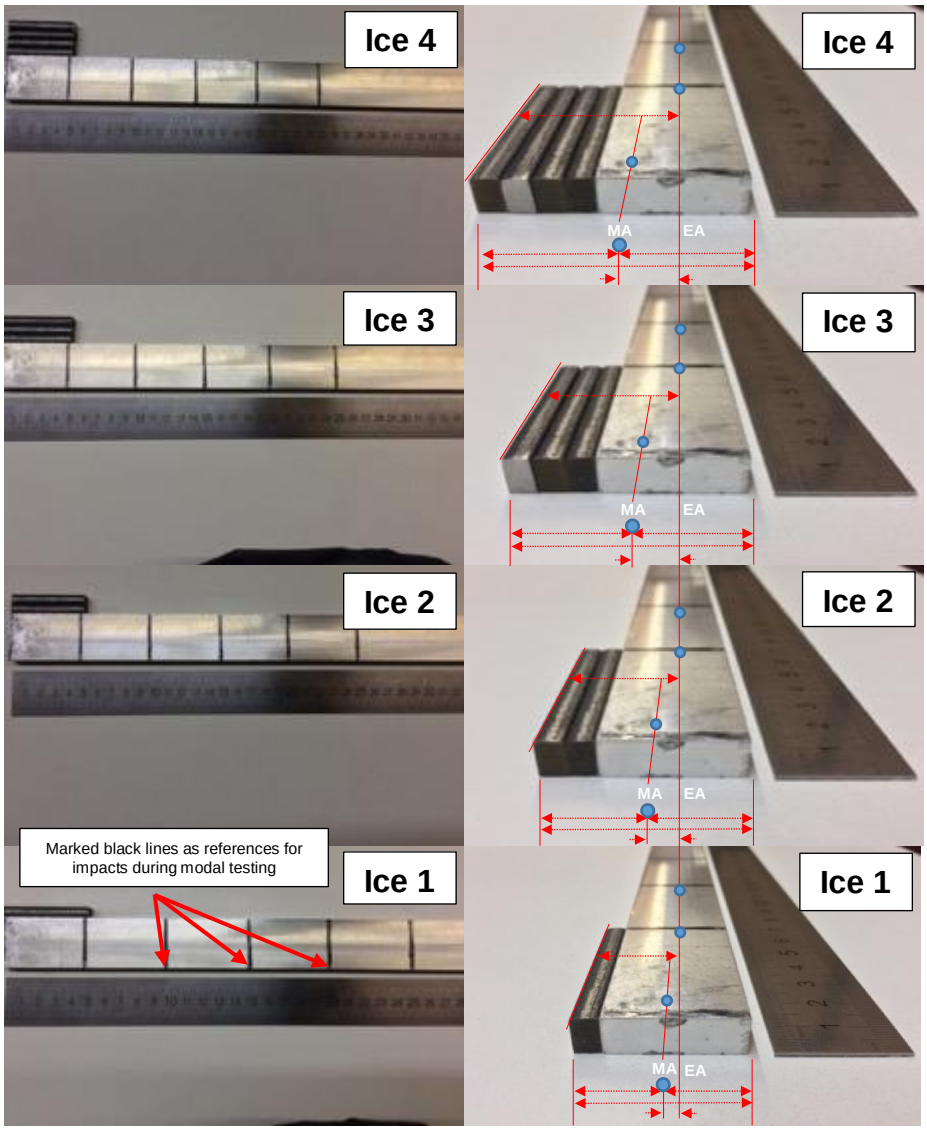

Figure 39. Experimental formulation of progressive Ice accretion levels (Tip ice).

4.4.3.- Damaged beam due Ice accretion on longitudinal “axial” axis

The third experimental stage is related to progressive addition of mass in the lateral face of the beam as shown in Fig 40. Changes in mass distribution is applied in spanwise direction “axial axis” and it develops progressively towards the beam’s root. First test of longitudinal case “Ice 1” can be approximately compared with last test of tip case “Ice 4”, since both bodies contribute similar weight at the tip.

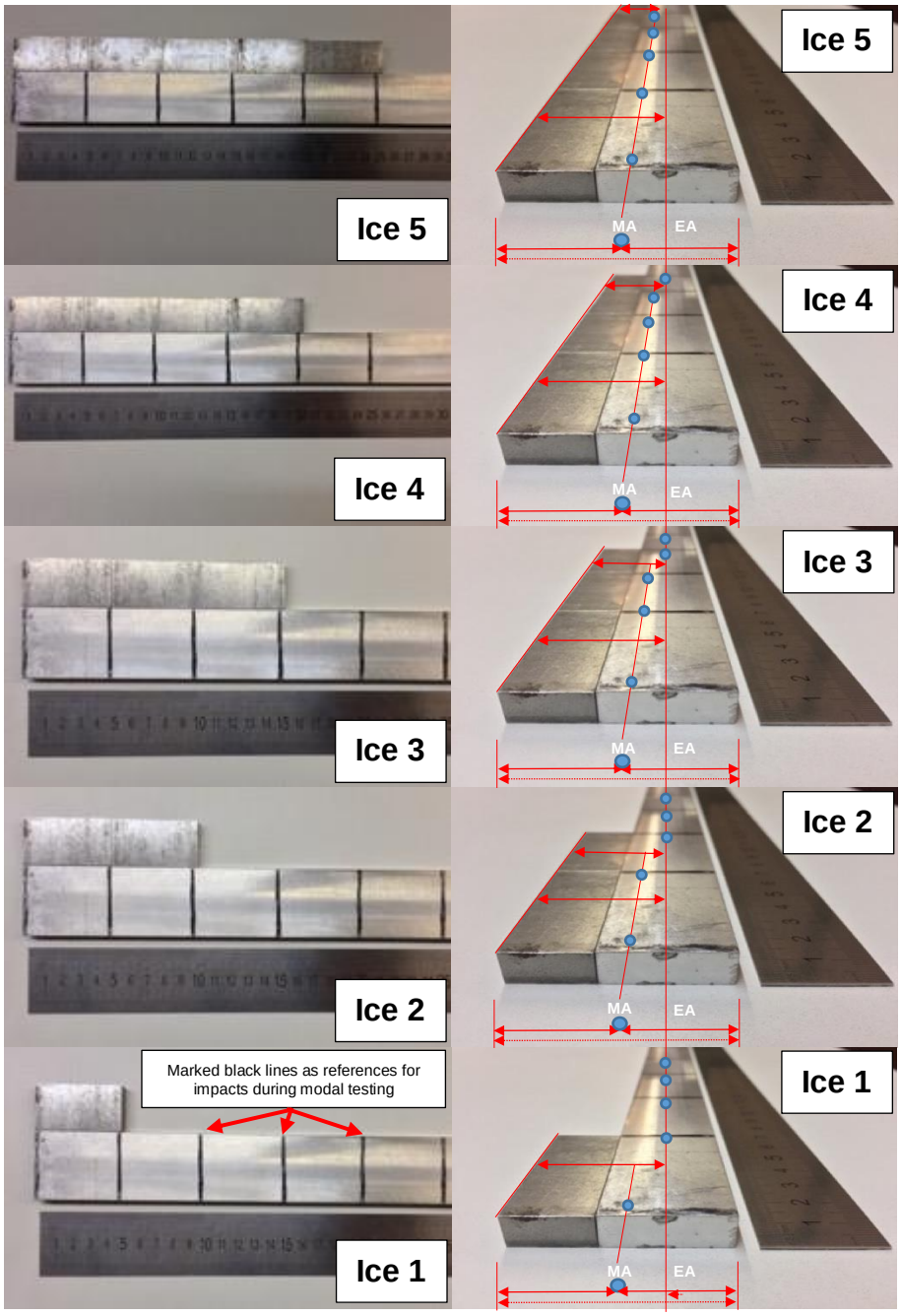

Figure 40. Experimental formulation of progressive Ice accretion levels (Longitudinal ice).

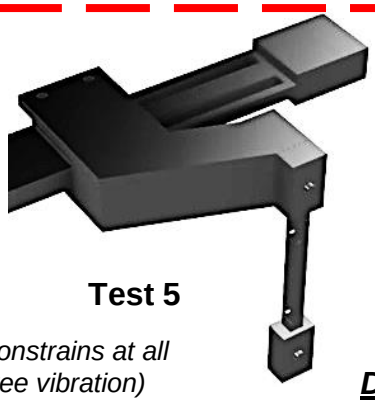

Test 5

No constrains at all (Free vibration)

Test 6

Damaged Pitch Link test conditions

Test	Description	Tightening Torque [Nm]
1	*Healthy*	*6 Nm*
2	*Damage 1*	*4 Nm*
3	*Damage 2*	*2 Nm*
4	*Damage 3*	*0.5 Nm*
5	*100 % damage on swashplate*	*Disconect PL arm with the ground base*
6	*100 % damage on upper Arm*	*Remove PL arm and leaving alone L-Arm*

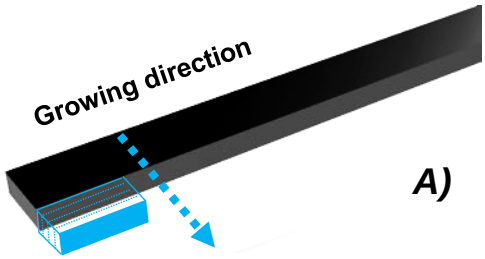

A)

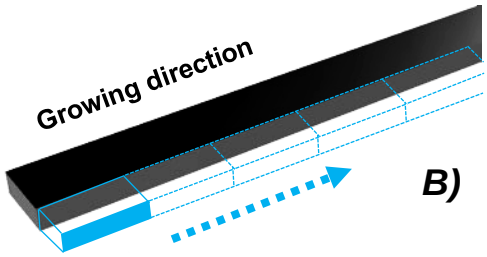

B)

Tip Ice accretion test conditions* – *A)

Test	Type	Mass [*Kg*]	Mass distribution [*Kg/m*]		C.G. Offset [m]
			Solid root beam	*Flexible beam*	
1	*Healthy*	*-*	*0.7909 Kg/m*	*0.7877 Kg/m*	*0 m*
2	*Ice 1*	*0.0224 Kg*	*0.8157 Kg/m*	*0.8125 Kg/m*	*0.003 m*
3	*Ice 2*	*0.0449 Kg*	*0.8407 Kg/m*	*0.8374 Kg/m*	*0.009 m*
4	*Ice 3*	*0.0677 Kg*	*0.8659 Kg/m*	*0.8626 Kg/m*	*0.015 m*
5	*Ice 4*	*0.0904 Kg*	*0.8911 Kg/m*	*0.8877 Kg/m*	*0.021 m*

Longitudinal Ice accretion test conditions* – *B)

Test	Type	Mass [*Kg*]	Mass distribution [*Kg/m*]		C.G. Offset [m]
			Solid root beam	*Flexible beam*	
1	*Healthy*	*-*	*0.7909 Kg/m*	*0.7877 Kg/m*	*0 m*
2	*Ice 1*	*0.0774 Kg*	*0.8767 Kg/m*	*0.8733 Kg/m*	*0.01 m*
3	*Ice 2*	*0.1548 Kg*	*0.9625 Kg/m*	*0.9589 Kg/m*	*0.01 m*
4	*Ice 3*	*0.2320 Kg*	*1.0481 Kg/m*	*1.0443 Kg/m*	*0.01 m*
5	*Ice 4*	*0.3092 Kg*	*1.1336 Kg/m*	*1.1297 Kg/m*	*0.01 m*
6	*Ice 5*	*0.3825 Kg*	*1.2149 Kg/m*	*1.2108 Kg/m*	*0.01 m*

Table 11.- Experimental framework for Pitch Link and Ice accretion.

4.5.- Limitations

Based in Fig. 41, the main limitations in test design was beam rectangular sections which are not similar like airfoil's blade and also there is no opportunity to apply a pre twisted angle on Pitch Link arm (typical command from swashplate). Test equipment limitation was the software used, which had the capability to obtain only 1 response from each free vibration testing, therefore more tests were needed. The experimental modal testing rig has the intention to represent a real helicopter component, from there subsequently to explore the selected changes/damages onto the beam and/or substructure mechanics for SHM purposes.

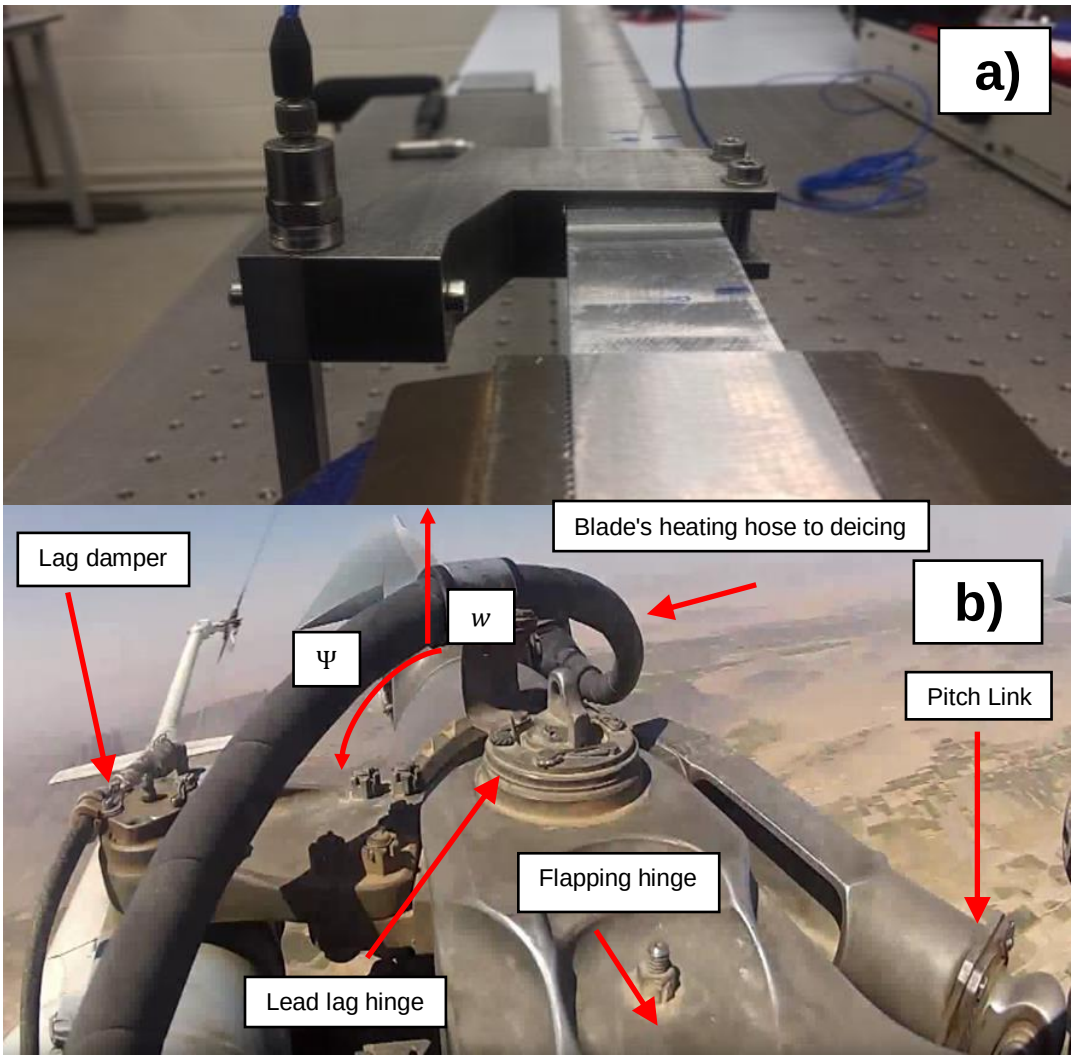

Figure 41. **a)** Experimental pitched beam vs. **b)** Rotorcraft lade view from rotor hub **[J].**

[J] https://www.youtube.com/watch?time_continue=4&v=Kw1rZ2yPi4c

CHAPTER 5 STRUCTURAL HEALTH AND MONITORING (SHM)

All Structural Health Monitoring (SHM) platforms, techniques and methods available for industry applications and laboratory experiments at universities has strongpoints, limitations, and the motivations of the project. On this research is being explored a novel SHM method. Where a systematic analysis is then implemented were based in eigenvalue and eigenfrequency modelling. The use of previous mentioned data provides clear insights, the possibility to assess the healthiness of the structure and system trends of how a pitched-blade behaves on various type-scenarios. On this research work, the novel SHM method is discussed along with the visualization of the calculations. All complete features and strategies for this SHM method is visualized in flowchart loop as shown in Fig. 42, where shows how the calculations are done and what is needed for each of the internal sub-tasks and its iteration blocks.

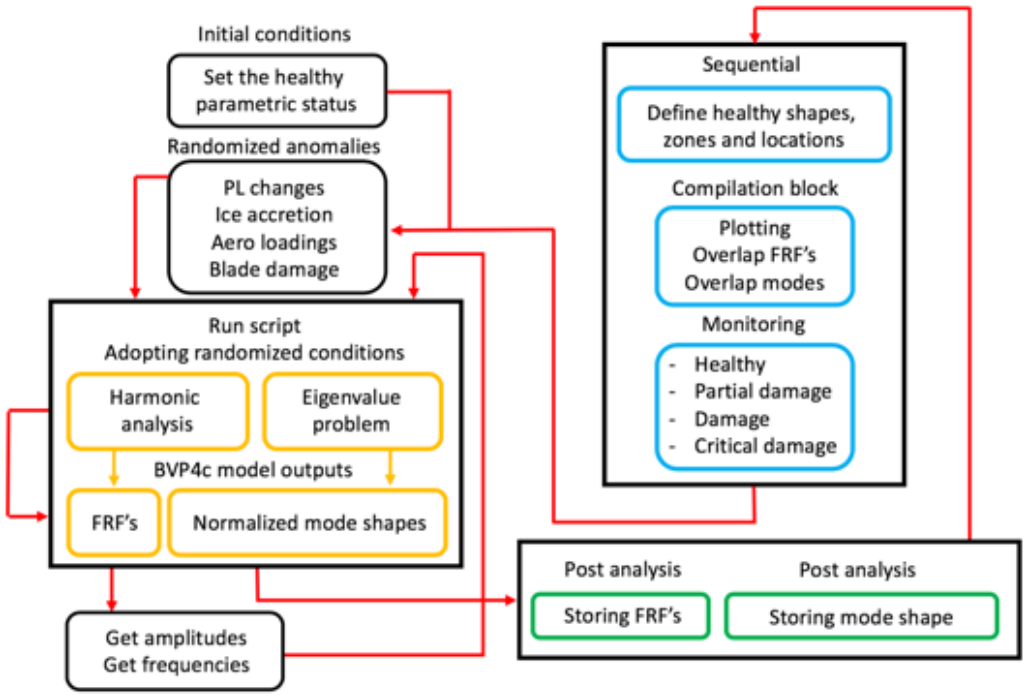

Figure 42. SHM methodology flowchart loop.

As starting point, it must be understood and set the representative healthy parametric nominal values, from there a randomized change are introduced into system for four different research lines (PL changes, Ice accretion, Aero loads and damages). These new value ranges are processed as harmonic analysis, after the final loop finishes, the obtained transfer function in frequency/amplitude domain is stored. The calculated frequencies are sent to an eigenvalue problem model to get the normalized modal vibrational shapes. At this point, it must be aware about the characteristics of the system under study (amplitudes, curvatures, peaks and mode shapes), where a sequential stage must set and define zones where the pitched blade max/min displacement location is permitted, and also the shape of the tip max/min displacement. From there the method relies in comparing as many iterations as possible and inspecting them in an independent frame of reference. More close insights, results and discussions are presented ahead this chapter.

5.1.- Non-rotating MPBVP formulation and validation

The development and validation process of the rotating blade model based on the implementation of a Collocation Method was solve for a free vibration analysis for a rotating, double tapered Timoshenko beam which there is coupling between flap-wise bending and torsional vibration. For this analysis, the model 4 was chosen as contains the full set of 3 governing differential equation of motion (for the flap-wise bending displacement "ω", angle due bending "φ", and torsional rotation "ψ") **[92],** and the parameters shown in Table 12 were used to calculate the resonant frequencies. The bending and torsional frequencies are the vertical red and blue dashed lines respectively and were calculated using a direct transform method DTM and are shown in Fig. 43 **[92]**.

Plus, on this study, an additional purpose was accomplished by calculating four more sets of FRF's to obtain the variations of natural frequencies of the rotational system in Vacuum, while the rotational speed "Ω" varies from 5, 20, 50 and 100 rad/s, the validation data is presented in Table 13.

Structural Parameters		
Length,	m	1
Torsional rigidity,	Nm^2	1.12599 x10^6
Mass moment of inertia,	*kgm*	0.5015
Second moment of area,	m^4	1.17187 x10^{-5}
Beam's Young modulus,	kgf/m^2	70 x10^9
Shear rigidity,	*N*	5.93654 x10^8
Mass per unit length,	*kg/m*	72
Taper ratios,	-	0.5
Coupling distance,	m	1 x10^3

Table 12.- Tapered beam parameters used on BVP4c model **[87]**.

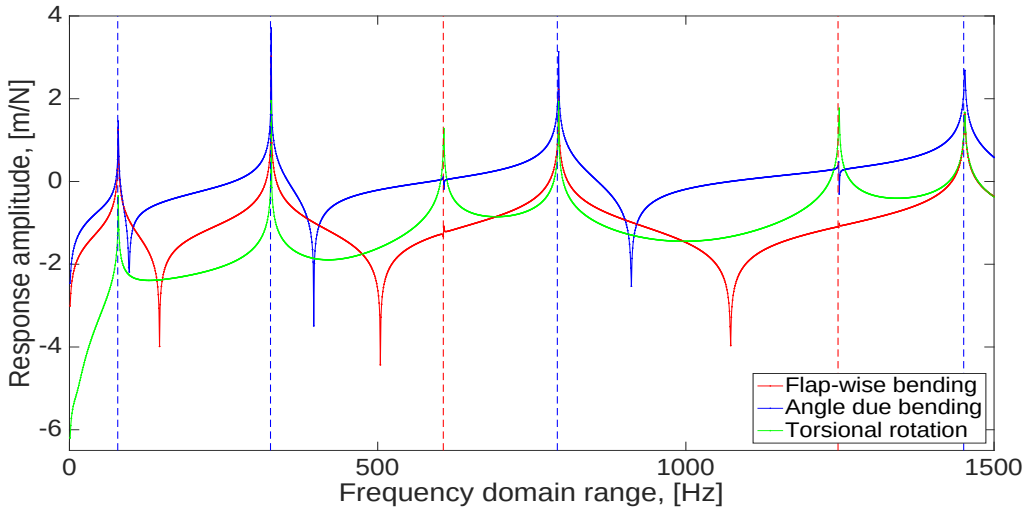

Figure 43. Tapered Timoshenko beam frequency response function.

Rotational speed (Rad/s)					
5			**20**		
Ref. [87]	***BVP4c***	**%**	**Ref. [87]**	***BVP4c***	**%**
78.267	*78.31*	0.0549	78.341	*78.46*	0.1517
326.06	*326*	0.0184	326.13	*326.1*	0.0092
606.4	*606.4*	0	606.42	*606.5*	0.0132
791.89	*791.3*	0.0746	791.95	*791.5*	0.0569
1246.8	*1247*	0.0160	1246.9	*1247*	0.0080
1450.7	*1449*	0.1173	1450.7	*1450*	0.0483
Rotational speed (Rad/s)					
50			**100**		
Ref. [87]	***BVP4c***	**%**	**Ref. [87]**	***BVP4c***	**%**
78.750	*79.06*	0.3921	80.192	*81.61*	1.7375
326.52	*326.7*	0.0551	327.9	*329*	0.3343
606.54	*606.7*	0.0264	606.98	*607.3*	0.0527
792.30	*792.2*	0.0126	793.54	*794.5*	0.1208
1247.1	*1247*	0.0080	1247.9	*1248*	0.0080
1451.1	*1450*	0.0759	1452.1	*1453*	0.0619

Table 13.- Tapered Timoshenko beam rotational speed variations.

Based on Table 13, shows minor errors on the variations and comparisons between the reference **[87]** and calculations performed on BVP4c model. After following in detail these tasks, it can be concluded that model platform on this work is quite acceptable. From the modelling point of view and applicability, all the equation of motions for the four models were evaluated under a specific range of frequency vibrations. For this purpose, the modal testing applied on the three cantilever beam was done by setting the experiments at 1000 Hz as maximum frequency vibration, therefore the complete data in that range was processed and all the amplitude peaks from the Frequency Response functions (FRF's) for all deflections subjected in the equation of motions. In this thesis, from the Fig. 43 and other figures related to the frequency response functions, the torsional rotation ψ "torsion angle" were multiplied times X_α "coupling distance", with the purpose that any section along the beam span, the deformation of the centroid ($\psi * X_\alpha$) as result of the twist motion can then be compared with the transverse displacements (*H*). This is related with the fact that both non-coincident centroid and shear axis are widely used for engineering purposes for many industrial applications such a turbines, compressor and rotorcraft blades. Additions of Ice accretion in helicopter blades when exposed to harsh winter surroundings increase both axis offsets. The reduction or addition of layers of corroded-eroded blade surfaces on large turbines on power stations changes axis offsets too. These changes on the axis offsets distances changes dramatically the total responses of any structure, then these distances needs to be accurate if the researcher requires to model transfer functions coming from the collected data. From the helicopter point of view modifies the nature of how blade would vibrate and respond, as an example on flutter analysis **[89]** this parameter plays a significant role since due the coupled

interactions between Aerodynamics, stiffness and inertial forces acting on the rotor blade. This dangerous phenomenon could increase dramatically when exists progressively changes on axis offsets, by all means changes in mass moment of inertia, more presence of torque, which could end up in a massive failure and/or damage within the rotor blade system. Therefore, constant monitoring tasks are highly considered for these cases. These influences are taking into consideration in all four models ahead in the presented experimental/modelling framework.

5.1.1.- Experimental case of study for a simple C-channel Aluminium beam

Stages and process of model validation with BVP4c, initially was carried out by running a modal analysis test on a non-rotating beam. For this test, an isotropic forged Aluminium C-channel blade like structure was used with parameter shown in Table 14, where reference point FRF was extracted by exciting beam on position Web Vertical Variable (WVV), as shown in Fig. 44.

Structural Parameters		
Beam length,	m	0.9278
Beam density,	kg/m^3	2250
Mass moment of inertia,	kgm	7.3961×10^{-5}
Second moment of area,	m^4	3.296×10^{-8}
Beam's Young modulus,	kgf/m^2	$70.9722336 \times 10^{-6}$
Mass per unit length,	kg/m	0.3809

Table 14.- C-channel beam parameters used on BVP4c.

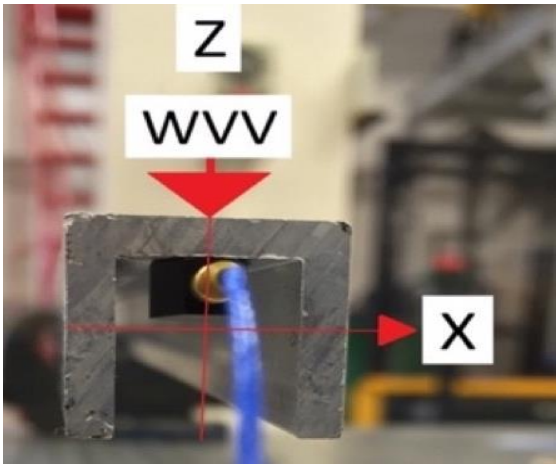

Figure 44. Point FRF of C-channel with excitation on the Web Vertical Variable face.

The modeling calculation to extract FRF's from BVP4c were done in two different forms. Firstly, by using the conventional 2 point Boundary Conditions (BC), one at the root and second at the tip. Secondly, the usage of 5 points Multi-Point BC's, where was applied 3 more BC's between root and tip, by using Multi-Points solver capabilities. The usage of the equation of motions (5) and (6) from the model **[89]** was adopted as the main ODE's on BVP4c solver. The structural dynamics of the C-channel and its results and validation process for the frequency response functions for both models are shown on Fig. 45.

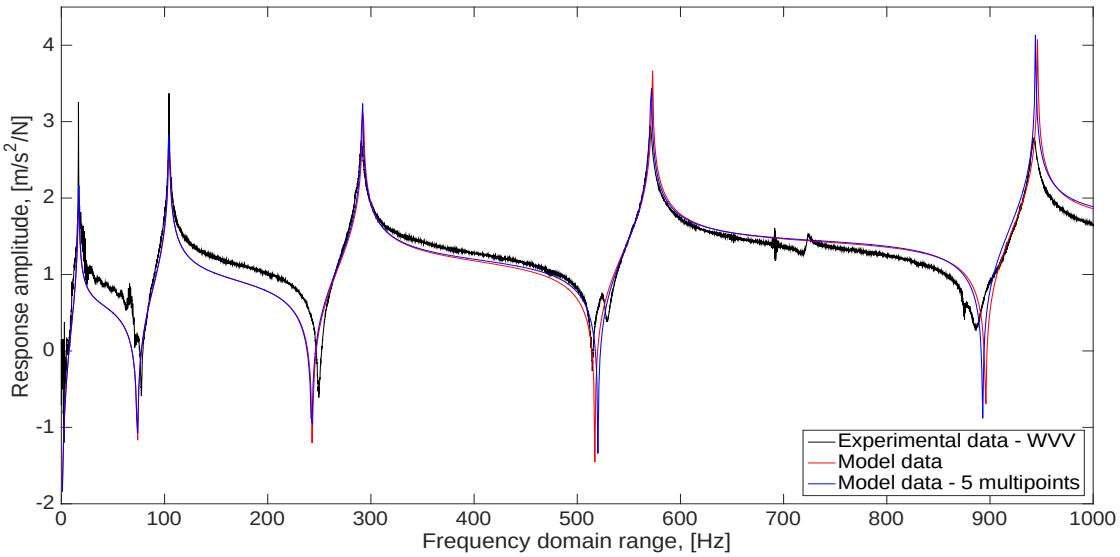

Figure 45. Frequency response functions for the experimental data (Black line), the 2 points BC's (Red line), and the 5 points BC's (Blue line).

The two transfer functions "red and blue" from the Fig. 45 are proving and validated the accuracy of the dynamic calculations using conventional Collocation Method and implementations of the Multi-Point (element segmentation) boundary conditions that correspond to the experimental FRF. The Multi-Point performs remarkable good and this method can be considered as novel in the current thesis platform work as this method gives the opportunity to include a discretize loading coming from Ice accretion loads and Pitch Link forces.

5.2.- Advanced cantilever beams and sectional properties to be modelled

Afterwards, the similar experimental work was done by using 2 different sets of Aluminium beams. Where on both Advanced beams the excitation reference point FRF was extracted by impacting the beam's tip with modal hammer on the location Beam Experimental Position (BEP) due that the sensor was attached on top of PL as shown in Fig. 46.

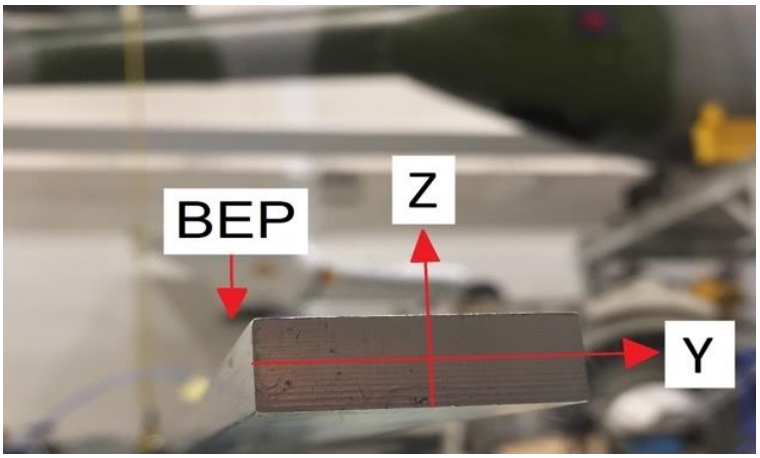

Figure 46. Point FRF of Advanced beam with offset extication on the beam excitation point.

Both Advanced beams were measured, and the sectional cross section parameters were measured and calculated and are presented in the Table 15. From this data it was implemented in the Multi-Point boundary value problem using the Collocation Method. These specs were introduced and spitted onto 12 sub domains to calculate both Advanced beam structural dynamics. The cut-out segments were measure and removed from the model.

	Stations			Units
	1	**2**	**3**	
r	0.0656	0.034	0.8025	m
ρA	0.3982	1.2272	1.8046	kg/m
E	7.239985×10^{9}	7.239985×10^{9}	7.239985×10^{9}	N/m^2
I_y	2.95×10^{-10}	2.1×10^{-6}	2.43×10^{-9}	m^4
I_α	3.08×10^{-5}	1.15×10^{-4}	6.7×10^{-5}	kgm
EI_y	2.1365	1.5526×10^{4}	17.6209	Nm^2
GJ	0.8753	5.5430	4.4461	Nm^2

Table 15.- Advanced beam parameters used on BVP4c.

The validation of both normal and Flexible Advanced beams are presented in the Fig. 47 and Fig. 48 respectively. These frequency response functions from the 4 models **[89,90,91,92]** matches quite nicely. On both figures appears vertical parallel lines which corresponds to the experimental resonant frequencies marked as the vertical red dashed lines for the bending frequencies and the vertical blue dashed lines that stands for the torsional frequencies. Notice both plots with sixth red dashed lines refers bending modes and only blue dashed line is torsion mode. Black transfer function is related to the experimental data from the laboratory.

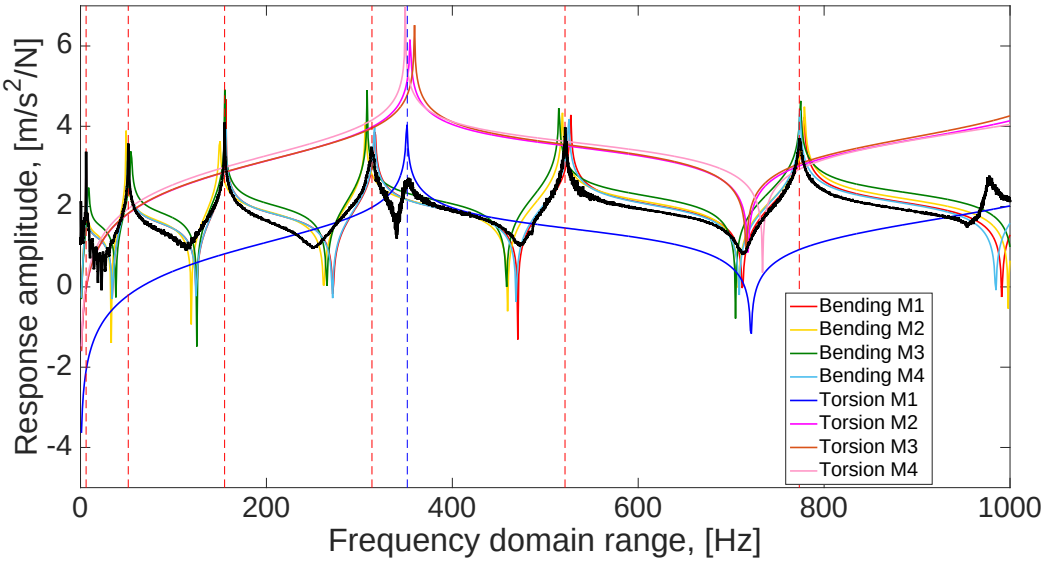

Figure 47. Frequency response functions for the Normal Advanced beam

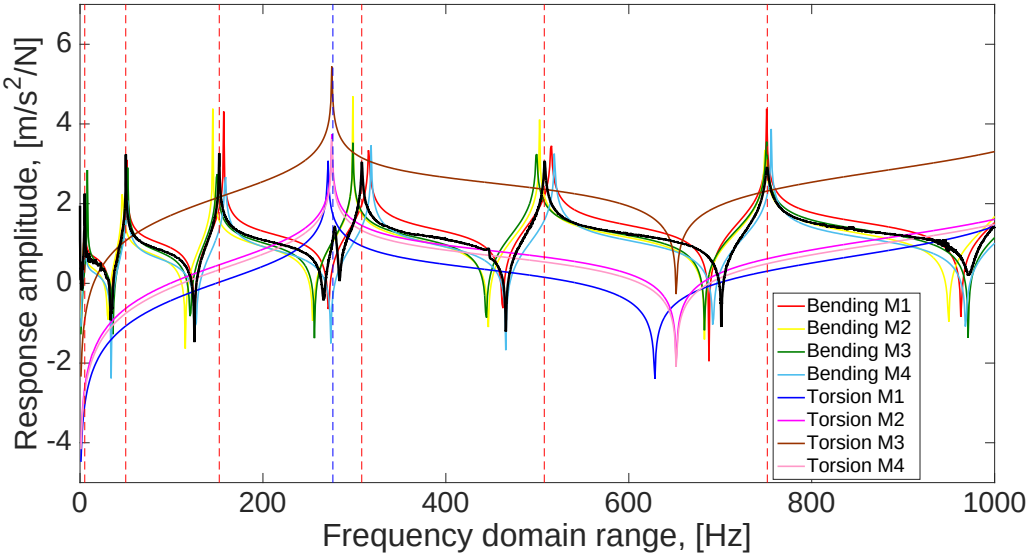

Figure 48. Frequency response functions for the Flexible Advanced beam.

5.2.1.- Post-analysis methods and techniques for damage detection

There are different SHM techniques and applications to monitored systems and their integrity, vertical lift industry is one of the many fields of interested and motivation. In order to investigate between the baseline and damages behaviours in the system, a good combination while adopting MAC **[100],** COMAC **[101],** DLAC **[102,103],** and FRAC **[104]** could provide outputs which are meant to be considered as common uses and objectives that have been reported in literature:

- To make validations in the experimental models.
- Create correlation between experimental-analytical models (mode pairing).
- Structural failure/damage detection
- To show us a map matrix between experimental and analytical models.
- Quality control and evaluation of data
- Error analysis in Modal vectors properties.
- Modal vector method to averaging experimental modal vector completion.
- Weighting for model updating.
- Optimal sensor placement to update a model

Before describing in details, the how to use the Bending-Torsional coupling vibrations on the damage detection methodology on this work, some of the basic concepts such as Modal Assurance Criterion (MAC), the Coordinate Modal Assurance Criterion (COMAC), and also the Damage Location Assurance Criterion (DLAC) tests, will be briefly mentioned. In general, all developments around these methods especially for MAC, has evolved in ways to be used for damage detection cases between the analytical experimental structural dynamics of any system configurations.

This work attempts to use MAC, COMAC, DLAC, and. FRAC methods for the analysis of a blade like structure (rotorcraft configuration), which aims to study potentially the interactions between the bending and torsional frequencies under different cases of study scenarios only in the experimental framework.

5.2.2.1.- Modal Assurance Criterion, (MAC)

This work also investigates the impacts of modal orthogonality between comparison sets of healthy modal eigenvector (as reference) with damaged modal eigenvector (changed reference) and study the influence of introduced damages on bending-torsional responses. The Modal Assurance Criterions were first shown in 1980 **[100]**. In general, technique measures and provides degrees of proportion (degree of linearity) between 2 modal vectors (analytical or experimental). Damage detection methodology will involve the study of healthy reference vs damaged references and explore which bending torsional modes are more sensitive than others and check the extent of the dissimilarity between the data using MAC values. The same method and equation can be used for the amplitude responses of the transfer functions in FRAC **[104]**. The confidence factor with value of 1, would mean a higher correlation coefficient between the modal vectors, and 0 would mean no similarity on the data. MAC equation (109) could be defined as:

$$MAC_{(r,q)} = \frac{\left|\left\{\Psi_A\right\}_r^T \left\{\Psi_x\right\}_q^*\right|^2}{\left(\left\{\Psi_A\right\}_r^T \left\{\Psi_A\right\}_r^*\right)\left(\left\{\Psi_x\right\}_q^T \left\{\Psi_x\right\}_q^*\right)} \qquad \textbf{(109)}$$

$\left\{\Psi_x\right\}_q$ = Eigenvector (reference) of complex mode x of vibration

$\left\{\Psi_A\right\}_r$ = Eigenvector (change) of complex mode A of vibration

$\left\{\Psi_A\right\}_r^*$ = Complex conjugate of $\{\Psi_A\}_r$

$\left\{\Psi_x\right\}_q^T$ = Transpose of $\{\Psi_X\}_q$

$\left\{\Psi_x\right\}_q^*$ = Complex conjugate of $\{\Psi_X\}_q$

5.2.1.2.- Coordinate Modal Assurance Criterion, (COMAC)

A continuation for MAC, would be COMAC **[101].** In this work, is adopted to identify which degree of freedom (measuring location) provides lowest/highest confidence factor (COMAC value). Calculations between mode pairs are adopted (e.g. experimental-experimental/analytical). For each mode pair comparison (degrees of freedom) there would be a COMAC value that will represent how similar these mode sets are. For the analysis, changes are introduced as uncertainty (localized input damage, increasing the mass distribution, altering sectional the properties, etc.) on the rotorcraft system and by comparing the mode sets data for all locations throughout the blade spam, ideally the high COMAC value between the healthy reference and the damaged reference for that specific location will confirm a good accuracy of the damage location (new uncertainty) for that match factor. The eigenvectors can be study with the equation (110), therefore COMAC values could be defined as:

$$COMAC_{(q)} = \frac{\sum_{r=1}^{1} \left| \Psi_{qr} \Phi_{qr} \right|^2}{\left(\sum_{r=1}^{1} \Psi_{qr} \Psi_{qr}^{*} \right) \left(\sum_{r=1}^{1} \Phi_{qr} \Phi_{qr}^{*} \right)} \qquad \textbf{(110)}$$

Ψ_{qr} **=** Modal coefficient for degree-of-freedom q, mode r.

Φ_{qr} **=** Modal coefficient for degree-of-freedom q, mode r.

5.2.1.3.- Damaged Location Assurance Criterion, (DLAC)

Simultaneously, during the processing time of the data used for COMAC work, it can be extended for DLAC. In this work, the method is applied by extracting a measured frequency change vector Δf, for a damage location that is unknown and the size of it and is then compared with a theoretical frequency change vector δfX, of a known damage location and size. In contrast, if a known damage is

applied in a particular location in a system, it can then iterate and compared for different damaged “foretelling” location. The DLAC **[102]** equation (111) will be providing the damage location correlation (DLAC factor) for individual damaged position named j. The result interpretations from equation have a trend of being from “0” to “1”, which cases with value “0” indicates a non-matching case and opposite value 1 indicates proper match of frequency variations. By following before statement, if these equations are applied for many positions j, throughout a beam damaged structure. Results with highest value can be considered as the damage location. Most research suggest an average between 4 to 15 modes as requirement to detect potentially good damage position. As higher number modes are required, can turn the calculation process less precise, sensitive and different respect to analytical approach. These ideas were considered for current work, although, depending on the nature of the structural dynamics of the studied beam and the number of modes present in the frequencies calculated range between 0 to 1000 Hz, from the previous, it can then consider up to “six eigenvectors” for analysis purposes. Any 2 FRF that represents similar input-output can be tested and compared, therefore the usage of natural frequencies has shown good way to apply diverse routines to measure the integrity of the structure, even though these types of methods could potentially require a good model to simulate the damage before jumping to an experimental rig to get the physical measurements.

$$DLAC_{(j)} = \frac{\left|\{\Delta f\}^T * \{\partial f_j\}\right|^2}{\left(\{\Delta f\}^T * \{\Delta f\}\right) * \left(\{\partial f_j\}^T * \{\partial f_j\}\right)} \qquad \textbf{(111)}$$

$\{\partial f_j\}$ = Theoretically frequency change vector.

$\{\Delta f\}$ = Measured frequency change vector.

5.3.- Damage detection discussion on results

- Experimental Ice accretion on Advanced beam without Pitch Link.

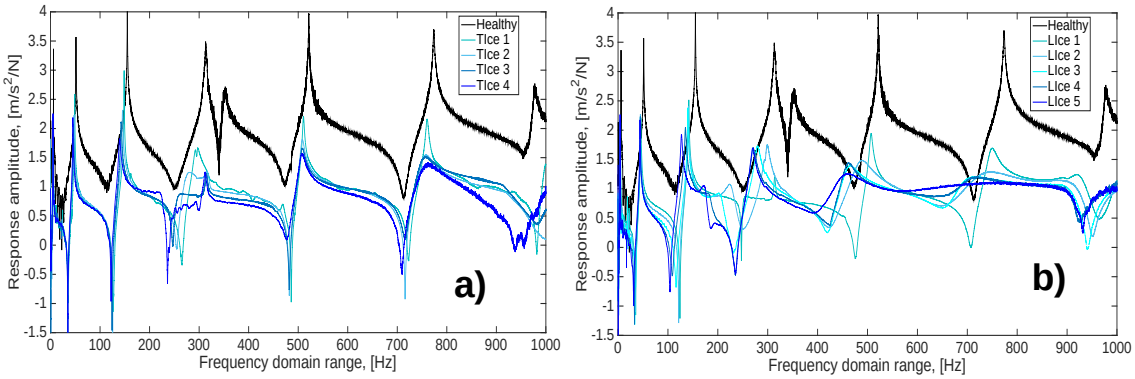

Figure 49. Experimental FRF's for Normal beam in **a)** Tip ice and **b)** Longitudinal ice.

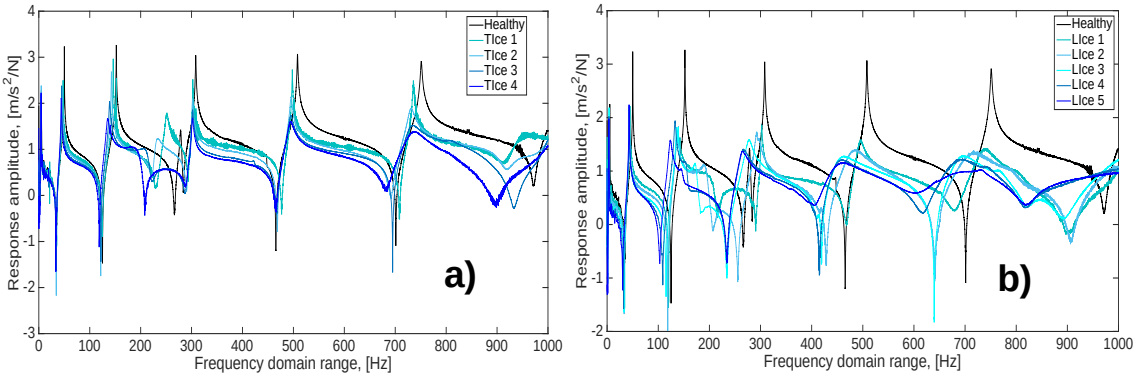

Figure 50. Experimental FRF's for Flexible beam in **a)** Tip ice and **b)** Longitudinal ice.

	B1	***B2***	***B3***	***B4***	***T1***	***B5***	***B6***
H	6.0000	51.4000	155.0000	313.0000	352.7000	521.3000	773.8000
Ice1	5.1000	45.7000	141.8000	314.1000	246.6000	507.3000	750.0000
Ice2	4.7000	44.8000	141.0000	299.3000	227.8000	487.5000	741.2000
Ice3	4.4000	44.7000	140.0000	280.5000	207.4000	466.4000	712.5000
Ice4	4.1000	44.6000	135.0000	271.3000	187.2000	461.4000	707.1000
Ice5	4.0000	44.0000	127.2000	269.6000	176.2000	456.4000	680.8000

Table 16.- Identified natural frequencies from changes in Longitudinal ice in Normal beam.

	B1	***B2***	***B3***	***B4***	***T1***	***B5***	***B6***
Ice1	-15.0000	-11.0895	-8.5161	0.3514	-30.0822	-2.6856	-3.0757
Ice2	-21.6667	-12.8405	-9.0323	-4.3770	-35.4125	-6.4838	-4.2130
Ice3	-26.6667	-13.0350	-9.6774	-10.3834	-41.1965	-10.5314	-7.9219
Ice4	-31.6667	-13.2296	-12.9032	-13.3227	-46.9237	-11.4905	-8.6198
Ice5	-33.3333	-14.3969	-17.9355	-13.8658	-50.0425	-12.4496	-12.0186

Table 17.- Frequencies residuals in Longitudinal ice for Normal beam. (Differences, 100x(U1-H)/H, [%])

	B1	***B2***	***B3***	***B4***	***T1***	***B5***	***B6***
H	6.0000	51.4000	155.0000	313.0000	352.7000	521.3000	773.8000
Ice1	5.6000	48.9000	148.6000	297.5000	292.2000	510.6000	759.6000
Ice2	5.4000	47.6000	145.5000	316.7000	279.8000	508.3000	757.6000
Ice3	5.2000	45.9000	142.5000	314.5000	251.5000	508.2000	757.2000
Ice4	5.0000	45.1000	138.0000	311.7000	220.2000	507.8000	763.1000

Table 18.- Identified natural frequencies from changes in Tip ice in Normal beam.

	B1	***B2***	***B3***	***B4***	***T1***	***B5***	***B6***
Ice1	-6.6667	-4.8638	-4.1290	-4.9521	-17.1534	-2.0526	-1.8351
Ice2	-10.0000	-7.3930	-6.1290	1.1821	-20.6691	-2.4938	-2.0936
Ice3	-13.3333	-10.7004	-8.0645	0.4792	-28.6929	-2.5129	-2.1453
Ice4	-16.6667	-12.2568	-10.9677	-0.4153	-37.5673	-2.5897	-1.3828

Table 19.- Frequencies residuals in Tip ice for Normal beam. (Differences, 100x(U1-H)/H, [%])

	B1	B2	B3	T1	B4	B5	B6
H	5.2000	50.1000	152.1000	278.3000	308.2000	508.1000	751.1000
Ice1	4.5000	44.7000	138.4000	209.8000	302.2000	495.7000	739.4000
Ice2	4.1000	43.5000	136.3000	187.3000	293.1000	484.4000	718.6000
Ice3	3.8000	43.4000	136.0000	173.0000	281.6000	462.8000	695.2000
Ice4	3.6000	43.3000	132.8000	155.4000	271.0000	457.1000	692.1000
Ice5	3.5000	42.9000	123.4000	149.6000	267.8000	454.9000	730.4000

Table 20.- Identified natural frequencies from changes in Longitudinal ice in Flexible beam.

	B1	B2	B3	T1	B4	B5	B6
Ice1	-13.4615	-10.7784	-9.0072	-24.6137	-1.9468	-2.4405	-1.5577
Ice2	-21.1538	-13.1737	-10.3879	-32.6985	-4.8994	-4.6644	-4.3270
Ice3	-26.9231	-13.3733	-10.5851	-37.8369	-8.6308	-8.9156	-7.4424
Ice4	-30.7692	-13.5729	-12.6890	-44.1610	-12.0701	-10.0374	-7.8551
Ice5	-32.6923	-14.3713	-18.8692	-46.2451	-13.1084	-10.4704	-2.7560

Table 21.- Frequencies residuals in Longitudinal ice in Flexible beam. (Differences, 100x(U1-H)/H, [%])

	B1	B2	B3	T1	B4	B5	B6
H	5.2000	50.1000	152.1000	278.3000	308.2000	508.1000	751.1000
Ice1	4.9000	47.6000	146.1000	250.3000	302.5000	497.8000	735.5000
Ice2	4.7000	45.8000	142.6000	227.4000	302.1000	495.3000	731.0000
Ice3	4.5000	44.9000	139.1000	217.1000	302.0000	495.1000	733.4000
Ice4	4.4000	43.9000	135.3000	198.6000	301.8000	494.6000	737.1000

Table 22.- Identified natural frequencies from changes in Tip ice in Flexible beam.

	B1	B2	B3	T1	B4	B5	B6
Ice1	-5.7692	-4.9900	-3.9448	-10.0611	-1.8494	-2.0272	-2.0770
Ice2	-9.6154	-8.5828	-6.2459	-18.2896	-1.9792	-2.5192	-2.6761
Ice3	-13.4615	-10.3792	-8.5470	-21.9907	-2.0117	-2.5586	-2.3565
Ice4	-15.3846	-12.3752	-11.0454	-28.6382	-2.0766	-2.6570	-1.8639

Table 23.- Frequencies residuals in Tip ice in Flexible beam. (Differences, 100x(U1-H)/H, [%])

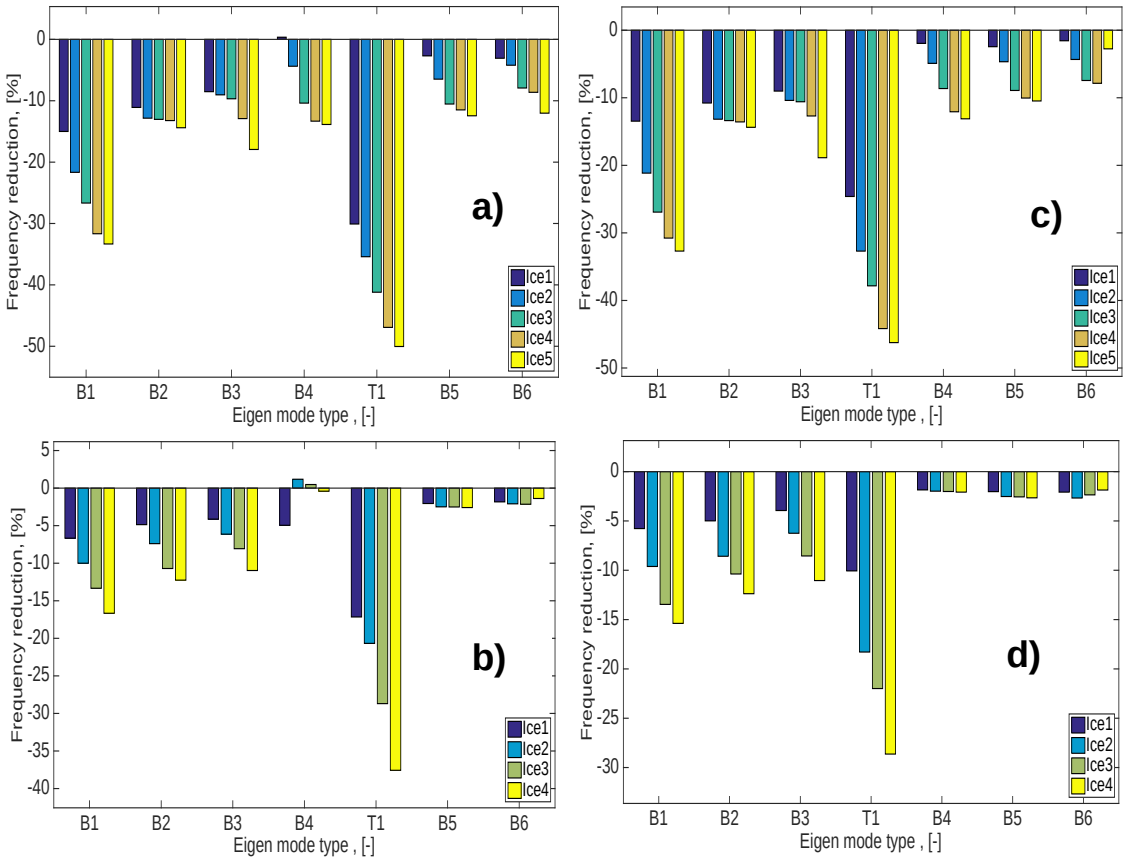

Figure 51. Experimental natural frequency reductions for: **a)** Normal beam Longitudinal ice, **b)** Normal beam Tip ice, **c)** Flexible beam Longitudinal ice, **d)** Flexible beam Tip ice.

The Fig. 49-50 shows the experimental data of Advanced beams without Pitch Link for both Advanced beams. The resonant frequency data was extracted and presented in the Tables 16-23, from both Advanced beams. Plotting the data from those tables as in the Fig. 51. From the resonant frequencies reduction plots, it can be noticed that first fundamental torsional and bending resonant frequencies are very sensitive. The behaviours of those frequencies has very good agreement according with the main hypothesis of what the weighting loading must generate to the structural dynamics, especially for the understanding that this is considered to be a blade-like test approximation. First test is the Longitudinal ice that means the solidification and/or crystallization starts to the tip towards to the root (5 Blocks). The second test is the Tip ice which means increase of ice only in the tip location (4 Blocks). These 4 blocks are similar in weight with 1 of the Longitudinal ice test.

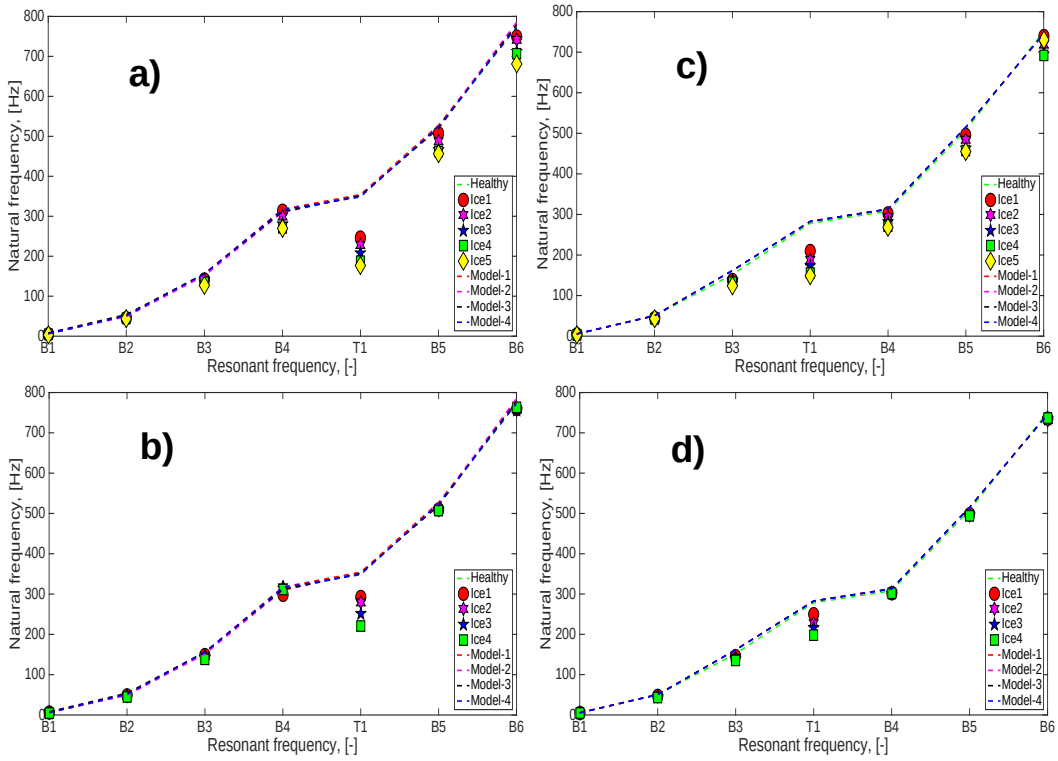

Figure 52. Changes per resonant frequencies for: **a)** Normal beam Longitudinal ice, **b)** Normal beam Tip ice, **c)** Flexible beam Longitudinal ice, **d)** Flexible beam Tip ice.

First torsional frequency reduction is also observed in the Fig. 52. Notice that those frequencies are compared with nominal healthy frequencies on four models. The effect of the loads due the weight of the ice is evaluate in the Fig. 53, being the torsional frequencies as in Fig. 53 **e)**, the most sensitives.

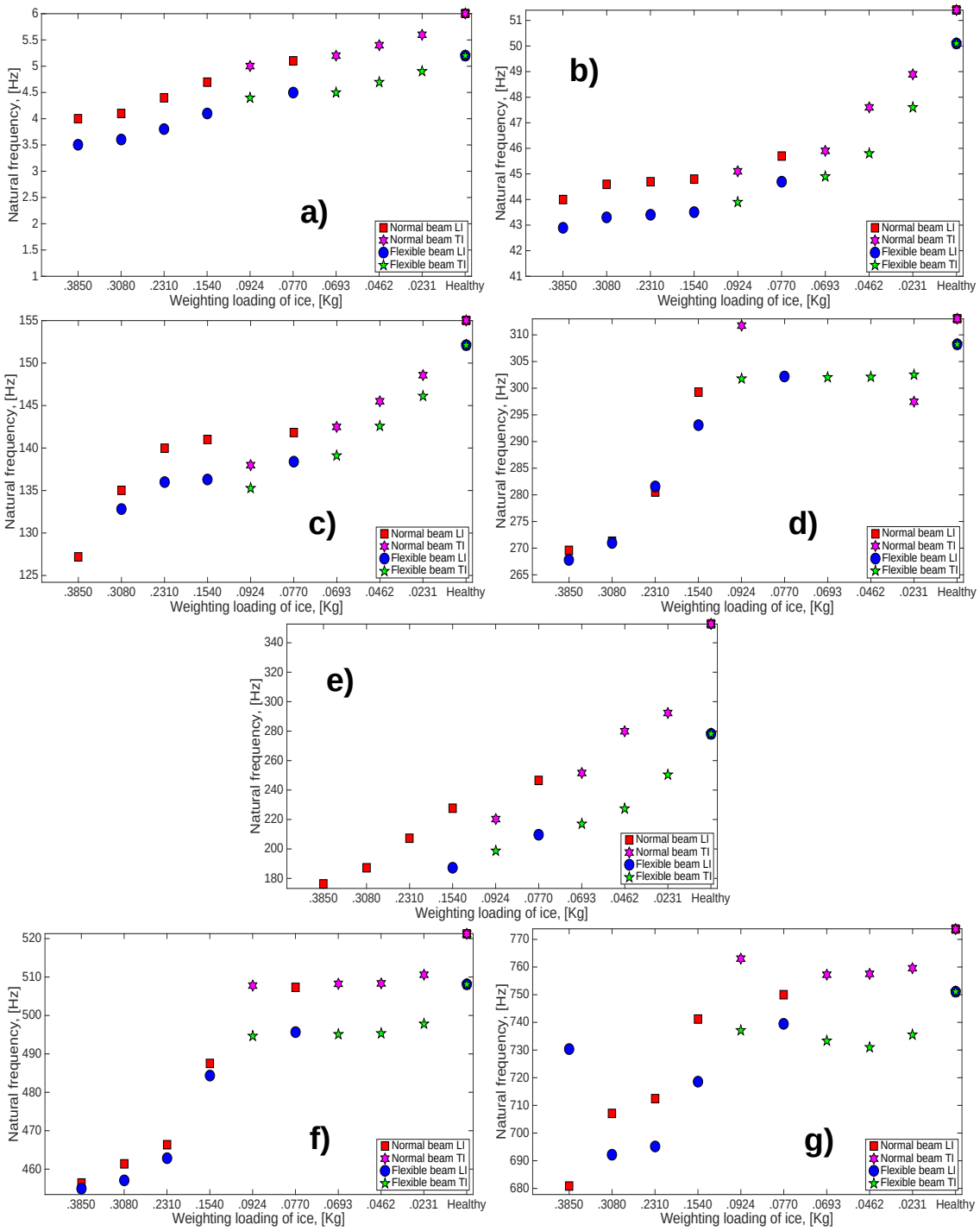

Figure 53. Natural frequency changes due ranges of weighting loads "Ice accretion" for: **a)** 1st Bending mode, **b)** 2nd Bending mode, **c)** 3rd Bending mode, **d)** 4th Bending mode, **e)** 1st Torsion mode, **f)** 5th Bending mode, and **g)** 6th Bending mode.

- *Experimental Pitch Link damages and Ice accretion on bolted Pitch Link.*

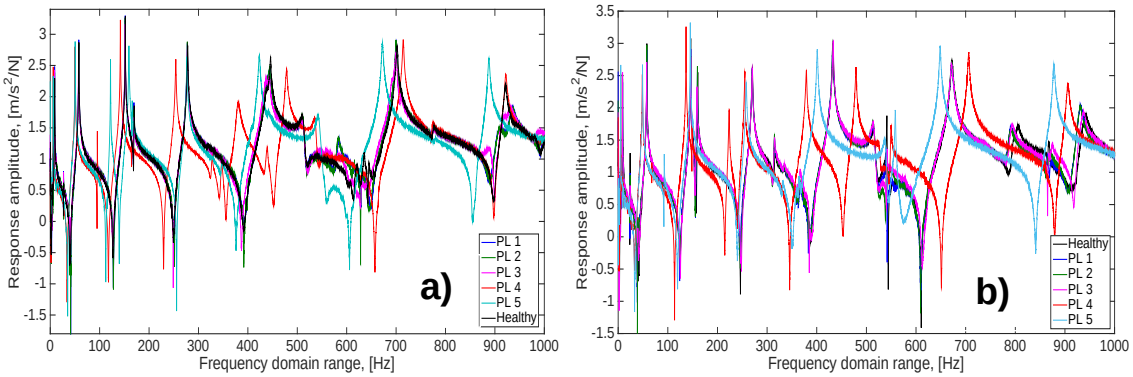

Figure 54. FRF's for bolted PL damages in **a)** Normal and **b)** Flexible beam.

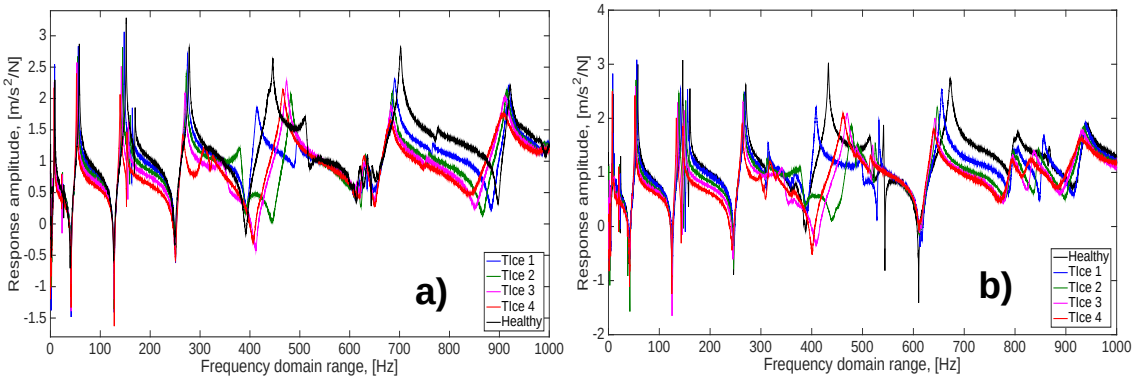

Figure 55. FRF's for bolted PL with Tip ice in **a)** Normal and **b)** Flexible beam.

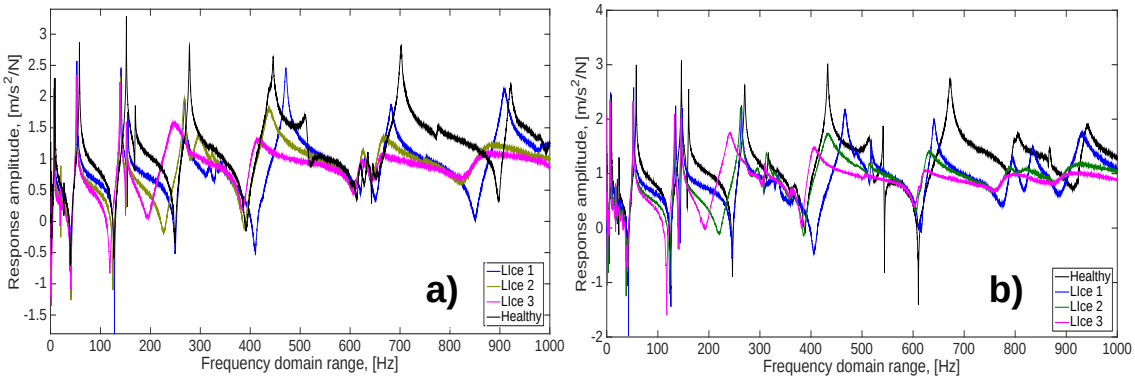

Figure 56. FRF's for bolted PL with Longitudinal ice in **a)** Normal and **b)** Flexible beam.

The FRF's from Fig. 54, 55, and 56 are presented in here only for the main reason to have visual comparisons between bolted Pitch Link arm and solid Pitch Link arm data. The novel SHM detection method in this thesis was only applied on the experimental/modelling data from Normal Advanced beam with solid Pitch Link.

- *Experimental Pitch Link damages and Ice accretion on solid Pitch Link.*

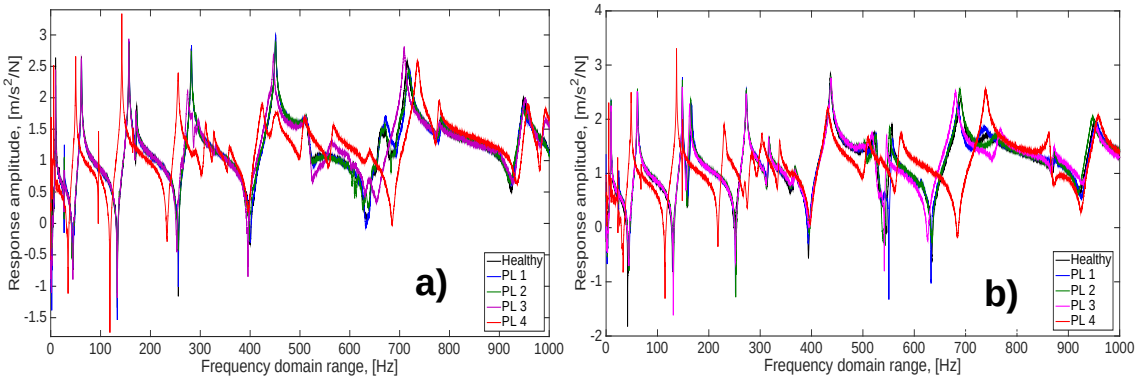

Figure 57. FRF's for solid PL damages in **a)** Normal and **b)** Flexible beam.

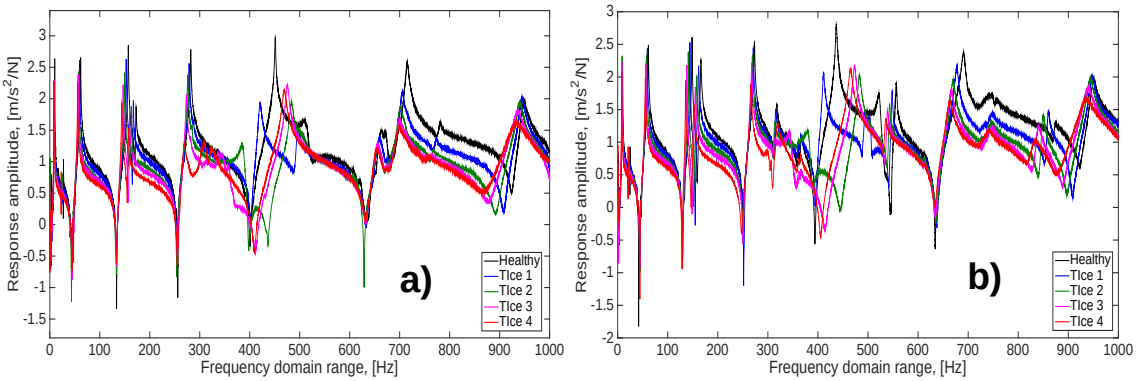

Figure 58. FRF's for solid PL with Tip ice in **a)** Normal and **b)** Flexible beam.

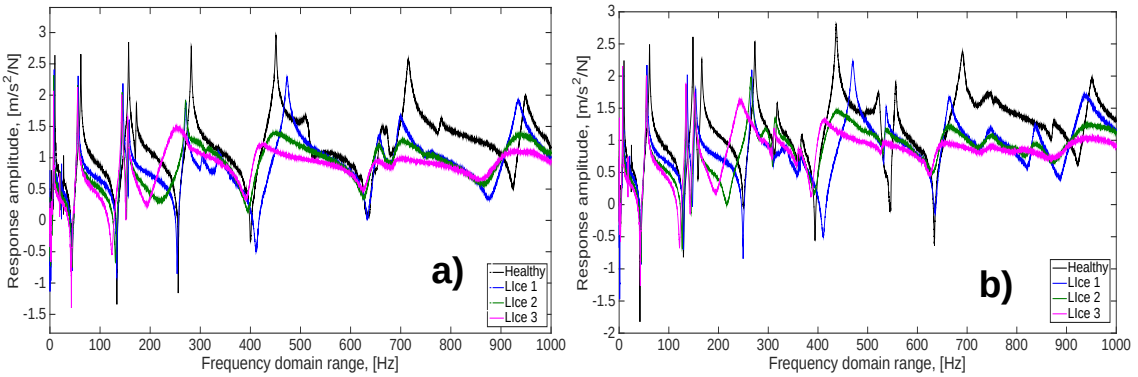

Figure 59. FRF's for solid PL with Longitudinal ice in **a)** Normal and **b)** Flexible beam.

The complete frequency reduction data from FRF's of the Fig. 57, 58, and 59 are presented in the next detailed solutions chapter as shown in the Fig. 60. Since both beams are closely similar the dynamics is expected to be similar, therefore the comparisons between model and experiments would be studied for the Normal Advanced beam data from the Fig. 57 **a)**, Fig. 58 **a)** and Fig. 59 **a)**.

5.3.1.- Detailed validation solutions

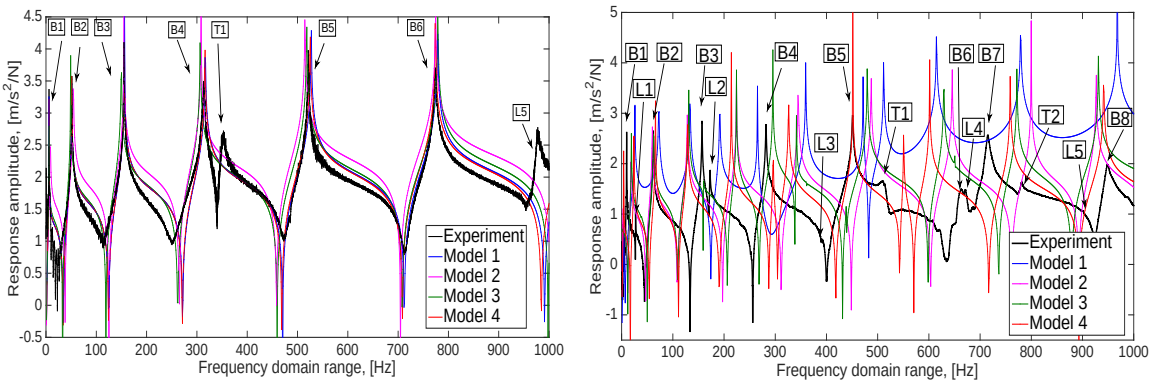

Figure 60. FRF's for Advanced beam: **a)** Without Pitch Link and with **b)** Pitch Link.

Exp.	*M1*	%	M2	%	M3	%	M4	%
6	**6.0060**	0.1000	**6.0060**	0.1000	**9.0090**	40.0959	**6.0060**	0.1000
51.4	**51.0511**	0.6811	**49.0490**	4.6810	**54.0541**	5.0337	**51.0511**	0.6811
155	**156.1562**	0.7432	**150.1502**	3.1786	**155.1552**	0.1001	**156.1562**	0.7432
313	**316.3163**	1.0539	**306.3063**	2.1617	**308.3083**	1.5103	**316.3163**	1.0539
352.7	**351.4000**	0.3693	**354.4000**	0.4808	**359.4000**	1.8818	**349.4000**	0.9400
521.3	**527.5275**	1.1875	**518.5185**	0.5350	**514.5145**	1.3102	**525.5255**	0.8073
773.8	**778.7788**	0.1000	**778.7788**	0.1000	**774.7748**	40.0959	**773.7738**	0.1000

Table 24.- Advanced beam without Pitch Link model accuracy.

Exp.	*M1*	%	M2	%	M3	%	M4	%
27.9	**26.0260**	*6.9502*	**18.0180**	*43.0418*	**19.0190**	*37.8566*	**24.0240**	*14.9294*
63.9	**73.0731**	*13.3940*	**60.0601**	*6.1954*	**62.0621**	*2.9182*	**66.0661**	*3.3333*
160	**133.1331**	*18.3308*	**128.1281**	*22.1234*	**131.1311**	*19.8322*	**129.1291**	*21.3544*
272.5	**265.2653**	*2.6907*	**224.2242**	*19.4377*	**224.2242**	*19.4377*	**214.2142**	*23.9507*
398.1	**359.3594**	*10.2291*	**344.3443**	*14.4807*	**295.2953**	*29.6526*	**296.2963**	*29.3215*
451.2	**471.4715**	*4.3941*	**487.4875**	*7.7315*	**479.4795**	*6.0772*	**451.4515**	*0.0557*
533.2	**511.5115**	*4.1521*	**-**	-	**-**	-	**550.5506**	*3.2019*
632	**614.6146**	*2.7892*	**645.6456**	*2.1361*	**629.6296**	*0.3758*	**601.6016**	*4.9284*
787.6	**778.7788**	*1.1263*	**799.7998**	*1.5371*	**771.7718**	*2.0301*	**758.7588**	*3.7302*
920.4	**967.9680**	*5.0380*	**926.9269**	*0.7066*	**930.9309**	*1.1377*	**940.9409**	*2.2071*

Table 25.- Advanced beam with Pitch Link model accuracy.

The complete model and experimentally correlation data from this research is extracted from Fig. 60, and presented in the Table 24, for the Advanced beam cases without the Pitch Link. A similar test cases are shown in the Table 25, with the Pitch Link. From both tables It can imply that the model accuracy is highly acceptable. The simulation cases for the Pitch Link were not quite accurate for models 2,3,4. Apparently for higher modes the accuracy are so closer to the experimental signal data. The opposite symptoms occurs for the first fourth resonant frequencies. Overall model accuracy is the model 1, potentially for being the simpler model from all of them.

5.3.2.- Criterion variables for healthy and damage data

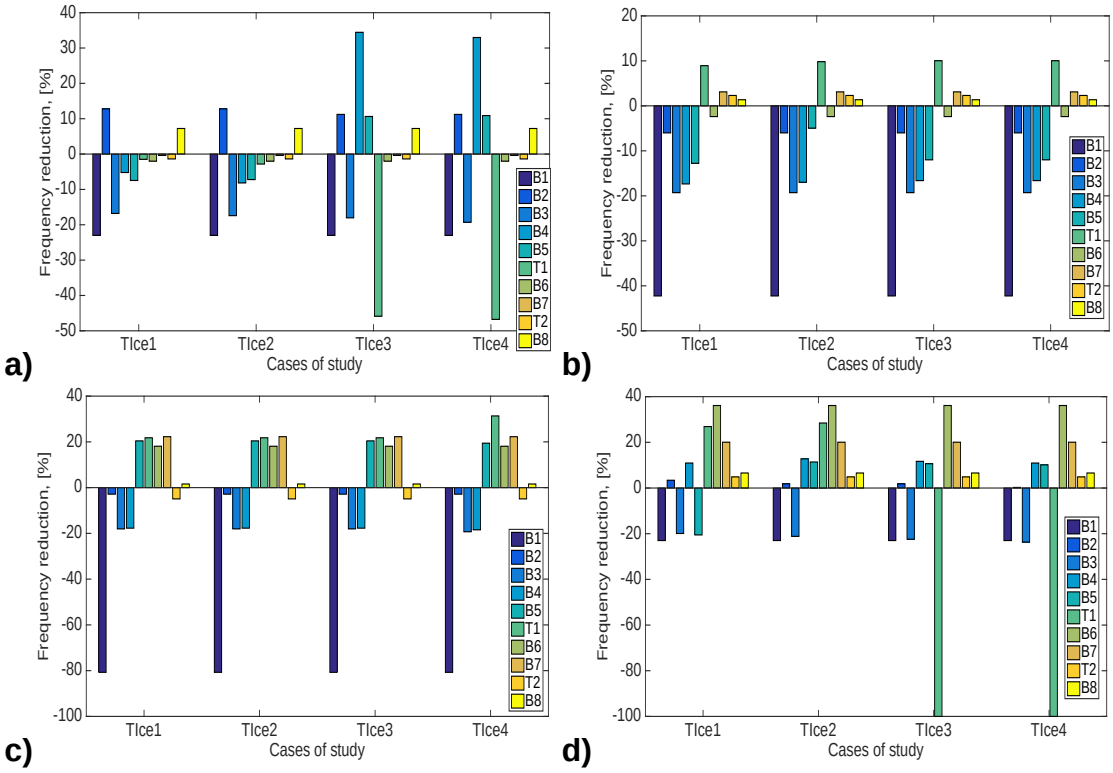

Figure 61. Modelling frequency reduction data in Tip ice for the four models as in **a)** Model 1, **b)** Model 2, **c)** Model 3, and **d)** Model 4.

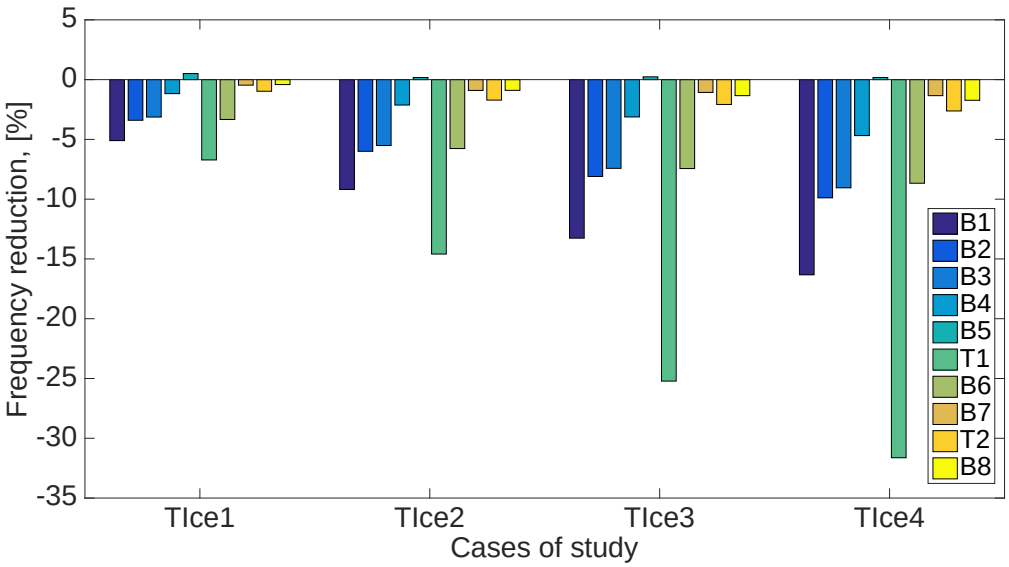

Figure 62. Experimental frequency reduction data in Tip ice.

The damages and insights presented in the Fig. 61 and 62, reveals that the progressive augmentation of Ice accretion at the tip comes with the increase addition of torque effects which shift the first fundamental torsional frequency.

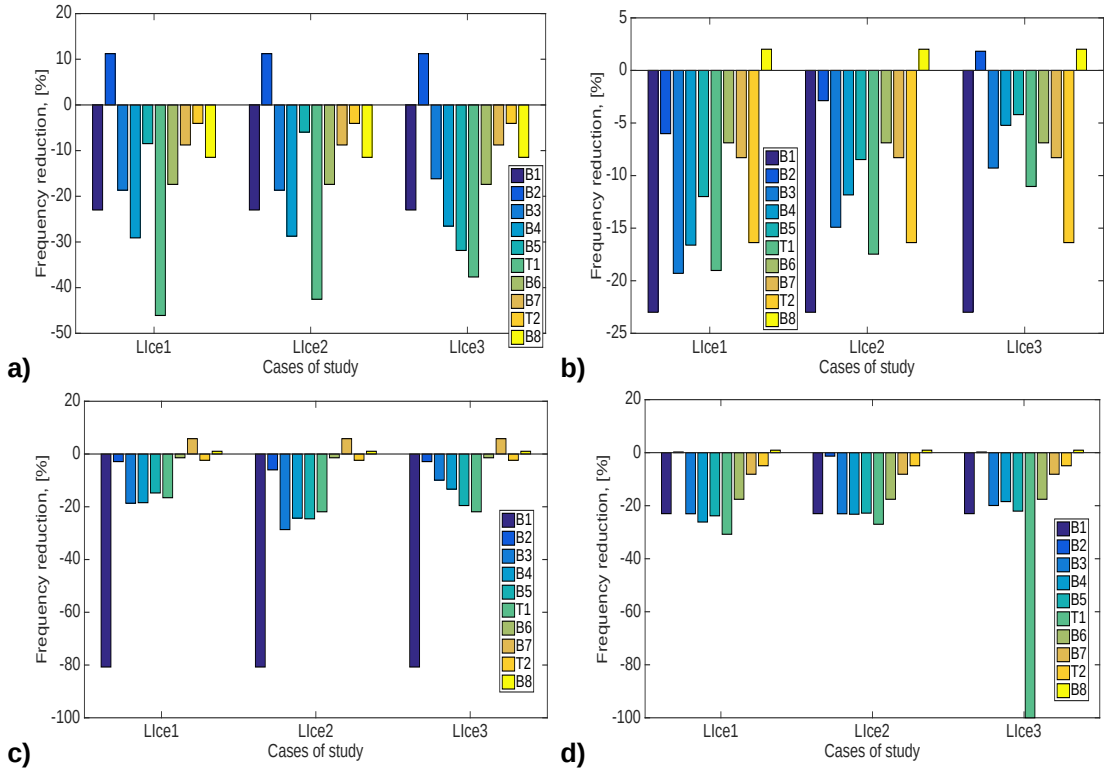

Figure 63. Modelling frequency reduction data in Longitudinal ice for the four models as in a) Model 1, b) Model 2, c) Model 3, and d) Model 4.

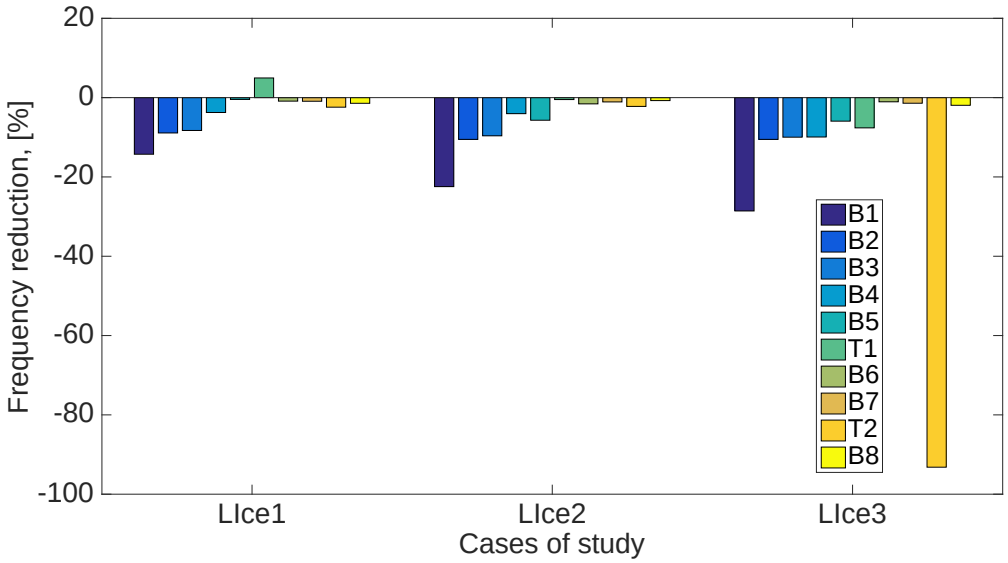

Figure 64. Experimental frequency reduction data in Logitudinal Ice.

As shown in the Fig. 63 and 64, it can be notice that the first fundamental bending and torsional resonant frequency modes are the most sensitive due Ice accretion. The information from this data suggest that majority of the monitoring systems should be related in supervising tasks with more attention on these first fundamental natural frequencies.

In this thesis experimental work, the changes in tightening torque at the Pitch Link arm does not generate significant structural changes as it can be seen in the results from the Fig. 65 and 66. The results shows no dramatic changes on the three Pitch Link conditions in changes in stiffness. This symptoms were also found in the modeling framework. These plots helps in understanding which modes are the sensitive and therefore directs research on deepening on the studies of the structural dynamics. Additional techniques should be implemented in order to obtain more information, a quick experimental-modelling MAC, FRAC, COMAC, and DLAC was ahead introduced to mapping properly the damages.

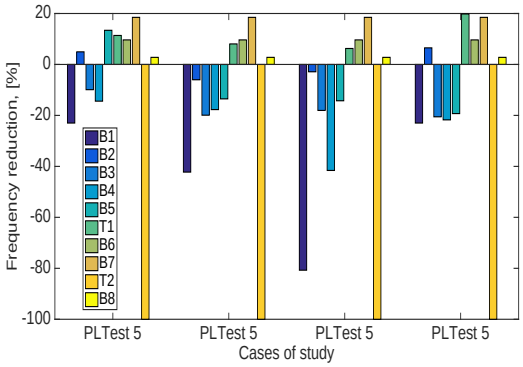

Figure 65. Modelling frequency reduction data in Pitch Link Test 5.

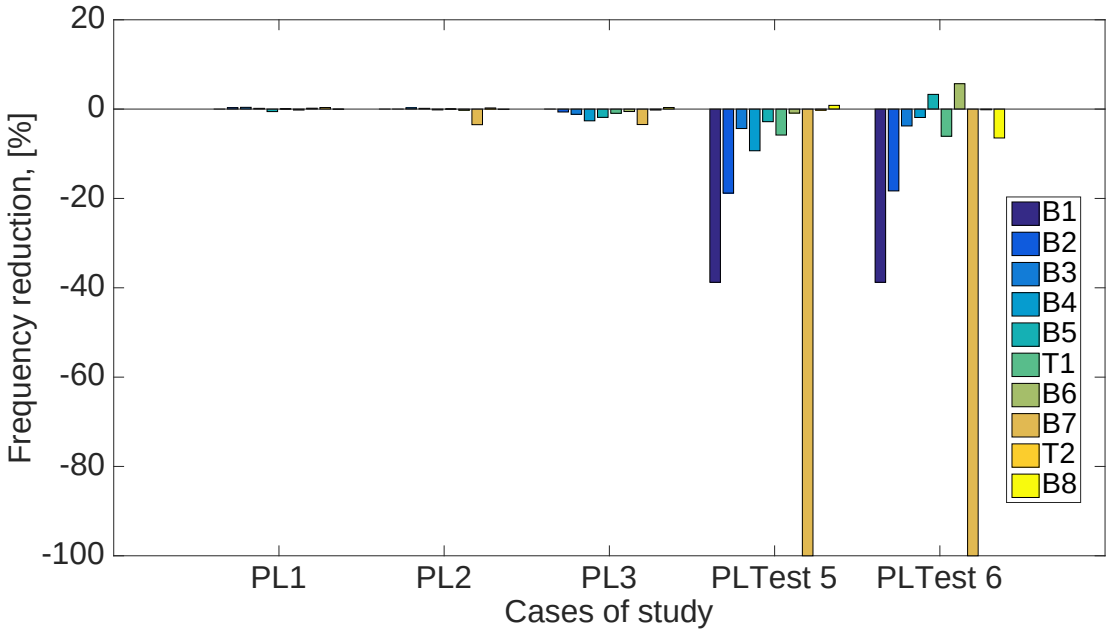

Figure 66. Experimental frequency reduction data in Pitch Link conditions.

5.3.3.- Reduced solutions for consistent check (fault detection)

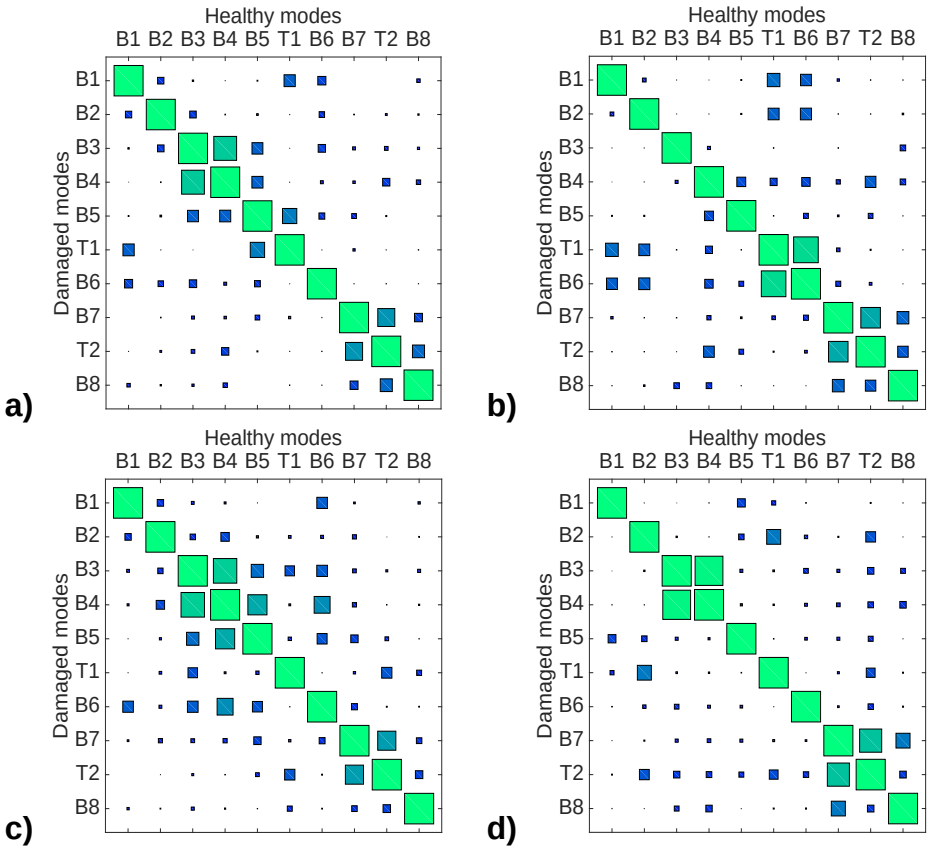

Figure 67. Auto MAC matrices for **a)** Healthy Advanced beam, **b)** Maximum Pitch Link damage, **c)** Tip ice 4 **d)** Longitudinal ice 3 FRF's for solid Pitch Link with Longitudinal ice.

The MAC matrix shows in the Fig. 67 **b)** that both torsional resonant modes are coupled with the sixth and septimal bending mode, more specially the septimal. The remarkable reference for healthy case as in the Fig. 67 **a)**, it can be observed that looks quite similar to Fig. 67 **c)**, the subsequent analysis on those differences are mainly related with the coupling around the third and fourth resonant modes. The general mapping of this system is shown on the FRAC matrix in the Fig. 68 **a)**, which shows that the collected amplitudes from vibrational test is able to identify the initial Pitch Link deformations that occurs on the first torsional mode as in the Fig. 68 **b)**. More complex damage detections were calculated and obtained using COMAC and DLAC techniques as shown in the Fig. 69 and 70.

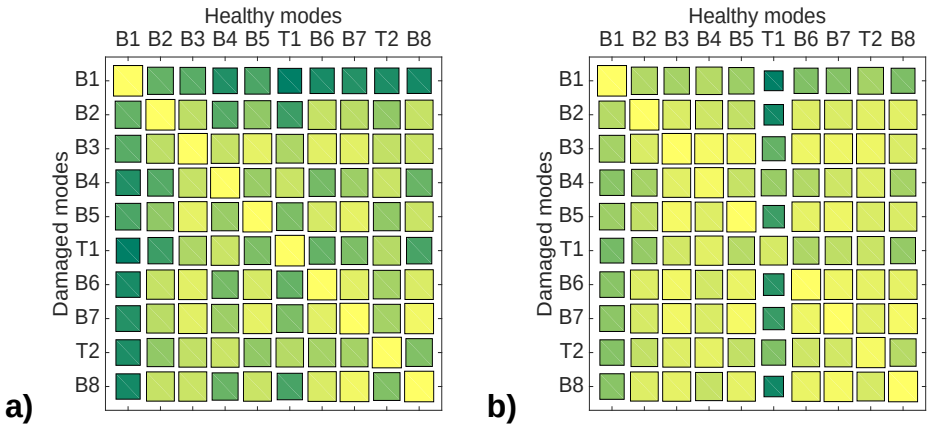

Figure 68. FRAC matrices for a) Healthy Advanced beams and b) Initial Pitch Link damage.

The damages were detected using the theory behind COMAC and DLAC principles, similar direction although different routes of research lines. The Fig. 69 and 70 **a)** detects the Ice accretion on the tip and Fig. 69 and 70 **b)** is related to the Pitch Link damage. The disadvantages of these techniques is the amount of time needed it in order to assamble the complete data, especially when the resaercher only uses 1 sensor for the whole experimental rig. A very well gap of understanding must be developed to increase the velocity of data manegement.

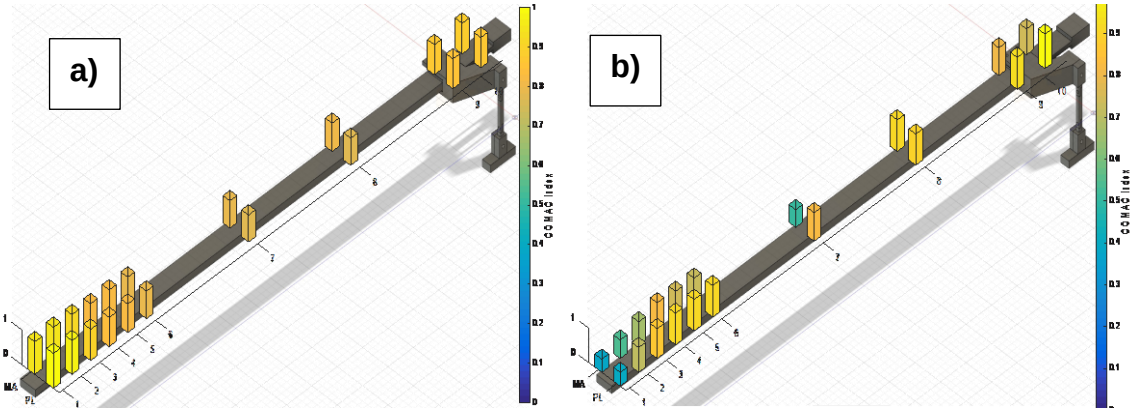

Figure 69. COMAC detection for **a)** Ice accretion detection, and **b)** Pitch Link damage.

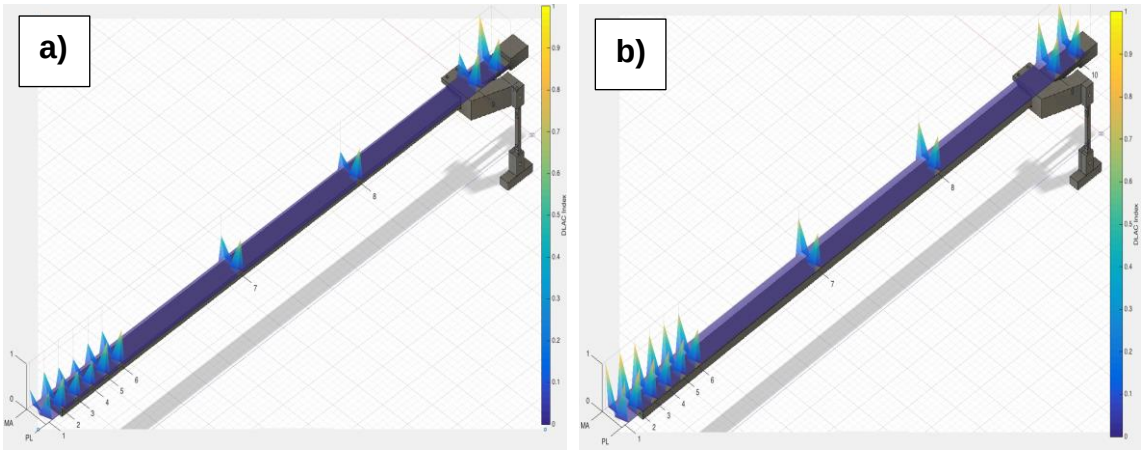

Figure 70. DLAC detection for **a)** Pitch Link damage and **b)** Ice accretion detection.

CHAPTER 6

APPLICATION: HELICOPTER DAMAGED BLADE

6.1.- Parametric selection criterion and validation for pitched blade system MBB Bo-105

The validation process for the Pitch Link in the rotor blade and its inducing features were carried out and also introduced and analyzed with two different geometrical changes. For this, five configurations of Pitch Links (PL) are shown in the Fig. 71, where two combinations of arms where applied in order to understand more about the rotorcraft pitched blade dynamics. On this BVP4c solver model, the helicopter blade parameters for German MBB Bo-105, were then segmented into three sections which are presented in Table 26. Where numerical values were selected randomized and an average selection were adopted, in order to get the closest accurate response. In other words, the parameter that provides closer match compared with the published rotational natural frequencies were considered to be the healthy responses for the rotorcraft system.

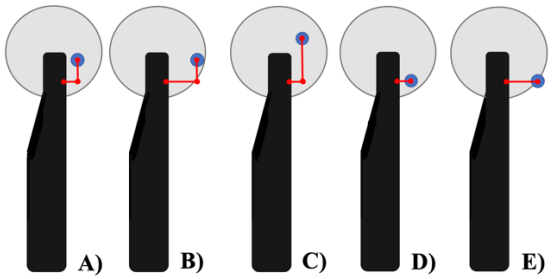

C = Chord's length, [0.27026 m]
Ω = Rotational speed, [44.51 rad/s].

Figure 71. L-shaped Pitch Link configurations: **a)** Nominal, and **b),c),d),e)** With variations.

	Stations			Units
	1	**2**	**3**	
r	0.0013	0.0630	4.9120	[m]
ρA	238.3007	9.1528	0.0149	[kg/m]
E	0	0.0170	0.0127	[m]
I_y	0	0	0.0011	[m^4]
I_α	0.6773	0.0461	0.0001	[kgm]
EI_y	2.4874x10^7	0.5882 x10^7	0.0103 x10^7	[Nm^2]
GJ	1.1998 x10^3	1.1998 x10^3	0.5454 x10^3	[Nm^2]
kAG	3.1277 x10^7	0.1201 x10^7	0.0002 x10^7	[N]

Table 26.- MBB Bo-105 helicopter's blade sectional parameters used on BVP solver.

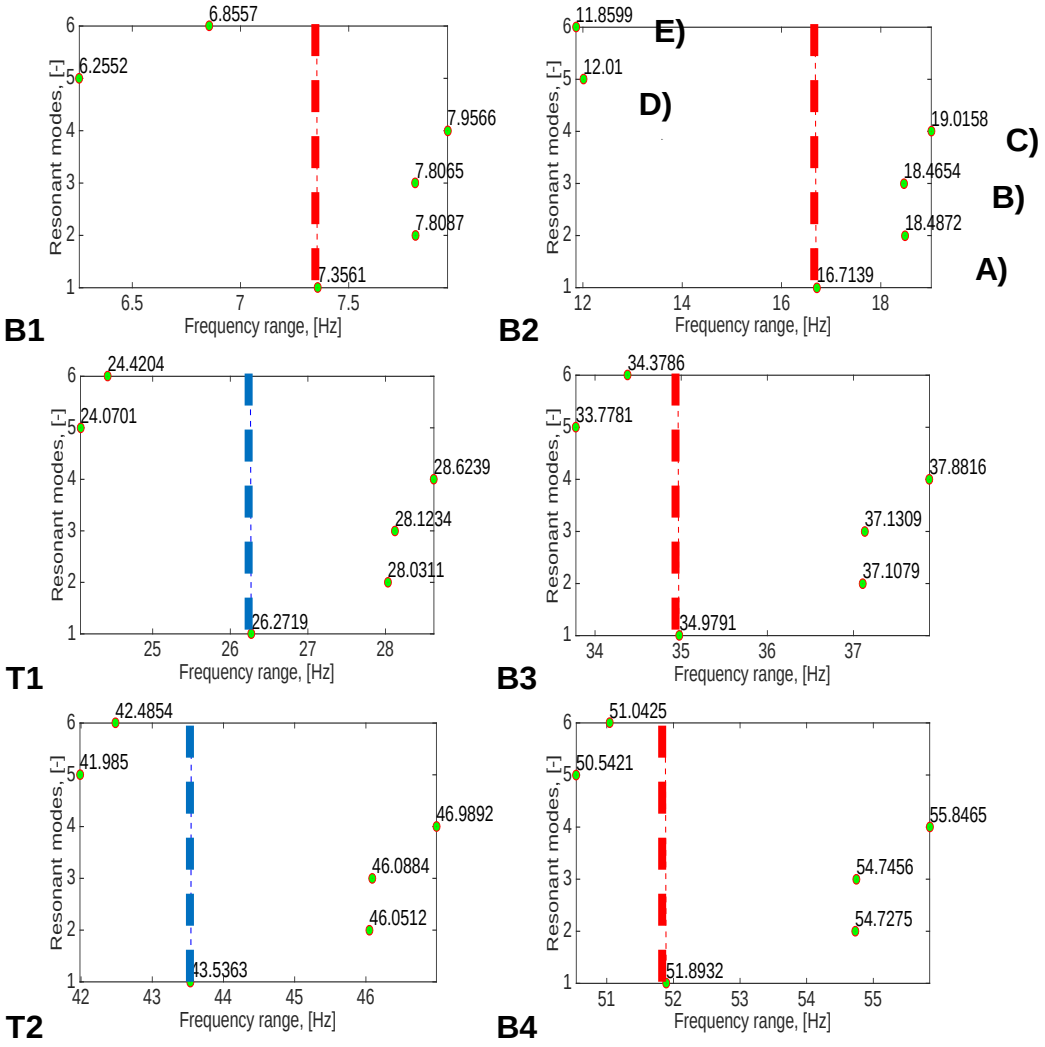

Figure 72. Frequency analysis per resonant mode vs. PL type.

The Fig. 72 shows insights on the natural frequencies changes from the PL configurations in the Fig. 71. Clearer insight in this study of resonant frequencies from PL configuration, a red dashed line shows published the natural frequencies. For L-shape arm from Fig. 71 **A)**,**B)**,**C)**, it can notice the higher frequencies, since it is quite clear that induces bending and torsion at the same time, where increases the stiffening on the blade section, therefore a higher values of natural frequencies will be expected. The opposite behavior occurs on the single torsional arm from the Fig. 71 **D)**,**E)**, as this configuration modify slightly the bending frequencies and a richer influence on the torsional response from the second and fifth mode.

The Fig. 73 shows the first fundamental bending and torsion modes, it can be notice that for the PL condition **A)**, **B)**, **C)**, which from the plots the torsional and bending modes were highly constrained at the PL location at the green arrows. This effects comes with the fact that bending and torsional moments are coupled with the L-shape arm, therefore it is expected to have these behaviours. From the Pitch Link conditions as in **D)**, **E)**, as the single torsional arm only controls the torsional moments and slightly changes bending responses as shown in Fig. 73. PL effects are highly related with coupled interaction of bending/twist responses.

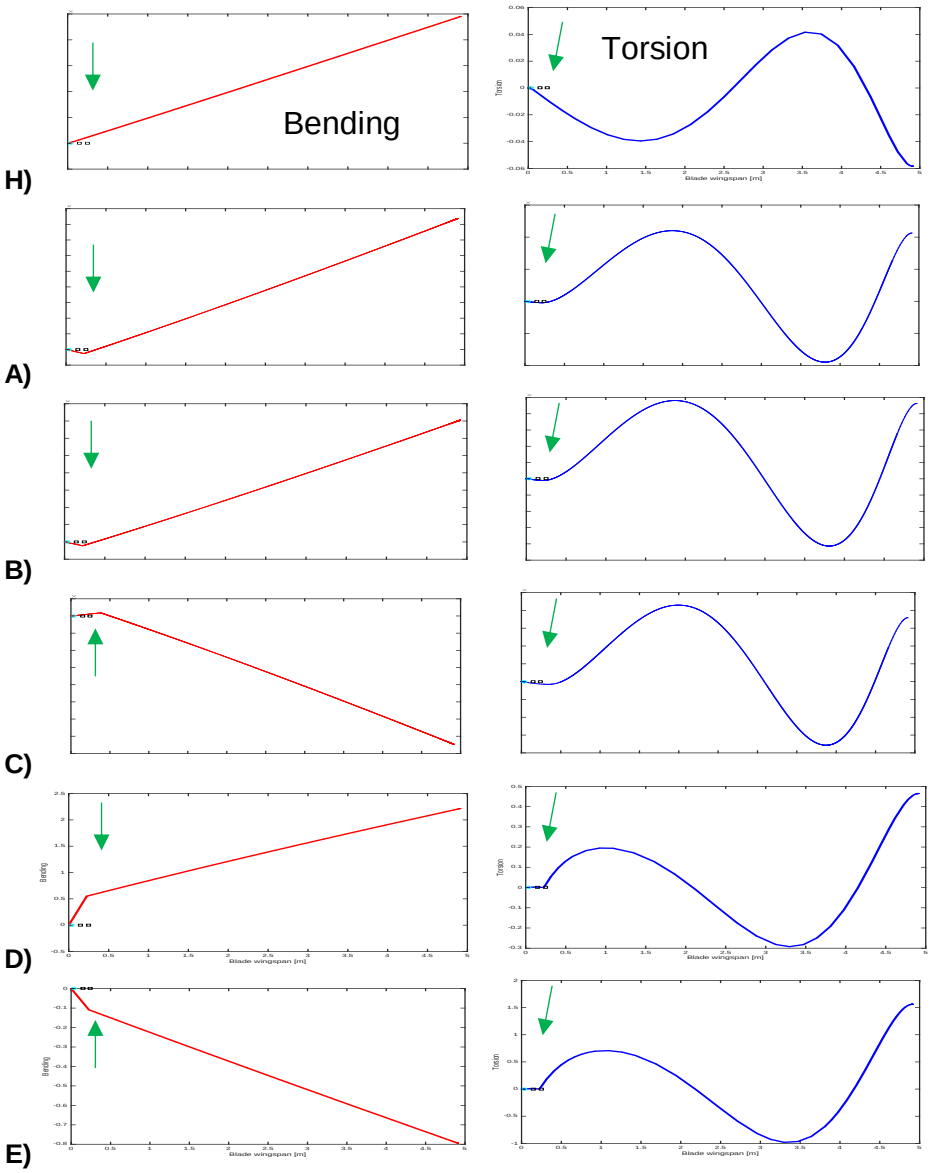

Figure 73. First fundamental normal mode shapes per PL type.

All the global parameters that were used for all the iterations and cases of study in this thesis are shown in the Table 27. The elastomer properties of the Pitch Link such as the stiffness and damping were evaluated from healthy condition and critical lower value for both stiffness and damping. Similar exploration was done for the torsional stiffness of the flapping hinge. In order to incorporate and observe the effect of the rotational speed, therefore the Campbell-Diagrams were adopted. Additional to previous, the breakdown of the weight of the body of ice for each case is shown in the Table 28. Notice that the Ice accretion case 7, is quite extreme and it never occurs in flight missions.

Type	Numerical value for BVP4c							Unit
K_{PL}	$1x10^9$	$1x10^8$	$1x10^7$	$1x10^6$	$1x10^5$	$1x10^4$	$1x10^3$	Nm^2
K_t	$2x10^9$	$2x10^8$	$2x10^7$	$2x10^6$	$2x10^5$	$2x10^4$	$2x10^3$	Nm^2
C_D	$3x10^9$	$3x10^8$	$3x10^7$	$3x10^6$	$3x10^5$	$3x10^4$	$3x10^3$	Ns/m
Ω	0.005	18.54	33.38	44.51	59.34	74.18	89.02	rad/s^2

Table 27.- General parameters of the MBB Bo-105 and SHM studies.

Type	Distributed Mass (Kg)			
	1 [88.2 %]	2 [11.3 %]	3 [0.5 %]	All [100 %]
ICE 1	$0.1499x10^{-8}$	$0.191 x10^{-9}$	$0.708 x10^{-18}$	$1.6900x10^{-9}$
ICE 2	$0.1499x10^{-6}$	$0.191 x10^{-7}$	$0.708 x10^{-14}$	$1.6900x10^{-7}$
ICE 3	$0.1499x10^{-4}$	$0.191 x10^{-5}$	$0.708 x10^{-10}$	$1.6900x10^{-5}$
ICE 4	0.001499	$0.191 x10^{-3}$	$0.708 x10^{-6}$	0.0017
ICE 5	0.1638	0.0209	0.0071	0.1918
ICE 6	8.5445	1.0906	2.8319	12.4670
ICE 7	153.6524	19.6127	70.7972	244.0623

Table 28. Ice accretion weight levels per blade airfoil sections.

6.2.- Optimization and model update calculations

The MBB Bo-105 applications were explored in non-rotating, rotating frame of reference under Vacuum, Aerodynamics using Quasi-Steady theory and Blade Element Method theory. Main idea of the exploration of these topics is to study the effects of non-rotating and rotational effects in those rotor blade. The main focus of analysis will be for the rotating cases of study.

6.2.1.- Non-rotating frame of reference performance $\Omega = 0$

6.2.1.1.- Dynamical structural influence by progressive damaged Pitch Link

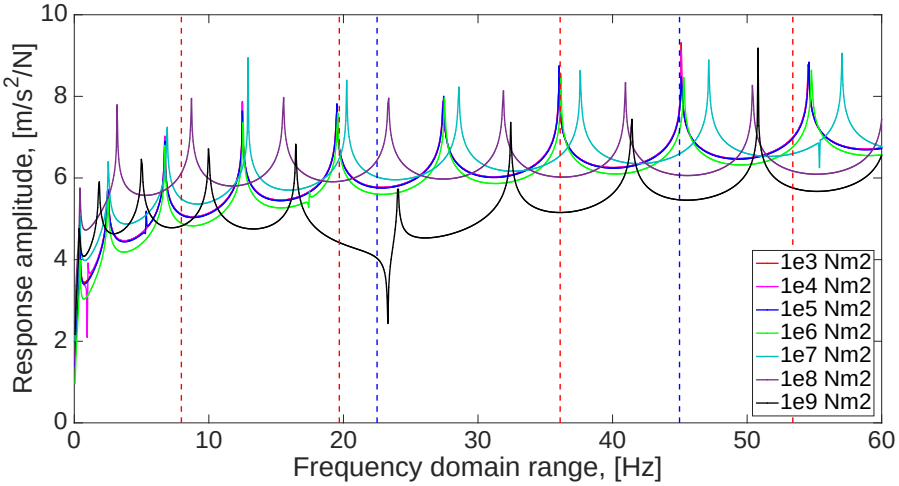

Figure 74. FRF's for damaged Pitch Link on Non-rotating blade.

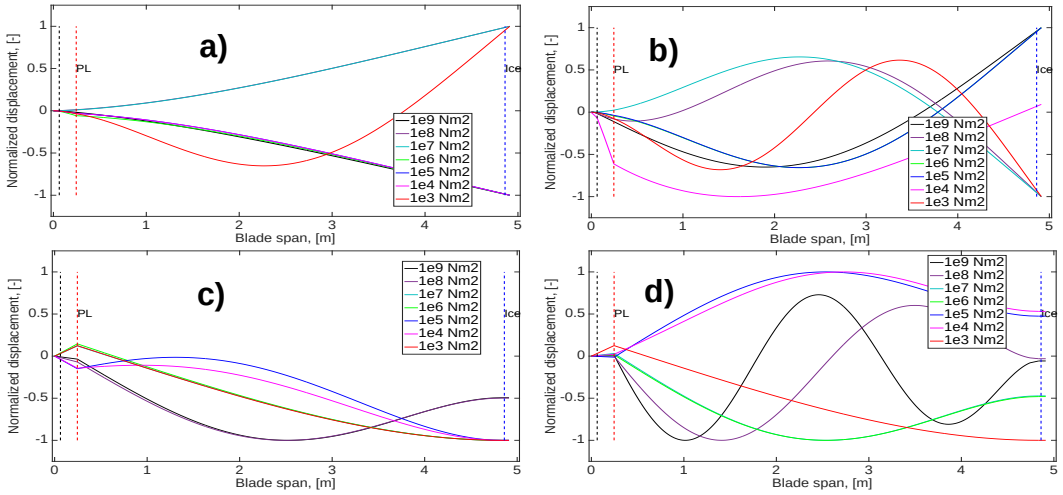

Figure 75. First and second modes due PL damage for: **a), b),** Bending, **c), d),** Torsion.

Usage of a non-rotating frame of reference for frequency response analysis was explored and calculated as shown in the Fig. 74. Where the Pitch Link Stiffness was altered and modified into 7 stages of progressive damage due the reduction of stiffness and damping coefficient of the elastomer material of Pitch Link actuator. The first and second normalized bending mode are shown in Fig. 75 **a)**, **b)**. Notice critical damage case such as red mode which is the most dynamically affected mode shapes specially for first and second torsional modes in Fig. 75 **c)**, **d)**, and slightly affected the first and second bending mode.

6.2.1.2.- Dynamical structural influence by progressive Ice accretion

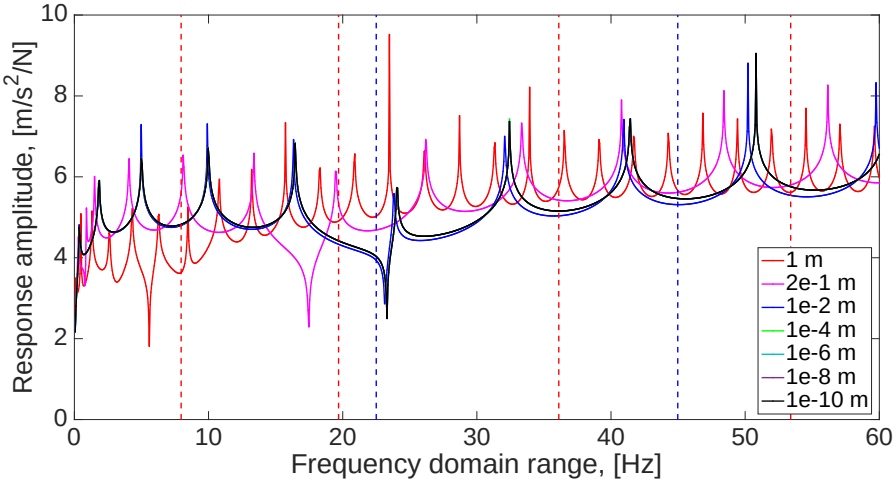

Figure 76. FRF's for Ice accretion damage on Non-rotating blade.

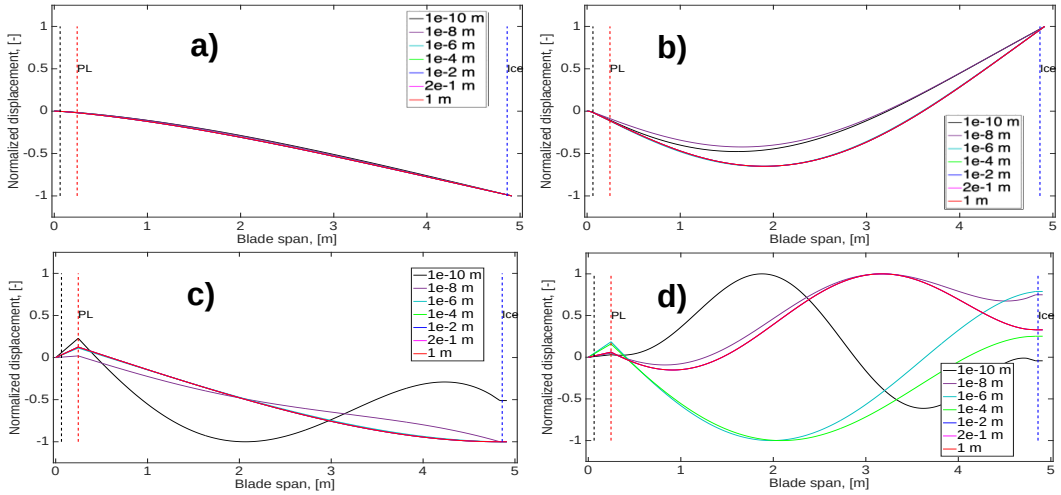

Figure 77. First and second modes due Ice damage for: **a), b)** Bending, **c), d),** Torsion.

Incorporation of Ice accretion onto the blade was applied for different stages of ice formation. Most critical case of ice is ICE 7 which is the simulation of a large block of ice added on tip's blade with a weight around 244 kilograms, justification of this proposed scenario is only and mainly the monitoring of resonant frequency changes from this case. The red FRF in the Fig. 76 shows lots of harmonic peaks due to the augment of mass distribution and taking into account that blade is not rotating. From the modes as shown in the Fig. 77, it can be notice that bending modes **a, b),** are not that affected. Although torsional modes **c), d)** produced from torque moments are more present specially for the second torsional mode.

6.3.1.- Rotating frame of reference performance $\Omega \neq 0$

6.3.1.1.- Dynamical structural influence by progressive damaged Pitch Link

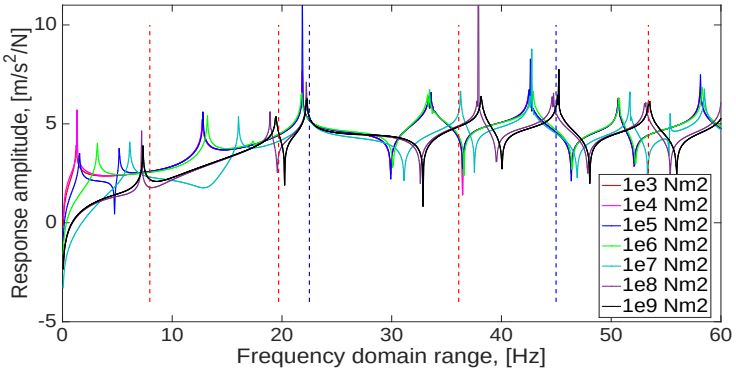

Figure 78. FRF's for damaged Pitch Link on Rotating blade in Vacuum.

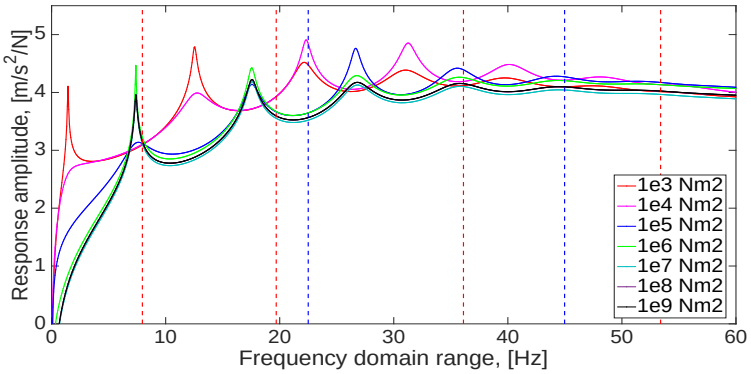

Figure 79. FRF's for damaged Pitch Link on Rotating blade in Quasi-Steady Aerodynamics.

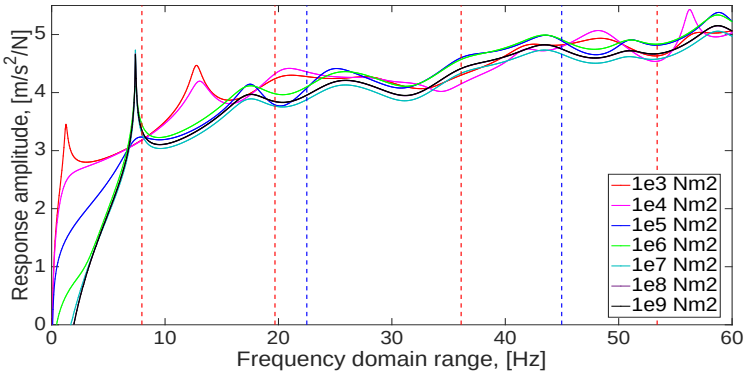

Figure 80. FRF's for damaged Pitch Link on Rotating blade in Blade Element Aerodynamics.

As shown in the FRF compilation from the Fig. 78, 79, and 80, where the presence of the Pitch Link damages were incorporated for Vacuum, Quasi-Steady Aerodynamics and Blade Element Aerodynamics. On the three of them it can be notice from the red FRF, the insight of the reduction of the first torsional resonant frequency and slightly the augment of first and second bending mode.

6.3.1.2- Dynamical structural influence by progressive Ice accretion

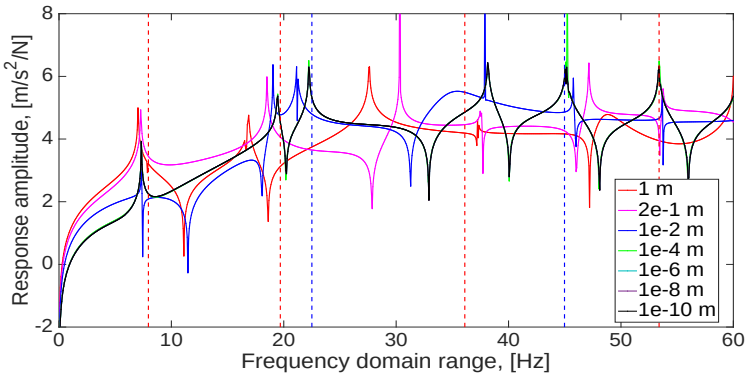

Figure 81. FRF's for Ice accretion on Rotating blade in Vacuum.

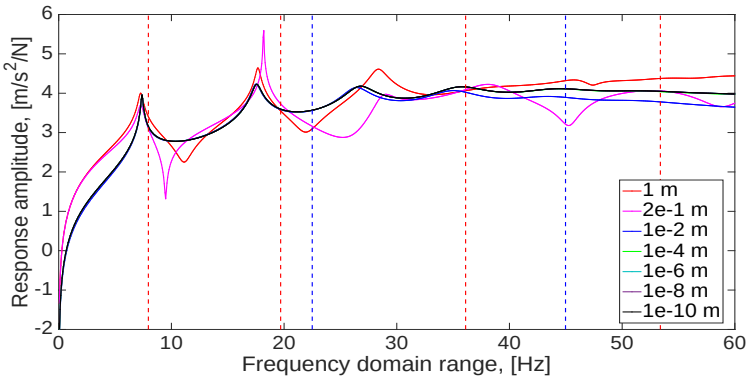

Figure 82. FRF's for Ice accretion Rotating blade in Quasi-Steady Aerodynamics.

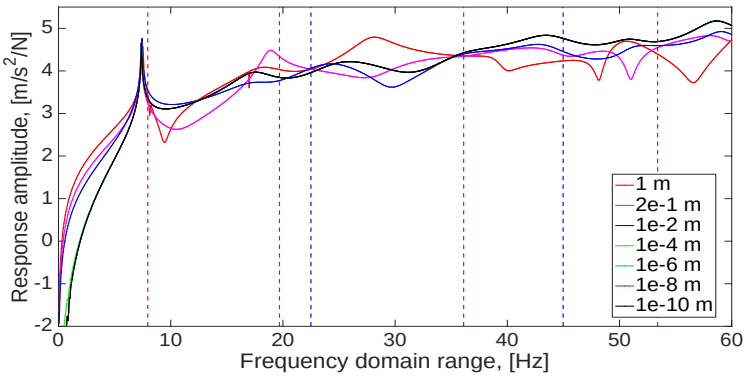

Figure 83. FRF's for Ice accretion on Rotating blade in Blade Element Aerodynamics.

The simulations of the Ice accretion were calculated in both Vacuum, Quasi-Steady and Blade Element Method Aerodynamics and are shown in the Fig. 81, 82, and 83. The loads due the weight of ice for critical damage as in the red FRF. This case produces in both torsional frequencies augments due to added torsional moments. Overall details of these effects are visualized in a clearer way under changes of rotational speeds which are shown in next Campbell-Diagram plots.

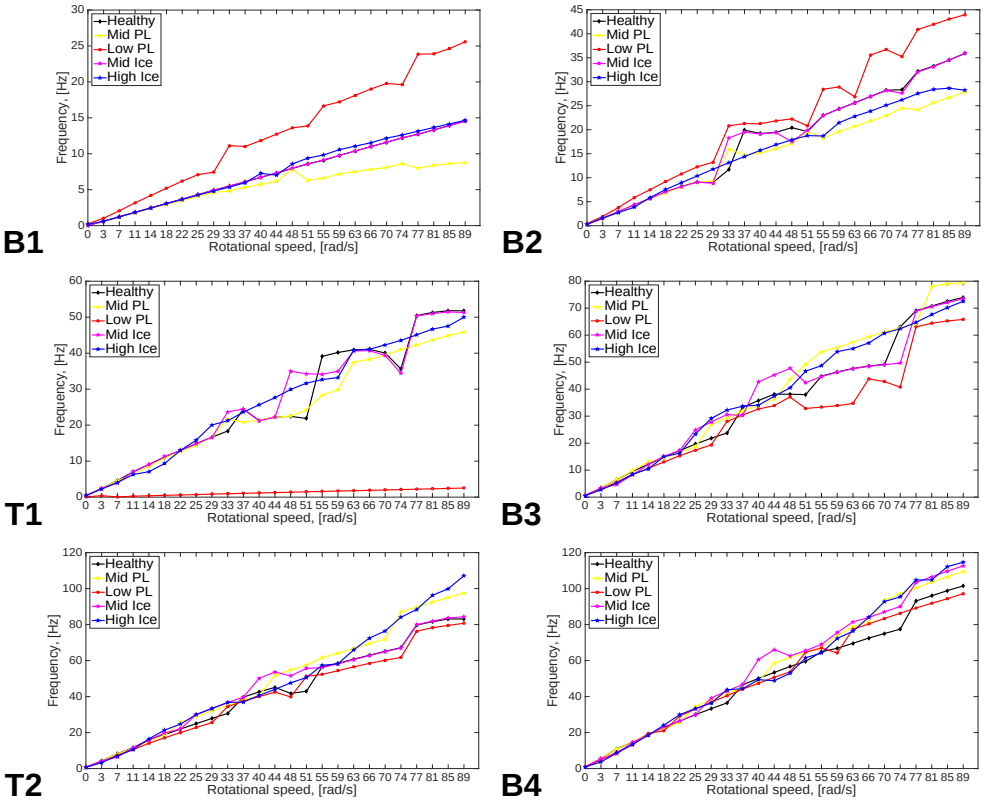

Figure 84. Campbell-Diagram for Rotating blade under Vacuum environment.

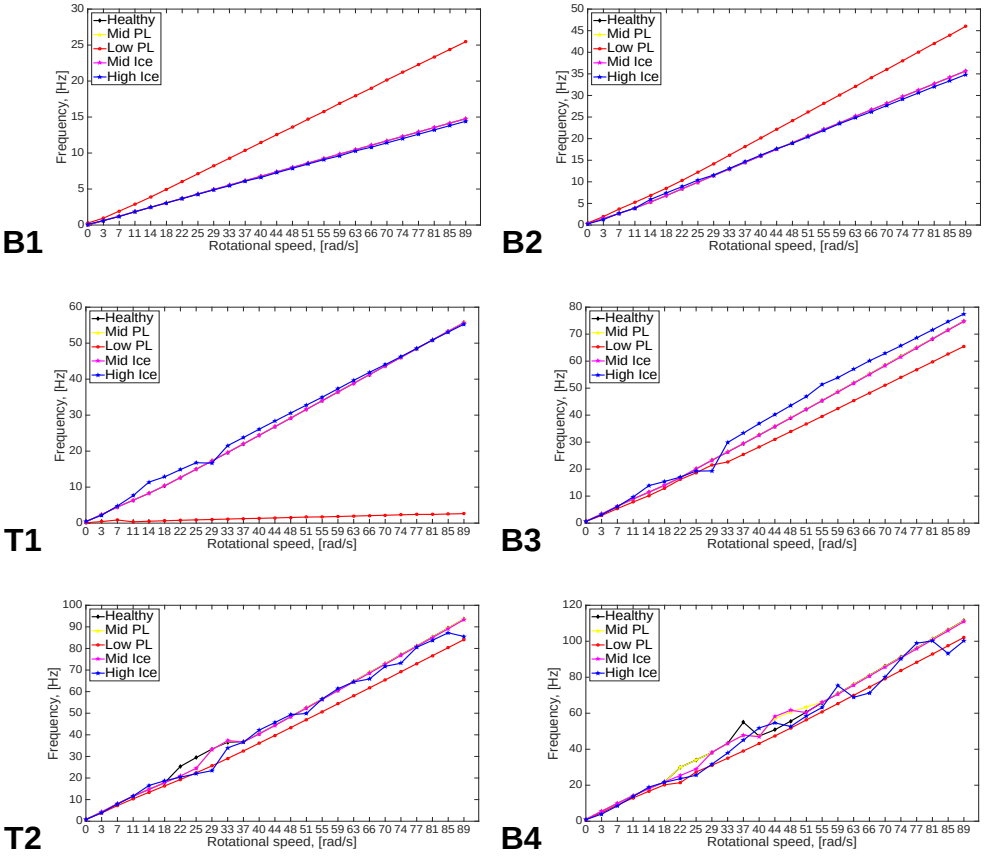

Figure 85. Campbell-Diagram for Rotating blade under Quasi-Steady Aerodynamics.

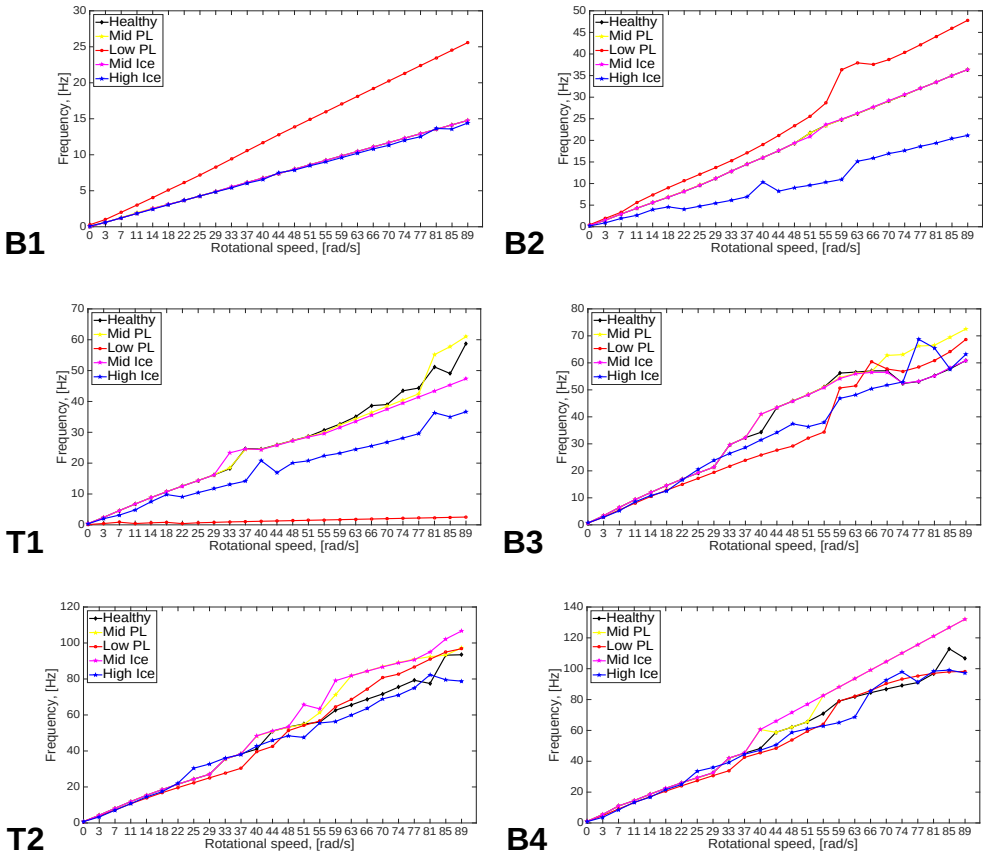

Figure 86. Campbell-Diagram for Rotating blade under Blade Element Aerodynamic.

The main conclusions from the Fig. 84, 85 and 86 are straightforward and clear; From these plots the effects of critical damage Pitch Link referred as red line causes that first and second bending moments augments slightly. Other reaction of these conditions is the reduction of the resonant torsional frequency due to the inducing dynamics of the Pitch Link L-shape arm. The L-shape arm aims to change in a coupled way both torsional and bending moment at the blade attachment location. These previous described results occurs on the 3 PL configurations. The Ice accretion results are not quite sensible to the rotational effects. From modelling perspective BVP4c for the Quasi-Steady Aerodynamics model results in a linear response, it seems the absence of free stream airflow in Vacuum turns in a less linear behaviours due to the lack of Aerodynamic forces acting on the blade span.

CHAPTER 7 CONCLUSIONS AND OUTLOOK

7.1.- Summary and conclusions

Before putting an end to this thesis, there is a lot to mention in order to conclude. The overall structure of the modelling platform and its results are plausible. In terms of calculation speed, there was a lot of delays on waiting the compilation of results. There is a big chance in debugging whole Matlab script's files, with main purpose of making sure that software will do the job in a quickly way. This is only one tertiary aspect if researcher have a faster computer at his/her office. The methodologies explored in this work could be considered or not the best suitable one. However, considering the idea of implementing calculations over a model capable to turn a body and/or system into lots of elements such as Finite Element Methods is highly appreciated. Idealization of having a platform capable of being divided onto lots of multi-subdomains or Multi-Points could be considered to be an implemented novelty, which will depend completely from the individual researcher's perspective. In this work, the usage of Multi-Point boundary conditions was extensively applied for the main purpose of introducing discretized loads or specific boundary condition sets. The novelty involves lots of innovating process, applications easy to execute/perform and more important its functionality. From the author's perspective of this thesis, the complete set of models implemented in this research work represent an excellent source for a certification process or validation of a well-planned experimental modal analysis work.

The presented and full results were sequential filtered, selected and then processed under different blocks inside of the SHM loop, the idea in the proposed SHM flowchart was to calculate/compute all the necessary information per each cycle of iteration. The results in this work reveals the critical sensitivity that the first fundamental bending and torsional resonant frequency experience under different force magnitudes acting and coming from the elastomer bearing or Pitch Link device. Additionally, to these discretized loads it was found that the addition and modelling of Ice accretion it also plays a significant role confirming that for some particular cases such as forces acting away the mass axis of the blade's airfoil are the perfect conditions to trigger and shift the torsional frequency responses, since the more away a weight force is acting from the mass axis, the higher is expected to be the applied torque moment. Other complementary situation such as the modelling and introduction of the Aerodynamic loading results is the critical amount of dampening effects on the helicopter's blade response. During modelling tasks, the dampened frequency response function makes so difficult to spot and to track down the resonant peaks. The previous cases of study turns in a hard time to judge whether if a round curvature in the plot represents the actual and real resonant peak frequency. Specially for these cases, when the SHM method performs it misses completely the identification, capture and storage of the frequency value, and therefore the subsequent calculation for the eigen-value problem that missing data it is no considered at all. Sometimes a quick visual inspection of the data is needed in order to judge if the resonant peak is located there. One of the most relevant results are the study and analysis of normalized damage mode shapes, with more emphasis on the ones affected by the Pitch Link actuators.

Where the reason of the analysis is mainly related with the understanding on the helicopter blade's dynamics. The global inspection of the proposed SHM outputs in this research work is the analysis of damage modes and correlated with the damage frequency values. Based in the listed objectives in this work it can be concluded the following aspects:

- The modelling platforms created are done in a rightly way, where the levels of precision and accuracy is quite decent and similar, these results are obtained for the healthy advanced beams without any Pitch Link attachment. The levels of accuracy for the advanced beams with Pitch Link are found to be not that precise for a few resonant frequencies, apparently for the higher modes computational modes are more accurate compared with the lower modes. From complete 4 model sets, the model 1 was capable to measure in general in a better way compared with the rest of the models. MBB B0-15 helicopter blade model was approached in a rightly way, its resonant frequencies are calculated correctly although the advantages of using Multi-Point boundaries conditions adds more accuracy to the calculations for the resonant frequencies. These actions introduces a major disadvantage since the higher the Multi-Points in the system it needs more time to process the results and the calculation time increases dramatically.

- The nature and the complete physics introduced onto the models were found to be the most precise approaches, accordingly with the literature review presented all the proper elements are considered for progressive changes that occurs during the Ice Accretion cases. The effects of mass

distribution, changes in the shapes airfoil profile was also assumed and applied, rotational effects that are generated due to centrifugal forced and the resistant forces due to cohesion and adhesion effects of the surfaces of the ice attached plays a significant role. The cases explores and the geometrical characteristics of the of the L-shape arm coupled with the Pitch Link arm formulation were approached using intimate parameters related to a real Pitch Link actuator. The idea of coupling all the possible deformations and angles were also adopted. The objectives were done rightly using this methodologies.

- The performance of the Structural Health Monitoring (SHM) method proposed was concluded that behaves in a plausible way. Since all the computational-experimental detection was focused completely based in the usage of the vibrational and modal analysis data. The detection platform in this thesis allows to obtain a proper extent of techniques and strategies in order to diagnose correctly the damages. Moreover, to be able to detect which normal mode shapes are the most sensible and in which location of the structure under study is the most critical in terms of deformations. To summarize it can be concluded from this work that the first fundamental bending and torsional resonant frequencies are the modes that must be of interested in all the helicopter damage detection methods. This is related with the fact that first bending frequency is the mode with larger amount of deflection, therefore more emphasis on the control of the blade dynamics. The coupling between bending and torsion could steer the blade into a critical vibrational scenario, specially when this are happening cyclically due to rotational effects.

7.2.- Thesis work contributions and ways forward for future work

The formatting and the objectives behind the chapter 6 is related to a closely real scenario that was somehow explored in details, although the deepening and the alternative SHM ideas involved was not accomplished at the full capacity range. The next stage of study should be the one related with the forward or backward operational flight, an upgrade on this Collocation Method towards simulations on a 3D regime. Having fully capabilities to represent correctly the morphology and sectional properties from any rotor blade configuration. Moreover, introducing the simulations of the climbing vertical displacements and/or descending helicopter actions over a helipad located in an oil rig platform in the middle of the ocean, while simulating these scenarios, intensive and nonlinear free stream airflow will be coming from a harsh winter atmosphere that causes a serious amount of loss of the thrust and the lift action on the flying unit. To have the opportunity to capture lots of screenshots or frames per second when the rotor blade is experiencing up and downwash deflections while these scenarios are occurring a set of the different intelligent substructures (such as the Pitch Link, Lag Dampers, Active Flaps, etc.) will be doing its tasks in order to mitigate, absorb, deviate or simply deform the blade. The reasoning of doing this is to be able to determine the causes and reactions and developing a training scheme for future aerospace engineers and pilots that share our passions in the aerospace field.

CHAPTER 8

APPENDICES

A-I.- List of references

[1] Azzam H. and Knight P., "Rotor system diagnostics and HUMS extensions for affordable CBM", 64th AHS International Annual Forum, vol. 3, May (2008), pp. (2120-2141), ISBN: 978-1-61782-929-1.

[2] Di Lorenzo E., Manzato S., Peeters B., and Marulo F., "Modal parameter estimation for operational wind turbines", 7th European Workshop on Structural Health Monitoring (EWSHM), July, (2014).

[3] Friswell M. I., Penny J.E.T. and Garvey S.D., "Parameter subset selection in damage location", Journal of Inverse problems in Engineering, vol. 5 (3), Feb. (1997), pp. (189-215), http://dx.doi.org/ 10.1080/174159797088027660.

[4] Musil M., Starek L., Titurus B., "Inverse problem in damage detection", E.M., (1999).

[5] Friswell M.I., "Damage detection using inverse methods", J. Philosophical transactions of the royal society A, vol. 365, Feb. (2007), pp. (393-410), doi: 10.1098/rsta.2006.1930.

[6] Titurus B. and Friswell M.I., "Parameter subset selection based damage detection of aluminum frame structure", 9th International Conference on Damage Assessment of Structures, J. of Physics: C.S. 305, July (2011), doi:10.1088/1742-6596/305/1/012092.

[7] Titurus B. and Friswell M.I., "Damage detection using successive parameter subset selections and multiple model residuals", Journal of Mechanical Systems and Signal Processing, Nov. (2013), doi: 10.1016/j.ymssp.2013.10.002.

[8] Ganeriwala S.N., "Using modal analysis for detecting cracks in wind turbine blades", Sound and Vibration, (2011).

[9] Deins K. E., Marinone T., Schultz R. A., Farinholt K. M., and Park G., "Modal analysis and SHM investigation of CX-100 wind turbine blade", IMAC XXIX, A conference and exposition on structural dynamics, Florida., (2011).

[10] Adams D., White J., Rumsey M., and Farrar C., "Structural health monitoring of wind turbines: method and application to HAWT", Wiley library, wind energy, (2011).

[11] Kostka P., Fidali M., Holeczek K., and Langkamp A., "Investigation of delamination effects on dynamic behavior of composite rotors", International Journal of Composite Materials, Volume 3 (6B), (2013), pp. (71-79).

[12] Ciang C.C., Lee J.R., and Bang H.J., "Structural health monitoring for a wind turbine system: a review of damage detection methods", Measurement science and technology, Volume 19, (12), (2008).

[13] Pitchford C.W., "Impedance-based structural health monitoring of wind turbine blades", Thesis M.S.M.E., Virginia Polytechnic Institute State University, Aug (2007).

[14] Myrent J. N., "Rotor blade operational data analysis methods and applications of health monitoring of wind turbines using integrated blade sensing", Thesis M.S.M.E., Purdue University, December, (2013).

[15] Dervilis N., Choi M., Taylor S.G., Barthorpe R.J., Park G., Farrar C.R., and Worden K., "On damage diagnosis for a wind turbine blade using patter recognition, Journal of Sound and Vibration 333, (2014), pp. (1833-1850).

[16] Tcherniak D., "Loss of rotor isotropy as a blade damage indicator for wind turbine structure health monitoring systems", 7th European Workshop on Structural Health Monitoring (EWSHM), July, (2014).

[17] McGugan M., Pereira G., Sorensen B.F., Toftegaard H., and Branner K., "Damage tolerance and structural monitoring for wind turbine blades", Philosophical transactions of the royal society, A 373, (2015).

[18] Tcherniak D., and Molgaard L.L., “Vibration-based SHM system: Application to wind turbine blades”, 11th International conferences on damage assessment of structures, Journal of physics: Conference 628, (2015).

[19] Tchrniak D., “Rotor anisotropy as a blade damage indicator for wind turbine structural health monitoring systems”, Mech Systems & Signal Processing 74, (2016), pp. (183-198).

[20] Yang W., Peng Z., Wei K., and Tian W., “Structural health monitoring of composite wind turbine blade: Challenges, issues and potential solutions”, IET, (2016).

[21] Pawar P.M. and Ganguli R., “Helicopter rotor health monitoring - a review”, Proc. I. Mech Eng, Part G, J. Aerospace Engineering, vol. 221, July (2007), pp. (631-647), doi:10.1243/09544100JAERO245.

[22] Civil Aviation Authority,“Safety review of offshore public transport helicopter operations in support of the exploitation of oil and gas”, (2014), CAP 1145.

[23] Azzam H. and Andrew M.J., “The use of math-dynamic models to aid the development of integrated health and usage monitoring systems”, Proc. I. Mechanical Engineering, Part G: J. Aerospace Engineering, vol. 206 (17), June (1992), pp. (71-76), doi:10.1243/PIME_PROC_1992_206_204_02.

[24] Ganguli R., Chopra I. and Haas D., “Formulation of a rotor-system damage detection methodology”, 36th Structures, Structural Dynamics and Materials Conference and Adaptive Structures Forum, AIAA, April (1995), pp. (302-312), doi:10.2514/6.1995-1230.

[25] Ganguli R., Chopra I. and Haas D., ”Simulations of helicopter rotor system structural damage, blade mistracking, friction and freeplay”, J. of Aircraft, vol. 35 (4), July (1998), pp. (591-597), doi:10.2514/2.2342.

[26] Ganguli R., Chopra I. and Haas D., “Detection of helicopter rotor system simulated faults using neural networks”, J. of the American Helicopter Society, vol. 42 (2), April (1997), doi:10.4050/JAHS.42.161.

[27] Ganguli R., Chopra I. and Haas D., "Helicopter rotor system fault detection using physics-based model and neural networks", AIAA Journal, vol. 36 (6), June (1998), pp. (1078-1086), doi: 10.2514/2.483.

[28] Ganguli R., “A fuzzy logic system for ground based health monitoring of a helicopter rotor using modal data”, J. of intelligent material systems and structures, vol. 12 (6), June (2001), pp. (397-408), doi:10.1106/104538902022598.

[29] Ganguli R., “Health monitoring of a helicopter rotor in forward flight using fuzzy logic”, AIAA Journal, vol. 40 (12), Dec 2002, pp. 2773-2781, doi:10.2514/2.1588.

[30] Stevens P.L., “Active interrogation of helicopter main rotor faults using trailing edge flap actuation”, PhD Dissertation, The Pennsylvania State University, Department of Mechanical and Nuclear Engineering, (2010).

[31] Yap, K.C. and Zimmerman, D.C., “Damage detection of gyroscopic systems using an Asymmetric Minimum Rank Perturbation Theory”, IMAC, (1999), pp. (1366-1372).

[32] Cattarius J. and Inman D.J., “Experimental verification of intelligent fault detection in rotor blades”, I. Journal of Systems Science, vol. 31 (11), Nov. (2010), pp. (1375-1379), doi: 10.1080/00207720050197767.

[33] Leaonard F., “Free-vibration behavior of a crack cantilever beam and crack detection”, Mechanical Systems and Signal Proc., Vol. 15(3), (2001), pp. (529-548).

[34] Abdel Wahab M.M., “Effect of modal curvatures on damage detection using model updating”, J. Mechanical systems and signal processing, vol. 15 (2), March (2001), pp. (439-445), doi: 10.1006/mssp.2000.1340.

[35] Sampaio R.P.C., Maia N.M.M. and Silva J.M.M., “Damage detection using the frequency response function curvature method”, Journal of Sound and Vibration, vol. 226 (5), Oct. (1999), pp. (1029-1042), doi: 10.1006/jsvi.1999.2340.

[36] Kiddy J. and Pines D., “Eigenstructure assignment technique for damage detection in rotating structures”, AIAA, vol. 36 (9), Sep. (1998), pp. (1680-1685), doi: 10.2514/2.571.

[37] Kiddy J. and Pines D., “Experimental validation of a damage detection technique for helicopter main rotor blades”, Proc. I. Mech Eng, Part I, vol 215 (3), Nov. 2000, pp. 209-220, doi:10.1243/0959651011540996.

[38] Hwang H.Y. and Kim C., “Damage detection in structures using a few frequency response measurements”, J. of Sound and Vibration, vol. 270 (1-2), Feb. 2004, pp. 1-14, doi: 10.1016/S0022-460X(03)00190-1.

[39] Purekar A.S., (2000), “Detecting damage in non-uniform beams using the dereverberated transfer function response”, Smart Materials, Vol. 9(4), pp. (429-444).

[40] Lakshmanan K.A. and Pines D., “Detecting crack size and location in composite rotorcraft flex beams”, Proc. SPIE - The International Society for Optical Engineering Smart Structures and Materials: S.S.I.S, (1997), pp. (408-416).

[41] Piatti J. P., ”Study on the detection and localization of damage in an Euler-Bernoulli beam”. Vibrations, shocks and noise, 19th Symposium VISHNO, (2014).

[42] Kiddy J. and Pines D., ”Constrained damaged detection technique for simultaneously updating mass and stiffness matrices”, American Institute of Aeronautics and Austronauts, Vol. 36(7), (1998), pp. (1332-1334).

[43] Messina A., Williams E.J. and Contursi T., “Structural damage detection by a sensitivity and statistical based method”, Journal of Sound and Vibration, vol. 216 (5), Oct. (1998), pp. (791-808), doi:10.1006/jsvi.1998.1728.

[44] Banerjee J.R., “Coupled bending-torsional dynamic stiffness matrix beam elements”, I. Journal for Numerical Methods in Engineering, vol. 28 (6), June (1989), pp. (1283-1298), doi: 10.1002/nme.1620280605.

[45] Jacklin S.A., “Full-scale wind tunnel test of an individual blade control system for a UH-60 helicopter”, American Helicopter Society 58th Annual Forum, (2002).

[46] Kessler C., “Active rotor control for helicopters: individual blade control and swashplateless rotor designs”, CEAS Aeronaut J, (2011), Vol 1, pp. (23-54).

[47] Salawu O.S., “Detection of structural damage through changes in frequency: a review”, Engineering structures, Vol. 19 (9), pp. (718-723).

[48] Lu Q., Ren G. and Zhao Y., “Multiple damage location with flexibility curvature and relative frequency change for beam structures”, J. of Sounds and Vibration, Jun. 2002, vol. 253 (5), pp. (1101-1114), doi:10.1006/jsvi.2001.4092.

[49] Pawar P.M., (2007), “Damage detection in beams using spatial Fourier analysis and neural networks”, Journal of intelligent Materials Systems and Structures, Vol. 18.

[50] Chandrashekhar M., (2009), “Structural damage detection using modal curvature and fuzzy logic”, Structural Health Monitoring Sage Publications.

[51] Shevtsov S.N., Akopyan V.A. and Rozhkov E.V., ”An approach to the problem of damage identification in an elastic rod based on the Timoshenko beam model”, Russian Journal of Nondestructive Testing, Vol. 47 (7), June (2011), pp. (480-490), doi: 10.1134/S1061830911070072.

[52] Lele S. and Maiti S., “Modelling of transverse vibration of short beams for crack detection and measurement of crack extension”, Journal of Sound and Vibration, (2002), Vol. 257, pp. (559-583).

[53] Shevtsov S.N., Zhilyaev I., Akopyan V.A. and Soloviev A., ”Identification of the damage in the beam-like structure on the basis of Timoshenko beam model”, International Conference on Innovative Tech, Sep. (2012), pp. (517-520), ISBN: 978-953-6326-77-8.

[54] Shevtsov S.N., Zhilyaev I., Akopyan V. and Remozov V., ”A probabilistic approach to the crack identification in the beam-like structure described by Timoshenko beam model”, 9th I.C. on Fracture & Strength of Solids, June (2013), pp. (1-10).

[55] Jalali H., “Linear contact interface parameter identification using dynamic characteristic equation”, Journal Mechanical Systems and Signal Processing, vol. 66, Jun. (2015), pp. (111-119), doi: 10.1016/j.ymssp.2015.05.012.

[56] Farrar C.R., and Lieven N.A.J., “Damage prognosis: the future of structural Health monitoring”, Philosophical transactions of the royal society 365, (2007), pp. (623-632).

[57] Pitchford C.W., “Impedance-based structural health monitoring of wind turbine blades”, Thesis M.S.M.E., Virginia Polytechnic Institute State University, Aug (2007).

[58] Deins K. E., Marinone T., Schultz R. A., Farinholt K. M., and Park G., “Modal analysis and SHM investigation of CX-100 wind turbine blade”, IMAC XXIX, A conference and exposition on structural dynamics, Florida., (2011).

[59] Kostka P., Fidali M., Holeczek K., and Langkamp A., “Investigation of delamination effects on dynamic behavior of composite rotors”, International Journal of Composite Materials, Volume 3 (6B), (2013), pp. (71-79).

[60] Dervilis N., Choi M., Taylor S.G., Barthorpe R.J., Park G., Farrar C.R., and Worden K., “On damage diagnosis for a wind turbine blade using patter recognition, Journal of Sound and Vibration 333, (2014), pp. (1833-1850).

[61] Tcherniak D., and Molgaard L.L., “Vibration-based SHM system: Application to wind turbine blades”, 11th International conferences on damage assessment of structures, Journal of physics: Conference 628, (2015).

[62] Mironov A., Doronkin P., Prilonsky A., and Kabashkin I., “Structural health monitoring of rotating blades on helicopters”, Vol. 20(3), (2016), pp. (110-122).

[63] Miller T.L., and Bond T.H., “Icing research tunnel test of a model helicopter rotor”, NASA TM 101978, 45th Annual forum and technology display, AHS, (1989).

[64] Hansman R.J., “The influence of Ice accretion physics on the forecasting of aircraft icing conditions”, 3rd International conference on the aviation weather system, (1989).

[65] Britton R.K., and Bond T.H., “A review on Ice accretion data from a model rotor icing test and comparison with theory”, NASA TM 103712, 29th Aerospace, AIAA, (1991).

[66] Scavuzzo R.J., Chu M.L., and Ananthaswany V., “Influence of aerodynamic forces in ice shedding”, Journal of aircraft, Vol. 31, No.3, May, (1994).

[67] Seifert H., and Richert F., “A recipe to estimate aerodynamics and loads on iced rotor blades”, BOREAS IV, March, (1998).

[68] Seifert H., “Technical requirements for rotor blades operating in cold climate”.

[69] Westerhellweg A, and Mönnich K, “Prediction of power production losses due to icing based on icing signs in wind measurements”.

[70] Metotest, Alpine test site gütsch, Cattin R., Dierer S., Kunz S., Heimo A. Russi G., and Russi M., “Icing and wind turbines: Swiss activities”, Winterwind, (2008).

[71] Fortin G., Perron J., “Spinning rotor blade tests in icing wind tunnel”, AIAA, Jun (2009).

[72] Brouwers E.W., Palacios J.L., and Smith E.S., “The experimental investigation of a rotor hover icing model with shedding”, AHS, 66th Annual Forum (2010).

[73] Dana S. R., “Detection of blade damage and ice accretion for health monitoring of wind turbines using integrated blade sensors”, Thesis M.S.M.E., Purdue University, Dec, (2011).

[74] Lehtomäki V., Hetmancsyk S., Durstewitz M., Baier A. Freudenreich K., and Argyriadis K., “Icedblades – Modelling of ice accretion on rotor blades in a coupled wind turbine tool”, Winterwind international wind energy conference, (2012).

[75] Adriana H., Holger K., and Laver M.O., “ice accretion on wind turbine blades”, 15th International workshop on atmospheric icing of structure, (2013).

[76] Meteotest, weather forecasts renewable energies air and climate environmental IT, “Evaluation of ice detection systems for wind turbines”, VGB research project 392, (2016).

[77] Tsipoki S., Häckell M.W., and Gribmann T., “Damage and ice detection on wind turbine rotor blades using a three-tier modular structural health monitoring framework”, (2017).

[78] Gao L., Liu Y., and Hu H., “An experimental study on icing physics for wind turbine icing mitigation”, 35th Wind energy symposium, AIAA SciTech Forum, (2017).

[79] Shi Q., "Model-based detection for ice on wind turbine blades", E.W.E.M.S.T., Delft University of technology, July, (2017).

[80] Bauchau O.A., and Liu Haiying, "On the modeling of hydraulic component in rotorcraft systems", Journal of the American Helicopter Society, April, (2006).

[81] A. Mander, D. Feszty, F. Nitzche, "Active Pitch Link actuator for impedance control of helicopter vibration", American Helicopter Society 64 Annual Forum, May, (2008).

[82] Tao S., Jianfeng T., and Haowen Wang., "Investigation of rotor control system loads", Chinese Journal of Aeronautics, Vol. 26 (5), (2013), pp. (1114–1124).

[83] Scarborough L.H., Rahn C.D., Smith E.C., and Koudela. K.L, "Coupled pitch links for Multiharmonic Isolation Using Fluidic Circuits", Journal of the AHS, Vol. (59), (2014).

[84] Lloyd H. Scarborough, III, "Dynamics of fluidic devices with applications to rotor pitch links", PhD Thesis, The Pennsylvania State University, May (2014).

[85] Dong H., Rahn C.D., Smith E.C., "Higher harmonic pitch link loads reduction using fluidlastic isolators", Proc IMechE part G: Journal of Aerospace Eng, Vol. 228 (3), (2014).

[86] Dong H., "Pitch link loads reduction of variable speed rotors by variable tuning frequency fluidlastic isolators", Chinese Journal Aero, Vol. 28 (5), (2015), pp. (1408–1415).

[87] I. Goulos, "Flexible Rotor Blade Dynamics for Helicopter Aeromechanics Including Comparisons with Experimental Data", The Aeronautical Journal, Vol. 119(1213), March (2015).

[88] J. A. Staley, "Validation of Rotorcraft Flight Simulation Program through Correlation with Flight Data for Soft-in-plane Hingeless Rotors", AMRDL, (1976).

[89] J.R. Banerjee, "Coupled Bending-Torsional Dynamic Stiffness Matrix for Beam Elements", Int. Journal for Numerical Methods in Eng., Vol. 28, (1989), pp. (1283-1298).

[90] S.H, R. Eslimy-Isfahany and J.R. Banerjee, "Use of Generalized in the Interpretation of Dynamic Response of Bending-Torsion Coupled Beams", Journal of Sound and Vibration, Vol. 238(2), (2000), pp. (295-308).

[91] O.O. Ozgumus, and M.O. Kaya, "Energy Expressions and Free Vibration Analysis of Rotating Double Tapered Timoshenko Beam Featuring Bending-Torsion Coupling", International Journal of Engineering Science 45, (2007), pp. (562-586).

[92] O.O. Ozgumus, and M. O. Kaya, "Energy Expressions and Free Vibration Analysis of Rotating Double Tapered Timoshenko Beam Featuring Bending-Bending-Torsion Coupling", Arch Appl Mech, Vol. 83, (2013), pp. (97-108).

[93] Auzinger W., Kneisl G., Koch O. and Weinmüller E.B., "A collocation code for boundary vauel problems in ordinary differential equations", Journal Institute for Applied Mathematics and Numeral Analisys Numerical Algorithms, vol 33 (1), Aug. (2003), pp. (27-39), doi: 10.1023/A:1025531130904.

[94] O.O. Ozgumus, and M.O. Kaya, "Formulation of flutter and vibration analysis of a hingeless helicopter blade in hover: Part I", Aircraft Engineering and Aerospace Technology: An International Journal 79(2), (2007), pp. (177-183).

[95] O.O. Ozgumus, and M.O. Kaya, "Formulation for flutter and vibration analysis of a hingeless helicopter blade in hover: Part II". Results of flutter stability and vibration analysis of a hingeless helicopter blade in hover, Aircraft Engineering and Aerospace Technology: An International Journal 79(3), (2007), pp. (231-237).

[96] D. H. Hodges, and R. A. Ormiston, "Stability of hingeless rotor blades in hover with pitch-link flexibility", AIAA Journal, Structural dynamics, and materials, May, (1976).

[97] D. H. Hodges, and R. A. Ormiston, "Stability of elastic bending and torsion of uniform cantilever rotor blades in hover with variable structural coupling", National Aeronautics and space Administration (NASA)/U.S. Army Air Mobility R&D Laboratory, April (1976).

[98] Greenberg, J. Mayo, "Airfoil in sinusoidal motion in a pulsating stream", MACA, (1947).

[99] Mahmuddin, Faisal, "Rotor blade performance analysis with Blade Element momentum theory", Vol. 105, May (2017), pp. (1123-1129). doi.org/10.1016/j.egypro.2017.03.477

[100] Humberto Peredo Fuentes and Manfred Zehn, “Application of the Craig-Bampton model order reduction method to a composite structure: MACco, COMAC, COMAC-S and eCOMAC”, Open Eng. (2016), Vol 6, pp. (185–198).

[101] F.L.M. dos Santos, B. Peeters, H. Van der Auweraer, L.C.S. Goes, W. Desmet., “Vibration-based damage detection for a composite helicopter main rotor blade”, Case Studies in Mechanical Systems and Signal Processing 3 (2016), pp. (22–27).

[102] T. Contursi, A. Messina, E. J. Williams, “A Multiple-Damage Location Assurance Criterion Based on Natural Frequency Changes”, Journal of Vibration and Control, 4: (1998), pp. (619-633).

[103] Marco A. Perez, Lluis Gil, Sergio Oller, “Impact damage identification in composite laminate using vibration testing, composite structures”, 108 (2014), pp 267-276.

[104] W. Heylen, S. Lammens, ”FRAC: A consistent way of comparing frequency response functions”, Belgian IUAP-50 programme.

A-II.- List of tables

A-III.- List of figures

A-IV.- List of equations

Type	Equation	Type	Equation
Earth's gravitational field	$g_e = 9.81\frac{N}{Kg}$	*L-shape arm's density*	$r_{Arm} = 7{,}850\frac{Kg}{m^3}$
Axial arm's length	$AAL = 0.1567\text{m} = 15.67cm$	*Radial arm's length*	$RAL = 0.235\text{m} = 23.5cm$
Axial arm's diameter	$D_{AAL} = 0.1\text{m} = 10cm$	*Radial arm's diameter*	$D_{RAL} = 0.15\text{m} = 15cm$
L-shape arm's volume	$Arm_{volume} = D_{AAL}{}^2 AAL + D_{RAL}{}^2 RAL = m^3$	*L-shape arm's mass*	$m_{Arm} = Arm_{Volume} r_{Arm}$
Piston's density	$r_{Piston} = 8{,}050\frac{Kg}{m^3}$	*Piston's radius*	$P_r = 0.025\text{m} = 2.5cm$
Piston's length	$P_L = 0.25\text{m} = 25cm$	*Piston's volume*	$P_{Volume} = pP_r^2 P_L = m^3$
Piston's mass	$m_{Piston} = P_{Volume} r_{Piston}$	*PL's mass*	$m_{PL} = m_P + m_{Arm}$
PL's linear length	$PL_{Length} = AAL + RAL + P_L$	*PL's mass distribution*	$M_{PL} = \frac{m_{PL}}{PL_{Length}}$
AAL weight segment	$W_{AAL} = M_{PL}\frac{AAL}{2}g_e = \frac{Kg}{m}\text{m}\frac{N}{Kg} = N$	*RAL weight segment*	$W_{RAL} = M_{PL}\frac{RAL}{2}g_e = \frac{Kg}{m}\text{m}\frac{N}{Kg} = N$
PL's weight segment	$W_{PL} = M_{PL} AAL g_e = \frac{Kg}{m}\text{m}\frac{N}{Kg} = N$	*Coupling pitch distance*	$e_P = e + \frac{C}{8} + \frac{C}{4}$

Equations 1.- Pitch Link L-shape arm's parameter and characteristic equations.

A-V.- List of nomenclature and symbols

δ = Variational operator,
t_1 = Initial interval from dynamic deflection,
t_2 = Final interval from dynamic deflection,
U = Kinetic energy,
$\Im$ = Potential energy,
W = Damping energy,
EI = Bending rigidity, [Nm^2].
GJ = Torsional rigidity, [Nm^2].
m = Mass per unit length, [Kg/m].
I_α = Polar mass moment of inertia per unit length about Y-axis, [Kgm].
x_α = Distance between centroid (Gs) to shear centre (Es) axis, [m].
H = Bending vertical displacement,
Ψ = Torsional angular deformation,
EI_1 = Bending rigidity about in plane axis (lead-lag), [Nm^2].
EI_2 = Bending rigidity about out of plane (flapping), [Nm^2].
GJ = Torsional rigidity, [Nm^2].
m = Mass per unit length, [Kg/m].
I_α = Polar mass moment of inertia per unit length about Y-axis, [Kgm].
x_a = Distance between elastic axis to mass axis, [m].
z_a = Distance between in-plane axis to mass axis, [m].
ω = Frequency of oscillation, [rad/s].
U = Lead-lag amplitudes of u,
W = Bending amplitudes of w,
Ψ = Torsional amplitudes of ψ,
T = Centrifugal force, [N].
kAG = Shear rigidity, [N].

ρ = Material density, [Kg/m^3].
ρA = Mass distribution, [Kg/m].
Ω = Constant rotational speed, [rad/s].
ω = Circular natural frequency of oscillation, [rad/s].
I_α = Mass moment of inertia about elastic axis, [m].
e_1, e_2 = Distance from center of flexure to centroid about Y and Z-axis, [m].
$I_{\eta\eta}$, $I_{\xi\xi}$ = Second moment of inertia about Y-axis and Z-axis, [m^4].
$I_{\xi\eta}$ = Polar moment of inertia about X-axis, [m^4].
$EI_{\xi\xi}$ = Bending rigidity about flap-wise deformations, [Nm^2].
$EI_{\eta\eta}$ = Bending rigidity about chord-wise deformations, [Nm^2].
$\bar{v}$ = Lead-lag bending displacement,
$\bar{w}$ = Flapping bending displacement,
$\bar{\Psi}$ = Torsional angle of deformation,
$\bar{\varphi}_y$ = Rotation angle due chord-wise bending,
$\bar{\varphi}_z$ = Rotation angle due flap-wise bending,
I_α = Mass moment of inertia about elastic axis, [Kgm].
e = Distance between centroid of cross section and elastic axis [m].
I_y = Second moment of inertia about Y-axis (in plane), [m^4].
I_z = Second moment of inertia about Z-axis (out of plane), [m^4].
w = Flapping bending displacement,
Ψ = Torsional angle of deformation,
φ = Rotation angle due to bending,
F_{spring} = Restoring force, [N].
K_{spring} = Spring stiffness, [N/m].
x_{spring} = Spring deformation, [m].
$RAL,\ AAL$ = Radial and Axial arm length, [m].
W_{RAL}, W_{AAL}, W_{PL} = Force acting through centre of gravity of RAL, AAL, and PL, [N].
F_{PL} = Total Pitch Link force, [N].
V = Volume of the hydraulic fluid, [m^3].
A = Area of piston ram, [m^2].
C_P = Capacitance of hydraulic fluid, [m^3/Pa].
P = Pressure of the hydraulic fluid, [MPa].
m_{PL} = Mass of the Pitch Link (Arm + Piston), [Kg].
C_D = Damping constant of the elastomer, [Ns/m].
K_{PL} = Stiffness of the elastomer, [N/m].
x_{PL} = Total Pitch Link arm deformation, [m].
$\dot{x}_{PL}$ = Pitch Link arm velocity, [rad/s].
$\ddot{x}_{PL}$ = Pitch Link arm acceleration, [rad/s^2].
g_e = Earth's gravitational constant, [m/s^2].
e_P, e_{I1}, e_{I2}, e_{I3} = Coupling distances for torque per segment due to ice, [m].
Δ_{Ice1}, Δ_{Ice2}, Δ_{Ice3} = Proportional gradient factors related to ice formation, [-].
m_{I1}, m_{I2}, m_{I3} = Mass per segment due to ice, [Kg].
W_{I1}, W_{I2}, W_{I3} = Gravitational weights per segments, [N].
$x_{(n)}$ = Tip's thickness of ice layer, [m].
dx = Axial length of body of ice, [m].
$m_{I(n)}$ = Mass of the body of ice, [Kg].
$V_{I(n)}$ = Volume of the body of ice, [m^3].
ρ_{Ice} = Density of the body of ice, [Kg/m^3].
$F_{Co(n)}$ = Cohesion force, [N].
AC_{Ice} = Cohesion surface or area of contact, [m^2].

σ = Cohesive ice strength, [m^2].
$F_{Ad(n)}$ = Shear adhesion force, [N].
τ = Shear adhesion strength, [kPa].
$S_{contact}dx$ = Volume of the body of ice, [m^3].
$F_{Ce(n)}$ = Centrifugal force, [N].
$Lift_{Healthy}$, $Drag_{Healthy}$ = Lift and drag healthy forces, [N].
$Lift_{Ice}$, $Drag_{Ice}$ = Lift and drag reduced forces due Ice damage, [N].
V_{eff} = Effective velocity of the airfoil, [rad/s].
V' = Reduced wind speed of the rotor, [rad/s].
α = Angle of attack,
Ω = Angular velocity of the rotor, [rad/s].
F_{Ice} = Aerodynamic force acting on the leading edge, [N].
C, $C_{(n)}$ = Healthy and re-updated chord (width) on the beam section, [m].
e, $x_{(n)}$ = Healthy and re-updated distance due ice (mass to elastic axis), [m].
$Height_{AL}$, $Height_{Ice(n)}$ = Healthy and re-updated height on beam section due ice, [m].
$Length_{beam}$,$Length_{Ice}$ = Healthy and re-updated length on beam section due ice, [m].
$Area_{AL}$, $Area_{Ice(n)}$ = Healthy and re-updated cross-sectional area of airfoil due ice, [m^2].
ρ_{AL}, ρ_{Steel} = Density of Aluminium and Steel, [Kg/m^3].
Ma, $Ma_{I(n)}$ = Healthy and re-updated mass distribution due ice, [Kg/m].
$I_{\alpha AL}$, $I_{\alpha Ice(n)}$ = Healthy and re-updated mass moment of inertia due ice, [Kgm].
E_{AL}, E_{Ice} = Aluminium and Steel's youngs modulus, [Kgf/m^2].
I_{y-AL}, $I_{y-Ice(n)}$ = Healthy and re-updated second moment of inertia due ice, [m^4].
G_{AL}, G_{Ice} = Aluminium and Steel's shear modulus, [Kgf/m^2].
J_{AL}, $J_{Ice(n)}$ = Healthy and re-updated torsional constants due ice, [m^4].
e_1, e_2 , e_3 = Distances of rotation to the force points per Steel's strip, [m].
W_{I1}, W_{I2} , W_{I3} = Gravitational forces of each Steel's strip studied cases, [N].
BC_{T1}, BC_{T2} , BC_{T3} = Boundary conditions for the torsional moments, [Nm].
U_p = Perpendicular velocity component, [rad/s^2].
U_T = Tangential velocity component, [rad/s^2].
U_∞ = Free stream velocity, [rad/s^2].
θ = Built-in pitch angle,
γ = Induced inflow angle,
α = Effective angle of attack,
dL = Lift force, [N].
dD = Drag force, [N].
dr = Blade Element length, [m].
ρ_∞ = Free stream density, [Kg/m^3].
a = Lift curve slope,
c = Chord length, [m].
C_1 = Sectional lift coefficient,
C_d = Sectional drag coefficient,
dR_F = Resultant force, [N].
dF_Z = Vertical force, [N].
dF_Y = In-plane force, [N].
V_i = Induced inflow velocity, [rad/s^2].
V_c = Climbing velocity, [rad/s^2].

A-VI.- Resume

MECHANICAL ENGINEER WITH A MASTER DEGREE IN BOTH MATERIALS SCIENCE AND AEROSPACE ENGINEERING

Name: Agustín De Jesús Gaxiola Peralta.

[redacted]

[redacted] ag14465@bristol.ac.uk , [redacted]

EDUCATION

2014-2018 M.Sc. by Research in Aerospace Engineering, University of Bristol, Bristol, England, United Kingdom.
Thesis topic: An experimental-modeling Pitch Link formulation for an induced ice damaged blade and its usage in the vibration-based rotorcraft-blade health monitoring.

2010-2012 Master Degree in Materials Science Qualified, Instituto Tecnológico de Saltillo, Saltillo, Coahuila, México.
Thesis topic: Analysis of mechanical and corrosion properties in irons joined by TIG and subsequently heat treated.

2004-2009 Mechanical Engineer Qualified, Instituto Tecnológico de Culiacán, Culiacán, Sinaloa, México.
Thesis topic: Development of a predictive maintenance program focused on vibration analysis in a hydroelectric plant.

LANGUAGE

Russian (Knowledge on the technical and daily basis words). University of Bristol Level 1 Grade 1 - Ab initio, "2017".
English (Score and IELTS test date: 6.0 overall band score), "7th June of 2014".

WORK EXPERIENCE

Hourly Paid Teaching Sessions during the academic year 2016/2017, working in the Aerospace Engineering subject Vibration 2, under the diverse assigned activities for the Experimental (Tuned Vibration Absober "TVA" tested on an Airfoil wing-rig) and Computational (Coding scripts in Matlab software to solve in an automated way many vibrational problems on structural dynamic systems) Laboratory tasks, University of Bristol, Bristol, England, United Kingdom, "February to March of 2017", (2 Months).

Weekly Inspection for defect, management and inventory of "small and medium models" transmission case batches inside of GLOVIS warehouse in Opelika, Alabama, United States of America (USA). Followed by a daily shipment of these Al-Si alloy castings for the machining-assembly process into the Tucson, Santa Fe, Elantra and Sonata models, running activities such like surface analysis after high pressure deburr process, leak behaviors on oil and lubrication lines and all the quality affairs related to functionality of the casting. Power Tech America, West Point, Georgia, United States of America (USA), "January to February of 2014", (5 Weeks).

Engineer process in Hyundai Motor Company Aluminum Die Casting plant; Working in area of high and low pressure die casting machines plus running the machining center lines of transmission cases, block and head cylinders, tool pre-setting and inventory, leak test machines, post-heat treatments of castings, mould maintenance and as well the impregnation process, Tijuana, Baja California, México, "June of 2013 to March of 2014", (9 Months).

Professional internship as a practicing and assistant in the development of a program of predictive maintenance focused on the mechanical vibration in pumps, compressors and turbines, in the hydroelectric power station, "Gral. Salvador Alvarado" of Comisión Federal de Electricidad, Sanalona, Culiacán, Sinaloa, México, "January to June of 2009", (5 Months).

Social service performed in the Government Palace of the state in Culiacán, Sinaloa, México. Performing activities as assistant in the programs of corrective and preventive maintenance of machinery type chillers in the area of refrigeration and air condition, "February to August of 2008", (5 Months).

PROFESSIONAL OBJECTIVE

My professional interest is to demonstrate my skills and develop myself by contributing knowledge in productive environments with labor guidelines. I find myself with a great energy and available to work, participate, get involved and earn my life with effort feeling that I am a part of the recent and technology industry.

SKILLS AND KNOWLEDGE

Computational modelling on any helicopter rotor-pitched-blade systems, the analysis of the blade aerodynamic profile under the rotating frame of reference and a quasi-steady non-rotating reference. The interpretation of the rotorcraft blade mode shapes and its usage in the damage detection techniques. Experimental testing on blade-like rigs and modal analysis with Helicopters approaches (blade damaged, Pitch-Link damage and Ice Accretion on blades). Metallurgical knowledge theoretical and practical on cast iron alloys, Steel alloys and non-ferrous alloys of the aluminum. Load preparations, modifying and refining of structure, molding methods, casting and feeding systems (high pressure die casting, gravity semi-permanent mold, investment casting and cosworth). Besides joining processes such like welding by GTAW (Gas tungsten arc welding), thermal treatments (annealing, normalizing, austempered, quenching, solubilized and aged), the properties of corrosion resistance (Interpretation of potentiodynamic polarization curves) and mechanical properties (Tensile and bending tests). Mechanical vibrations analysis due to features on components.

MANAGEMENT SOFTWARE

Matlab, Math Type, Autodesk Fusion 360, Maple, Minitab, Sigma Plot, Adobe Photoshop, Solidworks, Microsoft Office. Familiar with programs related to materials analysis: Scanning-Transmission electron microscopy and X-ray diffraction.

PUBLICATIONS AND CONFERENCES

Presentation titled “Pitch Link-induced beam bending-twist coupling and its use in vibration-based rotor health monitoring”, presented at the Vertical Lift Network (VLN) 2nd Annual technical workshop an initiative funded by Engineering and Physical Sciences Research Council (EPSRC), Shirgley Hall, Macclesfield, England, United Kingdom, “9th - 10th May of 2016”.

Article titled as “Effects of welding conditions by TIG and post weld heat treatment in ductile cast iron on the corrosion resistance”, Materials Science Forum, Volume 755, Pages 21-27, Trans Tech Publications, Switzerland, “April of 2013”.

Certificate of presenting for the contribution of “Effects of welding conditions by TIG and post weld heat treatment in ductile cast iron on the corrosion resistance”, in the Structural and Chemical Characterization of Metals Alloys and Compounds Symposium at the “XXI International Materials Research Congress” held in Cancun, Quintana Roo, México, “12th - 16th August of 2012”.

Recognition for the participation as speaker of the work entitled “Efecto de las condiciones de soldadura TIG en hierros nodulares sobre la resistencia a la corrosion en una solución de 3.5% NaCl” assigned in the board table “Ingenierías y Tecnologías”, Aguascalientes, Aguascalientes, México, “May of 2012”.

Recognition by the authoring and presentation of the poster entitled “Análisis de soldabilidad de hierros nodulares mediante soldadura por arco eléctrico”, “13ª feria de posgrados” organized for “Consejo Nacional de Ciencia y Tecnología” (CONACyT), in Ensenada, Baja California, Toluca, Estado de México and Mérida,Yucatan, “March of 2012”.

COURSES

3rd United Kingdom Vertical Lift Network (UKVLN) training event: “Introduction to Rotorcraft Handling Qualities and Flight Simulation”, University of Liverpool, Liverpool, England, United Kingdom, “23th June of 2016”.

2nd United Kingdom Vertical Lift Network (UKVLN) training event: “Introduction to Rotorcraft Performance, Stability and Control”, University of Manchester, Manchester, England, United Kingdom, “11th - 12th February of 2016”.

Hourly Paid Teaching (HPT) training and induction sessions for postgraduate students who undertake teaching as “Lab Demonstrator - Small Group Teaching” in academic year 2016/2017, University of Bristol, Bristol, England, United Kingdom, “3rd February of 2016”.

1st United Kingdom Vertical Lift Network (UKVLN) training event: “Introduction to Rotorcraft”, University of Glasgow, Glasgow, Scotland, United Kingdom, “5th - 6th November of 2015”.

Recognition by the valuable participation in the “7 Seminario de Fundición”, organized by Capitulo Estudiantil de la Sociedad Mexicana de Fundidores del Instituto Tecnológico de Saltillo (ITS), Saltillo, Coahuila, México, “April of 2012”.

Harmon Hall Diploma for successfully completing the four levels of the adult course, achieving a B1/B2 level on the common European Framework of Reference for Languages, Saltillo, Coahuila, México, “November of 2011”.

Recognition by the valuable participation in the “6 Seminario de Fundición”, organized by Instituto Tecnológico de Saltillo (ITS), Coahuila, México, “April of 2011”.

Recognition by the participation in the “32 Congreso Internacional de Metalurgia y Materiales”, organized by Instituto Tecnológico de Saltillo (ITS), Saltillo, Coahuila, México, “October of 2010”.

Diploma, Autocad 2006 edition, Modelling and computing course of 30hrs, taken at the Instituto Tecnológico de Culiacán (ITC), Culiacán, Sinaloa, México, “December of 2007”.

Recognition by the participation in the “20 Congreso Internacional de Ingeniería Mecánica”, Instituto Tecnológico y de Estudios Superiores de Monterrey (ITESM), Monterrey, Nuevo León, México, “October of 2007”.

Recognition by the participation in the “19 Congreso Internacional de Ingeniería Mecánica”, Instituto Tecnológico y de Estudios Superiores de Monterrey (ITESM), Monterrey, Nuevo León, México, “October of 2006”.

A-VII.- Compilation of computational model code scripts

MBB Bo-105 Quasi-Steady Aerodynamics on Ice accretion (Harmonic Analysis)

```
function RotaHeliBeamAeroElasticMBBB0105Ice
disp(' - RotaHeliBeamAeroElasticMBBB0105Ice - ')
load ABC4.mat kPL1 kf1 DC1 OMEGAR Wn NumOmega; load MICE2.mat I2; % load UNC.mat MB GJ EI
B1=0.0013; B2=0.0630; B3=0.2332; B4=0.2456; B5=0.4912; B6=0.7368;
B7=0.9822;B8=1.2278;B9=1.4734;B10=1.7190;B11=1.9646;B12=2.2102;B13=2.5066;B14=2.7012;B15=2.9468;B16=3.1924;B17=3.4385;  Cx=0;  Cz=0;  Cy=1;
B18=3.6905;B19=3.9293;B20=4.1747;B21=4.4272;B22=4.6660;B23=4.8362;B24=4.9120;uR=0;ur=0.2456;uF=B24;C=0.27026;Z=0.298*C;I1=0.001*1;
CI=C+(2.5*I1*Cz);ZI=0.298*CI;T1=.127*CI;C2=C+(2.5*I2*Cy);Z2=0.298*C2;T2=.127*C2;
 B=[B1 B2-B1 B3-B2 B4-B3 B5-B4 B6-B5 B7-B6 B8-B7 B9-B8 B10-B9 B11-B10 B12-B11 B13-B12 B14-B13 B15-B14 B16-B15 B17-B16 B18-B17 B19-B18 B20-B19
B21-B20 B22-B21 B23-B22 B24-B23]; DI=934; O=2*pi;
  R=[2600+((2600*(I1/100))*Cx)                                  2600+((2600*(I1/100))*Cx)                                  2600+((2600*(I1/100))*Cx)
     2600+((2600*(I1/100))*Cz)                                  2600+((934*(1-((I2*I2)+(I2/(2.5*((C+I2)/4)))+(I2/(5*((C+I2)/8))))))*Cy)];
  G=[(10.667567e8/(2*(1+0.33)))                                 (10.667567e8/(2*(1+0.33)))                                 (10.667567e8/(2*(1+0.33)))
     (10.667567e8/(2*(1+0.33)))                                 (10.667567e8/(2*(1+0.33)))];
 Bc=[B(1)                                                       B(2)                                                       B(3)+B(4)
     B23-(B(1)+B(2)+B(3)+B(4))                                  B24-B23];
 eG=[0                                                          0.0170                                                     0.0091
     0.0003                                                     0];
 eS=[0+((2.5*I1)*Cx)                                            0+((2.5*I1)*Cx)                                            0+((2.5*I1)*Cx)
     .0189+((2.5*I1)*Cz)                                        0+((2.5*I2)*Cy)];
 SC=[eG(1)+eS(1)                                                eG(2)+eS(2)                                                eG(3)+eS(3)
     eG(4)+eS(4)                                                eG(5)+eS(5)                                                ]; Xa=((C2/4)+(C2/8)+(SC(5)));
 MB=[0.139995                                                   0.139995                                                   0.149995
     0.010995                                                   0.010995]*(4.448222161526*0.45359237);
MI1=[((((((C/4)+(ZI/2))/2)*pi/2)*Bc(1)*(2.5*I1))*DI)*Cx        ((((((C/4)+(ZI/2))/2)*pi/2)*Bc(2)*(2.5*I1))*DI)*Cx
((((((C/4)+(ZI/2))/2)*pi/2)*Bc(3)*(2.5*I1))*DI)*Cx                                                                        ...
     ((((((CI/4)+(ZI/2))/2)*pi/2)*Bc(4)*(2.5*I1))*DI)*Cz       ((((((C2/4)+(Z2/2))/2)*pi/2)*Bc(5)*(2.5*I2))*DI)*Cy];
MI2=[((2*((C/8)*Bc(1)*(I1/2.5)))*DI)*Cx                        ((2*((C/8)*Bc(2)*(I1/2.5)))*DI)*Cx
((2*((C/8)*Bc(3)*(I1/2.5)))*DI)*Cx                                                                                       ...
     ((2*((CI/8)*Bc(4)*(I1/2.5)))*DI)*Cz                       ((2*((C2/8)*Bc(5)*(I2/2.5)))*DI)*Cy];
MI3=[((2*((SC(1))*Bc(1)*(I1/5)))*DI)*Cx                        ((2*((SC(2))*Bc(2)*(I1/5)))*DI)*Cx
((2*((SC(3))*Bc(3)*(I1/5)))*DI)*Cx                                                                                       ...
     ((2*((SC(4))*Bc(4)*(I1/5)))*DI)*Cz                        ((2*((SC(5))*Bc(5)*(I2/5)))*DI)*Cy];
DI1=[(SC(1)+(C/8)+((C/4)/2))*Cx                                (SC(2)+(C/8)+((C/4)/2))*Cx                                    (SC(3)+(C/8)+((C/4)/2))*Cx
     (SC(4)+(CI/8)+((CI/4)/2))*Cz                              (SC(5)+(C2/8)+((C2/4)/2))*Cy];
DI2=[(SC(1)+((C/8)/2))*Cx                                      (SC(2)+((C/8)/2))*Cx                                       (SC(3)+((C/8)/2))*Cx
     (SC(4)+((CI/8)/2))*Cz                                     (SC(5)+((C2/8)/2))*Cy];
DI3=[(SC(1)/2)*Cx                                              (SC(2)/2)*Cx                                               (SC(3)/2)*Cx
     (SC(4)/2)*Cz                                              (SC(5)/2)*Cy];
  M=[(MB(1)+(MI1(1)+MI2(1)+MI3(1)))/Bc(1)                      (MB(2)+(MI1(2)+MI2(2)+MI3(2)))/Bc(2)
(MB(3)+(MI1(3)+MI2(3)+MI3(3)))/Bc(3)                                                                                      ...
     (MB(4)+(MI1(4)+MI2(4)+MI3(4)))/Bc(4)                      (MB(5)+(MI1(5)+MI2(5)+MI3(5)))/Bc(5)];
 MA=[sum(M(1)+M(2)+M(3)+M(4)+M(5))                             sum(M(1)+M(2)+M(3)+M(4)+M(5))                              sum(M(1)+M(2)+M(3)+M(4)+M(5))
     sum(M(1)+M(2)+M(3)+M(4)+M(5))                             sum(M(1)+M(2)+M(3)+M(4)+M(5))];
IP=[(((M(1)/12)*((0.298*(.2+((2.5*I1)))).^2+(.2).^2))+(M(1)*SC(1).^2))+(((MI1(1)*DI1(1).^2)+(MI2(1)*DI2(1).^2)+(MI3(1)*DI3(1).^2)))
... (((M(2)/12)*((0.298*(.2+((2.5*I1)))).^2+(.2).^2))+(M(2)*SC(2).^2))+(((MI1(2)*DI1(2).^2)+(MI2(2)*DI2(2).^2)+(MI3(2)*DI3(2).^2)))
    (((M(3)/12)*( Z.^2+ C.^2))+(M(3)*SC(3).^2))+((MI1(3)*DI1(3).^2)+(MI2(3)*DI2(3).^2)+(MI3(3)*DI3(3).^2))
    (((M(4)/12)*(ZI.^2+CI.^2))+(M(4)*SC(4).^2))+((MI1(4)*DI1(4).^2)+(MI2(4)*DI2(4).^2)+(MI3(4)*DI3(4).^2))
    (((M(5)/12)*(Z2.^2+C2.^2))+(M(5)*SC(5).^2))+((MI1(5)*DI1(5).^2)+(MI2(5)*DI2(5).^2)+(MI3(5)*DI3(5).^2))];
 IF=[0.0000001                                                 0.0000001                                                  0.0000001
     0.0000001                                                 0.0000001]*0;
 IL=[0                                                         0                                                          0.0040
     0.00060                                                   (0.036*C2*Z2*(((Z2).^2)+((T2).^2)))];                      % .0011 .0011 ...
 GJ=[1.1998e3                                                  1.1998e3                                                   1.1969e3
     0.4448e3                                                  (((16/3)-((3.36*Z2/(C2))*(1-(Z2.^4/12*(C2).^4))))*((C2)*Z2.^3))*G(5)]; % .5454e3 .5454e3 ...
 EI=[2.4874e7                                                  0.5882e7                                                   0.0404e7
     0.0070e7                                                  (0.036*C2*Z2*(((Z2).^2)+((T2).^2)))*(G(5)*(2*(1+.33)))]; % .0103e7 .0103e7 ...
kAG=[M(1)*G(1)/R(1)                                            M(2)*G(2)/R(2)                                             M(3)*G(3)/R(3)
     M(4)*G(4)/R(4)                                            M(5)*G(5)/R(5)]*(0.8509);
%Airfoil lift curve slope[2pi/rad] Blades[-] Built-in pitch angle[rad] Air density[kg/m^3] Equilibrium elastic twist[rad] drag coefficient[-]
a=2*pi;                                 b=4;      Theta=0;                Rair=1.8139;        phi0=0;                                Cd=.045; Ci=.54; CR=1;
% Structural offset[m]                                 Axial and radial arm distance[m] FRF features[-] APL1=.2255-.1; APL2=.2255; PL stiffness[N/m]
 PL=0.0630;PL1=((ur*0.25)+0.235)-0.02;PL2=0.2456; AAL=(PL2-PL);RAL=(PL2-PL)*2.5;PF=1;M1=PF*PL2;M2=PF*((C/4)+(C/8)+SC(3));LD1=0.0630;
PLd=7850;  PLv=(.1).^2*(AAL+RAL); Ge=9.81; Pv=pi*0.06^2*0.3; Wpl=(Pv*8050/0.3)*Ge; PLf=(PLv*PLd); PLm=(PLf+(Pv*8050))/(AAL+RAL+.3); WPL=PLm*Ge;
WAAL=(PLf/AAL)*Ge; WRAL=(PLf/RAL)*Ge;
 CV=101971.62; Ap0=pi*((0.0381).^2); PpO=1.5; Pd0=PpO*CV; Cp0=1.7e-11;
eP3=(C/4)+(C/8)+SC(3);Cd3=(C/2)+(Z/2)+RAL+eP3;eP4=(C/4)+(C/8)+SC(4);Cd4=(C/2)+(Z/2)+RAL+eP4;
OMEGA=linspace(0,Wn*O,NumOmega); F11=1.123*OMEGAR;F12=2.78*OMEGAR;To1=3.176*OMEGAR;F13=5.097*OMEGAR;To2=6.349*OMEGAR;F14=7.537*OMEGAR;
for Omega_number=NumOmega:-1:1
if rem(Omega_number,100)==0
   fprintf(' - Podozhdite, Bertolet letit pryama seichaz - Gotov b    =    %d-%d\n',Omega_number,NumOmega)
end
   Omega=OMEGA(Omega_number); N1=11;N2=11;N3=11;N4=11; n1=linspace(1,10,10);n2=linspace(1,10,10);n3=linspace(1,10,10);n4=linspace(1,10,10);
is_PL=true; is_FH=true;
      Q1=B(1);        Q2=Q1+B(2);     Q3=Q2+B(3);     Q4=Q3+B(4);     Q5=Q4+B(5);     Q6=Q5+B(6);     Q7=Q6+B(7);     Q8=Q7+B(8);
Q9=Q8+B(9);    Q10=Q9+B(10);   Q11=Q10+B(11);  Q12=Q11+B(12);
     Q13=Q12+B(13);  Q14=Q13+B(14);  Q15=Q14+B(15);  Q16=Q15+B(16);  Q17=Q16+B(17);  Q18=Q17+B(18);  Q19=Q18+B(19);  Q20=Q19+B(20);
Q21=Q20+B(21);  Q22=Q21+B(22);  Ice=Q22+B(23);
solinit1=bvpinit([uR,B(1)*(n1/N1)/1.05,Q1,Q1,Q1+LD1*(n1/N1)/1.05,LD1,LD1,LD1+PL2*(n2/N2)/1.3,PL2,PL2,PL2+Q5*(n3/N3)/2,Q5,Q5+B(6)*n3/N3,Q6,Q6+B(7
)*n3/N3,Q7,Q7+B(8)*n3/N3,Q8, ...
Q8+B(9)*n3/N3,Q9,Q9+B(10)*n3/N3,Q10,Q10+B(11)*n3/N3,Q11,Q11+B(12)*n3/N3,Q12,Q12+B(13)*n3/N3,Q13,Q13+B(14)*n3/N3,Q14,Q14+B(15)*n3/N3,Q15,Q15+B(16
)*n3/N3,Q16, ...
Q16+B(17)*n3/N3,Q17,Q17+B(18)*n3/N3,Q18,Q18+B(19)*n3/N3,Q19,Q19+B(20)*n3/N3,Q20,Q20+B(21)*n3/N3,Q21,Q21+B(22)*n3/N3,Q22,Q22+B(23)*(n3/N3)/2,Ice,
Ice,Ice+B(24)*(n4/N4),uF],[0,0,0,0,0,0,0]);
          options1=bvpset('stats','off','RelTol',1e-3,'NMax',floor(258/3));
              sol1=BVP4c(@fcn_odel,@fcn_bcl,solinit1,options1);
              hij2=sol1.y([1 2 3 4 5 6]./1,end); hijacc2=(-Omega).^2*hij2; hijaccv2=hijacc2*(1019.4/11.2);
        hijaccvo2b=hijaccv2(1); hijaccv2(1)=hijaccvo2b;
       hijaccvo2bt=hijaccv2(3); hijaccv2(3)=hijaccvo2bt;
        hijaccvo2t=hijaccv2(5); hijaccv2(5)=hijaccvo2t;
Ha(:,Omega_number)=[Omega;hijaccv2]; Ia{1,Omega_number}=sol1.x; Ia{2,Omega_number}=sol1.y;
end
for     nX=NumOmega:-1:1
BeN1{1,nX}=(real(Ia{2,nX}(1,:))./max(abs(real((Ia{2,nX}(1,:))))))./((max([max(abs(real(Ia{2,nX}(1,:)))),max(abs(real(Ia{2,nX}(3,:)))),max(abs(re
al(Ia{2,nX}(5,:))))])));  BeN1(:);
RoN1{1,nX}=(real(Ia{2,nX}(3,:))./max(abs(real((Ia{2,nX}(3,:))))))./((max([max(abs(real(Ia{2,nX}(1,:)))),max(abs(real(Ia{2,nX}(3,:)))),max(abs(re
al(Ia{2,nX}(5,:))))])));  RoN1(:);
ToN1{1,nX}=(real(Ia{2,nX}(5,:))./max(abs(real((Ia{2,nX}(5,:))))))./((max([max(abs(real(Ia{2,nX}(1,:)))),max(abs(real(Ia{2,nX}(3,:)))),max(abs(re
al(Ia{2,nX}(5,:))))])));  ToN1(:);
end
for m=NumOmega:-1:1
H1a=[real(Ia{1,m}(1,:));[((real(BeN1{1,m}))./(max(abs(real(BeN1{1,m})))));((real(RoN1{1,m}))./(max(abs(real(RoN1{1,m})))));(((real(ToN1{1,m}))./
(max(abs(real(ToN1{1,m}))))).*Xa)]]; H1b(:,m)=H1a;
end
HAIFRF=(figure('units','normalized','outerposition',[0 0 1 1],'userdata',{H1b,OMEGA},'visible','off'));subplot(6,1,[1 2 3 4 5 6]); grid on,grid
minor,box on,axis on,set(gca,'FontSize', 35);hold on,
plot(Ha(1,:)./O,real(log10(abs(Ha(2,:)))),'r.-','linewidth',2);hold on,plot(Ha(1,:)./O,real(log10(abs(Ha(4,:)))),'g.-
','linewidth',2);plot(Ha(1,:)./O,real(log10(abs(Ha(6,:)))),'b.-','linewidth',2);hold on,
line([Fl1,Fl1]./(2*pi),get(gca,'ylim'),'Color','r','linestyle','--','linewidth',2);
line([Fl2,Fl2]./(2*pi),get(gca,'ylim'),'Color','r','linestyle','--','linewidth',2);
line([To1,To1]./(2*pi),get(gca,'ylim'),'Color','b','linestyle','--','linewidth',2);
line([Fl3,Fl3]./(2*pi),get(gca,'ylim'),'Color','r','linestyle','--','linewidth',2);
line([To2,To2]./(2*pi),get(gca,'ylim'),'Color','b','linestyle','--','linewidth',2);
line([Fl4,Fl4]./(2*pi),get(gca,'ylim'),'Color','r','linestyle','--','linewidth',2);
```

```
xlabel('Frequency domain range, [Hz]');ylabel('Response amplitude, [m/s^2/N]');legend('Bending','Angle','Torsion','Location','ne');
save RotaHeliBeamAeroElasticMBBB0105Ice MB GJ EI Ha Hlb HAIFRF C2 Xa
function dydx=fcn_odel(x,y,region)
         dydx=zeros(6,1); dydx(1)=y(2); dydx(3)=y(4); dydx(5)=y(6);
for n=5:-1:1
   switch region
         case n                                                          % Vi = Induce inflow velocities
 Cs=[C C C CI C2];   BA1=[Q1 LD1 PL2 Ice uF];
 Vi=[(-
((OMEGAR*Q1)*((((sign(Theta+(phi0*(0.75*Q1))))*(OMEGAR*Q1))*((pi*((b*C)/(pi*Q1)))/8))*(sqrt(1+(12/(pi*((b*C)/(pi*Q1))))*(abs(Theta+(phi0*(0.75*Q
1)))))-1))) ...
+(((OMEGAR.^2)*(Q1.^2))*(Theta+y(5)))+((OMEGAR.^2)*Q1*(((Cs(1)*cos(Theta))+((0.298*Cs(1)/2)*sin(Theta)))+(y(1)+(Cs(1)*cos(Theta+y(5)))+((0.298*C
s(1)/2)*sin(Theta+y(5)))))*(y(2)-y(3))) ...
       +((OMEGAR.^2)*((Q1*C)/2)*y(2))-((1i*Omega)*(OMEGAR*Q1)*y(1))+((1i*Omega)*((3/4)*C*OMEGAR*Q1)*y(5))-(((1i*Omega).^2)*(C/4)*y(1))) ...
      (-
((OMEGAR*LD1)*((((sign(Theta+(phi0*(0.75*LD1))))*(OMEGAR*LD1))*((pi*((b*C)/(pi*LD1)))/8))*(sqrt(1+(12/(pi*((b*C)/(pi*LD1))))*(abs(Theta+(phi0*(0
.75*LD1)))))-1))) ...
+(((OMEGAR.^2)*(LD1.^2))*(Theta+y(5)))+((OMEGAR.^2)*LD1*(((Cs(2)*cos(Theta))+((0.298*Cs(2)/2)*sin(Theta)))+(y(1)+(Cs(2)*cos(Theta+y(5)))+((0.298
*Cs(2)/2)*sin(Theta+y(5)))))*(y(2)-y(3))) ...
       +((OMEGAR.^2)*((LD1*C)/2)*y(2))-((1i*Omega)*(OMEGAR*LD1)*y(1))+((1i*Omega)*((3/4)*C*OMEGAR*LD1)*y(5))-(((1i*Omega).^2)*(C/4)*y(1))) ...
      (-
((OMEGAR*PL2)*((((sign(Theta+(phi0*(0.75*PL2))))*(OMEGAR*PL2))*((pi*((b*C)/(pi*PL2)))/8))*(sqrt(1+(12/(pi*((b*C)/(pi*PL2))))*(abs(Theta+(phi0*(0
.75*PL2)))))-1))) ...
+(((OMEGAR.^2)*(PL2.^2))*(Theta+y(5)))+((OMEGAR.^2)*PL2*(((Cs(3)*cos(Theta))+((0.298*Cs(3)/2)*sin(Theta)))+(y(1)+(Cs(3)*cos(Theta+y(5)))+((0.298
*Cs(3)/2)*sin(Theta+y(5)))))*(y(2)-y(3))) ...
       +((OMEGAR.^2)*((PL2*C)/2)*y(2))-((1i*Omega)*(OMEGAR*PL2)*y(1))+((1i*Omega)*((3/4)*C*OMEGAR*PL2)*y(5))-(((1i*Omega).^2)*(C/4)*y(1))) ...
      (-
((OMEGAR*Ice)*((((sign(Theta+(phi0*(0.75*Ice))))*(OMEGAR*Ice))*((pi*((b*CI)/(pi*Ice)))/8))*(sqrt(1+(12/(pi*((b*CI)/(pi*Ice))))*(abs(Theta+(phi0*
(0.75*Ice)))))-1))) ...
+(((OMEGAR.^2)*(Ice.^2))*(Theta+y(5)))+((OMEGAR.^2)*Ice*(((Cs(4)*cos(Theta))+((0.298*Cs(4)/2)*sin(Theta)))+(y(1)+(Cs(4)*cos(Theta+y(5)))+((0.298
*Cs(4)/2)*sin(Theta+y(5)))))*(y(2)-y(3))) ...
       +((OMEGAR.^2)*((Ice*CI)/2)*y(2))-((1i*Omega)*(OMEGAR*Ice)*y(1))+((1i*Omega)*((3/4)*CI*OMEGAR*Ice)*y(5))-(((1i*Omega).^2)*(CI/4)*y(1))) ...
      (-
((OMEGAR*uF)*((((sign(Theta+(phi0*(0.75*uF))))*(OMEGAR*uF))*((pi*((b*C2)/(pi*uF)))/8))*(sqrt(1+(12/(pi*((b*C2)/(pi*uF))))*(abs(Theta+(phi0*(0.75
*uF)))))-1))) ...
+(((OMEGAR.^2)*(uF.^2))*(Theta+y(5)))+((OMEGAR.^2)*uF*(((Cs(5)*cos(Theta))+((0.298*Cs(5)/2)*sin(Theta)))+(y(1)+(Cs(5)*cos(Theta+y(5)))+((0.298*C
s(5)/2)*sin(Theta+y(5)))))*(y(2)-y(3))) ...
       +((OMEGAR.^2)*((uF*C2)/2)*y(2))-((1i*Omega)*(OMEGAR*uF)*y(1))+((1i*Omega)*((3/4)*C2*OMEGAR*uF)*y(5))-(((1i*Omega).^2)*(C2/4)*y(1)))];
 A1=[(Rair*a*Cs(1)/2)*Vi(1) (Rair*a*Cs(2)/2)*Vi(2) (Rair*a*Cs(3)/2)*Vi(3) (Rair*a*Cs(4)/2)*Vi(4) (Rair*a*Cs(5)/2)*Vi(5)];
 A3=[(-(1i*Omega)*((Rair*a*Cs(1))/2)*((Cs(1).^2/4)*OMEGAR*Q1*y(5)))  (-(1i*Omega)*((Rair*a*Cs(2))/2)*((Cs(2).^2/4)*OMEGAR*LD1*y(5))) ...
      (-(1i*Omega)*((Rair*a*Cs(3))/2)*((Cs(3).^2/4)*OMEGAR*PL2*y(5))) (-(1i*Omega)*((Rair*a*Cs(4))/2)*((Cs(4).^2/4)*OMEGAR*Ice*y(5))) ...
      (-(1i*Omega)*((Rair*a*Cs(5))/2)*((Cs(5).^2/4)*OMEGAR*uF*y(5)))];
C1X=[((-(1i*Omega)*(2*R(1)*IL(1)*OMEGAR)*y(5))*CR)  ((-(1i*Omega)*(2*R(2)*IL(2)*OMEGAR)*y(5))*CR)  ((-(1i*Omega)*(2*R(3)*IL(3)*OMEGAR)*y(5))*CR)
      ((-(1i*Omega)*(2*R(4)*IL(4)*OMEGAR)*y(5))*CR)  ((-(1i*Omega)*(2*R(5)*IL(5)*OMEGAR)*y(5))*CR)];
C2X=[((+(1i*Omega)*(2*R(1)*IL(1)*OMEGAR)*y(3))*CR)  ((+(1i*Omega)*(2*R(2)*IL(2)*OMEGAR)*y(3))*CR)  ((+(1i*Omega)*(2*R(3)*IL(3)*OMEGAR)*y(3))*CR)
      ((+(1i*Omega)*(2*R(4)*IL(4)*OMEGAR)*y(3))*CR)  ((+(1i*Omega)*(2*R(5)*IL(5)*OMEGAR)*y(3))*CR)];
    CF=[((MI1(1)*Ice*OMEGAR.^2)+(MI2(1)*Ice*OMEGAR.^2)+(MI3(1)*Ice*OMEGAR.^2))*Cx ...
        ((MI1(2)*Ice*OMEGAR.^2)+(MI2(2)*Ice*OMEGAR.^2)+(MI3(3)*Ice*OMEGAR.^2))*Cx ...
        ((MI1(3)*Ice*OMEGAR.^2)+(MI2(3)*Ice*OMEGAR.^2)+(MI3(3)*Ice*OMEGAR.^2))*Cx ...
        ((MI1(4)*Ice*OMEGAR.^2)+(MI2(4)*Ice*OMEGAR.^2)+(MI3(4)*Ice*OMEGAR.^2))*Cz ...
        ((MI1(5)*Ice*OMEGAR.^2)+(MI2(5)*Ice*OMEGAR.^2)+(MI3(5)*Ice*OMEGAR.^2))*Cy]; Adh=1562000; Coh=165000;
   AdF=[((Adh*(Cs(1)*(2.5*I2)/4)*(uF-Ice))+(Adh*(Cs(1)*(I2/2.5)/8)*(uF-Ice))+(Adh*(SC(1)*(I2/5))*(uF-Ice)))*Cx ...
        ((Adh*(Cs(2)*(2.5*I2)/4)*(uF-Ice))+(Adh*(Cs(2)*(I2/2.5)/8)*(uF-Ice))+(Adh*(SC(2)*(I2/5))*(uF-Ice)))*Cx ...
        ((Adh*(Cs(3)*(2.5*I2)/4)*(uF-Ice))+(Adh*(Cs(3)*(I2/2.5)/8)*(uF-Ice))+(Adh*(SC(3)*(I2/5))*(uF-Ice)))*Cx ...
        ((Adh*(Cs(4)*(2.5*I2)/4)*(uF-Ice))+(Adh*(Cs(4)*(I2/2.5)/8)*(uF-Ice))+(Adh*(SC(4)*(I2/5))*(uF-Ice)))*Cz ...
        ((Adh*(Cs(5)*(2.5*I2)/4)*(uF-Ice))+(Adh*(Cs(5)*(I2/2.5)/8)*(uF-Ice))+(Adh*(SC(5)*(I2/5))*(uF-Ice)))*Cy];
   CoF=[((Coh*(Cs(1)/4)*(uF-Ice))+(Coh*(Cs(1)/8)*(uF-Ice))+(Coh*(SC(1))*(uF-Ice)))*Cx ...
        ((Coh*(Cs(2)/4)*(uF-Ice))+(Coh*(Cs(2)/8)*(uF-Ice))+(Coh*(SC(2))*(uF-Ice)))*Cx ...
        ((Coh*(Cs(3)/4)*(uF-Ice))+(Coh*(Cs(3)/8)*(uF-Ice))+(Coh*(SC(3))*(uF-Ice)))*Cx ...
        ((Coh*(Cs(4)/4)*(uF-Ice))+(Coh*(Cs(4)/8)*(uF-Ice))+(Coh*(SC(4))*(uF-Ice)))*Cz ...
        ((Coh*(Cs(5)/4)*(uF-Ice))+(Coh*(Cs(5)/8)*(uF-Ice))+(Coh*(SC(5))*(uF-Ice)))*Cy];
TorIce=[(+(((MI1(1)*Ice*OMEGAR.^2)*((Cs(1)/4)+(Cs(1)/16)))+((MI2(1)*Ice*OMEGAR.^2)*(2*Cs(1)/8))-((MI3(1)*Ice*OMEGAR.^2)*(SC(1)/2))) ...
         -(((Adh*(Cs(1)*(2.5*I2)/4)*(uF-Ice))*((Cs(1)/4)+(Cs(1)/16)))+((Adh*(Cs(1)*(I2/2.5)/8)*(uF-Ice))*(2*Cs(1)/8))-((Adh*(SC(1)*(I2/5))*(uF-
Ice))*(SC(1)/2))) ...
         -(((Coh*(Cs(1)/4)*(uF-Ice))*((Cs(1)/4)+(Cs(1)/16)))+((Coh*(Cs(1)/8)*(uF-Ice))*(2*Cs(1)/8))-((Coh*(SC(1))*(uF-Ice))*(SC(1)/2))))*Cx ...
        (+(((MI1(2)*Ice*OMEGAR.^2)*((Cs(2)/4)+(Cs(2)/16)))+((MI2(2)*Ice*OMEGAR.^2)*(2*Cs(2)/8))-((MI3(2)*Ice*OMEGAR.^2)*(SC(2)/2))) ...
         -(((Adh*(Cs(2)*(2.5*I2)/4)*(uF-Ice))*((Cs(2)/4)+(Cs(2)/16)))+((Adh*(Cs(2)*(I2/2.5)/8)*(uF-Ice))*(2*Cs(2)/8))-((Adh*(SC(2)*(I2/5))*(uF-
Ice))*(SC(2)/2))) ...
         -(((Coh*(Cs(2)/4)*(uF-Ice))*((Cs(2)/4)+(Cs(2)/16)))+((Coh*(Cs(2)/8)*(uF-Ice))*(2*Cs(2)/8))-((Coh*(SC(2))*(uF-Ice))*(SC(2)/2))))*Cx ...
        (+(((MI1(3)*Ice*OMEGAR.^2)*((Cs(3)/4)+(Cs(3)/16)))+((MI2(3)*Ice*OMEGAR.^2)*(2*Cs(3)/8))-((MI3(3)*Ice*OMEGAR.^2)*(SC(3)/2))) ...
         -(((Adh*(Cs(3)*(2.5*I2)/4)*(uF-Ice))*((Cs(3)/4)+(Cs(3)/16)))+((Adh*(Cs(3)*(I2/2.5)/8)*(uF-Ice))*(2*Cs(3)/8))-((Adh*(SC(3)*(I2/5))*(uF-
Ice))*(SC(3)/2))) ...
         -(((Coh*(Cs(3)/4)*(uF-Ice))*((Cs(3)/4)+(Cs(3)/16)))+((Coh*(Cs(3)/8)*(uF-Ice))*(2*Cs(3)/8))-((Coh*(SC(3))*(uF-Ice))*(SC(3)/2))))*Cx ...
        (+(((MI1(4)*Ice*OMEGAR.^2)*((Cs(4)/4)+(Cs(4)/16)))+((MI2(4)*Ice*OMEGAR.^2)*(2*Cs(4)/8))-((MI3(4)*Ice*OMEGAR.^2)*(SC(4)/2))) ...
         -(((Adh*(Cs(4)*(2.5*I2)/4)*(uF-Ice))*((Cs(4)/4)+(Cs(4)/16)))+((Adh*(Cs(4)*(I2/2.5)/8)*(uF-Ice))*(2*Cs(4)/8))-((Adh*(SC(4)*(I2/5))*(uF-
Ice))*(SC(4)/2))) ...
         -(((Coh*(Cs(4)/4)*(uF-Ice))*((Cs(4)/4)+(Cs(4)/16)))+((Coh*(Cs(4)/8)*(uF-Ice))*(2*Cs(4)/8))-((Coh*(SC(4))*(uF-Ice))*(SC(4)/2))))*Cz ...
        (+(((MI1(5)*Ice*OMEGAR.^2)*((Cs(5)/4)+(Cs(5)/16)))+((MI2(5)*Ice*OMEGAR.^2)*(2*Cs(5)/8))-((MI3(5)*Ice*OMEGAR.^2)*(SC(5)/2))) ...
         -(((Adh*(Cs(5)*(2.5*I2)/4)*(uF-Ice))*((Cs(5)/4)+(Cs(5)/16)))+((Adh*(Cs(5)*(I2/2.5)/8)*(uF-Ice))*(2*Cs(5)/8))-((Adh*(SC(5)*(I2/5))*(uF-
Ice))*(SC(5)/2))) ...
         -(((Coh*(Cs(5)/4)*(uF-Ice))*((Cs(5)/4)+(Cs(5)/16)))+((Coh*(Cs(5)/8)*(uF-Ice))*(2*Cs(5)/8))-((Coh*(SC(5))*(uF-Ice))*(SC(5)/2))))*Cy];
                                                                        % Aerodynamic and Ice accretion conditions
dydx(2)=((-((Omega.^2*MA(n))*y(1))-((Omega.^2*MA(n)*SC(n))*y(5))-((MA(n)*OMEGAR.^2*(-(ur+x)))*y(2))+(kAG(n)*y(4))-(Al(n)*BA1(n))-(((CF(n)-
AdF(n)-CoF(n))*(y(2)-y(3)))*BA1(n)))  /  (((MA(n)*OMEGAR.^2)*((ur*uF)-(ur*x)+(uF.^2/2)-(x.^2/2)))+kAG(n)));
dydx(4)=((-((R(n)*IF(n)*Omega.^2)*y(3))-((R(n)*IF(n)*OMEGAR.^2)*y(3))+(((MA(n)*SC(n)*OMEGAR.^2)*(ur+x))*y(5))-(kAG(n)*(y(2)-y(3)))-ClX(n)-
(Al(n)*BA1(n))-(((CF(n)-AdF(n)-CoF(n))*(y(2)-y(3)))*BA1(n)))  /  (EI(n)));
dydx(6)=((-((Omega.^2*IP(n))*y(5))-((Omega.^2*MA(n)*SC(n))*y(1))-(((R(n)*(IF(n)-
IL(n)))*OMEGAR.^2)*y(5))+(((MA(n)*SC(n)*OMEGAR.^2)*(ur+x))*y(3))-(((MA(n)*OMEGAR.^2*(-(ur+x)))*IP(n)*(1/MA(n)))*y(6))
                                                                        -C2X(n)-A3(n)-(TorIce(n)*(y(2)-y(3))))  /
(GJ(n)+(((MA(n)*OMEGAR.^2)*((ur*uF)-(ur*x)+(uF.^2/2)-(x.^2/2)))*IP(n)*(1/MA(n)))));
   otherwise
   end
end
end
function res=fcn_bc1(L,R)
%|uR       1          Q1|Q1         2        LD1|LD1        3        PL2|PL2        4        Ice|Ice        5          uF|
 z1a=L(1,1); z1b=R(1,1); z2a=L(1,2); z2b=R(1,2); z3a=L(1,3); z3b=R(1,3); z4a=L(1,4); z4b=R(1,4); z5a=L(1,5); z5b=R(1,5);
 u1a=L(2,1); u1b=R(2,1); u2a=L(2,2); u2b=R(2,2); u3a=L(2,3); u3b=R(2,3); u4a=L(2,4); u4b=R(2,4); u5a=L(2,5); u5b=R(2,5);
 v1a=L(3,1); v1b=R(3,1); v2a=L(3,2); v2b=R(3,2); v3a=L(3,3); v3b=R(3,3); v4a=L(3,4); v4b=R(3,4); v5a=L(3,5); v5b=R(3,5);
 w1a=L(4,1); w1b=R(4,1); w2a=L(4,2); w2b=R(4,2); w3a=L(4,3); w3b=R(4,3); w4a=L(4,4); w4b=R(4,4); w5a=L(4,5); w5b=R(4,5);
z1a=L(5,1);z1b=R(5,1);z2a=L(5,2);z2b=R(5,2);z3a=L(5,3);z3b=R(5,3);z4a=L(5,4);z4b=R(5,4);z5a=L(5,5);z5b=R(5,5);
u1a=L(6,1);u1b=R(6,1);u2a=L(6,2);u2b=R(6,2);u3a=L(6,3);u3b=R(6,3);u4a=L(6,4);u4b=R(6,4);u5a=L(6,5);u5b=R(6,5);
% I1 = I3 = Weight gravity bending and torsional moments
I2X=[((((MI1(1)*9.81)+(MI2(1)*9.81)-(MI3(1)*9.81))*Q1)*Cx)  ((((MI1(2)*9.81)+(MI2(2)*9.81)-(MI3(2)*9.81))*LD1)*Cx) ...
      ((((MI1(3)*9.81)+(MI2(3)*9.81)-(MI3(3)*9.81))*PL2)*Cx)   ((((MI1(4)*9.81)+(MI2(4)*9.81)-(MI3(4)*9.81))*Ice)*Cz) ...
      ((((MI1(5)*9.81)+(MI2(5)*9.81)-(MI3(5)*9.81))*uF)*Cy)];
I3X=[((((MI1(1)*9.81)*DI1(1))+((MI2(1)*9.81)*DI2(1))-((MI3(1)*9.81)*DI3(1)))*Cx)  ((((MI1(2)*9.81)*DI1(2))+((MI2(2)*9.81)*DI2(2))-
((MI3(2)*9.81)*DI3(2)))*Cx) ...
      ((((MI1(3)*9.81)*DI1(3))+((MI2(3)*9.81)*DI2(3))-((MI3(3)*9.81)*DI3(3)))*Cx)  ((((MI1(4)*9.81)*DI1(4))+((MI2(4)*9.81)*DI2(4))-
((MI3(4)*9.81)*DI3(4)))*Cz) ...
       ((((MI1(5)*9.81)*DI1(5))+((MI2(5)*9.81)*DI2(5))-((MI3(5)*9.81)*DI3(5)))*Cy)];
C11L=EI(1)*w1b+I2X(1);C21L=(((MA(1)*OMEGAR.^2)*(ur*uF-ur*Q1 +(uF.^2/2)-( Q1.^2/2)))*u1b)+(kAG(1)*(u1b-v1b))+I2X(1)*Q1; C31L=GJ(1)*uA1b+I3X(1);
C11R=EI(2)*w2a+I2X(1);C21R=(((MA(2)*OMEGAR.^2)*(ur*uF-ur*Q1 +(uF.^2/2)-( Q1.^2/2)))*u2a)+(kAG(2)*(u2a-v2a))+I2X(1)*Q1; C31R=GJ(2)*uA2a+I3X(1);
C12L=EI(2)*w2b+I2X(2);C22L=(((MA(2)*OMEGAR.^2)*(ur*uF-ur*LD1+(uF.^2/2)-(LD1.^2/2)))*u2b)+(kAG(2)*(u2b-v2b))+I2X(2)*LD1;C32L=GJ(2)*uA2b+I3X(2);
C12R=EI(3)*w3a+I2X(2);C22R=(((MA(3)*OMEGAR.^2)*(ur*uF-ur*LD1+(uF.^2/2)-(LD1.^2/2)))*u3a)+(kAG(3)*(u3a-v3a))+I2X(2)*LD1;C32R=GJ(3)*uA3a+I3X(2);
C13L=EI(3)*w3b+I2X(3);C23L=(((MA(3)*OMEGAR.^2)*(ur*uF-ur*PL2+(uF.^2/2)-(PL2.^2/2)))*u3b)+(kAG(3)*(u3b-v3b))+I2X(3)*PL2;C33L=GJ(3)*uA3b+I3X(3);
C13R=EI(4)*w4a+I2X(3);C23R=(((MA(4)*OMEGAR.^2)*(ur*uF-ur*PL2+(uF.^2/2)-(PL2.^2/2)))*u4a)+(kAG(4)*(u4a-v4a))+I2X(3)*PL2;C33R=GJ(4)*uA4a+I3X(3);
C14L=EI(4)*w4b+I2X(4);C24L=(((MA(4)*OMEGAR.^2)*(ur*uF-ur*Ice+(uF.^2/2)-(Ice.^2/2)))*u4b)+(kAG(4)*(u4b-v4b))+I2X(4)*Ice;C34L=GJ(4)*uA4b+I3X(4);
C14R=EI(5)*w5a+I2X(4);C24R=(((MA(5)*OMEGAR.^2)*(ur*uF-ur*Ice+(uF.^2/2)-(Ice.^2/2)))*u5a)+(kAG(5)*(u5a-v5a))+I2X(4)*Ice;C34R=GJ(5)*uA5a+I3X(4);
C15L=EI(5)*w5b+I2X(5);C25L=(((MA(5)*OMEGAR.^2)*(ur*uF-ur*uF +(uF.^2/2)-( uF.^2/2)))*u5b)+(kAG(5)*(u5b-v5b))+I2X(5)*uF; C35L=GJ(5)*uA5b+I3X(5);
if is_PL
% Bending moment
PL1L=((w3b)-((-(((PLm*((1i*Omega).^2*(z3b+(Cd3*zA3b)+AAL*(u3b-v3b))))+(DC1*((1i*Omega)*(z3b+(Cd3*zA3b)+AAL*(u3b-v3b))))...
```

```
      +((kPL1+(Ap0.^2/Cp0))*(z3b+(Cd3*zA3b)+AAL*(u3b-v3b)))-((Ap0/Cp0)*((Ap0*(z3b+(Cd3*zA3b)+AAL*(u3b-v3b)))-Cp0*Pd0))+WPL)*AAL)...
      +(WAAL*AAL/2)+(Wpl*AAL))/EI(3)));
PL1R=((w4a)-((-(((PLm*((li*Omega).^2*(z4a+(Cd4*zA4a)+AAL*(u4a-v4a))))+(DC1*((li*Omega)*(z4a+(Cd4*zA4a)+AAL*(u4a-v4a))))...
      +((kPL1+(Ap0.^2/Cp0))*(z4a+(Cd4*zA4a)+AAL*(u4a-v4a)))-((Ap0/Cp0)*((Ap0*(z4a+(Cd4*zA4a)+AAL*(u4a-v4a)))-Cp0*Pd0))+WPL)*AAL)...
      +(WAAL*AAL/2)+(Wpl*AAL))/EI(4)));
% Shear force
PL2L=((u3b-v3b)-(((-((PLm*((li*Omega).^2*(z3b+(Cd3*zA3b)+AAL*(u3b-v3b))))+(DC1*((li*Omega)*(z3b+(Cd3*zA3b)+AAL*(u3b-v3b))))...
      +((kPL1+(Ap0.^2/Cp0))*(z3b+(Cd3*zA3b)+AAL*(u3b-v3b)))-((Ap0/Cp0)*((Ap0*(z3b+(Cd3*zA3b)+AAL*(u3b-v3b)))-Cp0*Pd0))+WPL)...
      +(WAAL)+(WRAL)+(Wpl))+((MA(3)*OMEGAR.^2*(ur*uF-ur*PL2+(uF.^2/2)-(PL2.^2/2)))*u3b))/kAG(3)));
PL2R=((u4a-v4a)-(((-((PLm*((li*Omega).^2*(z4a+(Cd4*zA4a)+AAL*(u4a-v4a))))+(DC1*((li*Omega)*(z4a+(Cd4*zA4a)+AAL*(u4a-v4a))))...
      +((kPL1+(Ap0.^2/Cp0))*(z4a+(Cd4*zA4a)+AAL*(u4a-v4a)))-((Ap0/Cp0)*((Ap0*(z4a+(Cd4*zA4a)+AAL*(u4a-v4a)))-Cp0*Pd0))+WPL)...
      +(WAAL)+(WRAL)+(Wpl))+((MA(4)*OMEGAR.^2*(ur*uF-ur*PL2+(uF.^2/2)-(PL2.^2/2)))*u4a))/kAG(4)));
% Torsional moment
PL3L=((uA3b)-((-(((PLm*((li*Omega).^2*(z3b+(Cd3*zA3b)+AAL*(u3b-v3b))))+(DC1*((li*Omega)*(z3b+(Cd3*zA3b)+AAL*(u3b-v3b))))...
      +((kPL1+(Ap0.^2/Cp0))*(z3b+(Cd3*zA3b)+AAL*(u3b-v3b)))-((Ap0/Cp0)*((Ap0*(z3b+(Cd3*zA3b)+AAL*(u3b-v3b)))-Cp0*Pd0))+WPL)*(RAL+eP3))...
      +(WRAL*((RAL/2)+eP3))+(WAAL*(RAL+eP3))+(Wpl*(RAL+eP3)))/GJ(3)));
PL3R=((uA4a)-((-(((PLm*((li*Omega).^2*(z4a+(Cd4*zA4a)+AAL*(u4a-v4a))))+(DC1*((li*Omega)*(z4a+(Cd4*zA4a)+AAL*(u4a-v4a))))...
      +((kPL1+(Ap0.^2/Cp0))*(z4a+(Cd4*zA4a)+AAL*(u4a-v4a)))-((Ap0/Cp0)*((Ap0*(z4a+(Cd4*zA4a)+AAL*(u4a-v4a)))-Cp0*Pd0))+WPL)*(RAL+eP3))...
      +(WRAL*((RAL/2)+eP3))+(WAAL*(RAL+eP3))+(Wpl*(RAL+eP3)))/GJ(4)));
else PL1L=C13L;PL2L=C23L;PL3L=C33L;          PL1R=C13R;PL2R=C23R;PL3R=C33R;
end
if is_FH
     FH2L=w2b-(kf1*(u2b-v2b)/EI(2));        FH2R=w3a-(kf1*(u3a-v3a)/EI(3));
else FH2L=C12L;                             FH2R=C12R;
end
 res=[z1a;    v1a;    zA1a;
      z2a-z1b;v2a-v1b;zA2a-zA1b;    C11R-C11L;   C21R-C21L;   C31R-C31L;
      z3a-z2b;v3a-v2b;zA3a-zA2b;    FH2R-FH2L;   C22R-C22L;   C32R-C32L;
      z4a-z3b;v4a-v3b;zA4a-zA3b;    PL1R-PL1L-M1;PL2R-PL2L-PF;PL3R-PL3L-M2;
      z5a-z4b;v5a-v4b;zA5a-zA4b;    C14R-C14L;   C24R-C24L;   C34R-C34L;
                                          C15L;        C25L;        C35L];
end
disp(' ');disp(' - Zakanchivatsya - ');disp(' ');
end
```

Non-rotating Advanced beam on Ice accretion (Harmonic Analysis)

```
function NonRotaBanerjeeFT
disp(' - NonRotaBanerjeeFT - ')
load ABC1.mat kPL1 CC5 DD5 CC4 DD4 CC3 DD3 CC2 DD2 CC1 DD1 XI5 XI4 XI3 XI2 XI1 XI0 XIN5 XIN4 XIN3 XIN2 XIN1 XIT Ra1I NOmega
uR=0; uf=.9021; E=.0656; F=.034; G=.8025; A=.0049; B=.0151; C=.0099; D=.0301; T=.0301; W=1/8; N=.21; Q=E/6; U=F/4; V=.5525; I=.05;
EaI=20394324259.6; GaI=7851814839.93; Ge=9.81; MPL1=1; RA0=T/2; AAL=.051; RAL=.0535+T/2; Wpl=(.0852/.1015)*Ge;   PLf=.4679;
PLm=(PLf+.0852)/(AAL+RAL+.1015); PLmass=PLf+.0852; WPL=PLm*Ge; WAAL=PLf*Ge/AAL; WRAL=PLf*Ge/RAL; % CC=.0099; DD=.03108; W=41/3; N=1.05;
AAL=.051; RAL=.048; Wpl=(.0852/.1015)*Ge*0; PLf=.4679; PLm=(PLf)/(AAL+RAL); PLmass=PLf; WPL=PLm*Ge; WAAL=PLf*Ge/AAL; WRAL=PLf*Ge/RAL;
Ra1=2700; Ra2=2700; Ra3=2700; Ra4=2700; Ra5=2700; Ra6=2700; Ra7=2700; Ra8=2700;
Ea1=7239985113; Ea2=7239985113; Ea3=7239985113; Ea4=7239985113; Ea5=7239985113; Ea6=7239985113; Ea7=7239985113; Ea8=7239985113;
Ga1=Ea1/(2*(1+.33)); Ga2=Ea2/(2*(1+.33)); Ga3=Ea3/(2*(1+.33)); Ga4=Ea4/(2*(1+.33)); Ga5=Ea5/(2*(1+.33)); Ga6=Ea6/(2*(1+.33));
Ga7=Ea7/(2*(1+.33));  Ga8=Ea8/(2*(1+.33));
 a1=A*D; a2=B*D; a3=C*D; aA4=C*D; aS4=(CC5)*(DD5-D); aA5=C*D;aS5=(CC4)*(DD4-D); aA6=C*D;aS6=(CC3)*(DD3-D); aA7=C*D;aS7=(CC2)*(DD2-D);
aA8=C*D;aSB8=(CC1*(DD1-D))*XI1;
m11=a1*Q*Ra1;m12=a1*Q*Ra1;m21=a2*U*Ra2;m21a=PLmass*MPL1;m31=a3*V*Ra3;
aSS8=(CC1*(DD1-D))*XI0;
mA4=aA4*I*Ra4;mI4=aS4*I*Ra1I;mA5=aA5*I*Ra5;mI5=aS5*I*Ra1I;mA6=aA6*I*Ra6;mI6=aS6*I*Ra1I;
mA7=aA7*I*Ra7;mI7=aS7*I*Ra1I;mA8=aA8*I*Ra8;mIB8=aSB8*I*Ra1I;mIS8=aSS8*I*Ra1I;
ma1=m11/Q;mb1=m12/Q;ma2=m21/U;ma3=m31/V;ma4=(mA4+mI4*XI5)/I;ma5=(mA5+mI5*XI4)/I;ma6=(mA6+mI6*XI3)/I;
ma7=(mA7+mI7*XI2)/I;ma8=(mA8+mIB8*XI1+mIS8*XI0)/I;
ma=((ma1+mb1+mb1+mb1+mb1+ma1)/6)+((ma2+ma2+ma2+ma2+(m21a/U))/4)+ma3+((ma4+ma5+ma6+ma7+ma8)/5);
X2Y=((.06*F)*(.005)+(.01*.025/2)*(.0325)+(.024*.06/2)*(.0435)+(.024*.015)*(.0475)+(.011*.015)*(.0645))/((.06*F)+(.01*.025/2)+(.024*.06/2)+(.024*
.015)+(.011*.015));
Y2Y=((.01*.025/2)*(.0225)+(.024*.06/2)*(.033)+(.024*.015)*(.049)+(.011*.015)*(.049))/((.06*F)+(.01*.025/2)+(.024*.06/2)+(.024*.015)+(.011*.015))
;
%X2Y=((.06*F)*(.005)+(.01*.025/2)*(.0325)+(.024*.06/2)*(.0435)+(.024*.015)*(.0475))/((.06*F)+(.01*.025/2)+(.024*.06/2)+(.024*.015));
%Y2Y=((.01*.025/2)*(.0225)+(.024*.06/2)*(.033)+(.024*.015)*(.049))/((.06*F)+(.01*.025/2)+(.024*.06/2)+(.024*.015));
G1=D/2;   G2=D/2;   G3=D/2;   G4=D/2;     G5=D/2;         G6=D/2;         G7=D/2;         G8=D/2;        Gs=(G1+G2+G3+G4+G5+G6+G7+G8)/8;
S1=D/2;   S2=D/2;   S3=D/2;   S4=DD5/2;  S5=DD4/2;       S6=DD3/2;       S7=DD2/2;       S8=DD1/2;      Sc=(S1+S2+S3+S4+S5+S6+S7+S8)/8;
X1=(S1-G1)*0;X2=(S2-G2)+RAL*MPL1;X3=0;X4=(S4-G4)*XI5;X5=(S5-G5)*XI4;X6=(S6-G6)*XI3;X7=(S7-G7)*XI2;X8=(S8-G8)*(XI1+XI0); Xf=G8;
  Ia1=((ma1*(A.^2+D.^2))/12)+(ma1*X1.^2);  Ia2=((mb1*(A.^2+D.^2))/12)+(mb1*X1.^2); Ia3=((mb1*(A.^2+D.^2))/12)+(mb1*X1.^2);
  Ia4=((mb1*(A.^2+D.^2))/12)+(mb1*X1.^2);  Ia5=((mb1*(A.^2+D.^2))/12)+(mb1*X1.^2); Ia6=((ma1*(A.^2+D.^2))/12)+(ma1*X1.^2);
  Ia7=(((ma2*(B.^2+D.^2))/12)+(ma2*X2.^2))+(((m21a/U*((B+A*2).^2+.06.^2 ))/12)+(m21a/U*(-.005+X2Y).^2))*MPL1+(((m21a/U*((B+A*2).^2+.01.^2
))/12)+(m21a/U*(.0325+X2Y).^2))*MPL1...
+(((m21a/U*((B+A*2).^2+.024.^2))/12)+(m21a/U*(.0435+X2Y).^2))*MPL1+(((m21a/U*((B+A*2).^2+.024.^2))/12)+(m21a/U*(.0475+X2Y).^2))*MPL1+(((m21a/U*(
(B+A*2).^2+.011.^2))/12)+(m21a/U*(.0645+X2Y).^2))*MPL1;
 %Ia7=(((ma2*(B.^2+D.^2))/12)+(ma2*X2.^2))+(((m21a/U*((B+A*2).^2+.06.^2 ))/12)+(m21a/U*(-.005+X2Y).^2))*MPL1+(((m21a/U*((B+A*2).^2+.01.^2
))/12)+(m21a/U*(.0325+X2Y).^2))*MPL1...
 %    +(((m21a/U*((B+A*2).^2+.024.^2))/12)+(m21a/U*(.0435+X2Y).^2))*MPL1+(((m21a/U*((B+A*2).^2+.024.^2))/12)+(m21a/U*(.0475+X2Y).^2))*MPL1;
 Ia11=((ma3*(C.^2+D.^2))/12)+(ma3*X3.^2);
 Ia12=(((mA4/I*(C.^2+D.^2))/12)+(mA4/I*X4.^2))+(((mI4/I*(CC5.^2+(DD5-D).^2))/12)+(mI4/I*(X4+D/2).^2))*XI5;
 Ia13=(((mA5/I*(C.^2+D.^2))/12)+(mA5/I*X5.^2))+(((mI5/I*(CC4.^2+(DD4-D).^2))/12)+(mI5/I*(X5+D/2).^2))*XI4;
 Ia14=(((mA6/I*(C.^2+D.^2))/12)+(mA6/I*X6.^2))+(((mI6/I*(CC3.^2+(DD3-D).^2))/12)+(mI6/I*(X6+D/2).^2))*XI3;
 Ia15=(((mA7/I*(C.^2+D.^2))/12)+(mA7/I*X7.^2))+(((mI7/I*(CC2.^2+(DD2-D).^2))/12)+(mI7/I*(X7+D/2).^2))*XI2;
 Ia16=(((mA8/I*(C.^2+D.^2))/12)+(mA8/I*X8.^2))+(((mIB8*XI1+mIS8*XI0)/I*(CC1.^2+(DD1-D).^2))/12)+((mIB8*XI1+mIS8*XI0)/I*(X8+D/2).^2))*(XI0+XI1);
Ixla=((D*A.^3/12)+(a1*(C/2-C/2).^2)); Ix1b=((D*A.^3/12)+(a1*(C/2-C/2).^2)); Ix3=((D*C.^3/12)+(a3*(C/2-C/2).^2)); Ix2=((D*B.^3/12)+(a2*X2.^2));
%Ix2a=4.50785e-7;
 Ix2a=(((  .06*(B+A*2).^3/12)+(((B+A*2)*.06  )*(-.005+X2Y).^2))+((  .01*(B+A*2).^3/12)+(((B+A*2)*.01  )*(.0325+X2Y).^2))...
+((.0225*(B+A*2).^3/12)+(((B+A*2)*.0225)*(.0435+X2Y).^2)+((.0225*(B+A*2).^3/12)+(((B+A*2)*.0225)*(.0475+X2Y).^2))+((.01*(B+A*2).^3/12)+(((B+A*2
)*.01)*(.0645+X2Y).^2)))*MPL1;
%Ix2a=(((  .06*(B+A*2).^3/12)+(((B+A*2)*.06  )*(-.005+X2Y).^2))+((  .01*(B+A*2).^3/12)+(((B+A*2)*.01
)*(.0325+X2Y).^2))+((.0225*(B+A*2).^3/12)+(((B+A*2)*.0225)*(.0435+X2Y).^2))+((.0225*(B+A*2).^3/12)+(((B+A*2)*.0225)*(.0475+X2Y).^2)))*MPL1;
  Ix4=((D*C.^3/12)+(aA4*X4.^2));Ix14=(((DD5-D)*CC5.^3/12)+(aS4*(X4+D/2).^2));
  Ix5=((D*C.^3/12)+(aA5*X5.^2));Ix15=(((DD4-D)*CC4.^3/12)+(aS5*(X5+D/2).^2));
  Ix6=((D*C.^3/12)+(aA6*X6.^2));Ix16=(((DD3-D)*CC3.^3/12)+(aS6*(X6+D/2).^2));
  Ix7=((D*C.^3/12)+(aA7*X7.^2));Ix17=(((DD2-D)*CC2.^3/12)+(aS7*(X7+D/2).^2));
  Ix8=((D*C.^3/12)+(aA8*X8.^2));Ix18=(((DD1-D)*CC1.^3/12)+((aSB8*XI1+aSS8*XI0)*(X8+D/2).^2));
 Ila1=Ix1a;Ila2=Ix1b;Ila3=Ix1b;Ila4=Ix1b;Ila5=Ix1b;Ila6=Ix1a; Ila7=Ix2+Ix2a;Ila8=Ix2+Ix2a;Ila9=Ix2+Ix2a;Ila10=Ix2+Ix2a;
Ila11=Ix3;Ila12=Ix4;Ila13=Ix5;Ila14=Ix6;Ila15=Ix7;Ila16=Ix8;
Tc1a=(W-((N*A/D)*(1-(A.^4/12*D.^4))))*(D*A.^3); Tc1b=(W-((N*A/D)*(1-(A.^4/12*D.^4))))*(D*A.^3); Tc2=((W-((N*B/D)*(1-(B.^4/12*D.^4))))*(D*B.^3));
Tc3=(W-((N*C/D)*(1-(C.^4/12*D.^4))))*(D*C.^3);
 Tc2a=((1/3)-((0.21 *(    F/D*2)*(1-(    F.^4/12 *(D*2).^4))))*(D*2*      F.^3))...
     +((1/3)-((0.105*(.0225/.4 )*(1-(.0225.^4/192*(.4).^4 ))))*( .4*(.0225).^3))+(((.0225/F)*(0.07+0.076*(X2Y-(F/2))/F))*(2*(.0225+F+(3*(X2Y-
(F/2)))-sqrt(2*(2*(X2Y-(F/2))+F)*(2*(X2Y-(F/2))+.0225)))).^4)*MPL1;
  Tc4=((W-((N*C/D)*(1-(C.^4/12*D.^4))))*(D*C.^3));
Ja12=(((W-((N*CC5/((DD5-D)+XIN5))*(1-(CC5.^4/12*(DD5-D).^4))))*((DD5-D)*CC5.^3))*(XI5));
  Tc5=((W-((N*C/D)*(1-(C.^4/12*D.^4))))*(D*C.^3));
Ja13=(((W-((N*CC4/((DD4-D)+XIN4))*(1-(CC4.^4/12*(DD4-D).^4))))*((DD4-D)*CC4.^3))*(XI4));
  Tc6=((W-((N*C/D)*(1-(C.^4/12*D.^4))))*(D*C.^3));
Ja14=(((W-((N*CC3/((DD3-D)+XIN3))*(1-(CC3.^4/12*(DD3-D).^4))))*((DD3-D)*CC3.^3))*(XI3));
  Tc7=((W-((N*C/D)*(1-(C.^4/12*D.^4))))*(D*C.^3));
Ja15=(((W-((N*CC2/((DD2-D)+XIN2))*(1-(CC2.^4/12*(DD2-D).^4))))*((DD2-D)*CC2.^3))*(XI2));
  Tc8=((W-((N*C/D)*(1-(C.^4/12*D.^4))))*(D*C.^3));
Ja16=(((W-((N*CC1/((DD1-D)+XIN1))*(1-(CC1.^4/12*(DD1-D).^4))))*((DD1-D)*CC1.^3))*(XI1+XI0));                          D2=(D*F)*MPL1;
  D15=((DD5-D)*I)+XIN5; D14=((DD4-D)*I)+XIN4; D13=((DD3-D)*I)+XIN3; D12=((DD2-D)*I)+XIN2; D11=(((DD1-D)*I)*XIN1+((DD1-D)*I)*XI1)+(XI0);
Eeff2=(EaI*Ea2)/((Ea2*(1-(D2)))+(EaI*D2));
Eeff4=(Ea4*(1-(D15)))+(EaI*D15);Eeff5=(Ea5*(1-(D14)))+(EaI*D14);Eeff6=(Ea6*(1-(D13)))+(EaI*D13);Eeff7=(Ea7*(1-(D12)))+(EaI*D12);Eeff8=(Ea8*(1-
(D11)))+(EaI*D11); Geff2=(GaI*Ga2)/((Ga2*(1-(D2)))+(GaI*D2));
Geff4=(Ga4*(1-(D15)))+(GaI*D15);Geff5=(Ga5*(1-(D14)))+(GaI*D14);Geff6=(Ga6*(1-(D13)))+(GaI*D13);Geff7=(Ga7*(1-(D12)))+(GaI*D12);Geff8=(Ga8*(1-
(D11)))+(GaI*D11); Reff2=(Ra1I*Ra2)/((Ra2*(1-(D2)))+(Ra1I*D2));
  Ja1=Tc1a;  Ja2=Tc1b;  Ja3=Tc1b;  Ja4=Tc1b;  Ja5=Tc1b;  Ja6=Tc1a;  Ja7=Tc2+Tc2a; Ja8=Tc2+Tc2a; Ja9=Tc2+Tc2a; Ja10=Tc2+Tc2a;
Ja11=Tc3;Ja12=Tc4;Ja13=Tc5;Ja14=Tc6;Ja15=Tc7;Ja16=Tc8;
   N1=56;n1=linspace(1,55,55); N2=44;n2=linspace(1,43,43); N3=3297;n3=linspace(1,3296,3296); N4=35;n4=linspace(1,34,34);
N5=35;n5=linspace(1,34,34); OmegaA=linspace(0,1000,NOmega);
```

```
   Ea=[Ea1*I1a1 Ea1*I1a2 Ea1*I1a3 Ea1*I1a4 Ea1*I1a5 Ea1*I1a6 Ea2*I1a7*XIT+Eeff2*I1a7*MPL1 Ea2*I1a8*XIT+Eeff2*I1a8*MPL1
Ea2*I1a9*XIT+Eeff2*I1a9*MPL1 Ea2*I1a10*XIT+Eeff2*I1a10*MPL1 Ea3*I1a11 (Ea4*I1a12)*XIN5+(Eeff4*(I1a12+IxI4))*XI5
(Ea5*I1a13)*XIN4+(Eeff5*(I1a13+IxI5))*XI4 (Ea6*I1a14)*XIN3+(Eeff6*(I1a14+IxI6))*XI3 (Ea7*I1a15)*XIN2+(Eeff7*(I1a15+IxI7))*XI2
(Ea8*I1a16)*XIN1+(Eeff8*(I1a16+IxI8))*(XI1+XI0)];
   Ga=[Ga1*Ja1 Ga1*Ja2 Ga1*Ja3 Ga1*Ja4 Ga1*Ja5 Ga1*Ja6 Ga2*Ja7*XIT+Geff2*Ja7*MPL1 Ga2*Ja8*XIT+Geff2*Ja8*MPL1 Ga2*Ja9*XIT+Geff2*Ja9*MPL1
Ga2*Ja10*XIT+Geff2*Ja10*MPL1 Ga3*Ja11 (Ga4*Ja12)*XIN5+(Geff4*(Ja12+JaI12))*XI5 (Ga5*Ja13)*XIN4+(Geff5*(Ja13+JaI13))*XI4
(Ga6*Ja14)*XIN3+(Geff6*(Ja14+JaI14))*XI3 (Ga7*Ja15)*XIN2+(Geff7*(Ja15+JaI15))*XI2 (Ga8*Ja16)*XIN1+(Geff8*(Ja16+JaI16))*(XI1+XI0)];
   Ia=[Ia1 Ia2 Ia3 Ia4 Ia5 Ia6 Ia7 Ia7 Ia7 Ia7 Ia11 Ia12 Ia13 Ia14 Ia15 Ia16];
    X=[X1 X1 X1 X1 X1 X1 X1 X2 X2 X2 X2 X3 X4 X5 X6 X7 X8];
   Ra=[Ra1 Ra1 Ra1 Ra1 Ra1 Ra1 Ra2*XIT+Reff2*MPL1 Ra2*XIT+Reff2*MPL1 Ra2*XIT+Reff2*MPL1 Ra2*XIT+Reff2*MPL1 Ra2*XIT+Reff2*MPL1 Ra3 Ra4 Ra5 Ra6 Ra7 Ra8];
   F1=6;  F2=51.3;  F3=155;  F4=313.5;  F5=521.2;  F6=773.3;  T1=351.5;  L1=26.2;  L2=169.8;  L3=485.1;  L4=955.2;  is_PL=true;   is_PL2=true;
  WI5=9.81*(aS4*I*RaII)/I;         BM5a=WI5*(uf-(9*I/2)); BM5b=WI5*(uf-(7*I/2)); TM5=WI5*(X(12)+T/2);
  WI4=9.81*(aS5*I*RaII)/I;         BM4a=WI4*(uf-(7*I/2)); BM4b=WI4*(uf-(5*I/2)); TM4=WI4*(X(13)+T/2);
  WI3=9.81*(aS6*I*RaII)/I;         BM3a=WI3*(uf-(5*I/2)); BM3b=WI3*(uf-(3*I/2)); TM3=WI3*(X(14)+T/2);
  WI2=9.81*(aS7*I*RaII)/I;         BM2a=WI2*(uf-(3*I/2)); BM2b=WI2*(uf-(  I/2)); TM2=WI2*(X(15)+T/2);
  WI1=9.81*((aSB8+aSS8)*I*RaII)/I; BM1a=WI1*(uf-(  I/2)); BM1b=WI1*(uf       ); TM1=WI1*(X(16)+T/2);
for OmegaNumber=NOmega:-1:1
if rem(OmegaNumber,100)==0
   fprintf(' - Podozhdite, Bertolet letit pryama seichaz - Gotov b    =    %d-%d\n',OmegaNumber,NOmega)
end
  Omega=OmegaA(OmegaNumber);
Q1=E/6;Q2=2*E/6;Q3=3*E/6;Q4=4*E/6;Q5=5*E/6;Q6=E;Q7=E+F/4;Q8=E+2*F/4;Q9=E+3*F/4;Q10=E+F;Q11=.6521;Q12=.7021;Q13=.7521;Q14=.8021;Q15=.8521;Q16=.90
21;
      Z=[Q1 Q2-Q1 Q3-Q2 Q4-Q3 Q5-Q4 Q6-Q5 Q7-Q6 Q8-Q7 Q9-Q8 Q10-Q9 Q11-Q10 Q12-Q11 Q13-Q12 Q14-Q13 Q15-Q14 Q16-Q15];
solinit=bvpinit([uR,Z(1)*n1/N1,Q1,Q1,Q1+Z(2)*n1/N1,Q2,Q2,Q2+Z(3)*n1/N1,Q3,Q3,Q3+Z(4)*n1/N1,Q4,Q4,Q4+Z(5)*n1/N1,Q5,Q5,Q5+Z(6)*n1/N1,Q6,Q6,Q6+Z(7)
*n2/N2,... Q7,Q7,Q7+Z(8)*n2/N2,Q8,Q8,Q8+Z(9)*n2/N2,Q9,Q9,Q9+Z(10)*n2/N2,Q10,Q10,Q10+Z(11)*n3/N3,Q11,Q11,Q11+Z(12)*n4/N4,...
Q12,Q12,Q12+Z(13)*n5/N5,Q13,Q13,Q13+Z(14)*n5/N5,Q14,Q14,Q14+Z(15)*n5/N5,Q15,Q15,Q15+Z(16)*n5/N5,uf],[0,0,0,0,0,0]);
          options=bvpset('stats','off','RelTol',1e-3,'NMax',floor(4000/2));
              sol=BVP4c(@fcn_ode,@fcn_bc,solinit,options);
             hij1=sol.y([1 5],/1,end); hijaccl=-Omega.^2*(hij1);   hijaccv1=hijaccl*(10.33./11.83);
         hijaccvB=hijaccv1(1);                                    hijaccv1(1)=hijaccvB;
         hijaccvT=hijaccv1(2)*Xf;                                 hijaccv1(2)=hijaccvT;
        hijaccvBT=hijaccv1(1)+hijaccv1(2)*Xf+hijaccv1(2)*(C/2); hijaccv1(3)=hijaccvBT;
H1(:,OmegaNumber)=[Omega;hijaccv1]; I1{1,OmegaNumber}=sol.x; I1{2,OmegaNumber}=sol.y;
end
for     nX=NOmega:-1:1
BeN1{1,nX}=((real(I1{2,nX}(1,:))))./(max(abs(real(I1{2,nX}(1,:))))).//(max([max(abs(real(I1{2,nX}(1,:)))),max(abs(real(I1{2,nX}(5,:))))]));
BeN1(:);
ToN1{1,nX}=((real(I1{2,nX}(5,:))))./(max(abs(real(I1{2,nX}(5,:))))).//(max([max(abs(real(I1{2,nX}(1,:)))),max(abs(real(I1{2,nX}(5,:))))]));
ToN1(:);
end
for m=NOmega:-1:1
H1a={real(I1{1,m}(1,:));[((real(BeN1{1,m}))./(max(abs(real(BeN1{1,m}))))));(((real(ToN1{1,m}))./(max(abs(real(ToN1{1,m})))))).*Xf)]};
H1b(:,m)=H1a;
end
HBFTFRF=(figure('units','normalized','outerposition',[0 0 1 1],'userdata',{H1b,OmegaA},'visible','off'));subplot(6,1,[1 2 3 4 5 6]);grid on,grid
minor,box on,axis on,set(gca,'FontSize', 35);hold on,
plot(H1(1,:),log10(abs(H1(2,:)))),'r.-','linewidth',2);hold on,plot(H1(1,:),log10(abs(H1(3,:))),'b.-','linewidth',2);hold
on,plot(H1(1,:),log10(abs(H1(4,:)))),'y.-','linewidth',2);
line([F1,F1],get(gca,'ylim'),'Color','r','linestyle','--','linewidth',1); line([F2,F2],get(gca,'ylim'),'Color','r','linestyle','--
','linewidth',1);
line([F3,F3],get(gca,'ylim'),'Color','r','linestyle','--','linewidth',1); line([F4,F4],get(gca,'ylim'),'Color','r','linestyle','--
','linewidth',1);
line([F5,F5],get(gca,'ylim'),'Color','r','linestyle','--','linewidth',1); line([F6,F6],get(gca,'ylim'),'Color','r','linestyle','--
','linewidth',1);
line([T1,T1],get(gca,'ylim'),'Color','b','linestyle','--','linewidth',1); line([L1,L1],get(gca,'ylim'),'Color','k','linestyle','--
','linewidth',1);
line([L2,L2],get(gca,'ylim'),'Color','k','linestyle','--','linewidth',1); line([L3,L3],get(gca,'ylim'),'Color','k','linestyle','--
','linewidth',1);
line([L4,L4],get(gca,'ylim'),'Color','k','linestyle','--','linewidth',1);
xlabel('Frequency domain range, [Hz]'); ylabel('Response amplitude, [m/s^2/N]'); legend('Bending','Torsion','Location','ne');
save NonRotaBanerjeeFT Ra Ea H1 H1b HBFTFRF
function dydx=fcn_ode(x,y,region)
         dydx=zeros(6,1); dydx(1)=y(2); dydx(2)=y(3); dydx(3)=y(4); dydx(5)=y(6);
for n=16:-1:1
    switch region
           case n
dydx(4)=(((Omega.^2*ma)*(y(1)-(X(n)*y(5))))/Ea(n));
dydx(6)=((Omega.^2*(-(Ia(n)*y(5))+(ma*X(n)*y(1))))/Ga(n));
           otherwise
    end
end
end
function res=fcn_bc(L,R)
  z1a=L(1,1);   z1b=R(1,1);   z2a=L(1,2);   z2b=R(1,2);   z3a=L(1,3);   z3b=R(1,3);   z4a=L(1, 4);  z4b=R(1, 4);   z5a=L(1, 5);   z5b=R(1, 5);
z6a=L(1, 6);   z6b=R(1, 6);
  u1a=L(2,1);   u1b=R(2,1);   u2a=L(2,2);   u2b=R(2,2);   u3a=L(2,3);   u3b=R(2,3);   u4a=L(2, 4);  u4b=R(2, 4);   u5a=L(2, 5);   u5b=R(2, 5);
u6a=L(2, 6);   u6b=R(2, 6);
  v1a=L(3,1);   v1b=R(3,1);   v2a=L(3,2);   v2b=R(3,2);   v3a=L(3,3);   v3b=R(3,3);   v4a=L(3, 4);  v4b=R(3, 4);   v5a=L(3, 5);   v5b=R(3, 5);
v6a=L(3, 6);   v6b=R(3, 6);
  w1a=L(4,1);   w1b=R(4,1);   w2a=L(4,2);   w2b=R(4,2);   w3a=L(4,3);   w3b=R(4,3);   w4a=L(4, 4);  w4b=R(4, 4);   w5a=L(4, 5);   w5b=R(4, 5);
w6a=L(4, 6);   w6b=R(4, 6);
 z11a=L(5,1);  z11b=R(5,1);  z12a=L(5,2);  z12b=R(5,2);  z13a=L(5,3);  z13b=R(5,3);  z14a=L(5, 4); z14b=R(5, 4);  z15a=L(5, 5);  z15b=R(5, 5);
z16a=L(5, 6);  z16b=R(5, 6);
 u11a=L(6,1);  u11b=R(6,1);  u12a=L(6,2);  u12b=R(6,2);  u13a=L(6,3);  u13b=R(6,3);  u14a=L(6, 4); u14b=R(6, 4);  u15a=L(6, 5);  u15b=R(6, 5);
u16a=L(6, 6);  u16b=R(6, 6);
  z7a=L(1,7);   z7b=R(1,7);   z8a=L(1,8);   z8b=R(1,8);   z9a=L(1,9);   z9b=R(1,9); z010a=L(1,10);z010b=R(1,10); z011a=L(1,11); z011b=R(1,11);
z012a=L(1,12); z012b=R(1,12);
  u7a=L(2,7);   u7b=R(2,7);   u8a=L(2,8);   u8b=R(2,8);   u9a=L(2,9);   u9b=R(2,9); u010a=L(2,10);u010b=R(2,10); u011a=L(2,11); u011b=R(2,11);
u012a=L(2,12); u012b=R(2,12);
  v7a=L(3,7);   v7b=R(3,7);   v8a=L(3,8);   v8b=R(3,8);   v9a=L(3,9);   v9b=R(3,9); v010a=L(3,10);v010b=R(3,10); v011a=L(3,11); v011b=R(3,11);
v012a=L(3,12); v012b=R(3,12);
  w7a=L(4,7);   w7b=R(4,7);   w8a=L(4,8);   w8b=R(4,8);   w9a=L(4,9);   w9b=R(4,9); w010a=L(4,10);w010b=R(4,10); w011a=L(4,11); w011b=R(4,11);
w012a=L(4,12); w012b=R(4,12);
 z17a=L(5,7);  z17b=R(5,7);  z18a=L(5,8);  z18b=R(5,8);  z19a=L(5,9);  z19b=R(5,9); z110a=L(5,10);z110b=R(5,10); z111a=L(5,11); z111b=R(5,11);
z112a=L(5,12); z112b=R(5,12);
 u17a=L(6,7);  u17b=R(6,7);  u18a=L(6,8);  u18b=R(6,8);  u19a=L(6,9);  u19b=R(6,9); u110a=L(6,10);u110b=R(6,10); u111a=L(6,11); u111b=R(6,11);
u112a=L(6,12); u112b=R(6,12);
z013a=L(1,13);z013b=R(1,13);z014a=L(1,14);z014b=R(1,14);z015a=L(1,15);z015b=R(1,15);z016a=L(1,16);z016b=R(1,16);
u013a=L(2,13);u013b=R(2,13);u014a=L(2,14);u014b=R(2,14);u015a=L(2,15);u015b=R(2,15);u016a=L(2,16);u016b=R(2,16);
v013a=L(3,13);v013b=R(3,13);v014a=L(3,14);v014b=R(3,14);v015a=L(3,15);v015b=R(3,15);v016a=L(3,16);v016b=R(3,16);
w013a=L(4,13);w013b=R(4,13);w014a=L(4,14);w014b=R(4,14);w015a=L(4,15);w015b=R(4,15);w016a=L(4,16);w016b=R(4,16);
z113a=L(5,13);z113b=R(5,13);z114a=L(5,14);z114b=R(5,14);z115a=L(5,15);z115b=R(5,15);z116a=L(5,16);z116b=R(5,16);
u113a=L(6,13);u113b=R(6,13);u114a=L(6,14);u114b=R(6,14);u115a=L(6,15);u115b=R(6,15);u116a=L(6,16);u116b=R(6,16);
%    Bending moment          Shear force                    Torsion moment
 C11L=((Ea(1) )*  v1b);  C21L=(0.0*  u1b)-((Ea(1) )*  w1b);  C31L=((Ga(1))* u11b);
 C11R=((Ea(2) )*  v2a);  C21R=(0.0*  u2a)-((Ea(2) )*  w2a);  C31R=((Ga(2))* u12a);
 C12L=((Ea(2) )*  v2b);  C22L=(0.0*  u2b)-((Ea(2) )*  w2b);  C32L=((Ga(2))* u12b);
 C12R=((Ea(3) )*  v3a);  C22R=(0.0*  u3a)-((Ea(3) )*  w3a);  C32R=((Ga(3))* u13a);
 C13L=((Ea(3) )*  v3b);  C23L=(0.0*  u3b)-((Ea(3) )*  w3b);  C33L=((Ga(3))* u13b);
 C13R=((Ea(4) )*  v4a);  C23R=(0.0*  u4a)-((Ea(4) )*  w4a);  C33R=((Ga(4))* u14a);
 C14L=((Ea(4) )*  v4b);  C24L=(0.0*  u4b)-((Ea(4) )*  w4b);  C34L=((Ga(4))* u14b);
 C14R=((Ea(5) )*  v5a);  C24R=(0.0*  u5a)-((Ea(5) )*  w5a);  C34R=((Ga(5))* u15a);
 C15L=((Ea(5) )*  v5b);  C25L=(0.0*  u5b)-((Ea(5) )*  w5b);  C35L=((Ga(5))* u15b);
 C15R=((Ea(6) )*  v6a);  C25R=(0.0*  u6a)-((Ea(6) )*  w6a);  C35R=((Ga(6))* u16a);
 C16L=((Ea(6) )*  v6b);  C26L=(0.0*  u6b)-((Ea(6) )*  w6b);  C36L=((Ga(6))* u16b);
 C16R=((Ea(7) )*  v7a);  C26R=(0.0*  u7a)-((Ea(7) )*  w7a);  C36R=((Ga(7))* u17a);
 C17L=((Ea(7) )*  v7b);  C27L=(0.0*  u7b)-((Ea(7) )*  w7b);  C37L=((Ga(7))* u17b);
 C17R=((Ea(8) )*  v8a);  C27R=(0.0*  u8a)-((Ea(8) )*  w8a);  C37R=((Ga(8))* u18a);
 C18L=((Ea(8) )*  v8b);  C28L=(0.0*  u8b)-((Ea(8) )*  w8b);  C38L=((Ga(8))* u18b);
 C18R=((Ea(9) )*  v9a);  C28R=(0.0*  u9a)-((Ea(9) )*  w9a);  C38R=((Ga(9))* u19a);
 C19L=((Ea(9) )*  v9b);  C29L=(0.0*  u9b)-((Ea(9) )*  w9b);  C39L=((Ga(9))* u19b);
 C19R=((Ea(10))*v010a);  C29R=(0.0*u010a)-((Ea(10))*w010a);  C39R=((Ga(10))*u110a);
```

```
C110L=((Ea(10))*v010b); C210L=(0.0*u010b)-((Ea(10))*w010b); C310L=((Ga(10))*u110b);
C110R=((Ea(11))*v011a); C210R=(0.0*u011a)-((Ea(11))*w011a); C310R=((Ga(11))*u111a);
C111L=((Ea(11))*v011b); C211L=(0.0*u011b)-((Ea(11))*w011b); C311L=((Ga(11))*u111b);
C111R=((Ea(12))*v012a)+BM5a; C211R=(0.0*u012a)-((Ea(12))*w012a)+WI5; C311R=((Ga(12))*u112a)+TM5;
C112L=((Ea(12))*v012b)+BM5b; C212L=(0.0*u012b)-((Ea(12))*w012b)+WI5; C312L=((Ga(12))*u112b)+TM5;
C112R=((Ea(13))*v013a)+BM4a; C212R=(0.0*u013a)-((Ea(13))*w013a)+WI4; C312R=((Ga(13))*u113a)+TM4;
C113L=((Ea(13))*v013b)+BM4b; C213L=(0.0*u013b)-((Ea(13))*w013b)+WI4; C313L=((Ga(13))*u113b)+TM4;
C113R=((Ea(14))*v014a)+BM3a; C213R=(0.0*u014a)-((Ea(14))*w014a)+WI3; C313R=((Ga(14))*u114a)+TM3;
C114L=((Ea(14))*v014b)+BM3b; C214L=(0.0*u014b)-((Ea(14))*w014b)+WI3; C314L=((Ga(14))*u114b)+TM3;
C114R=((Ea(15))*v015a)+BM2a; C214R=(0.0*u015a)-((Ea(15))*w015a)+WI2; C314R=((Ga(15))*u115a)+TM2;
C115L=((Ea(15))*v015b)+BM2b; C215L=(0.0*u015b)-((Ea(15))*w015b)+WI2; C315L=((Ga(15))*u115b)+TM2;
C115R=((Ea(16))*v016a)+BM1a; C215R=(0.0*u016a)-((Ea(16))*w016a)+WI1; C315R=((Ga(16))*u116a)+TM1;
C116R=(         v016b); C216R=(                    w016b); C316R=(         u116b);
if is_PL
% Bending moment
 PL116L=real(v6b  -((((+(PLm*(1i*Omega).^2*(z6b  +(D/2)*z16b +(B/2)*z16b +RA0*z16b +(AAL-(Q8-Q6) )*u6b  ))+(kPL1*(z6b  +(D/2)*z16b +(B/2)*z16b
+RA0*z16b +(AAL-(Q8-Q6) )*u6b  ))+(kPL1*3*(1i*Omega)*(z6b  +(D/2)*z16b +(B/2)*z16b +RA0*z16b +(AAL-(Q8-Q6) )*u6b  ))+WPL)*(AAL-(Q8-Q6)
))+WAAL*(AAL-(Q8-Q6) )/2+Wpl*(AAL-(Q8-Q6) ))/Ea(6)));
 PL116R=real(v7a  -((((+(PLm*(1i*Omega).^2*(z7a  +(D/2)*z17a +(B/2)*z17a +RAL*z17a +(AAL-(Q8-Q6) )*u7a  ))+(kPL1*(z7a  +(D/2)*z17a +(B/2)*z17a
+RAL*z17a +(AAL-(Q8-Q6) )*u7a  ))+(kPL1*3*(1i*Omega)*(z7a  +(D/2)*z17a +(B/2)*z17a +RAL*z17a +(AAL-(Q8-Q6) )*u7a  ))+WPL)*(AAL-(Q8-Q6)
))+WAAL*(AAL-(Q8-Q6) )/2+Wpl*(AAL-(Q8-Q6) ))/Ea(7)));
 PL117L=real(v7b  -((((+(PLm*(1i*Omega).^2*(z7b  +(D/2)*z17b +(B/2)*z17b +RAL*z17b +(AAL-(Q8-Q7) )*u7b  ))+(kPL1*(z7b  +(D/2)*z17b +(B/2)*z17b
+RAL*z17b +(AAL-(Q8-Q7) )*u7b  ))+(kPL1*3*(1i*Omega)*(z7b  +(D/2)*z17b +(B/2)*z17b +RAL*z17b +(AAL-(Q8-Q7) )*u7b  ))+WPL)*(AAL-(Q8-Q7)
))+WAAL*(AAL-(Q8-Q7) )/2+Wpl*(AAL-(Q8-Q7) ))/Ea(7)));
 PL117R=real(v8a  -((((+(PLm*(1i*Omega).^2*(z8a  +(D/2)*z18a +(B/2)*z18a +RAL*z18a +(AAL-(Q8-Q7) )*u8a  ))+(kPL1*(z8a  +(D/2)*z18a +(B/2)*z18a
+RAL*z18a +(AAL-(Q8-Q7) )*u8a  ))+(kPL1*3*(1i*Omega)*(z8a  +(D/2)*z18a +(B/2)*z18a +RAL*z18a +(AAL-(Q8-Q7) )*u8a  ))+WPL)*(AAL-(Q8-Q7)
))+WAAL*(AAL-(Q8-Q7) )/2+Wpl*(AAL-(Q8-Q7) ))/Ea(8)));
 PL118L=real(v8b  -((((+(PLm*(1i*Omega).^2*(z8b  +(D/2)*z18b +(B/2)*z18b +RAL*z18b +(AAL-(Q8-Q8) )*u8b  ))+(kPL1*(z8b  +(D/2)*z18b +(B/2)*z18b
+RAL*z18b +(AAL-(Q8-Q8) )*u8b  ))+(kPL1*3*(1i*Omega)*(z8b  +(D/2)*z18b +(B/2)*z18b +RAL*z18b +(AAL-(Q8-Q8) )*u8b  ))+WPL)*(AAL-(Q8-Q8)
))+WAAL*(AAL-(Q8-Q8) )/2+Wpl*(AAL-(Q8-Q8) ))/Ea(8)));
 PL118R=real(v9a  -((((+(PLm*(1i*Omega).^2*(z9a  +(D/2)*z19a +(B/2)*z19a +RAL*z19a +(AAL-(Q8-Q8) )*u9a  ))+(kPL1*(z9a  +(D/2)*z19a +(B/2)*z19a
+RAL*z19a +(AAL-(Q8-Q8) )*u9a  ))+(kPL1*3*(1i*Omega)*(z9a  +(D/2)*z19a +(B/2)*z19a +RAL*z19a +(AAL-(Q8-Q8) )*u9a  ))+WPL)*(AAL-(Q8-Q8)
))+WAAL*(AAL-(Q8-Q8) )/2+Wpl*(AAL-(Q8-Q8) ))/Ea(9)));
 PL119L=real(v9b  -((((+(PLm*(1i*Omega).^2*(z9b  +(D/2)*z19b +(B/2)*z19b +RAL*z19b +(AAL+(Q9-Q8) )*u9b  ))+(kPL1*(z9b  +(D/2)*z19b +(B/2)*z19b
+RAL*z19b +(AAL+(Q9-Q8) )*u9b  ))+(kPL1*3*(1i*Omega)*(z9b  +(D/2)*z19b +(B/2)*z19b +RAL*z19b +(AAL+(Q9-Q8) )*u9b  ))+WPL)*(AAL+(Q9-Q8)
))+WAAL*(AAL+(Q9-Q8) )/2+Wpl*(AAL+(Q9-Q8) ))/Ea(9)));
 PL119R=real(v010a-((((+(PLm*(1i*Omega).^2*(z010a+(D/2)*z110a+(B/2)*z110a+RAL*z110a+(AAL+(Q9-Q8)
)*u010a))+(kPL1*(z010a+(D/2)*z110a+(B/2)*z110a+RAL*z110a+(AAL+(Q9-Q8)
)*u010a))+(kPL1*3*(1i*Omega)*(z010a+(D/2)*z110a+(B/2)*z110a+RAL*z110a+(AAL+(Q9-Q8) )*u010a))+WPL)*(AAL+(Q9-Q8) ))+WAAL*(AAL+(Q9-Q8)
)/2+Wpl*(AAL+(Q9-Q8) ))/Ea(10)));
PL1110L=real(v010b-((((+(PLm*(1i*Omega).^2*(z010b+(D/2)*z110b+(B/2)*z110b+RAL*z110b+(AAL+(Q10-
Q8))*u010b))+(kPL1*(z010b+(D/2)*z110b+(B/2)*z110b+RAL*z110b+(AAL+(Q10-
Q8))*u010b))+(kPL1*3*(1i*Omega)*(z010b+(D/2)*z110b+(B/2)*z110b+RAL*z110b+(AAL+(Q10-Q8))*u010b))+WPL)*(AAL+(Q10-Q8)))+WAAL*(AAL+(Q10-
Q8))/2+Wpl*(AAL+(Q10-Q8)))/Ea(10)));
PL1110R=real(v011a-((((+(PLm*(1i*Omega).^2*(z011a+(D/2)*z111a+(B/2)*z111a+RA0*z111a+(AAL+(Q10-
Q8))*u011a))+(kPL1*(z011a+(D/2)*z111a+(B/2)*z111a+RA0*z111a+(AAL+(Q10-
Q8))*u011a))+(kPL1*3*(1i*Omega)*(z011a+(D/2)*z111a+(B/2)*z111a+RA0*z111a+(AAL+(Q10-Q8))*u011a))+WPL)*(AAL+(Q10-Q8)))+WAAL*(AAL+(Q10-
Q8))/2+Wpl*(AAL+(Q10-Q8)))/Ea(11)));
% Shear force
 PL126L=real(w6b  +(((+(PLm*(1i*Omega).^2*(z6b  +(D/2)*z16b +(B/2)*z16b +RA0*z16b +(AAL-(Q8-Q6) )*u6b  ))+(kPL1*(z6b  +(D/2)*z16b +(B/2)*z16b
+RA0*z16b +(AAL-(Q8-Q6) )*u6b  ))+(kPL1*3*(1i*Omega)*(z6b  +(D/2)*z16b +(B/2)*z16b +RA0*z16b +(AAL-(Q8-Q6) )*u6b  ))+WPL-(0.0*u6b)
+WAAL+WRAL+Wpl)/Ea(6))));
 PL126R=real(w7a  +(((+(PLm*(1i*Omega).^2*(z7a  +(D/2)*z17a +(B/2)*z17a +RAL*z17a +(AAL-(Q8-Q6) )*u7a  ))+(kPL1*(z7a  +(D/2)*z17a +(B/2)*z17a
+RAL*z17a +(AAL-(Q8-Q6) )*u7a  ))+(kPL1*3*(1i*Omega)*(z7a  +(D/2)*z17a +(B/2)*z17a +RAL*z17a +(AAL-(Q8-Q6) )*u7a  ))+WPL-(0.0*u7a)
+WAAL+WRAL+Wpl)/Ea(7))));
 PL127L=real(w7b  +(((+(PLm*(1i*Omega).^2*(z7b  +(D/2)*z17b +(B/2)*z17b +RAL*z17b +(AAL-(Q8-Q7) )*u7b  ))+(kPL1*(z7b  +(D/2)*z17b +(B/2)*z17b
+RAL*z17b +(AAL-(Q8-Q7) )*u7b  ))+(kPL1*3*(1i*Omega)*(z7b  +(D/2)*z17b +(B/2)*z17b +RAL*z17b +(AAL-(Q8-Q7) )*u7b  ))+WPL-(0.0*u7b)
+WAAL+WRAL+Wpl)/Ea(7))));
 PL127R=real(w8a  +(((+(PLm*(1i*Omega).^2*(z8a  +(D/2)*z18a +(B/2)*z18a +RAL*z18a +(AAL-(Q8-Q7) )*u8a  ))+(kPL1*(z8a  +(D/2)*z18a +(B/2)*z18a
+RAL*z18a +(AAL-(Q8-Q7) )*u8a  ))+(kPL1*3*(1i*Omega)*(z8a  +(D/2)*z18a +(B/2)*z18a +RAL*z18a +(AAL-(Q8-Q7) )*u8a  ))+WPL-(0.0*u8a)
+WAAL+WRAL+Wpl)/Ea(8))));
 PL128L=real(w8b  +(((+(PLm*(1i*Omega).^2*(z8b  +(D/2)*z18b +(B/2)*z18b +RAL*z18b +(AAL-(Q8-Q8) )*u8b  ))+(kPL1*(z8b  +(D/2)*z18b +(B/2)*z18b
+RAL*z18b +(AAL-(Q8-Q8) )*u8b  ))+(kPL1*3*(1i*Omega)*(z8b  +(D/2)*z18b +(B/2)*z18b +RAL*z18b +(AAL-(Q8-Q8) )*u8b  ))+WPL-(0.0*u8b)
+WAAL+WRAL+Wpl)/Ea(8))));
 PL128R=real(w9a  +(((+(PLm*(1i*Omega).^2*(z9a  +(D/2)*z19a +(B/2)*z19a +RAL*z19a +(AAL-(Q8-Q8) )*u9a  ))+(kPL1*(z9a  +(D/2)*z19a +(B/2)*z19a
+RAL*z19a +(AAL-(Q8-Q8) )*u9a  ))+(kPL1*3*(1i*Omega)*(z9a  +(D/2)*z19a +(B/2)*z19a +RAL*z19a +(AAL-(Q8-Q8) )*u9a  ))+WPL-(0.0*u9a)
+WAAL+WRAL+Wpl)/Ea(9))));
 PL129L=real(w9b  +(((+(PLm*(1i*Omega).^2*(z9b  +(D/2)*z19b +(B/2)*z19b +RAL*z19b +(AAL+(Q9-Q8) )*u9b  ))+(kPL1*(z9b  +(D/2)*z19b +(B/2)*z19b
+RAL*z19b +(AAL+(Q9-Q8) )*u9b  ))+(kPL1*3*(1i*Omega)*(z9b  +(D/2)*z19b +(B/2)*z19b +RAL*z19b +(AAL+(Q9-Q8) )*u9b  ))+WPL-(0.0*u9b)
+WAAL+WRAL+Wpl)/Ea(9))));
 PL129R=real(w010a+(((+(PLm*(1i*Omega).^2*(z010a+(D/2)*z110a+(B/2)*z110a+RAL*z110a+(AAL+(Q9-Q8)
)*u010a))+(kPL1*(z010a+(D/2)*z110a+(B/2)*z110a+RAL*z110a+(AAL+(Q9-Q8)
)*u010a))+(kPL1*3*(1i*Omega)*(z010a+(D/2)*z110a+(B/2)*z110a+RAL*z110a+(AAL+(Q9-Q8) )*u010a))+WPL-(0.0*u010a)+WAAL+WRAL+Wpl)/Ea(10))));
PL1210L=real(w010b+(((+(PLm*(1i*Omega).^2*(z010b+(D/2)*z110b+(B/2)*z110b+RAL*z110b+(AAL+(Q10-
Q8))*u010b))+(kPL1*(z010b+(D/2)*z110b+(B/2)*z110b+RAL*z110b+(AAL+(Q10-
Q8))*u010b))+(kPL1*3*(1i*Omega)*(z010b+(D/2)*z110b+(B/2)*z110b+RAL*z110b+(AAL+(Q10-Q8))*u010b))+WPL-(0.0*u010b)+WAAL+WRAL+Wpl)/Ea(10))));
PL1210R=real(w011a+(((+(PLm*(1i*Omega).^2*(z011a+(D/2)*z111a+(B/2)*z111a+RA0*z111a+(AAL+(Q10-
Q8))*u011a))+(kPL1*3*(1i*Omega)*(z011a+(D/2)*z111a+(B/2)*z111a+RA0*z111a+(AAL+(Q10-Q8))*u011a))+WPL-(0.0*u011a)+WAAL+WRAL+Wpl)/Ea(11))));
% Torsional moment
 PL136L=real(u16b -((((+(PLm*(1i*Omega).^2*(z6b  +(D/2)*z16b +(B/2)*z16b +RA0*z16b +(AAL-(Q8-Q6) )*u6b  ))+(kPL1*(z6b  +(D/2)*z16b +(B/2)*z16b
+RA0*z16b +(AAL-(Q8-Q6) )*u6b  ))+(kPL1*3*(1i*Omega)*(z6b  +(D/2)*z16b +(B/2)*z16b +RA0*z16b +(AAL-(Q8-Q6) )*u6b
))+WPL)*RA0)+WRAL*(RA0/2)+WAAL*RA0+Wpl*RA0)/Ga(6)));
 PL136R=real(u17a -((((+(PLm*(1i*Omega).^2*(z7a  +(D/2)*z17a +(B/2)*z17a +RAL*z17a +(AAL-(Q8-Q6) )*u7a  ))+(kPL1*(z7a  +(D/2)*z17a +(B/2)*z17a
+RAL*z17a +(AAL-(Q8-Q6) )*u7a  ))+(kPL1*3*(1i*Omega)*(z7a  +(D/2)*z17a +(B/2)*z17a +RAL*z17a +(AAL-(Q8-Q6) )*u7a
))+WPL)*RAL)+WRAL*(RAL/2)+WAAL*RAL+Wpl*RAL)/Ga(7)));
 PL137L=real(u17b -((((+(PLm*(1i*Omega).^2*(z7b  +(D/2)*z17b +(B/2)*z17b +RAL*z17b +(AAL-(Q8-Q7) )*u7b  ))+(kPL1*(z7b  +(D/2)*z17b +(B/2)*z17b
+RAL*z17b +(AAL-(Q8-Q7) )*u7b  ))+(kPL1*3*(1i*Omega)*(z7b  +(D/2)*z17b +(B/2)*z17b +RAL*z17b +(AAL-(Q8-Q7) )*u7b
))+WPL)*RAL)+WRAL*(RAL/2)+WAAL*RAL+Wpl*RAL)/Ga(7)));
 PL137R=real(u18a -((((+(PLm*(1i*Omega).^2*(z8a  +(D/2)*z18a +(B/2)*z18a +RAL*z18a +(AAL-(Q8-Q7) )*u8a  ))+(kPL1*(z8a  +(D/2)*z18a +(B/2)*z18a
+RAL*z18a +(AAL-(Q8-Q7) )*u8a  ))+(kPL1*3*(1i*Omega)*(z8a  +(D/2)*z18a +(B/2)*z18a +RAL*z18a +(AAL-(Q8-Q7) )*u8a
))+WPL)*RAL)+WRAL*(RAL/2)+WAAL*RAL+Wpl*RAL)/Ga(8)));
 PL138L=real(u18b -((((+(PLm*(1i*Omega).^2*(z8b  +(D/2)*z18b +(B/2)*z18b +RAL*z18b +(AAL-(Q8-Q8) )*u8b  ))+(kPL1*(z8b  +(D/2)*z18b +(B/2)*z18b
+RAL*z18b +(AAL-(Q8-Q8) )*u8b  ))+(kPL1*3*(1i*Omega)*(z8b  +(D/2)*z18b +(B/2)*z18b +RAL*z18b +(AAL-(Q8-Q8) )*u8b
))+WPL)*RAL)+WRAL*(RAL/2)+WAAL*RAL+Wpl*RAL)/Ga(8)));
 PL138R=real(u19a -((((+(PLm*(1i*Omega).^2*(z9a  +(D/2)*z19a +(B/2)*z19a +RAL*z19a +(AAL-(Q8-Q8) )*u9a  ))+(kPL1*(z9a  +(D/2)*z19a +(B/2)*z19a
+RAL*z19a +(AAL-(Q8-Q8) )*u9a  ))+(kPL1*3*(1i*Omega)*(z9a  +(D/2)*z19a +(B/2)*z19a +RAL*z19a +(AAL-(Q8-Q8) )*u9a
))+WPL)*RAL)+WRAL*(RAL/2)+WAAL*RAL+Wpl*RAL)/Ga(9)));
 PL139L=real(u19b -((((+(PLm*(1i*Omega).^2*(z9b  +(D/2)*z19b +(B/2)*z19b +RAL*z19b +(AAL+(Q9-Q8) )*u9b  ))+(kPL1*(z9b  +(D/2)*z19b +(B/2)*z19b
+RAL*z19b +(AAL+(Q9-Q8) )*u9b  ))+(kPL1*3*(1i*Omega)*(z9b  +(D/2)*z19b +(B/2)*z19b +RAL*z19b +(AAL+(Q9-Q8) )*u9b
))+WPL)*RAL)+WRAL*(RAL/2)+WAAL*RAL+Wpl*RAL)/Ga(9)));
 PL139R=real(u110a-((((+(PLm*(1i*Omega).^2*(z010a+(D/2)*z110a+(B/2)*z110a+RAL*z110a+(AAL+(Q9-Q8)
)*u010a))+(kPL1*(z010a+(D/2)*z110a+(B/2)*z110a+RAL*z110a+(AAL+(Q9-Q8)
)*u010a))+(kPL1*3*(1i*Omega)*(z010a+(D/2)*z110a+(B/2)*z110a+RAL*z110a+(AAL+(Q9-Q8) )*u010a))+WPL)*RAL)+WRAL*(RAL/2)+WAAL*RAL+Wpl*RAL)/Ga(10)));
PL1310L=real(u110b-((((+(PLm*(1i*Omega).^2*(z010b+(D/2)*z110b+(B/2)*z110b+RAL*z110b+(AAL+(Q10-
Q8))*u010b))+(kPL1*(z010b+(D/2)*z110b+(B/2)*z110b+RAL*z110b+(AAL+(Q10-
Q8))*u010b))+(kPL1*3*(1i*Omega)*(z010b+(D/2)*z110b+(B/2)*z110b+RAL*z110b+(AAL+(Q10-
Q8))*u010b))+WPL)*RAL)+WRAL*(RAL/2)+WAAL*RAL+Wpl*RAL)/Ga(10)));
PL1310R=real(u111a-((((+(PLm*(1i*Omega).^2*(z011a+(D/2)*z111a+(B/2)*z111a+RA0*z111a+(AAL+(Q10-
Q8))*u011a))+(kPL1*(z011a+(D/2)*z111a+(B/2)*z111a+RA0*z111a+(AAL+(Q10-
Q8))*u011a))+(kPL1*3*(1i*Omega)*(z011a+(D/2)*z111a+(B/2)*z111a+RA0*z111a+(AAL+(Q10-
Q8))*u011a))+WPL)*RA0)+WRAL*(RA0/2)+WAAL*RA0+Wpl*RA0)/Ga(11)));
else PL116L=C16L;PL126L=C26L;PL136L=C36L;  PL117L=C17L;PL127L=C27L;PL137L=C37L;  PL118L=C18L;PL128L=C28L;PL138L=C38L;
PL119L=C19L;PL129L=C29L;PL139L=C39L;  PL1110L=C110L;PL1210L=C210L;PL1310L=C310L;
     PL116R=C16R;PL126R=C26R;PL136R=C36R;  PL117R=C17R;PL127R=C27R;PL137R=C37R;  PL118R=C18R;PL128R=C28R;PL138R=C38R;
PL119R=C19R;PL129R=C29R;PL139R=C39R;  PL1110R=C110R;PL1210R=C210R;PL1310R=C310R;
end
PF=1;M2T=1*Xf;
  res=[z1a;       u1a;       z11a;
       z2a-  z1b;  u2a-  u1b; z12a- z11b;  C11R- C11L; C21R- C21L; C31R- C31L;
       z3a-  z2b;  u3a-  u2b; z13a- z12b;  C12R- C12L; C22R- C22L; C32R- C32L;
       z4a-  z3b;  u4a-  u3b; z14a- z13b;  C13R- C13L; C23R- C23L; C33R- C33L;
       z5a-  z4b;  u5a-  u4b; z15a- z14b;  C14R- C14L; C24R- C24L; C34R- C34L;
```

```
      z6a-  z5b;  u6a-  u5b; z16a- z15b;  C15R- C15L; C25R- C25L; C35R- C35L;
      z7a-  z6b;  u7a-  u6b; z17a- z16b;  PL116R-PL116L;  PL126R-PL126L;  PL136R-PL136L;
      z8a-  z7b;  u8a-  u7b; z18a- z17b;  PL117R-PL117L;  PL127R-PL127L;  PL137R-PL137L;
      z9a-  z8b;  u9a-  u8b; z19a- z18b;  PL118R-PL118L;  PL128R-PL128L;  PL138R-PL138L;
    z010a-  z9b;u010a-  u9b;z110a- z19b;  PL119R-PL119L;  PL129R-PL129L;  PL139R-PL139L;
    z011a-z010b;u011a-u010b;z111a-z110b; PL1110R-PL1110L;PL1210R-PL1210L;PL1310R-PL1310L;
    z012a-z011b;u012a-u011b;z112a-z111b; C111R-C111L;C211R-C211L;C311R-C311L;
    z013a-z012b;u013a-u012b;z113a-z112b; C112R-C112L;C212R-C212L;C312R-C312L;
    z014a-z013b;u014a-u013b;z114a-z113b; C113R-C113L;C213R-C213L;C313R-C313L;
    z015a-z014b;u015a-u014b;z115a-z114b; C114R-C114L;C214R-C214L;C314R-C314L;
    z016a-z015b;u016a-u015b;z116a-z115b; C115R-C115L;C215R-C215L;C315R-C315L;
                                         C116R;      C216R-PF;   C316R-M2T];
end
disp(' '); disp(' - Zakanchivatsya - '); disp(' ');
end
```